

12-2015

Prediction of Laser Ablation in Brain: Sensitivity, Calibration, and Validation

Samuel J. Fahrenholtz

Follow this and additional works at: https://digitalcommons.library.tmc.edu/utgsbs_dissertations



Part of the [Numerical Analysis and Scientific Computing Commons](#), and the [Translational Medical Research Commons](#)

Recommended Citation

Fahrenholtz, Samuel J., "Prediction of Laser Ablation in Brain: Sensitivity, Calibration, and Validation" (2015). *The University of Texas MD Anderson Cancer Center UTHealth Graduate School of Biomedical Sciences Dissertations and Theses (Open Access)*. 610.
https://digitalcommons.library.tmc.edu/utgsbs_dissertations/610

This Dissertation (PhD) is brought to you for free and open access by the The University of Texas MD Anderson Cancer Center UTHealth Graduate School of Biomedical Sciences at DigitalCommons@TMC. It has been accepted for inclusion in The University of Texas MD Anderson Cancer Center UTHealth Graduate School of Biomedical Sciences Dissertations and Theses (Open Access) by an authorized administrator of DigitalCommons@TMC. For more information, please contact digitalcommons@library.tmc.edu.

PREDICTION OF LASER ABLATION IN BRAIN: SENSITIVITY, CALIBRATION, AND VALIDATION

by

Samuel John Fahrenholtz, B.Sc.

APPROVED:

R. Jason Stafford, Ph.D.
Advisory Professor

James Bankson, Ph.D.

David Thomas Alfonso Fuentes, Ph.D.

John D. Hazle, Ph.D.

Arvind Rao, Ph.D.

APPROVED:

Dean, The University of Texas
Graduate School of Biomedical Sciences at Houston

PREDICTION OF LASER ABLATION IN BRAIN: SENSITIVITY, CALIBRATION, AND VALIDATION

A DISSERTATION

Presented to the Faculty of
The University of Texas
Health Science Center at Houston
and
The University of Texas
M. D. Anderson Cancer Center
Graduate School of Biomedical Sciences
in Partial Fulfillment

of the Requirements

for the Degree of

DOCTOR OF PHILOSOPHY

by

Samuel John Fahrenholtz
B.Sc., Kansas State University, 2009
Houston, Texas

December 2015

©Copyright by Samuel John Fahrenholtz, 2015.
All rights reserved.

In the style of Johann Sebastian Bach,



Acknowledgments

I thank R. Jason Stafford, PhD, for claiming me as I vacillated through times of shameful helplessness and brilliant autonomy. I thank David Fuentes, PhD, for directing me to fruitful computational tools and skepticism, enabling *eureka!* moments. I thank John D. Hazle, PhD, for his leadership at MD Anderson and within the AAPM, providing a community capable of so much innovation and service. I thank Jim Bankson, PhD, for his affable yet rigorous approach to working in research. I thank Arvind Rao, PhD, for being a data scientist with whom I can communicate.

I thank my undergraduate peers for suffering through myriad late nights and pizza runs — Frank Male and Josh McIlvain. I thank my medical physics peers, especially the scrubs of SCRB3. I also thank scientific mentors of the past. In particular, Drs. Itzik Ben-Itzhak and Tobin Munsat who provided me opportunity in their labs without expectation. I am grateful to Drs. Weaver, Sorensen, Corwin, and Washburn for their generous style of pedagogy. I thank my uncle, Robert John, for sparking a quest for knowledge in fourth grade by introducing Kepler's laws and giving me a physics workbook.

I thank my church community at West University Baptist for none succeed apart from the Body. I thank my wife for her support and commiseration through graduate studies. I am eager to see our future adventures unfold.

I thank my fellowship program, TL1TR000369 of the National Center for Translational Sciences of the National Institutes of Health. The director Dr. Hood and mentors Deans Barton and Blackburn provided practical advice and understood the frustrations of academic training without losing the zeal to discover and solve problems. The fellowship training elucidated the process of translating discoveries and techniques into the clinic. This dovetails with the ultimate desire and gestalt of my life's work: to help people via physics.

Abstract

The surgical planning of MR-guided laser induced thermal therapy (MRgLITT) stands to benefit from predictive computational modeling. The dearth of physical model parameter data leads to modeling uncertainty. This work implements a well-accepted framework with three key steps for model-building: model-parameter sensitivity analysis, model calibration, and model validation.

The sensitivity study is via generalized polynomial chaos (gPC) paired with a transient finite element (FEM) model. Uniform probability distribution functions (PDFs) capture the plausible range of values suggested by the literature for five model parameters. The five PDFs are input separately into the FEM model to gain a probabilistic sensitivity response of the model to the input PDFs. The result demonstrates the model output variance is dominated by the three optical parameters and the two remaining parameters contribute less.

The second aim is model calibration, given the need to acquire model parameter data of greater precision sans physical measurement. The availability of a relatively large cohort of $N = 22$ clinical laser ablations of metastases gradient-based inverse problems provides inference of the optical parameter values, the most sensitive parameter as indicated by gPC, from patient MR temperature imaging (MRTI). In order to accelerate the bioheat model for iteration during parameter optimization, two simplified models are conceived: (1) a homogeneous, transient FEM model implemented on GPU and (2) a homogeneous, steady-state, analytic model implemented on GPU. After model optimization — i.e., calibration — the model validation immediately follows via leave-one-out cross-validation (LOOCV). LOOCV compares the two trained models' predictive performances. During LOOCV, the FEM model correctly predicts 15 of 22; the steady state model correctly predicts 17 of 22. A steady state model using naïve literature values correctly predicts only 10 of 22. When training on an $N = 20$ cohort tailored to only include ablations near steady state, the trained steady state model correctly predicts 19 of 20 patient datasets versus the 8 of 20 predicted by an untrained steady state model.

The conclusion is model training is an effective means of improving model performance when there is lack of accurate and precise parameter data in the literature, especially when there is little prospect of improving data quality. A key to success in this model-training paradigm is to have a training/calibration cohort that has adequate similarity to the predicted/validation cohort.

Table of Contents

Acknowledgments	v
Abstract	vi
Table of Contents	vii
List of Figures	x
List of Tables	xii
Abbreviations	xiv
1 Introduction	1
1.1 Hypothesis	3
1.2 Specific aims	4
1.3 Dissertation organization	4
2 Background	6
2.1 Hyperthermia, ablation, and minimally invasive interventions	7
2.2 MR-guided laser induced thermal therapy in brain	8
2.2.1 MRgLITT in oncology	8
2.2.2 Epileptogenic foci	10
2.2.3 Imaging and surgical technique	12
2.3 Thermal damage models	13
2.3.1 Arrhenius process	13
2.3.2 Thermal dose: an example	14
2.3.3 Cumulative equivalent minutes	15
2.3.4 Lethal threshold temperature	16
3 Generalised polynomial chaos-based uncertainty quantification for planning MRgLITT procedures	19
3.1 Abstract	20
3.2 Introduction	21
3.3 Methods	24
3.3.1 Mathematical model of uncertainty	24

3.3.2	Constitutive data	30
3.3.3	Optical parameter uncertainty	30
3.3.4	Multiplanar magnetic resonance thermal imaging in phantom and animal models	31
3.3.5	Computational methods	34
3.4	Results	36
3.5	Discussion	41
4	A Model Evaluation Study for Treatment Planning of Laser Induced Thermal Therapy	46
4.1	Abstract	47
4.2	Introduction	47
4.3	Methods	50
4.3.1	Thermometry data	50
4.3.2	Simulation of bioheat transfer within laser irradiated tissue	52
4.3.3	Analytic steady state solution	54
4.3.4	Model calibration	55
4.3.5	Leave-one-out cross-validation	57
4.4	Results	62
4.5	Discussion	64
4.6	Conclusion	68
5	A global search-based optimization and prediction paradigm for laser ablation	70
5.1	Introduction	70
5.2	Methods	71
5.2.1	Inverse problem	71
5.2.2	Patient datasets	72
5.2.3	Description of the steady state model	72
5.2.4	Objective functions	79
5.2.5	Global parameter search in μ_{eff} - ω space	80
5.2.6	Leave-one-out cross-validation and vector map manipulation	81
5.3	Results	87
5.3.1	Characterization of steady state model kernel	87
5.3.2	Optimization	87
5.3.3	Leave-one-out cross-validation performance	88
5.4	Discussion	89

5.5 Conclusion	94
6 Conclusion	97
Appendix A: 2D optimization of MRTI datasets	102
Appendix B: Additional results for Chapter 5	133
Appendix C: Alternate patient cohort and validation results	140
Bibliography	146
Vita	178

List of Figures

1.1	Treatment of brain metastasis	3
3.1	Non-linear constitutive model	27
3.2	Sensitivity of temperature	33
3.3	Phantom experiment	35
3.4	Temporal profiles	36
3.5	Spatial profiles of temperature in canines	39
3.6	Stochastic isotherm contours in canines	40
4.1	Visualase [®] applicator	59
4.2	Representative result	60
4.3	Histogram of optimized parameters	60
4.4	DSC performance during optimization and leave-one-out cross-validation	64
5.1	Superposition of individual 2D global optimizations	86
5.2	Descriptive statistics maps of global optimization	88
5.3	Choice of parameters during LOOCV	95
5.4	Choice of parameters during LOOCV	96
A.1	MRTI dataset #0495 summary	103
A.2	MRTI dataset #0415 summary	104
A.3	MRTI dataset #0435 summary	105
A.4	MRTI dataset #0440 summary	106
A.5	MRTI dataset #0447 summary	107
A.6	MRTI dataset #0436 summary	108
A.7	MRTI dataset #0457 summary	109
A.8	MRTI dataset #0497 summary	110
A.9	MRTI dataset #0409 summary	111
A.10	MRTI dataset #0466 summary	112
A.11	MRTI dataset #0468 summary	113
A.12	MRTI dataset #0471 summary	114

A.13 MRTI dataset #0476 summary	115
A.14 MRTI dataset #0417 summary	116
A.15 MRTI dataset #0477 summary	117
A.16 MRTI dataset #0488 summary	118
A.17 MRTI dataset #0491 summary	119
A.18 MRTI dataset #0496 summary	120
A.19 MRTI dataset #0490 summary	121
A.20 MRTI dataset #0378 summary	122
A.21 MRTI dataset #0402 summary	123
A.22 MRTI dataset #0389 summary	124
A.23 MRTI dataset #0385 summary	125
A.24 MRTI dataset #0438 summary	126
A.25 MRTI dataset #0455 summary	127
A.26 MRTI dataset #0453 summary	128
A.27 MRTI dataset #0450 summary	129
A.28 MRTI dataset #0451 summary	130
A.29 MRTI dataset #0418 summary	131
A.30 MRTI dataset #0414 summary	132
B.1 Temperature field from a single isotropic point	134
B.2 2D temperature profiles	135
B.3 Approximation of a line source	136
B.4 Linearity of temperature field with applied laser power	137
B.5 Mean map of L_2 optimization	138
B.6 Mean map of Hausdorff distance	139
C.1 Leave-one-out cross-validation; $N = 20$ cohort	146

List of Tables

3.1	Constitutive data	28
3.1	Constitutive data	29
4.1	Constitutive data	53
4.2	Percentile performance	61
4.3	DSC threshold performance	63
5.1	Constitutive data	77
5.2	Convergence of increasing isotropic point sources	83
5.3	Descriptive statistics performance for $N = 22$ datasets during optimization	84
5.4	Descriptive statistics performance for $N = 22$ datasets during LOOCV . .	85
C.1	MRTI dataset exclusion	141
C.2	MRTI dataset differences between Chapter 4 and 5	142
C.3	Descriptive statistics performance for $N=20$ datasets	144
C.4	DSC threshold performance for $N = 20$ datasets	144
C.5	Descriptive statistics performance comparing two LOOCV algorithms . . .	145

Abbreviations

CA Cryoablation. [x](#), [6](#), *Glossary:* [Cryoablation](#)

CEM Cumulative equivalent minutes. *Section 2.3.3.* [x](#)

CT Computed tomography. [x](#), [xiii](#), [10](#)

DSC Dice similarity coefficient. [x](#), [15](#), *Glossary:* [Dice similarity coefficient](#)

ECoG Electrocorticography. [x](#), [9](#)

EF Epileptogenic focus. [9](#), *Glossary:* [Epileptogenic focus \(EF\)](#)

HGG High grade glioma. [x](#), [xvii](#), [xviii](#), [7](#), *Glossary:* [High grade glioma](#)

HIFU High-intensity focused ultrasound. [x](#), [xiii](#), [xv](#), [6](#), [15](#), *Glossary:* [High-intensity focused ultrasound](#)

icEEG Intracranial electroencephalogram. [x](#), [9](#)

iMRI Intraoperative MRI. [x](#), [11](#), *Glossary:* [Intraoperative MRI](#)

LTtDM Lethal threshold temperature damage model. *Section 2.3.4.* [x](#), [15](#)

MRgLITT Magnetic resonance-guided laser induced thermal therapy. [x](#), [1](#), [15](#)

MRTI Magnetic resonance temperature imaging. [x](#), [xviii](#), [10](#), [14](#), [15](#), *Glossary:* [Magnetic resonance temperature imaging](#)

MWA Microwave ablation. [x](#), [6](#), *Glossary:* [Microwave](#)

NMR Nuclear magnetic resonance. [x](#), [10](#), *Glossary:* [Nuclear magnetic resonance](#)

PRF Proton resonance frequency. [x](#), [xvii](#), [10](#)

RF Radiofrequency. [x](#), [xvi](#), *Glossary:* [Radiofrequency](#)

RFA Radiofrequency ablation. [x](#), [xvi](#), [xvii](#), [6](#), [15](#), *Glossary:* [Radiofrequency](#)

SRS Stereotactic radiosurgery. [x](#), [1](#), [8](#), *Glossary:* [Stereotactic radiosurgery](#)

WBRT Whole brain radiation therapy. [x](#), [1](#), *Glossary:* [Whole brain radiation therapy](#)

Glossary

Capacitive heating Capacitive heating is a noninvasive modality of dielectric heating via electromagnetic waves. Capacitive heating is used to create hyperthermic temperatures, e.g., 42 °C, in large body regions. For superficial applicators, designs include multiple channels arranged in multiple rings surrounding a length of axial body positions, e.g., three rings with four channels each. Within the rings, there is a bolus of deionized water to mediate power delivery. Devices' power outputs are in the range of 400 W to 1600 W and oscillate at 100 MHz [1,2]. There also exist interstitial applicators. [x](#), [6](#)

Catheter-based ultrasonic device An acoustic thermal ablation device that gains access to targets via body lumina, including major vasculature, or percutaneous minimally invasive surgery. These devices have a variety of designs that include independently operating elements that can be directed. Once the device is positioned, heat delivery takes about 10 min to 30 min. Since catheter-based ultrasonic devices are placed proximal to their targets, they use higher acoustic frequencies than [high-intensity focused ultrasound \(HIFU\)](#) and operate at 8 MHz to 10 MHz [3–5]. [x](#), [6](#), [15](#)

Chemical ablation Chemical ablation is the injection of substances, either acetic acid or more commonly ethanol, to induce tissue death. As an example, percutaneous ethanol injection (PEI) uses a 22-gauge needle to access a target lesion, commonly hepatocellular carcinomas. Through the needle, 2 ml to 5 ml of nearly pure ethanol is injected, depending on lesion size. The procedure requires multiple surgical sessions for efficacy. Guidance is via ultrasound or [computed tomography \(CT\)](#) [6,7]. [x](#), [6](#)

Critical structure Critical structures are healthy tissues and/or organs that have been deemed essential to the patients survival or quality of life. A proposed intervention cannot impose undue damage to those tissues and/or organs. In radiation therapy, this concept manifests as dose limits. [x](#), [2](#)

Cryoablation Cryoablation uses interstitial probes to access target lesions. Liquid nitrogen or argon cool the tip to −125 °C and −187 °C, respectively. Argon-based devices have thinner diameters. Another innovation is the use of heated helium gas (67 °C) in order to speed the necessary thawing [6,8]. [x](#)

Dice similarity coefficient The Dice similarity coefficient (DSC) was proposed by Dice [9] and has been used extensively in imaging science. Its equation is defined in [the text](#). The purpose of the DSC is to quantify the overlap of two binary masks. A valuable property of the DSC is that it does not count true negatives, i.e., coincident zero values in the binary masks. [x](#)

Evidence-based medicine Evidence-based medicine is a preeminent idea in the healing arts that demands patient care decisions be driven by data. Common difficulties in following this simple idea is the dearth of definitive data or conflicting data. To resolve this dilemma, various experts and groups of experts have suggested hierarchies of data, called **levels of evidence**. An example of a lower level of evidence is a case study or medical practice guidelines informed by the gestalt of tradition. A high level of evidence is a randomized controlled trial; the highest level is usually considered a meta-analysis of randomized controlled trials. A capable introduction can be found in [10]. [x](#), [7](#)

High grade glioma A classification of particularly dangerous primary brain neoplasms, i.e., anaplastic astrocytomas (Grade III astrocytoma) and glioblastomas (Grade IV astrocytoma). The same novel and standard of care interventions are often applied to both disease groups, so the classification of high grade glioma is used. [x](#), [xvii](#)

High-intensity focused ultrasound Modern [HIFU](#) uses phased array piezoelectric elements to direct acoustic waves into a target lesion. The purpose is either heating or mechanical disruption of the tissue. Heating can be for hyperthermia, ablation, or release of a targeting drug. Mechanical disruption is for the purpose of targeted drug release or transient tissue alteration, such as disrupting the blood brain barrier. [HIFU](#) is noninvasive, an obvious clinical boon. In order to reach the target tissue, acoustic frequencies are typically 1.0 MHz to 1.5 MHz with the extremes ranging from 0.6 MHz to 7 MHz [3]. [x](#)

Intraoperative MRI An iMRI suite is the combination of an operating room and a surgery-dedicated MRI. There exist iMRI designs that are expressly designed for neurosurgery, e.g., the BrainSUITE. [x](#)

Irreversible electroporation A percutaneous ablation modality that uses electric pulses to introduce pores into affected cells. The pores undermine the homeostasis of the cells, leading to tissue ablation. A typical protocol uses 90 pulses of 70 μ s to 100 μ s,

1500 V to 3000 V, and 25 A to 45 A. As a non-thermal ablation modality, the theoretical advantage of irreversible electroporation is to enable physicians to ablate tumors even nearer to major vasculature than thermal ablation modalities [11, 12]. x, 6

Isoeffect Because thermal damage is realized through a time-temperature integrated process, different time-temperature histories can lead to the same biological/physiological effect. This engenders the idea of an isoeffect, where two heating histories can induce the same result, e.g., the same magnitude of cell kill in cultured Chinese hamster ovary cells [13]. x, 14

Magnetic resonance temperature imaging There are an assortment of five major MR contrast mechanisms that can measure temperature [14, 15]. The most important for this dissertation is the proton resonance frequency (PRF) shift method. The other four are T1 relaxation rate, T2 relaxation rate, proton density-weighted images to measure available magnetization, and diffusion-weighted images to measure temperature-dependent diffusion rates. Each class of MRTI has an abundance of pulse sequences to interrogate the subject contrast. Near real-time temperature imaging, via phase contrast imaging to monitor PRF shift, empowers minimally invasive laser surgery. x

Microwave Microwave (MW) refers to a broad and ill-defined bandwidth of the electromagnetic spectrum, depending on the particular field of science or engineering being considered. In medical hyperthermia, it refers to specific, approved frequencies of electromagnetic waves: 433 MHz, 915 MHz, or 2.45 GHz [6, 16]. Interestingly, 2.45 GHz is found in consumer microwave ovens while 915 MHz is employed in larger commercial or industrial microwave ovens. MW ablation devices use interstitial waveguides that lead to antennae, introducing ablative electromagnetic waves. Compared to [radiofrequency ablation \(RFA\)](#), MW ablation typically uses fewer antennae than [RFA](#) uses electrodes. The MW antennae can heat further, i.e., 2 cm to 3 cm, and have directional antennae [16]. The peak power of MW ablation devices range from 50 W to 80 W. x

Nuclear magnetic resonance Nuclear magnetic resonance is the fundamental physical phenomenon that once combined with spatial localization led to the advent of MRI. Lauterbur and Mansfield are credited with the application of magnetic field gradients to an NMR device for localization [17, 18]. Ernst was also integral to the application of Fourier transform-based reconstruction in MRI [19]. The magnetic properties

of matter that were investigated via NMR are also in MRI, e.g., T1 and T2 rates' dependence on temperature, magnitude of B_0 , and physical arrangement. Nuclei with unpaired spins are available for NMR and MRI measurement. Experiments and techniques from NMR have been widely adapted for use in MRI, e.g., the Hahn echo of NMR is the spin echo of MRI [20]. Perhaps even more importantly, the [proton resonance frequency \(PRF\)](#) shift of water protons was discovered in NMR experiments and used in MRI [21]. [x](#)

Radiofrequency Radiofrequency (RF) refers to a broad and ill-defined bandwidth of the electromagnetic spectrum, depending on the particular field of science, industry, or engineering being considered. In medical hyperthermia and ablation, it refers to a narrower range of alternating current frequencies of 350 kHz to 500 kHz [8]. These alternating currents are emitted from or between interstitial electrodes which cause ablative heating. Some [RFA](#) devices have one electrode; some have many [6]. Relative to other ablative modalities, RFA devices can have very high peak power outputs, in excess of 200 W. [x](#)

Stereotactic radiosurgery Stereotactic radiosurgery (SRS) is a common intervention in the management of [high grade glioma \(HGG\)](#) and metastases. Unlike typical external beam radiation therapy regimes, SRS is delivered in one or a few fractions. It is carefully executed to ensure the highest possible precision, which necessitates a skull frame, same-day image simulation, and treatment planning. Dose depends on focal lesion size. In Andrews et al.'s randomized controlled trial, lesions with the broadest diameter ≤ 2 cm were treated to 24 Gy, lesions with the broadest diameter 2 cm to 3 cm were treated to 18 Gy, and lesions ≥ 4 cm were treated to 15 Gy [22]. SRS carries a risk for radiation necrosis. There are Co-60 and linear accelerator-based SRS systems. [x](#), [xvii](#), [xviii](#)

Temozolomide This drug has been found to improve treatment of newly diagnosed [high grade gliomas](#) if administered concomitantly with [SRS](#). This is standard of care and has a high level of evidence advocating its use [23]. Temozolomide has been investigated for the management of brain metastases; however, efficacy is marginal [24].

[8](#)

Temperature probe This is a broad reference to thermocouples and fluorescent temperature probes. In experiments, temperature probes are used interstitially in experiments

to validate [magnetic resonance temperature imaging \(MRTI\)](#) [14]. In the clinic, temperature probes can be integrated with a thermal applicator, e.g., the Monteris laser applicator [25]. [x](#), [14](#)

Thermochemical ablation This is the injection of a neutralized acid-base mixture. The acid-base mixing occurs within a catheter immediately before introduction into the target tissue. The resulting mixture is a salt solution hot enough to induce thermal ablation. [26]. [x](#), [6](#)

Whole brain radiation therapy Whole brain radiation therapy (WBRT) is a common intervention in the management of [high grade glioma \(HGG\)](#) and brain metastases. WBRT is delivered over 3 to 4 weeks for a total of about 35 Gy in the whole brain [22]. WBRT has been found to suppress the development of new neoplasms, improving progression free survival. Unfortunately, WBRT can induce psychological symptoms. In present management of HGG and brain metastasis, WBRT is always paired with [SRS](#). [x](#)

Chapter 1

Introduction

Magnetic resonance-guided laser induced thermal therapy (MRgLITT), an emerging minimally invasive procedure, has curried interest in the neurosurgery community as a tool to treat metastases, primary cancers, radiation necrosis, and epilepsy. Based on reviews of brain metastasis incidence data, Eichler and Loeffler estimate the annual incidence of brain metastasis to be nearly 200,000 cases per year and 8% to 10% of adults who ever suffer cancer will present with symptomatic brain metastases [27]. Patients receiving surgical resection of metastases live significantly longer—median survivals of 11 months versus 3 months [28, 29]. Also, palliation of brain metastases improves neurological symptoms, improving quality of life and transcending a sense of therapeutic nihilism in the face of poor survival statistics [30]. In addition to metastases, some 22,850 primary cancers of the central nervous system occur, mostly in brain [31]. Of these, more than 14,000 are [high grade gliomas \(HGG\)](#) [32–34].

For malignant brain neoplasms, a chief intervention in the standard of care armamentarium is external beam radiation therapy, delivered as either [whole brain radiation therapy \(WBRT\)](#) or [stereotactic radiosurgery \(SRS\)](#) or both (WBRT+SRS) [27, 35]. Using MRI to image 516 metastases after SRS, evidence of recurrence or radiation necrosis, a serious complication, appears in up to 30% of treated lesions [36]. Both conditions typically demand aggressive management, in context of the patient’s health. More widely considered, incidence of symptomatic radiation necrosis ranges from 2% to 17% depending on the

radiation therapy delivered and disease state [27].

In addition to primary neoplasms, metastases, and radiation necrosis of the brain, MRgLITT has been identified to treat a fourth malady of the brain, epileptogenic foci [37–45]. Epilepsy has an incidence of about 150,000 per year [46]. Of these, an estimated 20% to 40% of patients’ epilepsy is not well managed via pharmaceuticals [47–50]. For these medically intractable cases, surgery is a possible intervention, albeit carefully considered [51, 52]. Together, these conditions represent a host of patients who stand to benefit from MRgLITT and would otherwise have limited treatment options. The primary advantages of MRgLITT over traditional interventions are brief hospitalizations, reduced risk of surgical complication, no ionizing radiation, and the possibility of retreatment as necessary [53–55].

While the laser applicator’s placement is guided by MR imaging, deciding the laser’s applicator’s intended placement is exclusively driven by the physician’s prerogative and experience. An accurate computational model that can *a priori* predict the laser’s heating improves surgical planning by indicating the location and number of required laser applicators [56, 57]. This information would effectively minimize the incidence of unsatisfactory laser applicator placements, either because of inadequate target coverage or unacceptable heating of **critical structures**. There are a number of significant challenges that prevent accurate *a priori* planning from entering common clinical practice, including the following: lack of accurate bioheat and optical properties [58, 59], accounting for nonlinear bioheat and optical properties [60–63], heterogeneous bioheat and optical properties [62], convective boundary conditions [64], and approximations of laser-tissue interactions [57, 65]. In order to expedite the conception and implementation of a clinically useful MRgLITT planning algorithm, a train-and-predict paradigm is adopted.

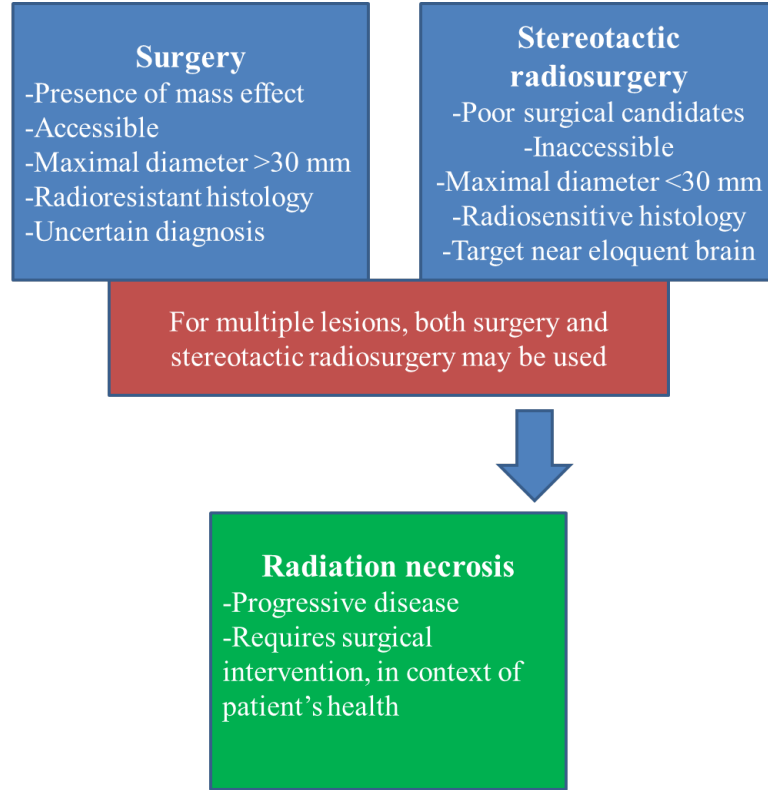


Figure 1.1: This flowchart describes the first-line treatments available for metastatic brain tumors, which are surgical resection and stereotactic radiosurgery [35]. Surgical resection tends to be more appropriate for larger, more accessible tumors, while stereotactic radiosurgery is for smaller and deeper metastases. If there are multiple metastases present, both interventions may be given. Following stereotactic radiosurgery, there is a risk of radiation necrosis, which also may require surgical resection.

1.1 Hypothesis

Computational modeling techniques can create thermal predictions for MR-guided laser induced thermal therapy matching the MR temperature imaging with a Dice similarity coefficient greater than 0.7 with a $\geq 95\%$ probability.

1.2 Specific aims

The following specific aims are designed upon a well-accepted framework of predictive model-building, described by Oden et al. [66].

1.

Sensitivity and uncertainty analysis: Stochastic simulations will propagate the uncertainty found in the literature parameters into probabilistic predictions, demonstrating the bioheat transfer equation’s sensitivity to parameter variance.

2.

Model calibration: Models of varied complexity will be trained on MR temperature imaging of clinical laser ablations.

3.

Simulated model validation: Leave-one-out cross validation will compare the simulated predictive performance of the trained models and a model using naïve literature values.

1.3 Dissertation organization

This dissertation begins with a brief, need-driven justification for the work. The [second chapter](#) is a review of salient information. The [third chapter](#) is a publication addressing the first specific aim [59]. In Chapter 3, a transient finite element method (FEM) model is used. Aims 2 and 3 are found in Chapters 4 and 5; both Chapters have both model calibration and validation, but consider different models. The [fourth chapter](#) is a publication and is also the calibration and validation of the FEM model [67]. The [fifth chapter](#) is previously unpublished work and is the calibration and validation of a surrogate model for the FEM model. The sixth and final chapter is Discussion. Appendix A lists the clin-

ical ablation data used in Chapters 4 and 5; Appendix [B](#) displays results from Chapter 5 demonstrating a model's convergence and alternative objective functions. Appendix [C](#) compares the transient finite element method model of Chapter 4 and the steady state of Chapter 5 as directly as possible. The PDF document is richly linked using the `hyperref` package in \LaTeX . The reader may quickly view a list of abbreviations, a glossary, a list of mathematical notation, and PDF bookmarks for chapters, sections, and subsections. If the reader is following a link to the Bibliography, it is recommended that he or she use **Alt+Left Arrow**, the present MS Windows hotkey in Adobe Reader or Acrobat, for a quick return to the previous view in the PDF document.

Chapter 2

Background

The oncological application of heat has roots deep in history, as early as 5000 years ago [68]. The Edwin Smith Surgical Papyrus is an Egyptian medical text of 48 case studies, including the use of hyperthermia in breast cancer [69, 70]. The text is dated within a few hundred years after the emergence of Egyptian writing itself [71]. Beginning in the 1600s, many physicians have recorded tumor regression in pyrexia patients [72]. By the 1880s, such observations created impetus for Coley to administer a toxic concoction of sterile bacteria to patients, inducing fever in order to limit cancer growth [73]. While Coley's *modus operandi* conflated hyperthermia with immunomodulation [74], Westermarck was the first to isolate the application of heat as a cancer therapy, published in 1898 [75]. Westermarck's method was to circulate heated water through containers that were in contact with inoperable uterine carcinomas. The water's temperature was 42 °C to 44 °C, remarkably within the useful hyperthermic temperature ranges identified by careful, modern experimentation [68, 76–83].

2.1 Hyperthermia, ablation, and minimally invasive interventions

In present use, the therapeutic heating of tissue to supraphysiological temperatures has two primary regimes: hyperthermia and ablation. They are defined by the length time for heating and the magnitude of the heating. Hyperthermia is characterized by lower temperatures, i.e., 40 °C to 46 °C, and longer times, 0.5 h to 5 h [78]. In clinical use, these ranges are narrowed depending on the purpose of the heating — 40 °C to 44 °C and 30 min to 90 min [1, 83–85]. Conversely, ablation is characterized by higher temperatures and shorter heating times. The typical temperatures and times in ablation are modality-dependent.

The contemporaneous use of hyperthermia is not as a standalone therapy and is instead an adjuvant to other interventions, namely radiation therapy, chemotherapy, or immunomodulation and eclectic combinations thereof [86–92]. Hyperthermic temperatures can modify the tissue environment in a variety ways, including signal modulation, blood perfusion increase, and biomechanical modification of tumor microenvironment [91, 93]. The addition of heat is intended to improve the therapeutic margin of the adjuvant interventions, as some animal model studies dramatically demonstrate [90]. Contemporary hyperthermia protocols in humans involve regional hyperthermia, e.g., heating a thigh or pelvis. Regional heating methods include radiative heating or [capacitive heating](#) [86, 94].

In contrast to hyperthermia, thermal ablation exists as a primary intervention in vast array of body sites, and can be the preferred intervention when the lesion is deemed inoperable or the maximum radiation dose has been delivered [6]. There are a plurality of catheter-based, percutaneous ablative devices and even a noninvasive ablation modality, [high-intensity focused ultrasound \(HIFU\)](#). The list of percutaneous thermal interventions includes [radiofrequency ablation \(RFA\)](#), [microwave ablation \(MWA\)](#), laser, [catheter-based ultrasonic devices](#), [thermochemical ablation](#), and [cryoablation \(CA\)](#). Along with the thermal percutaneous interventions, the following nonthermal percutaneous modalities compete

for consideration in the same clinical uses: [chemical ablation](#) and [irreversible electroporation](#).. A chosen modality for ablation rarely has a [high level of evidence](#) demonstrating its primacy in terms of common efficacy measures, e.g., two-year survival or overall survival or progression free survival. Even when randomized controlled trial data comparing ablative modalities to each other and/or surgical resection are available, the conclusion is not always definitive or else new emerging modalities need evaluation as well, ergo mitigating the finality of conclusions [11,95–101]. While the medical research literature does not represent a canon advising a particular modality, minimally invasive ablative modalities pose many advantages over surgical resection. Namely, morbidity and cost can be reduced in traditional surgical targets while introducing new surgical targets only accessible via these minimally invasive procedures.

2.2 MR-guided laser induced thermal therapy in brain

Magnetic resonance-guided laser induced thermal therapy (MRgLITT) is a particular realization of image-guided, minimally invasive thermal ablation. It has found utility in a variety of body sites, and significant interest for brain [102]. As explained in [Chapter 1](#), MRgLITT in brain has significant research efforts to ameliorate primary cancers, metastases, radiation necrosis, and epileptogenic foci. The following subsections address the standard of care for the aforementioned ailments and the surgical technique of MRgLITT.

2.2.1 MRgLITT in oncology

Management of [high grade gliomas \(HGG\)](#) and secondary tumors in the brain are among the most difficult challenges in medicine [31,35]. Like much of oncology, treatment of brain neoplasms is characterized by radiation, chemotherapy, and surgical resection [35, 103]. Unfortunately, therapeutic improvement is made in small steps and in very specific disease states in order to maintain a high level of evidence. Examples include dose-finding for

targeted therapy of HGGs [104], the addition of adjuvant chemotherapy [105], using meta-analysis to evaluate traditional interventions at a high level of evidence [23], or novel measures of progression and response to better consider concomitant interventions [106]. Given the poor prognosis of both HGGs and brain metastases, there are a plurality of investigative interventions with targeted therapy/immunomodulation drawing significant interest [24, 107].

In context of other treatments for brain neoplasms, the comparative effectiveness of MRgLITT is not in a position to be evaluated. Presently, the safety of MRgLITT has been well demonstrated, and some prospective patient recruitment has been done. The ability for MRgLITT to access deep tumors and re-treat lesions as they emerge makes MRgLITT a favorable surgical intervention for the management of aggressive brain neoplasms [55, 108–112]. Explicitly, the surgical trauma burden associated with MRgLITT is small enough that physicians have deemed repeated ablations are warranted in order to extend life and improve quality of life. For the time being, all patients receiving MRgLITT have already undergone first-line therapies — [stereotactic radiosurgery \(SRS\)](#) with concomitant [temozolomide](#) and/or surgical resection [35] — or have been critically evaluated for first-line therapies.

Significant work in treating HGG with MRgLITT has been accomplished by a multi-institutional, interdisciplinary team, including neurosurgeons, neuroradiologists, radiation oncologists, and medical oncologists [111]. Mohammadi et al. represents the best attempt to document the treatment of HGGs with MRgLITT to date. Patients were retrospectively analyzed. Of 34 treated patients, 12 had died after 7.2 months. 10 succumbed to disease progression and two from other causes. 13 ablations were considered conformal to the target and were shown to have statistically better progression-free survival. The primary conclusions were that (1) better long-term control, defined by progression-free survival and survival, was achieved by conformal laser heating versus nonconformal ablation and (2) some HGGs were amenable to conformal laser delivery. Comparative effectiveness to other

interventions was beyond the scope of the study.

A dangerous side effect of radiation therapy in the brain is radiation necrosis. The incidence of radiation necrosis is not widely tracked, but disparate studies report incidence rates of 2% to 17% and climb as high as 30% in previously untreated patients [27,36]. A 5% to 10% incidence rate of symptomatic radiation necrosis in *de novo* patients receiving radiation therapy seems plausible [113]; it is suffice to accept the incidence of radiation necrosis in brain to be a small but appreciable fraction of radiation therapy patients. Patients who have already undergone SRS, are treated to 16 Gy to 22 Gy, or have large treatment volumes are at considerably greater risk of radiation necrosis with rates up to 50% [113,114]. Patients afflicted with radiation necrosis benefit from surgical treatment if they are otherwise not imminently threatened — i.e., Karnofsky performance status > 70 , control of extracranial disease, > 3 months life expectancy [109,112]. MRgLITT is well positioned to treat patients with many previous surgical and radiation interventions; their wound healing is likely compromised, making MRgLITT an appealing treatment option over traditional resection [113]. There is a growing number of investigations where MRgLITT has treated radiation necrosis [109,112,115,116] in addition to reviews [113,117].

2.2.2 Epileptogenic foci

A significant fraction, $\sim 20\%$ to 40% , of epilepsy patients are pharmaco-resistant [47–50]. Consequently, these patients may be considered for surgery to ameliorate seizures with about 50% being eligible for operation [118]. However, given the inherent risks of neurosurgery, surgical patients typically have debilitating symptoms and targets amenable to surgery. Epilepsy control outcomes depend on the site of operation [118], but will be considered as one group for this discussion. Surgery can provide good control at early time points — between 60% and 70% seizure control for the first two years [118] — but the efficacy of surgery is not definite with about half of surgical patients having epileptic relapse at five and ten years’ follow-up [118]. Nonetheless, compassionate care can demand

drastic intervention in the face of intractable epilepsy and even significantly reduce the costs of patient management [50]. Furthermore, there is evidence that epilepsy control is underutilized and neurologists overestimate the risks of the operation [119–123].

The surgical target in epilepsy surgery is known as an [epileptogenic focus \(EF\)](#) or foci. A primary method to localize EF is [intracranial electroencephalogram \(icEEG\)](#). icEEG can create image-like maps called [electrocorticography \(ECoG\)](#) for localizing EF and studying human cognition in general [124]. ECoG has high spatio-temporal resolution and can be registered with anatomical MR scans. An example clinical ECoG spatio-temporal resolution is ~ 1 mm with sampling rates of ~ 1.0 kHz. Considerably faster sampling rates are possible but result in prohibitively large datasets. icEEG is invasive and takes a considerable amount of time of hospitalized monitoring, up to two weeks [125], to adequately localize EF.

Minimally invasive interventions are an attractive method to reduce surgical trauma and increase the therapeutic margin of epilepsy surgery, with MRgLITT being a leading novel modality [43, 117]. There are a growing number of publications documenting its use [37–42, 44, 45]. The results are promising, but nuanced by the realities of epilepsy management. Generally, there are three post-operative seizure outcomes.

1. Patients were seizure-free.
2. Patients derived meaningful seizure control and/or their condition was well controlled by drugs after surgery.
3. The patients conditions remained intractable.

For MRgLITT epilepsy surgery to become preferred to techniques involving craniotomy, MRgLITT will need to be demonstrated to have better control or fewer side effects in a randomized controlled trial. Regarding the possibility of improved efficacy, improvement of non-invasive EF localization would behoove MRgLITT epilepsy surgery. The listed publications of MRgLITT epilepsy surgeries use non-invasive localization methods, since

performing a craniotomy and subsequent icEEG would nullify non-invasive benefits of MRgLITT. Namely, the MRgLITT investigators use permutations of video electroencephalogram (EEG), MRI, FDG-PET, SPECT, and Wada testing. At present, MRgLITT epilepsy surgeons are not using the gold standard localization technique, icEEG-based ECoG. A new avenue for non-invasive localization is coincident PET/MR [126]. However, the potential for minimally invasive operation is compelling enough for surgeons at specialized epilepsy centers to investigate MRgLITT.

2.2.3 Imaging and surgical technique

The two features that empower MRgLITT are stereotactic surgery and real-time temperature measurement via MR. Stereotactic laser techniques were first used in the brain and guided via CT [127]. MR-monitored laser-tissue effects were well explored by Jolesz et al. [128]. Their investigation described MRTI contrast mechanisms that were T1- and T2-weighted. The methods clearly showed changes, but the practical utility was limited by the hysteresis of T1 and T2 in heat shocked tissues and the need to observe the cooling in order to demonstrate degree of thermal insult. Later, proton resonance frequency (PRF)-shift thermometry was co-opted from nuclear magnetic resonance (NMR) [21] and described by Ishihara et al. and De Poorter et al. [129–131]. Real-time PRF-shift thermometry provides a robust, linear relationship to monitor temperature in MRgLITT. The challenges of PRF thermometry include lipid-rich tissue and motion [15]. Both challenges have their own extensive bodies of research addressing them, e.g., [132, 133].

The combination of effective MRTI and stereotaxis led to the advent of modern MRgLITT. There are two major laser applicator vendors: Monteris Medical NeuroBlate[®] and Medtronic Visualase[®]. Chapters 3, 4, and 5 of the dissertation will focus on the Visualase[®] device; a device description can be found in Chapter 3. The following description of MRgLITT is based on sundry publications, some that describe the MR suite being separate from the neurosurgery operating room [39] and some utilizing an intraoperative MRI (iMRI)

[67]. The positive impact of an iMRI is well described by Hawasli et al. [110]. They planned four surgeries that used multiple bore holes. However, they had two more surgeries where a single bore hole was indicated in pre-surgical planning, but additional bore holes were deemed necessary mid-procedure. The presence of an iMRI enabled the addition of more bore holes, without undue extension of the operation's time length. Without an iMRI, the alternative is to shuttle the patient between the neurosurgery operating room and the reserved diagnostic MRI, while under anesthesia and with implanted laser applicator(s). Accurate computational models for planning would reduce the necessity of changes to the surgical plan. Critically, this advantage is exaggerated in cases where the neurosurgery operating room is separate from the MR suite. More about the technique is described in Chapters 3 and 4.

2.3 Thermal damage models

2.3.1 Arrhenius process

As Dewhurst et al., Pearce, and Dewey elegantly describe in their reviews [78, 83, 134], thermal damage manifests through a time-integrated Arrhenius rate process given by

$$\Omega = \ln \left(\frac{c(t)}{c(t_0)} \right) = \int_{t_0}^t A \exp \left(\frac{-E_a}{RT(\tau)} \right) d\tau \quad (2.1)$$

where t_0 and t respectively are the initial and end time points. Ω is a ratio of the endpoint concentration of native/unablated proteins, $c(t)$, to initial proteins, $c(t_0)$. A is the frequency factor, R is the universal gas constant, E_a is the activation energy of the protein's transition of state, and t is the absolute temperature. E_a and A are empirical and vary with whatever process the investigator is interested, e.g., transepidermal necrosis in porcine model [135].

2.3.2 Thermal dose: an example

The first obvious implication of Equation (2.1) is that there are myriad combinations of time and temperature that arrive at the same value of Ω . Chicken eggs have been used by many hyperthermia/ablation investigators to model the time-temperature-dependent coagulation process, e.g., [128, 136]. As a heuristic example, consider cooking an egg. A chicken egg from the grocery store can experience the four following elevated temperature regimes: low heat with short time or pasteurization, 60 °C for 3.5 min; moderate heat for a long time like sous-vide, 62.8 °C for 0.75 h to 2.0 h; high heat for a short time like scrambled or fried eggs, > 71.1 °C; and finally excessive and charring heat, > 250 °C for 2.0 min for a few seconds [137–139]. These temperature regimes are an excellent demonstration the time-history qualities of hyperthermia and ablation.

The pasteurization case illustrates a heat shock that is intended to kill *Salmonella* bacteria but does not perturb the egg because the heat shock is sub-coagulative to the egg. The clinical analog is a temperature range of 37 °C to 40 °C. While it is conceivable that such a small temperature rise may increase blood perfusion and marginally gain the benefits of hyperthermia, < 40 °C is not clinically used.

The sous-vide case is analogous to hyperthermia, where the coagulation process is gradual and takes a very long time to become terminal. Critically, an egg has different components, i.e., the white and the yolk, that have different activation energies, E_a . For the sous-vide case, the difference in E_a engenders a coagulation rate difference between the white and the yolk. At 45 min, the white is appreciably coagulated, while the yolk yet flows. By 2.0 h, both egg components are nearly terminally coagulated. This state transition is exactly described by Equation (2.1) since the concentration of denatured protein dominates the log ratio of

$$\Omega = \ln \left(\frac{c(t)}{c(t_0)} \right).$$

With extended heating, Ω may continue to rise prodigiously, but the quantity of mass of

native protein transitioning into a denatured state is vanishingly small. The quantity of Ω is really only meaningful at the lower range, i.e., less than 2.3. In Pearce’s 2013 review [82], it is pointed out that thermal damage is detectable in histology with about $\frac{c(t)}{c(t_0)} \approx 90.5\%$ or $\Omega = 0.1$ and a “sure kill” in all tissue types corresponds to $\frac{c(t)}{c(t_0)} = 10\%$ or $\Omega \approx 2.3$. Again, in the clinic, the hyperthermia temperature regime is implemented as an adjuvant to a primary intervention. Typically, the denaturation of proteins — the accumulation of Ω , i.e., thermal dose — is not the direct goal of clinical hyperthermia.

Next, a fried egg only needs to reach an excessively hot temperature and total coagulation is essentially immediately complete; this is analogous to thermal ablation. Through these culinary examples, a second obvious implication of Equation (2.1) is that there is an effect limit of hyperthermia and ablation. Once enough native protein has denatured, the tissue is irreversibly damaged and further application of heat has no effect. This is in contrast to other interventions like radiotherapy where excessive dose in the target is not the limiting factor; radiation dose is limited by the tolerance of healthy tissue and accuracy of treatment delivery.

Finally, excessive heating is undesirable in cooking an egg because it burns. Furthermore, pyrolyzation the egg creates mutagens [137]. Likewise in ablation, temperatures near and beyond 100 °C create vaporization or charring that result in patient complications, damage to the percutaneous applicator, and/or tissue changes that undermine the intended heat delivery. To avoid deleterious high heat, both hyperthermia and ablation use control points where the temperature is not allowed to exceed a certain value. Control points are monitored via MRTI or temperature probes within the interstitial applicator.

2.3.3 Cumulative equivalent minutes

Another means to describe thermal damage is the cumulative equivalent minutes (CEM) model, described in [78, 82, 83, 134]. The fundamental idea is to quantify the amount of time a subject must be held at a constant temperature in order to generate an [isoeffect](#)

compared to a standard temperature, often 43 °C. This leads to an equation that allows the conversion from an applied temperature for an applied time to be compared to the standard temperature in a standard time increments, i.e., 1 minute. For the case of the standard temperature being 43 °C, it is

$$CEM_{43} = \int_{t_0}^t (R_{CEM})^{(43^{\circ}\text{C}-T(\tau))} d\tau \quad (2.2)$$

where CEM_{43} is the number of minutes at 43 °C required to match an isoeffect generated by holding the subject at a different temperature, T in °C, for time, t in minutes. The choice of the standard temperature being 43 °C is informed by Sapareto et al.’s work [13]. At all hyperthermic temperatures, the rate of cell kill is exponential with temperature. However, in the case of Chinese hamster ovary cells, the exponential base, R_{CEM} , below 43 °C is smaller than above 43 °C. This transition temperature is called the breakpoint in hyperthermia parlance. In Sapareto’s review [76], the exponential base is modeled as a discrete transition from 0.25 to 0.50 as temperature increases beyond 43 °C. Dewhirst et al. indicates that while the standard temperature could always be the breakpoint temperature of the target, it is more convenient for researchers and clinicians to choose a broad standard which is 43 °C [78]. The value of R_{CEM} varies depending the tissue or cell line and whether the heat shocked sample is *in vivo* or *in vitro* [78]. Traditionally, R_{CEM} is 0.25 and 0.50 for values below and above 43 °C, respectively.

2.3.4 Lethal threshold temperature

Since page 13, this dissertation has used data-driven arguments to extol the use of thermal damage models that incorporate time-temperature history — namely, Equations (2.1) and (2.2). However, in the case short ablations, a [lethal threshold temperature damage model \(LTTDM\)](#) can delineate between live and dead tissue after the heat shock. Given the importance of time-temperature models, clearly, the meaning and context of “short”

and “ablation” require explanation. “Ablation” immediately precludes any hyperthermia. “Short” would be ≤ 2.0 min for the entire heat delivery. That forbids LTTDM’s application to ablations that are either several minutes, the sum result of repeated short ablations, or steered applicators — e.g., [RFA](#), most [HIFU](#), [catheter-based ultrasonic devices](#), and steered laser ablations. Despite the list of limitations, the LTTDM is applicable to Medtronic’s Visaulase® (Louisville, Colorado) laser applicator for use in [magnetic resonance-guided laser induced thermal therapy \(MRgLITT\)](#).

Yung et al. investigated the use of the three damage models — Arrhenius, Section 2.3.1; CEM, Section 2.3.3; and LTTDM — to each other in four laser-ablated *in vivo* normal canine brains [140]. It is critical to recapitulate their work as a justification for using the LTTDM. In the experiments, the laser ablations were monitored by real-time [MRTI](#), providing the necessary temperature information to make damage predictions. For each damage model, the demarcation of live or dead was allowed to vary. Namely, the Arrhenius process damage model’s prediction of dead tissue was thresholded by Ω , and the value of Ω varied from 0.01 to 10.2. Secondly, the CEM model’s damage prediction was thresholded between 10 CEM₄₃ and 1200 CEM₄₃. Thirdly, the temperature threshold for the LTTDM was varied between 51 and 71 °C.

For the many different predictions made by the three damage models, a regional comparison was made to post-ablation, post-contrast T1-weighted images, a recognized surrogate of evaluating the extent of ablation [141]. The comparison was made via [Dice similarity coefficient \(DSC\)](#). Yung et al. reported the maximum DSC possible for each of the three models as well as the DSC by using previously cited damage thresholds. The result was the maximum DSC achieved by the three damage models had the same mean and similar standard deviation. Furthermore, the DSC values calculated by using the previously cited damage model parameters were very close to the maximum possible. In summary, for the case of short ablations, all three damage models matched the post-ablation, post-contrast T1-weighted image — the study’s gold standard — and robustly produced high

DSC values for a variety of damage model threshold choices.

Chapter 3

Generalised polynomial chaos-based uncertainty quantification for planning MRgLITT procedures

This Chapter is a near-verbatim quotation of Fahrenholtz et al. [59]. The Chapter uses English grammar and spelling of the United Kingdom. The only intended modifications are the numbering of citations, equation numbers, figure numbers, table numbers, and section numbers. The citations are numbered according to the dissertation, as opposed to the quoted journal article. Among the Specific Aims, this Chapter addresses Aim 1. Its citation, according to the Informa Healthcare format, is thus:

Samuel J. Fahrenholtz, R. Jason Stafford, Florian Maier, John D. Hazle, and David Fuentes, *International Journal of Hyperthermia*, 2013(29)4:324-35

Copyright ©2013, Informa Healthcare. Reproduced with permission of Informa Healthcare. Informa Healthcare materials are now made available from Taylor & Francis.

3.1 Abstract

Purpose: A generalised polynomial chaos (gPC) method is used to incorporate constitutive parameter uncertainties within the Pennes representation of bioheat transfer phenomena. The stochastic temperature predictions of the mathematical model are critically evaluated against MR thermometry data for planning MR-guided laser-induced thermal therapies (MRgLITT). *Methods:* The Pennes bioheat transfer model coupled with a diffusion theory approximation of laser tissue interaction was implemented as the underlying deterministic kernel. A probabilistic sensitivity study was used to identify parameters that provide the most variance in temperature output. Confidence intervals of the temperature predictions are compared to MR temperature imaging (MRTI) obtained during phantom and *in vivo* canine ($n = 4$) MRgLITT experiments. The gPC predictions were quantitatively compared to MRTI data using probabilistic linear and temporal profiles as well as 2-D 60 °C isotherms. *Results:* Optical parameters provided the highest variance in the model output (peak standard deviation: anisotropy 3.51 °C, absorption 2.94 °C, scattering 1.84 °C, conductivity 1.43 °C, and perfusion 0.94 °C). Further, within the statistical sense considered, a non-linear model of the temperature and damage-dependent perfusion, absorption, and scattering is captured within the confidence intervals of the linear gPC method. Multivariate stochastic model predictions using parameters with the dominant sensitivities show good agreement with experimental MRTI data. *Conclusions:* Given parameter uncertainties and mathematical modelling approximations of the Pennes bioheat model, the statistical framework demonstrates conservative estimates of the therapeutic heating and has potential for use as a computational prediction tool for thermal therapy planning.

3.2 Introduction

Magnetic resonance-guided laser-induced thermal therapy (MRgLITT) is a minimally invasive ablative procedure that can rapidly ($< 180\text{s}$) deliver heat to treat focal cancerous lesions or radiation necrosis in the brain [115, 142]. The optical fibre is placed through a burr hole into the target disease via stereotaxy, analogous to an image-guided stereotactic biopsy [108, 142]. MRgLITT for patient-specific treatment of focal cancerous lesions in brain presents an attractive treatment option with significantly less impact on the patient compared to conventional surgical procedures. For many anatomical sites of interest, magnetic resonance image (MRI) guidance provides a means for planning, targeting, monitoring and verifying the delivery of these therapies in a single, closed-loop session. To this end, several FDA-cleared MRgLITT systems (Monteris www.monteris.com, Visualase www.visualaseinc.com) have become commercially available. These systems facilitate MRgLITT procedures on any modern clinical MRI scanner and are currently in post-market studies at multiple institutions [37, 55, 108, 142–146]. The goal of the therapy is to treat a targeted tissue volume, $< 3\text{ cm}$ in diameter, in such a highly controlled manner so as not to incur damage to nearby normal tissue structures which would result in complications.

Proton resonance frequency-based thermometry or magnetic resonance temperature imaging (MRTI) provides a means to real-time monitor the heat distribution during the therapy [147, 148]. MRTI’s temperature information improves the safety and efficacy of MRgLITT by allowing the physician to avoid overheating, tissue vaporisation, and charring near the laser and prevent treating tissue beyond disease extent. However, in the current paradigm, visual assessment of multiple structures in multiple planes, even with the aid of user-assigned critical monitoring points, presents a delivery paradigm that is inherently difficult to manage. Integration of mathematical modelling and computational science techniques with the clinical imaging information available may prove useful for MRgLITT before and during the procedure, either by predicting the result of a treatment before the

surgery, or during surgery to improve MRTI and robustly estimate lost information due to data corrupting motion, low signal-to-noise-ratio (SNR), excessive heating, and catheter-induced signal voids [149–152]. These enhanced realtime monitoring approaches may further assist in more safely and accurately controlling therapy delivery for increased efficacy of the procedure [153, 154]. The availability of increasingly powerful high performance and portable computing resources, such as NVIDIA[®] graphics processing units (GPUs) [155] and Intel[®] many integrated core (MIC) architecture [156], indicates that the presence of computational science is likely to continue escalating in these image-guided thermal therapy procedures.

The development of computational tools for planning hyperthermia and ablation therapies has received significant attention for improving therapy outcomes [4, 61, 147, 157–159]. With predictive modelling, the laser fibre placement can be planned in a virtual environment to improve the likelihood of a successful and short treatment. A common method for predictive modelling of the distribution of induced heating in blood perfused tissue is the Pennes bioheat transfer equation (BHTE) [160] solved with a finite element method (FEM) [60, 62, 65]. A difficulty in obtaining accurate results from the BHTE is the uncertainty incurred by using homogeneous literature values of biothermal and optical constitutive values for patient-specific planning. Uncertainty is further increased with incorporating the additional complexity of investigating the non-linear effects of temperature-dependent or thermal dose-dependent constitutive parameters.

Truly predictive prospective computer modelling requires substantial validation efforts and novel computer modelling techniques that incorporate the inherent uncertainties of the computer model into the predicted solution [161–163]. Monte Carlo modelling is the quintessential example of incorporating uncertainty into the computer model output. While a Monte Carlo approach would provide the necessary probabilistic outputs, the computational cost required to simulate a sufficient number of realisations is large. There exist methods to improve the convergence of Monte Carlo through the quasi-Monte Carlo

method, Latin hypercube sampling, and the Markov Chain Monte Carlo method [164–168].

Another successful technique to accelerate uncertainty quantification (UQ) is generalised polynomial chaos (gPC) expansion. gPC provides a means of providing the model with UQ prodigiously faster than Monte Carlo for computations using few random input variables, i.e. < 10 variables. gPC is originally based on the work of Wiener [169]. This method used a high order Hermite polynomial as a spectral approximation for model outputs. Nearly 50 years later, Ghanem and Spanos identified the spectral approximation as a viable tool in FEM modelling of stochastic differential equations [170]. Xiu and Karniadakis demonstrated that the convergence of spectral methods for solutions to differential equations were optimised by matching certain input functions’ distributions with corresponding output polynomials, known as the Wiener-Askey scheme [171]. For similar diffusive type equations, gPC’s convergence to a mean solution, $N < 10$ realisations, compares exceptionally favourably, pointwise error $< 1.E-2$, when compared with Monte Carlo’s $N = 20\,000$ realisations [171, 172]. gPC has already been applied to an eclectic list of studies. The topics include radiation oncology, combustion modelling, nuclear reactor design, and robotic dynamics on rugged terrain [173–176].

Here we investigate the use of a stochastic form of the BHTE coupled to a diffusion theory approximation of light transport in tissue for improving the decision-making utility of thermal modelling. Temperature-dependent constitutive values are mathematically characterised via an assumed probability distribution providing the ability to perform uncertainty quantification via generalised polynomial chaos and provide quantitative confidence levels in the computer model predicted temperature for each spatial location at each time point.

3.3 Methods

3.3.1 Mathematical model of uncertainty

Ignoring discretisation errors, computer implementations of mathematical models fundamentally have uncertainty in their representation and predictions of physical phenomena [66] due to two dominant sources of inherent variability. (1) Simplifications are needed to make the algorithm practical. For example, in this work we employ a Pennes bioheat transfer equation (Equation 3.1) with a perfusion term that represents the manifestation of a complex and tortuous microvasculature on the bulk continuum scale heat transfer. (2) The computer model parameters are not known precisely. In this application, optical and biothermal parameters are taken from literature values and are empirical representations of non-linear temperature and damage-dependent phenomena. Further, the parameters fail to incorporate patient- and tissue-specific variability resulting from heterogeneities.

This investigation aims to manage model parameter uncertainty associated with a stochastic form of Pennes bioheat transfer equation for blood perfused tissues (Equation 3.1). The motivating idea is that the Pennes' representation of the physics of the bioheat transfer phenomena coupled with statistical methods of uncertainty quantification may synergistically provide a reliable prediction model regardless of constitutive parameter uncertainties and mathematical modelling approximations.

$$\begin{aligned}
\rho c_p \frac{\partial u}{\partial t}(\vec{x}, t, \vec{Z}) - \nabla \cdot (k(\vec{Z}) \nabla u) + \omega(\vec{Z}) c_{blood} (u - u_a) &= \mu_a q_{laser}(\vec{x}, t, \vec{Z}) \\
q_{laser}(\vec{x}, t, \vec{Z}) &= \int_{U_{tip}} \frac{P(t)}{\text{Vol}(U_{tip})} \frac{3 \mu_{\text{eff}} \exp(-\mu_{\text{eff}} |\vec{x} - \vec{\xi}|)}{4 \pi |\vec{x} - \vec{\xi}|} d\vec{\xi} \\
\vec{x} \in U \setminus U_{tip} \quad \mu_{tr} &= \mu_a(\vec{Z}) + \mu_s(\vec{Z}) (1 - g(\vec{Z})) \quad \mu_{\text{eff}} = \sqrt{3 \mu_a(\vec{Z}) \mu_{tr}} \\
\Omega(t) &= \int_0^t A e^{\frac{-E_A}{R u(\tau)}} d\tau \quad -k(\vec{Z}) \nabla u \cdot \vec{n} = 0 \quad \text{on } \partial U \\
u(\vec{x}, 0, \vec{Z}) &= u^0 \quad \text{in } U \\
\vec{Z} &\equiv (Z_k, Z_{\omega^{native}}, Z_{\omega^{coag}}, Z_g, Z_{\mu_a^{native}}, Z_{\mu_a^{coag}}, Z_{\mu_s^{native}}, Z_{\mu_s^{coag}})
\end{aligned} \tag{3.1}$$

Here, ρ is the tissue density, c_p is the specific heat of tissue, k is the tissue conductivity; ω is the tissue micro perfusion primarily due to capillaries, c_{blood} is the specific heat of blood, and u_a denotes the arterial core blood temperature. The laser source term, q_{laser} , is modelled using a standard diffusion approximation [65]. Power is denoted P , the volume of applicator is denoted U_{tip} , and the volume of the biological domain is denoted U . Optical parameters include the absorption, scattering, and anisotropy factor, denoted μ_a , μ_s , and g , respectively. Arrhenius damage model, Ω , parameters are denoted, A , E_A , and R . The objective of this work is to use this mathematical model to predict the 4D temperature field, u , as a function of a random vector, \vec{Z} , with a known probability distribution that mathematically represents our uncertainty the optical parameters, perfusion, and conduction, $\vec{Z} \equiv (Z_k, Z_{\omega^{native}}, Z_{\omega^{coag}}, Z_g, Z_{\mu_a^{native}}, Z_{\mu_a^{coag}}, Z_{\mu_s^{native}}, Z_{\mu_s^{coag}})$.

Statistical methods provided by uncertainty quantification techniques such as generalised polynomial chaos provide novel methodologies for modelling the complex bioheat transfer phenomena. In particular, it is well known that the constitutive parameters behave non-linearly with temperature increase and tissue damage. Constitutive parameters that account for damage-dependent non-linearities of the perfusion, thermal conductivity, and optical parameters [177] are generally more scarce than the linear counterparts and the variability of the mathematical form of the constitutive nonlinearities seen within the

literature suggests a potentially higher degree of uncertainty within the non-linear parameters [4, 62, 147, 178, 179]. Here we will consider the uncertainty associated with both linear and non-linear constitutive forms of the perfusion, absorption, and scattering. A goal of our work is to investigate if a relatively simple linear model with physically meaningful bounds on constitutive values can be coupled with stochastic methods to produce useful predictions. Stochastic parameters associated with linear forms of the BHTE are chosen by the following expressions that are spatially homogenous and constant in time.

$$\begin{aligned} k(\vec{Z}) &= Z_k \quad \omega(\vec{Z}) = Z_{\omega^{native}} \quad g(\vec{Z}) = Z_g \\ \mu_a(\vec{Z}) &= Z_{\mu_a^{native}} \quad \mu_s(\vec{Z}) = Z_{\mu_s^{native}} \end{aligned} \tag{3.2}$$

While several empirical models of non-linearities are available, for feasibility, a common form of the constitutive non-linearities (Equation 3.3) was considered for absorption, scattering, and perfusion as a function of Arrhenius thermal damage, Ω . As seen in Figure 3.1, for this particular analytical form chosen [62], undamaged constitutive values transition to coagulated values between the temperature range of 51–61 °C. Similar to previous studies [140] of the time-temperature histories relevant to MRgLITT, the tissue is fully damaged at a threshold of approximately 61 °C.

$$\begin{aligned} \mu_a(\vec{Z}) &= Z_{\mu_a^{native}} + \frac{\Omega}{\ln 2 + \Omega} (Z_{\mu_a^{coag}} - Z_{\mu_a^{native}}) \\ \mu_s(\vec{Z}) &= Z_{\mu_s^{native}} + \frac{\Omega}{\ln 2 + \Omega} (Z_{\mu_s^{coag}} - Z_{\mu_s^{native}}) \\ \omega(\vec{Z}) &= Z_{\omega^{native}} + \frac{\Omega}{\ln 2 + \Omega} (Z_{\omega^{coag}} - Z_{\omega^{native}}) \end{aligned} \tag{3.3}$$

The native conduction, Z_k , perfusion, $Z_{\omega^{native}}$, optical scattering, $Z_{\mu_s^{native}}$, optical absorption, $Z_{\mu_a^{native}}$, and the optical anisotropy, Z_g , as well as the coagulated values of the absorption, $Z_{\mu_a^{coag}}$, scattering, $Z_{\mu_s^{coag}}$, and perfusion, $Z_{\omega^{coag}}$, are understood mathematically as uniform random variables with quantitative bounds given in Table 3.1. As seen in Figure 3.1, the uncertainty range of constitutive non-linearities is considered as a subset of the uncertainty within the linear UQ problem.

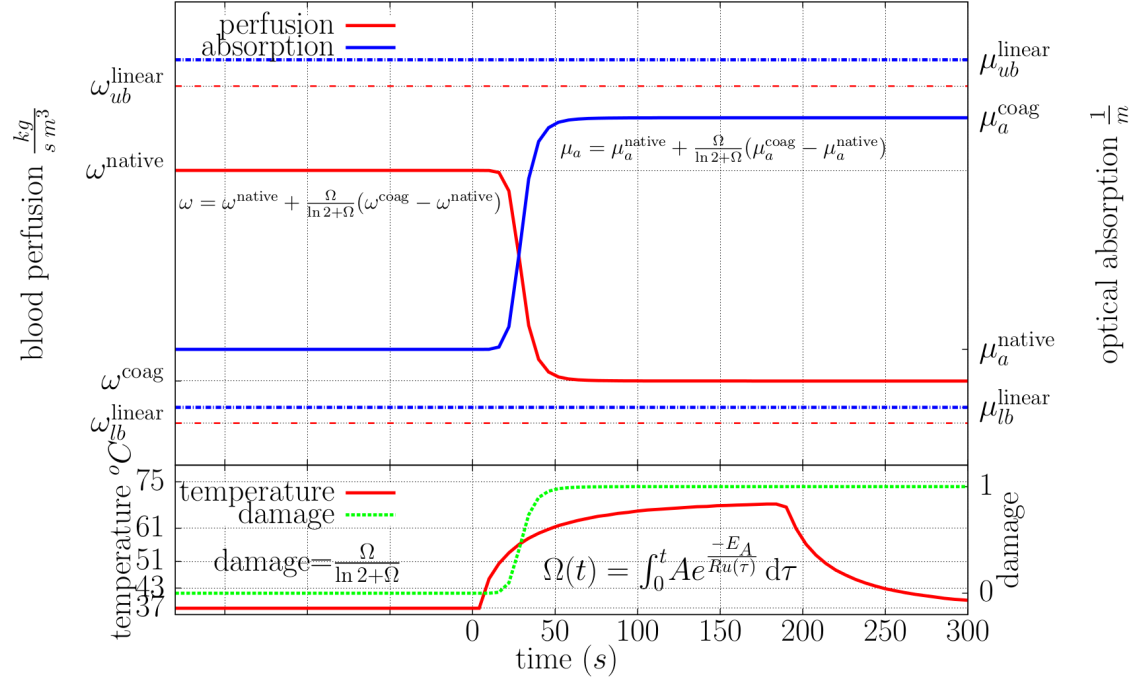


Figure 3.1: A graphical illustration of the non-linear constitutive model [62] used for the perfusion and optical absorption is shown. The scattering behaves similar to the absorption. Damage, perfusion, and absorption are plotted as a function of a time-temperature history representative of those observed in MRgLITT procedures. As shown, the native undamaged constitutive values transition into coagulated constitutive values between temperatures of approximately 51 °C–61 °C. Similar to previous results [140], the tissue is fully damaged at a threshold of 61 °C.

Table 3.1: Literature-based constitutive values [79, 80, 177, 180–186]. A table of the constitutive values used for perfusion, conduction, absorption, and scattering is shown. Uniform distributions are denoted $U(a, b)$. Deterministic values are otherwise used. Values for density, specific heat, and Arrhenius parameters are as follows: $\rho = 1045$ (kg/m³), $c_{blood} = 3840$ (J/kg/K), $c_p = 3600$ (J/kg/K), $A = 3.1\text{E}98$ (s), $E_A = 6.28\text{E}5$ (J/mol), $R = 8.314$ (J/mol/K).

Figure	ω [kg/(m ³ s)]	k [W/m K]	μ_a (1/m)	μ_s (1/m)	g (Unity)
2A	$U(3, 9)$	0.527	500	14000	0.88
2A	6	$U(0.490, 0.527)$	500	14000	0.88
2A	6	0.527	$U(400, 600)$	14000	0.88
2A	6	0.527	500	$U(11200, 16800)$	0.88
2A	6	0.527	500	14000	$U(0.88, 0.95)$
2B	6	0.527	Linear $U(50, 600)$	14000	0.88
2B	6	0.527	Native $U(50, 300)$	14000	0.88
			Coag. $U(300, 600)$		
2B	6	0.527	500	Linear $U(5000, 50000)$	0.88
2B	6	0.527	500	Native $U(5000, 30000)$	0.88
				Coag. $U(30000, 50000)$	

Coag., coagulated.

Table 3.1: Literature-based constitutive values [79, 80, 177, 180–186]. A table of the constitutive values used for perfusion, conduction, absorption, and scattering is shown. Uniform distributions are denoted $U(a, b)$. Deterministic values are otherwise used. Values for density, specific heat, and Arrhenius parameters are as follows: $\rho = 1045$ (kg/m³), $c_{blood} = 3840$ (J/kg/K), $c_p = 3600$ (J/kg/K), $A = 3.1\text{E}98$ (s), $E_A = 6.28\text{E}5$ (J/mol), $R = 8.314$ (J/mol/K).

Figure	ω [kg/(m ³ s)]	k [W/m K]	μ_a (1/m)	μ_s (1/m)	g (Unity)
2C	Linear U (0, 9)	0.527	500	14000	0.88
2C	Native U (3,9)	0.527	500	14000	0.88
	Coag. U (0, 3)				
2D	U (3, 9)	U (0.490, 0.527)	U (400, 600)	U (11200, 16800)	0.88
3	0	0.527	U (4, 200)	U (11200, 16800)	U (0.85, 0.95)
4, 5, 6	6	0.527	U (400, 600)	U (11200, 16800)	U (0.85, 0.95)
5A (WM)	U (3, 9)	0.527	320	46900	0.88

Coag., coagulated;

WM, white matter.

3.3.2 Constitutive data

Constitutive parameter values [80,177,180–183,187] used in simulating the bioheat transfer for the *in vivo* brain data and *ex vivo* phantom set-up are provided in Table 3.1. Variability in the model parameters [78,177,183] was input into the gPC model as uniformly distributed random variables using the bounds shown in Table 3.1. The variability in the ranges presented encompasses all conceivable healthy values as well as the extremum of constitutive non-linear dependence on temperature. The values for the Arrhenius dose parameters listed in Table 3.1 are from Henriques and Moritz’s classic work [135]. The choice of dose parameters is dependent on what end point is sought. Here the threshold is tissue death by any heating effects shortly (< 20 min) after treatment. The dose analysis for the four canines, described by Yung et al. [140], demonstrates that an Arrhenius dose module using Henriques’ dose values leads to agreement with post-treatment, post-contrast T1-weighted MRI.

3.3.3 Optical parameter uncertainty

Relatively large variability may be seen in optical parameter values reported in the literature, Table 3.1. These differences may be associated with different techniques for *in vivo* and *in vitro* measurements, different radiative transport models, and differences in preparation of tissue specimens [188,189]. The non-linear behaviour of optical parameters is well known [62,177,190–192] and further increases the uncertainties in optical properties. For example, a 10% increase in the absorption coefficient and a 2–4-fold increase in the scattering coefficient was seen between native and coagulated brain tissue [177,191]. Further, the blood content of the tissue has been seen to affect the optical properties [193]. Significant changes in the optical properties of the blood can be expected with varying concentrations of haematocrit and oxygen concentration. There is also great uncertainty in the tumour type to use for the optical parameter values as well as blood content of the tumour. This

may particularly contribute to the uncertainty in the optical parameters when irradiating heterogeneous tumours where the patient-specific blood content and the amount of cerebral spinal fluid (CSF) present may vary significantly.

Grey matter optical parameter values— μ_a , μ_s , and g —were used in simulating MRgLITT in normal canine brain tissue. For non-linear simulations, the values of absorption and scattering were set to represent the native state and transition to a coagulated state (Equation 3.3). The range of optical values used in the linear simulation for comparison against the nonlinear simulation is a superset of the range of the native and coagulated transition, listed in Table 3.1, Figure 3.2(B) and (C).

3.3.4 Multiplanar magnetic resonance thermal imaging in phantom and animal models

Simulations were compared to MRTI data obtained from a safety and feasibility study of MRgLITT conducted in the brains of four clinically normal mixed breed hounds (20–25 kg) [65, 140]. MRTI data was also obtained from an MRgLITT heating experiment in a perfusionless *ex vivo* tissue phantom [154] constructed from an excised canine prostate embedded within 1% agar, Figure 3.3. MRTI data was acquired on a 1.5 T MRI scanner (ExciteHD[®], GE Healthcare Technologies, Waukesha, WI) with an 8-channel, receive-only phased array head coil (MRI Devices, Gainesville, FL) and a 2D multi-slice 8-shot EPI sequence [194] (flip angle (FA) = 60°, field of view (FOV) = 20 × 20 cm, slice thickness 4 mm, TR/TE = 544/20 ms, encoding matrix of 256 × 128, with 5–6 s per update). The procedures were conducted under institutional protocol. The canines were anaesthetised with ketamine/midazolam (Versed) solution (ketamine, 10 mg/kg; midazolam, 0.5 mg/kg; and glycolpyrrolate, 0.01 mg/kg), incubated, and aspirated with a mixture of 2% isoflurane/oxygen. Once the dogs were anaesthetised, a burr hole was introduced in the right parietal bone of each animal. In each case, the laser applicator was percutaneously placed through the burr hole and into the clinically normal brain. The silica applicator was 400 µm

in diameter with a 1-cm axial length for laser diffusion. The laser wavelength was 980 nm with a maximum power of 15 W (Photex 15, BioTex, Houston, TX). The applicator was water cooled with a maximum flow of 15 ml/min. Power histories are shown in Figures 3.3 and 3.4. Fluoroptic probes were not included to attempt to avoid susceptibility artefact.

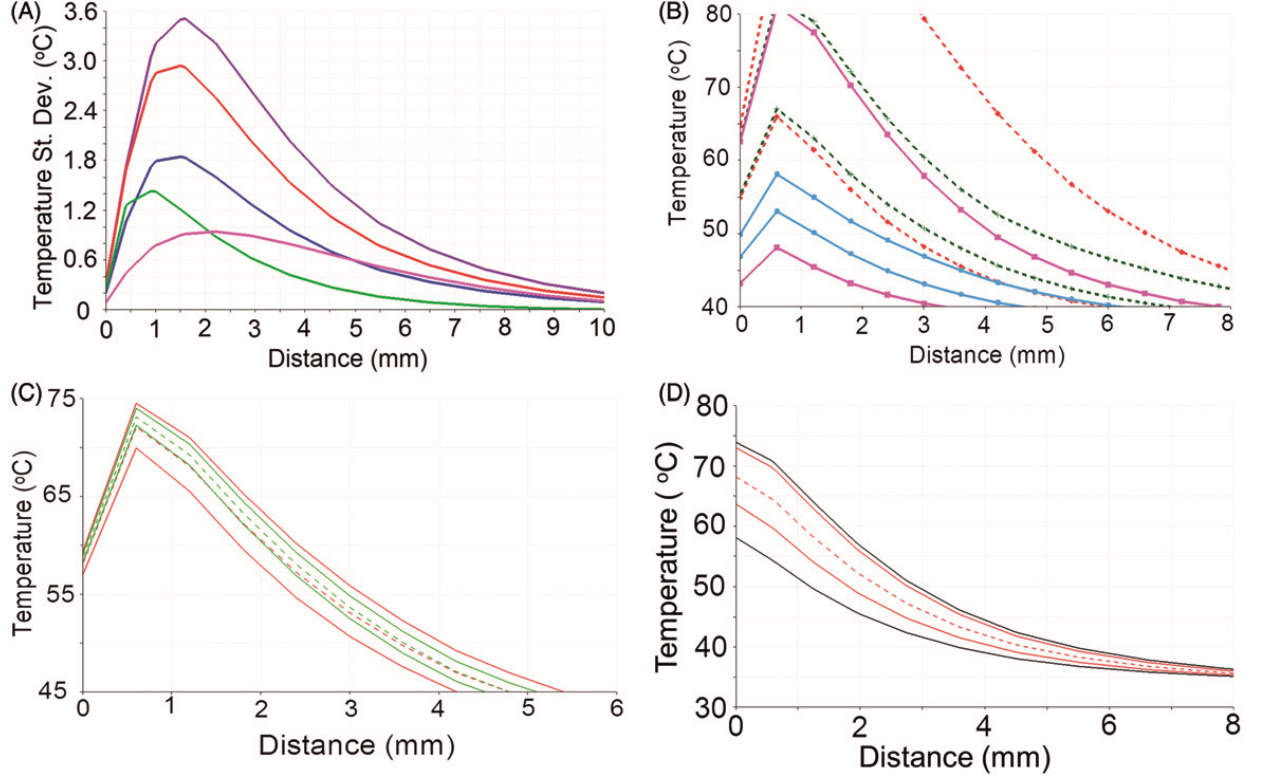


Figure 3.2: These plots are spatial profiles that demonstrate the properties of a stochastic BHTE, with inputs listed in Table 3.1. A is a linear sensitivity study; each colour represents data from a univariate model, i.e. one parameter is varied while all others are constant. A has the following plots, listed from low to high variance at peak heating: perfusion (fuchsia), conductivity (green), optical scattering (blue), optical absorption (red), and optical anisotropy (violet). The parameters' relative sensitivities can be seen in this figure. For example, perfusion is proportionally varied more than the optical absorption and scattering parameters, but the optical parameters still have a greater temperature variance. The BHTE is most sensitive to the anisotropy factor in this study. B and C are a sensitivity study comparing linear and non-linear perfusion parameters; For B and C, the solid lines represent the CDF = 2.3 and 97.7%; the enclosed region is the central 95% confidence interval. B has optical absorption (red and green with dashed lines) and scattering (fuchsia and blue with solid lines) while C has perfusion. The linear cases' inputs vary the concerned parameter over a range that includes both the native and coagulated states of the non-linear case. The plots demonstrate coagulation affecting the temperature distributions. D simultaneously varies optical scattering, optical absorption, conductivity, and perfusion. The difference between the worst-case scenarios (black) and CDF = 1% and 99% (red) is shown.

3.3.5 Computational methods

A hexahedral finite element mesh that conforms to the geometric details of the water cooled laser applicator [65, 195] was created in CUBIT (Sandia National Laboratories, Albuquerque, NM) [196]. A 21 °C Dirichlet boundary condition representing the water-cooled catheter was applied to the domain of the applicator. Simulations at several mesh spatial resolutions were run at quarter symmetry to ensure numerical convergence; 13968/47368/169680 element meshes with 15770/50898/177549 corresponding nodes were evaluated. The DAKOTA software (Sandia National Laboratories) [197] was used to implement the generalised polynomial chaos expansion. Similar to ensuring convergence of the mesh resolution, the number of polynomial chaos basis functions used in the gPC expansion was increased until the truncation error of the gPC expansion was negligible [198]. This was achieved by computing the difference between a lower order and a higher order gPC expansion. When the maximum pointwise difference between a lower order and a higher order gPC expansion was < 0.001 °C, the gPC expansion was assumed converged. Using DAKOTA, the gPC expansion order is inferred from the quadrature order in probability space. A quadrature order of four was found to achieve truncation error convergence in the gPC expansion. For comparison to gPC, a worst-case scenario approach was also run [199]. The worst-case scenario approach provides the extreme upper and lower bound of the temperature distribution by considering the extrema of the input parameter variability.

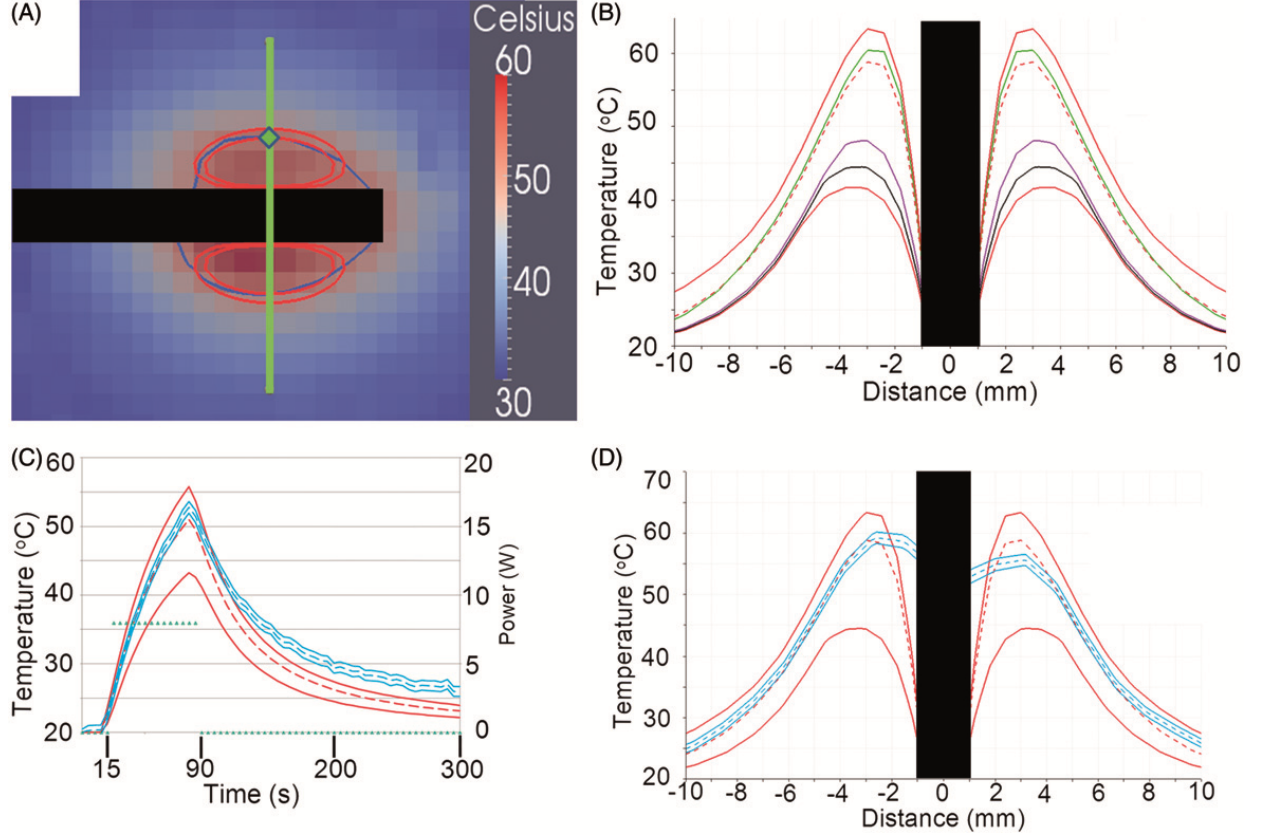


Figure 3.3: The trivariate joint uncertainty of the optical absorption, scattering, anisotropy are input for the gPC simulations. Model parameters are listed in Table 3.1. A is the MRTI of the phantom study at $t = 90$ s. The inner red contour is the 50°C isotherm for the model's mean and the outer red contour is for the CDF = 97.3%; CDF = 2.3% never reaches 50°C. The dark blue contour is the MRTI's 50°C isotherm. Only one MRTI isotherm is displayed because the MRTI variance is very small; $\pm 2\sigma$ of MRTI noise is 2°C. The black rectangles in A, B, and D occlude where the laser fibre was. The superimposed green line represents the location for linear profiles B and D. A green diamond indicates the location of the temporal profile in C. D compares the linear profile of the central 95% confidence intervals of the model and MRTI. In plot D, the model's mean tracks very well with the MRTI, particularly near the laser fibre (± 6 mm). D also dramatically shows the potential for non-Gaussian distributions to arise in the temperature model, further illustrated in B. B shows various CDF values tracked in the gPC computer package, DAKOTA. The top red is CDF = 99%, green is the median (50%), red dashed line is the mean, violet is 5%, black is 2.3%, bottom red is 1%. Note the extreme skewness of the model's temperature output near the fibre, as evidenced by the mean and median being much nearer the higher percentage CDFs than the lower percentage CDFs. The power, displayed as green points, is provided units on the right vertical axis of C.

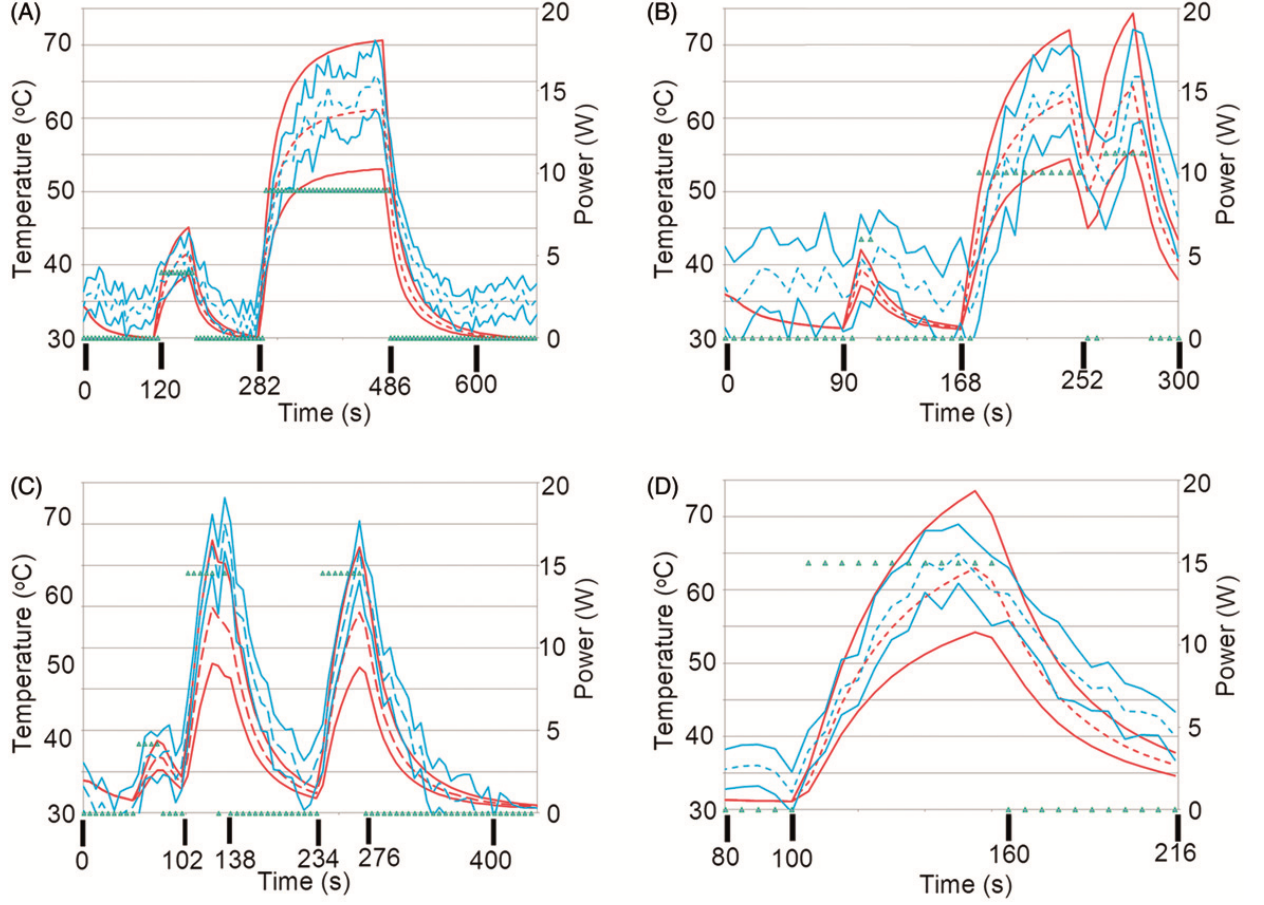


Figure 3.4: These temporal profiles, A through D, are temporal profiles from canines 1 through 4, respectively. The red and blue dashed and solid lines represent the same mean and CDF values listed in Figure 3.5. The green points represent the power history. The spatial locations of the temporal profiles are shown in Figure 3.6 via the green diamonds. A and D show the best agreement of the four plots. B is more successful at the beginning of the imaging sequence but the model is much colder at later time points. C tends to be somewhat cooler, but significant overlap remains between the MRTI and model distributions.

3.4 Results

A sensitivity study of the thermal conduction, perfusion, absorption, scattering, and anisotropy is presented in Figure 3.2. The sensitivity study was performed by investigating the effect of the uncertainty range of each parameter individually on the resulting temperature field's standard deviation (Figure 3.2A) or mean and 95% confidence interval (Figure 3.2B-D). Here the 95% confidence intervals are reported as the output cumulative temperature

distribution (CDF) between 2.5% and 97.5%. Representative profiles of the temperature field’s standard deviation resulting from considering the uncertainty in thermal conduction, perfusion, absorption, scattering, and anisotropy individually is shown in Figure 3.2(A). Results in Figure 3.2(A) are shown for the linear heat transfer problem near the maximum heating time point. Given the physically meaningful distributions found in the literature, Table 3.1, the resulting temperature field was found to be least sensitive to the perfusion and most sensitive to the anisotropy. The sensitivities in Figure 3.2(A) can be summarised by listing their peak standard deviations in °C: g 3.51; μ_a 2.94; μ_s 1.84; k 1.43; and ω 0.94. The sensitivity of the absorption, scattering, and perfusion non-linear parameters on the resulting temperature distribution is shown in Figure 3.2(B) and (C). As seen in Figure 3.1, the uncertainty in the linear problem was assumed to be bound the total nonlinear variations and the resulting linear temperature field bounds the non-linear temperature field, Figure 3.2(B) and (C). The effect of thermal coagulation is seen to shift the means of the output distributions for the non-linear perfusion, absorption, and scattering (not shown). Figure 3.2(D) demonstrates the difference between uncertainty quantification from multivariate generalised polynomial chaos and worst-case scenarios as an estimate for uncertainty quantification.

Of the five univariate gPC expansions considered, the sensitivity of the final temperature distribution 95% confidence interval for the MRgLITT simulations is seen to be least sensitive to conduction and perfusion variability. Subsequent MRgLITT simulations consider the trivariate joint uncertainty of the optical parameters, absorption, scattering and anisotropy, for comparison to MR thermometry data. The thermometry data shown was generated using standard complex phase differencing techniques and SNR-based estimates of the Gaussian uncertainty in the measured temperature value [65].

Figure 3.3 compares the 95% confidence interval of the gPC MRgLITT simulation to MRTI data acquired during an *ex vivo* heating of canine prostate tissue. The phantom provides a perfusion-less environment to compare theory to experiment. The trivariate joint

uncertainty of the absorption, scattering and anisotropy are input into the gPC simulations. Model parameters used are provided in Table 3.1. Figure 3.3(A) shows a temperature map of the MRTI near a maximum time heating point. A plot of temperature over time comparing measured to predicted values of temperature is shown in Figure 3.3(C). The power history is provided on the right axis. A spatial profile of the experimental and simulation temperature values is shown in Figure 3.3(B) and (D). The location of the spatial profiles and temporal profiles are provided in Figure 3.3(A). During heating, good agreement is seen between the measured and predicted temperature values.

The trivariate joint uncertainty of the absorption, scattering and anisotropy are input into the gPC simulations and compared to MRTI data acquired during four canine MRgLITT experiments. The comparison is provided in Figures 3.4-3.6. MRTI from the four canine MRgLITT procedures is shown in Figure 3.6. Contours of the 60 °C isotherm of the MRTI are compared to the 95% confidence interval of the gPC predictions. Locations of spatial and temporal profiles used in Figures 3.4 and 3.5 are shown. An additional simulation varying perfusion only and using optics parameters from white matter is shown to compare the differences in input parameters from white matter to grey matter, Figure 3.5(A). The white matter-based, ω -univariate simulation shown in Figure 3.5(A) is clearly much colder and led to the decision to use grey matter weighted optics parameters in the trivariate simulations, shown in Table 3.1. Spatial and temporal profiles, seen in Figures 3.4 and 3.5, show that canines 1 and 2 had a majority of overlapping regions between the MRTI and the simulations' 95% confidence intervals. It should be noted that canines 3 and 4's disagreement occurs relatively distant from the laser fibre.

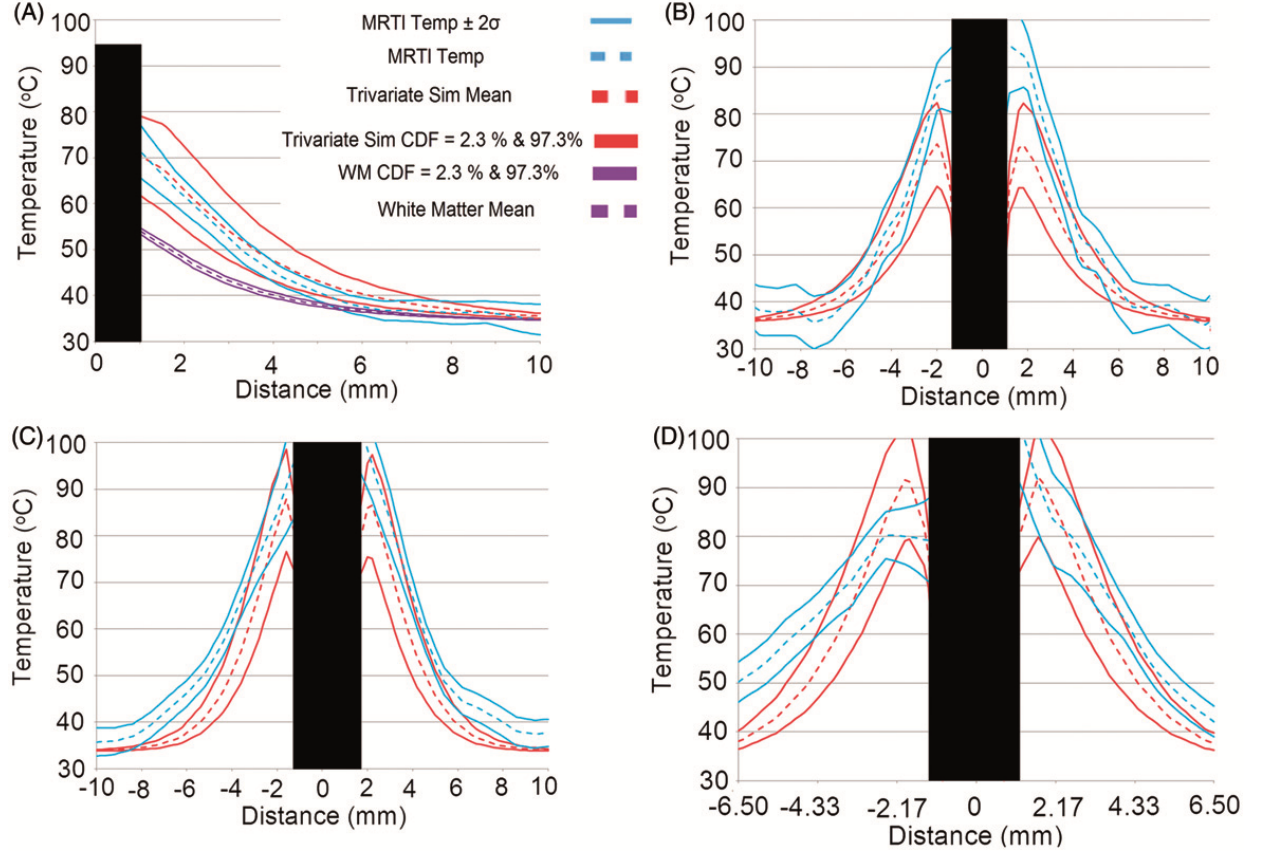


Figure 3.5: Plots A through D correspond to canines 1 through 4 at the same time points described in Figure 3.6. A also contains a perfusion univariate model that uses optical scattering and absorption from white matter tissue (violet). The black rectangles obfuscate the portions of the linear profiles that are on the laser fibres because those regions provide invalid comparisons. A suggests that white matter optical scattering and absorption parameters produce profoundly colder temperatures. In plots A and B the trivariate model tends to overlap the MRTI well. Plots C and D show some agreement near the fibre (± 3 mm), but diverge at further distances.

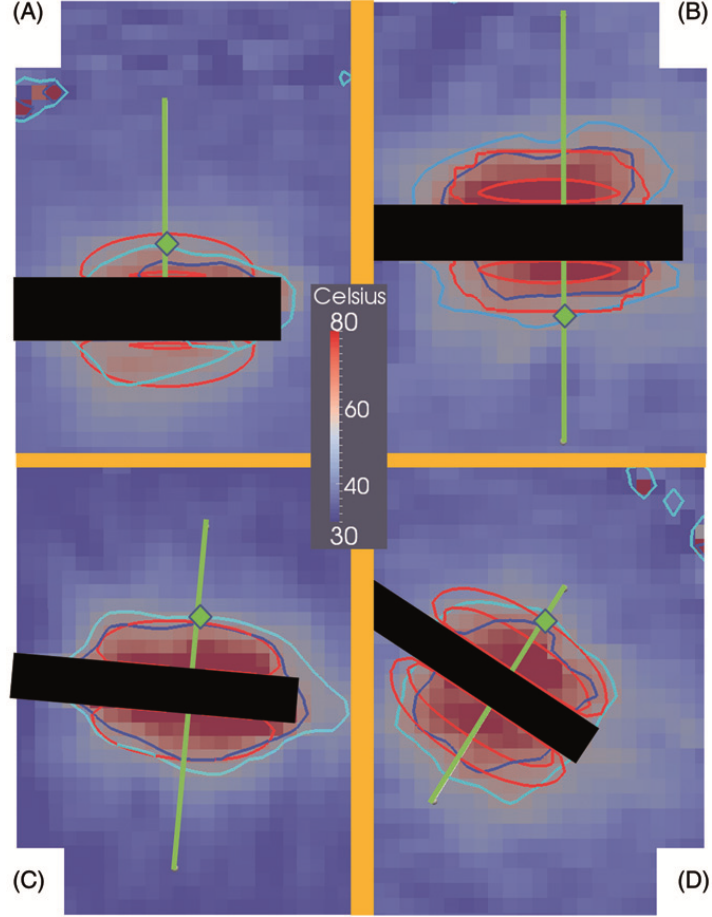


Figure 3.6: These images are MRTI from the four canine normal brain MRgLITT ablations. All images are from a slice that intersects the longitudinal axis of the laser applicator. Images A, B, C and D respectively correspond to canines 1, 2, 3 and 4 near maximum heating times $t = 432$ s, 222 s, 120 s, and 135 s. The superimposed green lines represent where the linear profiles for the four canines are plotted for Figure 3.5. Green diamonds indicate the location of temporal profiles in canine Figure 3.4. The black rectangles in each image are where the laser fibres were. The concentric red contours correspond to the predicted 60°C isotherm contours with probabilities $\text{CDF} = 2.3\%$ and 97.7% . The areas between the red contours represent the central 95% of the model's temperature distribution. According to the model, the $\text{CDF} = 2.3\%$ contour has a high probability of occurring, i.e. 97.7% . The dark blue and light blue contours respectively are the 60°C isotherms from the MRTI temperature $\pm 2\sigma$ of MRTI noise.

3.5 Discussion

A generalised polynomial chaos (gPC) method was used to propagate the uncertainty in the biothermal and optical parameters. A finite element-based stochastic form of the 3D Pennes bioheat transfer model was implemented for these purposes. The ability to accept plausible distributions of the biothermal and optical parameters and output realistic distributions of the temperature mean and variance is a novel aspect of gPC-based simulation. In a probabilistic bioheat simulation the challenge shifts from utilising the most precise constitutive values to identifying an appropriate input distribution. However, when using gPC, the model input distributions are limited to the Wiener-Askey scheme [171]. The two distributions considered were the Gaussian and uniform distributions. Because Gaussian distributions have been successfully and ubiquitously applied to probabilistic natural phenomena, Gaussian distributions were initially identified as an option. However, Gaussian distributions are positive from $-\infty$ to $+\infty$. In order to be physical, the constitutive values must be positive. If a Gaussian distribution was applied to the constitutive input distributions, the model would be influenced by non-physical inputs. The uniform distribution was chosen for use in the constitutive value distributions because it is straightforward to restrict the distribution to physical values.

The sensitivity study, displayed in Figure 3.2, shows the output variance of the five univariate models. It is important to note the relative input variance, based on published literature values, to the output variance. For example, ω is varied from $3 \text{ kg m}^{-3} \text{ s}^{-1}$ to $9 \text{ kg m}^{-3} \text{ s}^{-1}$, i.e. the variance is the mean $\pm 50\%$. When compared to the variance of μ_a (mean $\pm 20\%$), it is evident that the BHTE is much more sensitive to μ_a than ω . Namely, even though ω is proportionally varied more than μ_a , the output temperature variance due to ω is considerably less than μ_a . The parameters found to produce the greatest variances were the optical parameters. Further, for the parameter range considered, the confidence intervals of temperature simulations using non-linear temperature and damage-dependent

perfusion, scattering, and absorption (Equation 3.3) is bounded by the linear temperature simulations. Within this statistical setting, the linear problem with its associated uncertainty is used as a surrogate for the more complex non-linear bioheat transfer phenomena. The linear form of the optical parameters, μ_a , μ_s , and g , were used in the trivariate gPC-based MRgLITT simulations for comparison with the phantom experiments and canine ablations.

Comparison of worst-case scenarios and gPC estimates, Figure 3.2(D), demonstrate that the deterministic worst-case scenarios do not adequately capture the bulk of the statistical information in multivariate simulations, the worst-case scenarios only indicate the extrema. This is particularly true as the joint uncertainty of progressively more parameters is expanded in probability space. It is conceivable that worstcase scenarios could approximate gPC estimates in special cases, for example univariate simulations or parameters with low sensitivity yielding low output variance. However, these same special cases are less likely to require uncertainty quantification, which is the reason we used to legitimise our focus on the optics when comparing the trivariate models for the gPC-based MRgLITT simulations.

A more exhaustive application of uncertainty quantification to LITT would also examine the effect of other bioheat parameters, for example ρ , c_t , and μ_a , and thermal dose parameters. Uncertainty in the dose parameters (either Arrhenius or cumulative effective minute (CEM) models) [77] depends on the temporal length of the hyperthermia treatment. In the case of relatively temporally short, spatially small $> 60^\circ\text{C}$ ablations, thermal dose models predict the spatial transition between coagulative necrosis of tissue and survival is small. However, for sub-ablative hyperthermia where thermal dose is accumulated over greater time, variance in thermal dose parameters may lead to appreciable spatial variance in the lethal threshold region or other interesting thermal dose levels. Future studies should investigate uncertainty in thermal dose parameters' effect on thermal dose uncertainty, especially for temporally longer hyperthermia treatments.

Regarding the MRTI for canine 1, Figures 3.4-3.6, it should be noted that the canine’s brain ventricle was punctured by the catheter. The ventricle leaked cerebral spinal fluid (CSF) into the catheter’s insertion tract and ultimately pooled near one side of the laser fibre. The effect of the CSF on the thermal ablation can be seen as reduced temperature for the lower side of the thermal lesion in Figure 3.1. The effect is most obvious in the MRTI’s 60 °C isotherms. The model did not account for the presence of the CSF and therefore the regions affected by the CSF were excluded from analysis. Regarding the MRTI in general, the pixels imaging the laser fibre and very proximal regions affected by susceptibility artefact were not included in the linear profiles or isotherm contours. Further sources of discrepancy between simulation and MRTI during the cooling regime, Figures 3.3(C) and 3.4, are not seen in studies with external optical fibres [200] and are likely due to inaccuracies of the Dirichlet boundary condition to model the convective cooling of the catheter. Validation of physics-based models [57, 201] of the convective heat transfer of the cooling fluid through the laser applicator is a topic of future work.

Despite multivariate gPC expansions being more appropriate for thermal therapy simulation, univariate gPC expansions may be used in future investigations to identify which parameters create the greatest variance of the temperature output, and subsequently restrict the gPC expansion to parameters that affect the temperature output the greatest. Improving the input distributions for the constitutive values should be investigated. Ideally, the model’s constitutive distributions would reflect the natural distributions of the constitutive parameters. The Wiener-Askey scheme includes gamma and beta distributions that are each a set of parameterised distributions. Both gamma and beta distributions include distributions that are not negative and resemble the Gaussian distribution’s distinctive ‘bell curve’. While Gaussian-like distributions exist, there is presently no particular reason any single distribution should work best. It may be sufficient to attempt an array of distributions in order to discover distributions that minimise the difference between the model and MRTI. Future investigations should additionally explore further statistical metrics of

the model’s outcome. Possible tests include using spatio-temporal pixel-wise statistical tests for the difference or similarity between the model’s mean and MRTI’s temperature. The common example test for the difference of means is the Student’s t -test, however, the model’s polynomial expansion is not generally a Gaussian distribution so other tests should be sought.

This investigation took the natural step of comparing the model’s confidence interval to the MRTI’s confidence interval. In the case of gPC, the polynomial expansion probability distribution function was integrated to yield the polynomial expansion’s CDF. The CDF in turn indicated the probability of a threshold temperature (e.g. the temperature is $> 60^{\circ}\text{C}$) as a function of distance from the laser fibre. These probabilities have a clear use in planning for thermal ablations. A stochastic simulation with temperature UQ gives the surgeon a probabilistic measure of the temperature. There are at least two methods of clinically using temperature UQ. First, the physician can plan the ablation using the stochastic model’s mean temperature prediction and the variance about the mean. For example, if a physician observes a large variance about the mean, the simulation cannot be implicitly trusted. Alternatively, temperature UQ could aid ablation planning by displaying an isotherm that is very likely to occur. For example, the physician could plan the ablation based on the $\text{CDF} = 5\%$ level. That is, the model would display a treated region that has a 95% chance of occurring. While deterministic thermal predictions do not have a measure of their uncertainty, a stochastic simulation provides confidence intervals. An example would be a surface contour that demarcates a volume that has at least a 95% probability of reaching 60°C . Uncertainty quantification to create a ‘high probability of treatment’ contour is a highly desired goal. An accurate, high probability of treatment contour would allow physicians to quantify a measure of the probability of success. Also, there is little risk of overtreatment if the contour exceeds the desired treatment region; MRgLITT’s real-time MRTI provides the physician with feedback for ceasing treatment.

In conclusion, results demonstrate the utility of generalised polynomial chaos (gPC)

expansion techniques to propagate parameter uncertainties through the computer model of bioheat transfer, and quantify uncertainties in the resulting output temperature distributions. Given parameter uncertainties and mathematical modelling approximations of the Pennes bioheat model, the 95% confidence intervals within the statistical framework demonstrate conservative estimates of the thermal therapy outcome and have potential for use as a computational prediction tool for thermal treatment planning.

Acknowledgements

The authors are grateful for discussions with Ivo Babuška on uncertainty quantification applied to non-linear partial differential equations.

Declaration of interest

The research in this paper was supported in part through NIH grants 5T32CA119930-03, 1R21EB010196-01, CA016672, and TL1TR000369. Canine data was obtained from BioTex, under grants R43-CA79282, R44-CA79282, R43-AG19276. The authors would also like to thank the DAKOTA [197], ITK [202], Paraview [203], PETSc [155], libMesh [204], and CUBIT [196] communities for providing enabling software for scientific computation and visualisation. Simulations were performed using allocations at the Texas Advanced Computing Center. The authors alone are responsible for the content and writing of the paper.

Chapter 4

A Model Evaluation Study for Treatment Planning of Laser Induced Thermal Therapy

This Chapter is a near-verbatim quotation of Fahrenholtz et al. [67]. Among the specific aims, this Chapter is the calibration and simulated validation of the finite element method model. The Chapter uses English grammar and spelling of the United Kingdom. The only intended modifications are the numbering of citations, equation numbers, figure numbers, table numbers, and section numbers. The citations are numbered according to the dissertation, as opposed to the quoted journal article. Its citation, according to the Taylor & Francis online-only format, is thus:

Samuel J. Fahrenholtz, Tim Y. Moon, Michael Franco, David Medina, Shabbar Danish, Ashok Gowda, Anil Shetty, Florian Maier, John D. Hazle, Roger J. Stafford, Tim Warburton, David Fuentes. "A model evaluation study for treatment planning of laser-induced thermal therapy." *International Journal of Hyperthermia*, 2015;31(7):705-14.

Copyright ©2015, Taylor & Francis. Reproduced with permission of Taylor & Francis.

4.1 Abstract

A cross-validation analysis evaluating computer model prediction accuracy for a priori planning magnetic resonance-guided laser-induced thermal therapy (MRgLITT) procedures in treating focal diseased brain tissue is presented. Two mathematical models are considered. (1) A spectral element discretisation of the transient Pennes bioheat transfer equation is implemented to predict the laser-induced heating in perfused tissue. (2) A closed-form algorithm for predicting the steady-state heat transfer from a linear superposition of analytic point source heating functions is also considered. Prediction accuracy is retrospectively evaluated via leave-one-out cross-validation (LOOCV). Modelling predictions are quantitatively evaluated in terms of a Dice similarity coefficient (DSC) between the simulated thermal dose and thermal dose information contained within $N = 22$ MR thermometry datasets. During LOOCV analysis, the transient model's DSC mean and median are 0.7323 and 0.8001 respectively, with 15 of 22 DSC values exceeding the success criterion of $\text{DSC} \geq 0.7$. The steady-state model's DSC mean and median are 0.6431 and 0.6770 respectively, with 10 of 22 passing. A one-sample, one-sided Wilcoxon signed-rank test indicates that the transient finite element method model achieves the prediction success criteria, $\text{DSC} \geq 0.7$, at a statistically significant level.

4.2 Introduction

Approximately 211 000 patients in the USA present each year with brain tumours. Of these, 38 000 are benign primary tumours, 23 000 malignant primary tumours, and 150 000 are metastatic, originating largely from lung, breast, and melanoma [35,205–208]. The average life expectancy for patients with primary and metastatic malignancies in the brain, from time of diagnosis until death, is approximately 12–16 months. Five-year survival is among the lowest of all cancers. Current treatment options include conventional surgery,

stereotactic radiosurgery (SRS), or chemotherapy. Surgical resection may be preferred for patients presenting with a single, solitary lesion, or lesions greater than 2.5–3.0 cm in which the size or location of the tumour causes neurological symptoms such as seizures, headaches, cognitive or motor deficits, that can be resolved by reducing the volume of the disease. SRS, such as Gamma Knife[®], is typically performed on patients with multiple tumours, tumours under 2.5 cm in diameter, and deep seated tumours [209]. An additional target in the brain is epileptogenic foci for patients with medically refractory epilepsy, where MRgLITT is being considered for the surgical armamentarium for those patients [37, 43]. Unfortunately, patients with malignant recurrences who have reached maximum radiation dose limitations and complications with surgical resection create a group of patients with no remaining conventional treatment options; meanwhile patients with medically refractory epilepsy have limited interventions available. Magnetic resonance-guided laser-induced thermal therapy (MRgLITT) presents an alternative, minimally invasive thermal ablation technique for these groups of patients and has been safely and successfully applied to each [55, 108, 109, 142, 143, 210, 211].

Under MR guidance, the laser applicator is carefully navigated through critical structures and placed directly into the diseased tissue to induce ablative heating and destroy the tissue. Real-time thermometry of the treatment volume during laser heating provides a mechanism by which it is possible to deliver these therapies in both a safe and effective manner [15, 148, 212, 213] as well as to estimate the extent of tissue damage [78, 214, 215]. However, the heating induced by the laser is not constrained exclusively to tumour tissue and nearby tissue damage is possible. For these procedures to progress to standard of care, a priori determination of the optimal placement of the laser catheter(s) is crucial for achieving a more conformal delivery of therapy over the target volume with minimal co-morbidity of intervening or adjacent tissue. Surgical workflows in which the operating room and MRI suite are separate [37, 39] escalate the advantages of a predictive model.

This manuscript focuses on the development of a practical methodology for evalu-

ating computer model predictions for a priori planning the procedure, given N datasets from previous procedures. Evaluation focuses on prediction accuracy for guiding applicator placement. Retrospective analysis of MR thermometry data acquired during previous procedures is essential to train or calibrate the computer model parameters. The machine learning and statistics community have a rich history in applying various algorithmic and physics-based data models to reach conclusions from a given dataset [216, 217]. Here we assume that a Pennes bioheat transfer model [160] provides representative predictions of the physical process underlying the heating observed within the MR thermometry data. This physics-based approach provides a theoretically sound and concise methodology to statistically summarise the high dimensional thermometry dataset with a low dimensional model parameter subset.

Two distinct modelling approaches are pursued: 1) A GPU implementation of an unstructured hexahedral spectral element method for predicting the bioheat transfer is developed, and 2) a computationally inexpensive algorithm for predicting the heat transfer from a linear superposition of analytic point source heating functions is also presented as a reference implementation. Combined with the data, the two modelling approaches presented provide an environment to critically evaluate model accuracy and selection for therapy planning of MRgLITT. Both approaches build intuition into the prediction by repetitively training the underlying physics model to statistically match representative datasets. Predictions are critically evaluated in terms of solution efficiency and accuracy for prospective treatment planning of MRgLITT procedures. Leave-one-out cross-validation (LOOCV) is used to simulate the clinical scenario in which N datasets from previous procedures are available to calibrate the computer model. LOOCV provides an objective framework to critically estimate the accuracy and confidence in predicting the outcome of the procedure for the $N + 1$ patient [218–222].

4.3 Methods

4.3.1 Thermometry data

MR thermal monitoring from MRI-guided stereotactic laser-induced thermal therapy (LITT) was considered in $N = 22$ MR thermometry datasets. The datasets were vetted for motion artefacts, low signal-to-noise, and catheter-induced signal voids that spuriously reduce the modelling accuracy. Each patient was treated with the Visualase Thermal Therapy System (Visualase, Houston, TX). The Visualase[®] system includes a 15 W 980 nm diode laser, a cooling pump, and a laser applicator set. The laser applicator set is disposable and consists of a 400 μm core silica fibre optic with a cylindrical diffusing tip housed within a 1.65 mm diameter saline-cooled polycarbonate cooling catheter [109, 215]; see Figure 4.1. Applicator cooling lines and laser fibre optics are connected through a waveguide between the control room and the bore of the MR magnet. An MR-compatible head holder is used to secure the patient’s head. The trajectory to the targeted tumour lesion was obtained using the Brainlab navigation system (Brainlab, Westchester, IL). A battery-powered hand drill was used to place a threaded plastic bone anchor within the skull. The laser applicator is secured to the threaded plastic bone anchor. The Visualase[®] system imports images from a 3D MPRAGE sequence to verify applicator position within the lesion. The depth is determined by the navigation software and is input retrospectively within this study.

MR temperature imaging was performed on a 1.5 T MRI (GE Healthcare Technologies, Waukesha, WI) using a 2D gradient echo sequence [223] (flip angle = 30° , field of view = $24 \times 24 \text{ cm}^2$, matrix size = 256×128 , repetition time/echo time = 37.5/20 ms, receive-only head coil, 5 s per update). The imaging plane was chosen perpendicular to the axial direction of the applicator and allowed monitoring of critical structure regions. The Visualase[®] workstation communicates with the MR scanner to obtain raw DICOM imaging data during the procedure. The temperature-dependent water proton resonance frequency shift is measured by calculating the complex phase difference observed during

heating. The water proton resonance frequency chemically shifts to lower frequencies with higher temperatures (caused by rupture, stretching, bending of hydrogen bonds) [129]. The total temperature change, Δu , is proportional to the measured phase change, $\delta\phi$.

$$\Delta u = \frac{\delta\phi}{2\pi\alpha \cdot \gamma B_0 \cdot \text{TE}}$$

Here α is the temperature sensitivity coefficient, γ is the gyromagnetic ratio of water, B_0 is the static magnetic field strength, and TE is the echo time. A baseline body temperature of $u_0 = 37.0^\circ\text{C}$ is assumed to obtain absolute temperature. An Arrhenius rate process model [224] was used to evaluate the thermal dose resulting from the time-temperature history of the laser exposure.

$$\Omega(t) = \int_0^t A e^{\frac{-E_A}{Ru(\tau)}} d\tau \quad (4.1)$$

In this Arrhenius thermal dose model, the frequency factor, A , and the activation energy, E_A , are experimentally determined kinetic parameters. The values for A and E_A were $3.1\text{E}98 \text{ s}^{-1}$ and $6.28\text{E}5 \text{ (J/mol)}$, respectively, and have been used in previous studies [61, 142, 145]. R is the universal gas constant. The thermal dose was assumed to be lethal at doses $\Omega \geq 1$ as seen in previous reports [142, 145].

Prior to treatment delivery, a low power test pulse — e.g., 4 W for 30 s — is applied to verify the position of the diffusion fibre optic within the catheter. The test pulse is sufficient to allow thermal visualisation but not cause thermal damage. Multiple thermal imaging datasets are available per patient; only the therapeutic pulses are considered in this study. A representative laser power profile used during the therapy is shown in Figure 4.1. All DICOM header information was imported into an SQLite database to provide efficient queries and organise thermometry data for reproducible analysis and processing. The schema provided by the Slicer [225] DICOM module was used as a template for the table structure. The object identifier (OID) of the SQL table was used to provide anonymous references to the data. The SQL functions, `group by`, `group_concat`, and `count`, were

used in quality assurance of the data location, number of files, for example. Metadata needed for the analysis included the following.

1. The applicator orientation and heating region of interest (ROI) were manually identified within the imaging datasets for input into the computer models discussed in the sections immediately below.
2. A text file containing the relevant laser power history for each imaging dataset was parsed and input into the simulation. The power history provides information on the heating and cooling time intervals during the procedure.

4.3.2 Simulation of bioheat transfer within laser irradiated tissue

A time-dependent Pennes [160] bioheat transfer equation provides a computer model for predicting the temperature field resulting from the laser tissue interaction.

$$\begin{aligned}
\partial u_t - \nabla \cdot (\alpha \nabla u) + \frac{\omega c_{blood}}{\rho c_p} (u - u_a) &= \frac{1}{\rho c_p} q_{laser} \quad \text{in } U \setminus U_{tip} \quad (4.2) \\
q_{laser}(x, t) &= \int_{U_{tip}} \frac{p(t) \mu_{eff}^2}{\text{Vol}(U_{tip})} \frac{\exp(-\mu_{eff} \|x - \xi\|)}{4\pi \|x - \xi\|} d\xi \quad x \in U \setminus U_{tip} \\
\alpha &= \frac{k}{\rho c_p} \quad \mu_{eff} = \sqrt{3\mu_a \mu_{tr}} \quad \mu_{tr} = \mu_a + \mu_s(1 - g) \\
n \cdot (\alpha \nabla u) &= 0 \quad \text{on } \partial U \quad n \cdot (\alpha \nabla u) = h(u - u_{cooling}) \quad \text{on } \partial U_{tip}
\end{aligned}$$

Here the tissue specific heat, c_p ; tissue density, ρ ; thermal conductivity, k ; perfusion, ω ; blood specific heat, c_{blood} ; and arterial blood temperature, u_a , are deterministic model parameters obtained from the literature [183, 226, 227], see Table 4.1. The laser source, q_{laser} , is a deterministic function of the applied power, $p(t)$; optical scattering, μ_s ; optical absorption, μ_a ; anisotropy factor, g ; and distance, $\|x - \xi\|$, from the source, U_{tip} . Active cooling of the water flowing through the applicator is modelled by a Robin or mixed boundary condition in which the temperature flux at the applicator interface is proportional to the

convection coefficient, h , and the temperature difference between the cooling fluid $u_{cooling}$ and the tissue. A diagram of the Visualase[®] applicator used in this application is shown in Figure 4.1.

Table 4.1: Constitutive data [183, 226, 227]

k [$\frac{\text{W}}{\text{mK}}$]	ω [$\frac{\text{kg}}{\text{m}^3\text{s}}$]	g [Unity]	μ_s [cm^{-1}]	μ_a [cm^{-1}]	ρ [$\frac{\text{kg}}{\text{m}^3}$]
0.527	9.0	0.88	14000	500	1045
c_{blood} [$\frac{\text{J}}{\text{kgK}}$]	c_p [$\frac{\text{J}}{\text{kgK}}$]	h [$\frac{\text{W}}{\text{Km}^3}$]	$u_{cooling}$ [$^{\circ}\text{C}$]	u_a [$^{\circ}\text{C}$]	
3840	3600	100	21	37	

An implicit Euler time discretisation is used to reduce the time-dependent bioheat equation, Equation (4.2), into a sequence of elliptical problems. Hexahedral Lagrange elements (polynomial order = 3) were used in the finite element discretisation of the spatial domain. These elements use a tensor product of Gauss-Lobatto-Legendre (GLL) interpolation nodes and are commonly referred to as spectral elements. A matrix-free preconditioned conjugate gradient algorithm is used to solve the linear system of equations inherent in the discretisation. An overlapping additive Schwarz preconditioner is used since the local block problem on each element is well suited for the block-coupled parallelism of the wide SIMD cores on the GPU. The matrix-free approach minimises the storage requirements and data movement of the finite element elliptical solvers. The preconditioned conjugate gradient algorithm does not explicitly demand the system matrix to be stored but only requires the evaluation of matrix vector products, and the structure of the tensor product hexahedral elements allow this action to be computed with $\mathcal{O}(N^4)$ operations per degree- N finite element. Avoiding assembly and storage of the stiffness matrix on the GPU allows the solver to handle discretisations with a large number of elements to compensate for the limited memory on the GPU. This algorithmic approach is shown to have high computational efficiency on the non-uniform memory architecture of modern GPUs [228].

All computations were performed on the template hexahedral mesh shown in Figure 4.1(B). For each simulation the template was registered to the observed laser location

for each patient. The mesh consists of disjoint regions for the applicator and tissue. A quadrilateral mesh was extruded axially along the applicator to create the base of the hexahedral finite element mesh. The mesh for the tissue conforms to the surface of the application and extends sufficiently far to ensure that the boundary does not influence the heating. The discretisation consists of $N_{dof} = 844\,032$ total GLL nodes. The degrees of freedom across the volume of the applicator were removed; the effect of the room-temperature cooling fluid which protects the laser fibre during heating were considered through the boundary conditions at the surface nodes. Similar to previous studies [65], multiple mesh resolutions were considered to ensure convergence of the discretised solution; a mesh resolution approximating the 1 mm pixel size near the applicator was used. Multiple time resolutions were also evaluated to ensure convergence of the time stepping scheme.

4.3.3 Analytic steady state solution

A steady-state version of the Pennes bioheat equation, Equation (4.2), was also considered as a surrogate model for the therapy planning, in order to investigate the accuracy of a simpler, trained model. Constant coefficients are assumed. A one-dimensional spherically symmetrical radial decomposition of the solution, $u(r) - u_a = \frac{\mathcal{R}(r)}{r}$, simplifies the analysis of the differential operator in spherical coordinates.

$$\frac{\omega c_{blood}}{\rho c_p} \frac{\mathcal{R}(r)}{r} - \frac{\alpha}{r} \frac{d^2 \mathcal{R}}{dr^2} = \frac{\mu_{eff}^2 P \exp(-\mu_{eff} r)}{4 \pi r}$$

$$u(r_1) = u_0 \quad \left. \frac{du}{dr} \right|_{r_2} = 0 \quad r_1 < r_2$$

From classical theory [229], the general solution is the linear combination of the homogeneous solution, u_h , and a particular solution, $u_p = \frac{1}{r} (A \exp(-\mu_{eff} r) + B r \exp(-\mu_{eff} r))$.

From classical theory [229], the general solution is the linear combination of the homogeneous solution, u_h , and a particular solution, $u_p = \frac{1}{r} (A \exp(-\mu_{eff} r) + B r \exp(-\mu_{eff} r))$.

In this case, the particular solution was obtained from the method of undetermined

coefficients for $A, B \in \mathbb{R}$.

$$u = \underbrace{C_1 \frac{\exp\left(\sqrt{\frac{\omega c_{blood}}{k}} r\right)}{r} + C_2 \frac{\exp\left(-\sqrt{\frac{\omega c_{blood}}{k}} r\right)}{r}}_{u_h} + \underbrace{\frac{\mu_{eff}^2 P \exp(-\mu_{eff} r)}{4 \pi r (\omega c_{blood} - k \mu_{eff}^2)}}_{u_p} + u_a \quad (4.3)$$

The boundary conditions are used to determine the coefficients of the homogeneous solution. Applicator cooling is specified by the boundary condition at $r = r_1 = 0.75$ mm. The domain is assumed large enough that no heat flux is observed at the far boundary, $r = r_2 = 1$ m.

$$\begin{bmatrix} \frac{\exp\left(\sqrt{\frac{\omega c_{blood}}{k}} r_1\right)}{r_1} & \frac{\exp\left(-\sqrt{\frac{\omega c_{blood}}{k}} r_1\right)}{r_1} \\ \left. \frac{d}{dr} \frac{\exp\left(\sqrt{\frac{\omega c_{blood}}{k}} r\right)}{r} \right|_{r_2} & \left. \frac{d}{dr} \frac{\exp\left(-\sqrt{\frac{\omega c_{blood}}{k}} r\right)}{r} \right|_{r_2} \end{bmatrix} \begin{bmatrix} C_1 \\ C_2 \end{bmatrix} = \begin{bmatrix} u_0 - u_p(r_1) - u_a \\ - \left. \frac{du_p}{dr} \right|_{r_2} \end{bmatrix}$$

The one-dimensional solution provides an estimate of the heating from a single point source with applicator boundary at r_1 . Mathematica 7 (Wolfram, Champaign, IL) was used to determine and verify all coefficients. Then, `ccode` was used to write out the kernel. Similar analytical solutions are provided in Giordano et al. [230–232]. Heating caused by the cylindrical geometry of the diffusing tip was modelled as evenly distributed point sources, $M = 10$, along the axial dimension of the applicator at positions r_{0_i} .

$$u = \sum_{i=1}^M u_h(r - r_{0_i}) + u_p(r - r_{0_i}) \quad (4.4)$$

4.3.4 Model calibration

For each thermometry dataset discussed above, an inverse problem was solved to calibrate both computer models considered for the heating observed. Previous work [59] showed that the optical parameters provided the highest sensitivity in the temperature predictions over

the range of physically meaningful model parameters. Consequently, optical parameters were considered in the optimisation. The analytical form of the standard diffusion approximation for the laser source term concisely represents the heating as a function of the single optical parameter, μ_{eff} . At the end of optimisation for one MRTI dataset, the dataset has a corresponding optimal μ_{eff} that is constant in space and time.

The out-of-plane translation component, z , of the mesh template shown in Figure 4.1 was also optimised. The physics of the MR thermometry data acquisition averages the temperature over the slice thickness and the translation update is implemented to tune the registration of the computational domain to the MR thermometry data. The remaining input parameters are assumed fixed.

The Dakota (Sandia National Laboratories, Albuquerque, NM) [197] [197] library was used to optimise μ_{eff} for the transient and steady-state models. The L_2 error over space and time was used as the objective function.

$$(\mu_{calib}, z_{calib}) = \arg \min_{(\mu_{eff}, z)} \sum_{k=1}^{N_{step}} \|u(t_k) - u^{MRTI}(t_k)\|^2$$

Thermometry data is denoted u^{MRTI} . All time steps were considered for the transient analysis of the computer model presented above. For the steady-state model presented above, the objective function was the L_2 norm between the model and the MRTI's maximum heating time point. A quasi-Newton optimisation method, `opp_q_newton`, was implemented as the optimisation algorithm for both models. Gradients of the objective functions were computed using numerical finite differences. The calibration was solved as a bound constrained optimisation problem. A physically feasible parameter bound on the optimisation of the optical parameters, $\mu_{eff} \in [0.8, 400] \text{ m}^{-1}$, was obtained from the literature [227]. During calibration, the initial value for μ_{eff} was 180 m^{-1} . The initial value was calculated via the μ_{eff} identity from Equation (4.2) and the μ_a , μ_s , and g values from Table 4.1. The slice thickness of the MR thermometry data was used to bound the optimisation of the

template out of plane translation.

4.3.5 Leave-one-out cross-validation

Leave-one-out cross-validation (LOOCV) is a method for estimating a trained, i.e. calibrated, model's accuracy in prediction [218–222]. Within this context, developing a ‘predictive model’ refers to the process by which we can confidently assign a probability to a treatment outcome, such as full tumour destruction or damage to surrounding healthy tissue. Similar to the human cognitive process, the predictive computer model is built from prior experience using MR temperature imaging data used to monitor the procedure. The datasets are used to calibrate the computer model parameters as discussed in the [previous section](#). The LOOCV algorithm is executed as:

- for each thermometry dataset $i = 1, \dots, N$
 - The average value for the optical coefficient, $\overline{\mu_{eff}^i}$, is learned from the calibration results, μ_{calib}^j , on the remaining $j \neq i$ datasets.

$$\overline{\mu_{eff}^i} = \frac{1}{N-1} \sum_{j \neq i} \mu_{calib}^j$$

- Tissue damage on the i -th dataset is predicted by using the average, $\overline{\mu_{eff}^i}$, values from the $j \neq i$ cohort. The Dice similarity coefficient (DSC) provides an estimate of the agreement with Arrhenius damage measured from thermometry data.

$$DSC(\overline{\mu_{eff}^i}) = 2 \frac{A \cap B}{A + B} \quad \overline{\mu_{eff}^i} \neq \mu_{calib}^j$$

The DSC measures the area of overlap between the area enclosed by the Arrhenius damage model for the thermometry data, A , and the computer model prediction, B . The Arrhenius damage, Equation (4.1), is computed from the simulated temperature field of the transient analysis. The isotherms are used as the damage model for the steady-state

analysis. Previous work in canine brain demonstrated that the 57 °C isotherm produced damage regions similar to the Arrhenius model for the ablation regime considered in this study [140].

The trained model’s predictive ability is evaluated by analysing the distribution of DSC values from the N iterations of LOOCV. A one-sample, one-sided Wilcoxon signed-rank test examines whether the trained model prediction’s median exceeds $DSC \geq 0.7$. One-sample calculations were computed using a threshold DSC value, 0.7, as the null hypothesis H_0 .

$$H_0 : DSC = 0.7 \quad H_1 : DSC > 0.7$$

The value chosen is a commonly accepted value in image processing literature [9, 140, 233]; $DSC = 1$ implies complete agreement between the measure and predicted damage model, i.e. the predicted and measured damage volumes completely overlap. A two-sample, paired Wilcoxon signed-rank test was used to compare whether the two models’ prediction medians were statistically different from one another. All statistical tests and descriptive statistics were evaluated on GraphPad Prism 6.01 (GraphPad Software, La Jolla, CA).

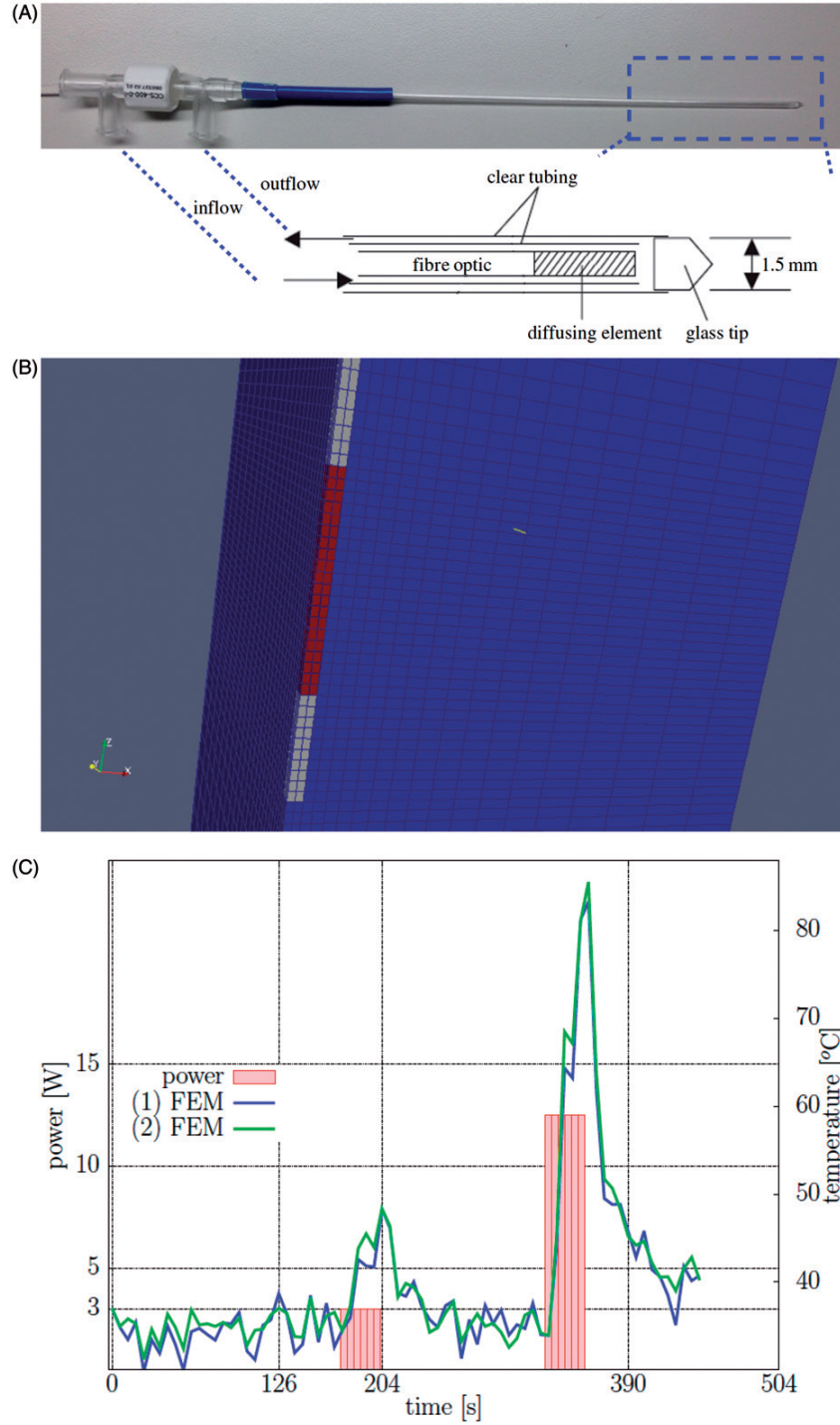


Figure 4.1: (A) The Visualase[®] applicator modelled in this application and a diagram of the photon emitting diffusing tip and the cooling fluid are shown. (B) A finite element mesh conforms to the applicator and is used as the template for the calculations. (C) A representative time-temperature history profile is shown of the thermometry data at two points within the brain tissue, ~ 1 mm from the applicator. The corresponding power history is also shown.

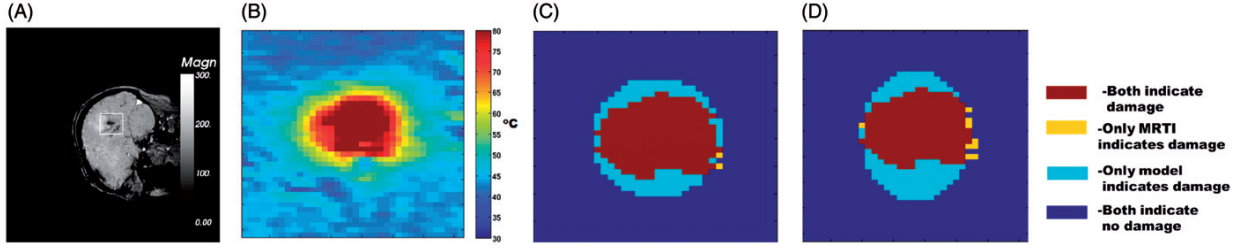


Figure 4.2: Representative thermometry data and calibrated model damage predictions. (A) The magnitude of the complex valued thermometry data provides a visualisation of the anatomy and is provided as a reference. The applicator trajectory is observed as a signal void in the image. The ROI displayed has a $3.75 \times 3.28 \text{ cm}^2$ field of view and is shown in (B)–(D). (B) MR thermometry at maximum heating is shown. (C) finite element method (FEM) model-predicted Arrhenius damage is compared to Arrhenius damage based on MRTI. (D) A comparison of the steady-state damage model is shown. The steady-state damage model is the region enclosed by the 57°C isotherm. The colour map indicates the geometrical overlap used in DSC calculations; the legend is at right (C). Respective DSC values for the FEM model (C) and steady-state model (D) are $\text{DSC} = 0.8385$ and $\text{DSC} = 0.7442$.

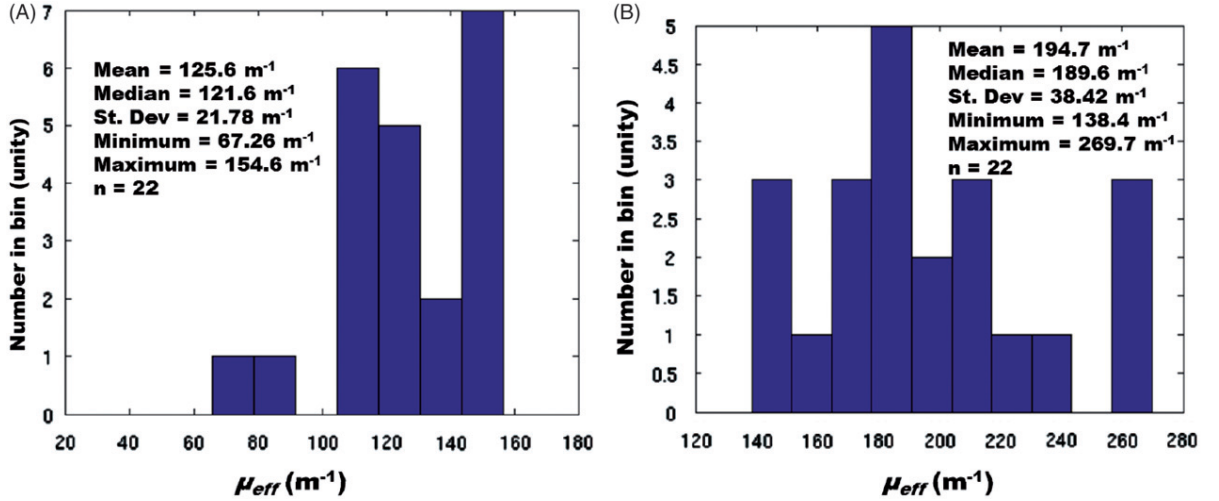


Figure 4.3: Presented here are histograms of calibration analysis from the transient FEM model (A) and steady-state model (B), shown left and right, respectively. Both histograms have a bin width of 13.0 m^{-1} . The optical parameters, μ_{eff} , recovered from each thermometry dataset considered are shown. For each calibration the bound constrained optimisation was restricted to a range obtained from literature, $\mu_{eff} \in [0.8, 400] \text{ m}^{-1}$. Leave-one-out cross-validation was performed using these 22 μ_{eff} values. The nominal value in brain tissue obtained from Welch and van Gemert [39] is $\mu_{eff} = 180 \text{ m}^{-1}$.

Table 4.2: The descriptive statistics for μ_{eff} during optimisation and DSC performance during optimisation and LOOCV ($N = 22$). The transient solve of the Pennes bioheat equation using the Arrhenius damage, Equation 1, is denoted by FEM. Steady-state analysis using the 57°C isotherm damage model is denoted SS. Note that all DSC, skewness, and kurtosis quantities are unitless. %-ile refers to percentiles, e.g., 25%-ile means the dataset’s DSC performance exceeds 25% of the population DSC values in ranked order.

Descriptive Statistic	FEM	SS μ_{eff} (m^{-1})	FEM	SS DSC opt.	FEM	SS DSC LOOCV
Minimum	67.26	138.4	0.4865	0.3421	0	0.3312
25%-ile	115.5	167.2	0.7356	0.5789	0.6709	0.5617
Median	121.6	189.6	0.8142	0.6925	0.8001	0.6770
75%-ile	146.1	212.4	0.8652	0.7259	0.8429	0.7257
Maximum	154.6	269.4	0.8972	0.8476	0.8859	0.8143
Mean	125.6	194.7	0.7824	0.6493	0.7323	0.6431
Standard Deviation	21.78	38.42	0.1091	0.1274	0.1930	0.1289
Skewness	-0.7906	0.5714	-1.432	-1.190	-2.830	-1.150
Kurtosis	1.026	-0.2562	1.609	1.142	9.919	0.6817

4.4 Results

Representative thermometry images and calibrated computer model predictions are shown in Figure 4.2. The measured and predicted thermal dose is displayed. The Arrhenius damage model is shown for the transient model predictions, Equation (4.2), and the thermometry data. The 57°C isotherm damage model is shown for the steady-state analysis, Equation (4.4). Significant variability is seen in the heating due to local patient tissue heterogeneities, tumour location, and nearby heat sinks in the brain such as large blood vessels and cerebral spinal fluid (CSF). This is reflected by the nonellipsoidal shape of the isotherms and corresponding damage volume in the Arrhenius estimates of the damage. However, the calibrated thermal damage predictions show acceptable agreement, i.e. Dice similarity coefficient (DSC) ≥ 0.7 [233], between the measured and predicted tissue damage in multiple patients.

The calibration process applied to each thermometry dataset provides a histogram of μ_{eff} values in which the optimal agreement between the model’s prediction and the MR thermometry is observed for each model. The histogram of the μ_{eff} values for both the transient and steady-state model calibrations is shown in Figure 4.3. Literature values of the expected optical properties are provided as a reference. Extrema of the feasible set are obtained from the range of values observed in the literature. Descriptive statistics of the optimised μ_{eff} values, DSC during optimisation, and DSC during LOOCV for both models is provided in Table 4.2; meanwhile, percentiles corresponding to interesting DSC thresholds are presented in Table 4.3.

The overall DSC performance from both models during LOOCV analysis is provided in Figure 4.4. The performance is summarised by the number of datasets that pass a given DSC threshold; the plot is analogous to the Kaplan-Meier survival curve. During LOOCV, the transient model had 15 of 22 datasets pass the DSC ≥ 0.7 success criterion, while the steady-state model passed 10 of 22.

Table 4.3: The percentiles that correspond to several interesting DSC thresholds. The ‘opt.’ and ‘LOOCV’ columns refer to the same groups of datasets described in Table 4.2, as well as the datasets plotted in Figure 4.4. The smaller the percentile value, the better the model’s performance. ‘0’ indicates all values pass at the given threshold; ‘100’ indicates no values pass.

DSC threshold (Unity)	FEM (%-ile)	SS DSC opt. (%-ile)	FEM (%-ile)	SS DSC LOOCV (%-ile)
0.4	0	8.357	5.776	7.176
0.5	2.996	13.34	6.652	14.06
0.6	11.36	27.34	12.97	27.52
0.7	15.25	57.64	30.35	58.61
0.75	30.53	83.22	41.36	85.11
0.8	44.36	95.12	49.97	96.14
0.85	67.19	100	82.06	100

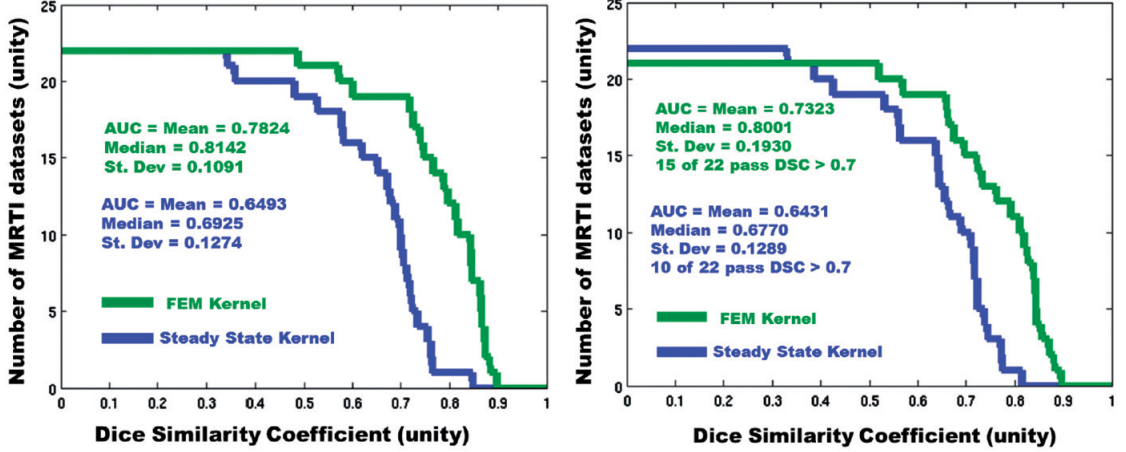


Figure 4.4: Here, the overall predictive performance, measured by DSC, is displayed for both models. (A) Left is the performance during optimisation, and (B) the right is during LOOCV. The horizontal axis displays increasing DSC thresholds; the vertical axis displays the number of datasets that pass the DSC threshold. Greater area under the curve (AUC) indicates better prediction. In the FEM LOOCV plot, there is one dataset that has a DSC = 0 and therefore does not appear on the plot.

The two-sample, paired Wilcoxon signed-rank test rejected the null hypothesis with a p value of 0.0059; i.e. the difference of the transient and steady-state models' medians of DSC during LOOCV was statistically significant. The one-sample, one-sided Wilcoxon signed-rank test for the transient model rejected the null hypothesis with a p value of 0.029; i.e. the transient model's median of DSC during LOOCV was ≥ 0.7 at a statistically significant level. The one-sample, one-sided Wilcoxon signed-rank test for the steady-state model accepted the null hypothesis with a p value of 0.0732; i.e. the steady-state model's median of DSC during LOOCV was not ≥ 0.7 at a statistically significant level.

4.5 Discussion

Given the number of available datasets, the LOOCV analysis provides a methodology to recapitulate the clinical scenario for treatment planning. Prior knowledge and experience is embodied within the thermometry data from the previous N ablations. Information from the previous ablations is extracted by calibrating a computer model to the available

data. In this case, we calibrate our optical parameter to the thermometry data. Modelling goals are to ultimately utilise the calibrated model in optimising the thermal dose delivery. The success or failure of this paradigm is related to several factors. First, there must be a sufficient quantity of retrospective datasets for the training to converge. Second, the cohort of retrospective datasets used in training must have sufficient similarity within the group and to the prediction scenarios. Third, the model must be able to describe clinically relevant ablations.

If the LOOCV analysis only includes datasets that can be optimised to have $\text{DSC} \geq 0.7$, both models perform very well. This is because the calibrated μ_{eff} values have a much tighter distribution; i.e. datasets with an optimal $\text{DSC} \geq 0.7$ had similar μ_{eff} values. Given this investigation is framed as a prediction on the $N + 1$ patient, cherry-picking the successful optimisations is inappropriate. Indeed, optimisation results with $\text{DSC} < 0.7$ are included in the LOOCV analysis as seen in the descriptive statistics, Table 4.2. However, it is worth realising that successful optimisations have similar μ_{eff} values and perhaps information beyond the thermometry data would allow the calibration to be grouped into similar cohorts. For example additional meta information on the primary disease type, tumour location and treatment history would provide useful information in the analysis that may demonstrate clustering during the calibration and would further classify the tissue type.

The two models presented provide a canonical model selection comparison of the trade-off between the time investment in the algorithm, efficiency of the numerical implementation, and accuracy required for predicting the final endpoint of the application. The two-sided, two-sample paired Wilcoxon signed-rank test indicates the predictive results' medians are significantly different and only the transient model's median DSC performance was significantly ≥ 0.7 . As a quantitative reference, the forward solve mapping between model parameters, Table 4.1, and temperature field is considered the fundamental computational operation of this study. Total run times in the analysis are proportional to the total

number of forward solve iterations in the optimisation and LOOCV analysis. The run times for the forward solves in this study averaged $1.87\text{E}2$ s and $1.12\text{E}1$ s for the transient model GPU implementation and steady-state CPU implementation; respectively. These numbers are intended to provide intuition for the observed practical run times on a local CPU (Intel Xeon, 6 core, 2.4 GHz, double precision peak 57 Gflops) workstation with attach GPU accelerators (NVIDIA Tesla M2070 double precision peak 515 Gflops) available to this study. The finite element discretisation of the governing equations requires significant expertise of the GPU computing architecture as well as detailed algorithmic understanding of both the finite element technology and matrix-vector multiply within the iterative linear system solver to maximise floating point operation throughput and minimises memory transactions latencies. As opposed to explicitly storing and reading matrix entries from global memory, the matrix-free method recalculates the local matrix entries needed within the linear system solve. This memory access design pattern has demonstrated a $4\text{--}10\times$ speed up over the matrix explicit methods [228, 234, 235]. Meanwhile, the steady-state superposition analysis, Equation (4.4), provides treatment predictions with fewer floating point operations and would be selected under Occam’s razor [236] philosophy highly preferential to simplicity. While all kernels for the present spectral element methods and preconditioned conjugate gradient method were hand coded in this manuscript, library implementations of the matrix-free iterative solver approach are also appearing [237, 238].

The finite element discretisation of the governing equations, however, provides significant opportunity for further physics-based improvements including higher order model spherical harmonic expansions in the laser fluence model [239]. As seen in Figure 4.3, the chosen models introduce a bias in the model parameter recovery that differs from published literature values. The bias may arise from inaccuracies in the modelling assumptions, perhaps most significant being the use of optical tissue properties that are invariant in space and time. The literature has clear examples where temperature/damage dependent and spatio-temporal dependent parameters are critical to the prediction [62, 63]. The use of

thermometry data during only the test pulse is also expected to influence the recovered optical properties. The choice to use a single constant parameter for full time history of each MRTI dataset is motivated by the practical model training focus of this investigation. Higher order physics models of the fluence are expected to provide the highest accuracy in recovering the optical parameters during the calibration process and for characterising the tissue properties.

The finite element discretisation of the governing equations also provides a rigorous physics-based methodology to incorporate tissue heterogeneities into the treatment prediction. Calibrations of the spatially heterogeneous optical parameter field have been shown to provide highly accurate predictions [240–242]. The inclusion of spatially varied, damage-dependent, and multiple parameters should be pursued in future efforts. Adjoint-based methods of computing the gradient of the objective function are necessary to efficiently optimise in the higher dimensional parameter space. Tissue heterogeneities could similarly be incorporated into the steady-state superposition analysis, Equation (4.4), in a patient-specific ‘ad hoc’ manner. However, this would violate the underlying homogeneous tissue parameter assumptions which provided the mathematical structure for the concise analytical solution. A Gaussian process [243, 244] framework may be appropriate in which the model parameters recovered may be interpreted as hyper-parameters for the covariance kernels. Similar to physics-based model calibration, optimisation of the hyper-parameters in the Gaussian process kernels offers a complementary trade-off between data fitting and smoothing. Further, Gaussian processes allow for prior information to be used and provide a full probabilistic prediction and an estimate of the uncertainty.

Model calibration and training was limited to thermometry data in these efforts. The predictive capabilities are expected to improve with more information provided by pre-treatment MR imaging such as dynamic contrast-enhanced imaging or perfusion imaging to help guide the selection of the model parameters, especially if these preoperative images can inform the optical parameters. Incorporating tissue heterogeneities into the model

predictions would also require segmentations of the neuro-anatomy as a template for the regional heterogeneity. Each direction would benefit from the forethought of including these data acquisitions into the therapy protocol. For example, current brain segmentation techniques [245] require high resolution FLAIR, T2, and T1 imaging with and without contrast. The SQL database used in organising all data was vital to the reproducibility of the analysis in these efforts; this additional information must be incorporated. Tools for communicating with the neuronavigation software to locate the fibre would also provide further information to improve the analysis throughput and reproducibility. Passive tracking of the applicator location using fiducials placed on the fibre would additionally provide the registration information needed to align the computational domain of the mathematical model.

4.6 Conclusion

Currently, the neurosurgeon reviews anatomical MR images to plan his/her trajectory to reach the tumour with neuronavigation software, but does not have the capability to visualise outcomes of the laser ablation using various trajectories beforehand. Fully developed and commercially implemented predictive computer models will extend this functionality to include a priori visualisation and optimisation of the potential outcomes for complex treatment scenarios (multiple applicators/trajectories) in which the laser ablation is performed near a critical structure within a heterogeneous tissue environment. This work presents a step in this direction and demonstrates the feasibility in establishing a confidence in these predictions. Consideration of other available metadata to improve prediction accuracy is a topic of on-going research.

Acknowledgments

The authors would like to thank Roger McNichols, PhD, for his assistance in clinical laser ablation as well as the DAKOTA [197], ITK [202], Paraview [203], and CUBIT [196] communities for providing enabling software for scientific computation and visualisation.

Declaration of Interest

The research in this paper was supported in part through grants from the O'Donnell Foundation, US National Science Foundation AIR-1312048, US National Institutes of Health 1R21EB01016-01, National Center for Advancing Translational Sciences of the National Institutes of Health TL1TR000369, US Department of Defence W81XWH-14-1- 0024, and the Cancer Center Support Grants CA016672 and CA79282. Research was jointly conducted at the MD Anderson Center for Advanced Biomedical Imaging in part with equipment support from General Electric Healthcare. At the time of this work, Visualase, Inc. and BioTex, Inc. provided the surgical device technology and services. Anil Shetty and Ashok Gowda were employed by those companies. Since that time, Medtronic, Inc. has acquired Visualase, Inc., and employs Anil Shetty. BioTex, Inc. employs Ashok Gowda. Shabbar Danish has received educational honoraria from Medtronic, Inc. The authors alone are responsible for the content and writing of the paper.

Chapter 5

A global search-based optimization and prediction paradigm for laser ablation

5.1 Introduction

This chapter is an exploration of using the closed-form, analytic [steady state model \(SSM\)](#) of Section [4.3.3](#) in the logical extreme. In order to orient the reader, this Chapter is the calibration and validation of the SSM — i.e., Specific Aims 2 and 3 for the SSM. Chapter [4](#) is the calibration and validation of the FEM model. The time-independent SSM represents a surrogate model for the transient FEM model. While this Chapter represents a comparison between the two trained models, it is important to understand that the goal here is not demonstrate the primacy of a particular model. Rather, the Chapter’s purpose is twofold. First, the results of this Chapter demonstrate the trained SSM is an improvement over a naïve SSM. Secondly, the SSM’s performance should be a surrogate for the FEM model.

The SSM’s key strength is its speed engendered by its simplicity. In Chapter [4](#), the SSM was implemented within a [central processing unit \(CPU\)](#) architecture. The time to run one forward solve was 11.21 s; a gradient-based optimization for one [MRTI](#) dataset was 5 min to 10 min. The optimization space was $\mu_{eff} \in [0.8, 400] \text{ m}^{-1}$. In this chapter, the SSM is implemented within a [graphics processing unit \(GPU\)](#)-accelerated architecture,

yielding prodigiously fast runtimes. The consequence of pairing the SSM with GPUs is the ability to intensively sample the parameter optimization space. The general method of Chapter 5 is similar to Chapter 4. The premise is to use a train-and-predict scheme where an inverse problem trains a model to fit MRTI data from patients.

5.2 Methods

In this chapter, the $N = 22$ cohort of data is the same as from Chapter 4; the difference is found in the improvement of the [steady state model \(SSM\)](#) via [graphics processing unit \(GPU\)](#)-accelerated simulation. The inverse problem is described first. Following the exposition of the inverse problem, the components of the inverse problem are expounded.

5.2.1 Inverse problem

Broadly speaking, an inverse problem brings a simulation into agreement with physical reality by varying the simulation's input parameters. An inverse problem requires four components:

1. **Gold standard measure of physical reality**

A gold standard measurement of physical reality provides a goal for the simulation to fit. In this Chapter, the gold standard physical measurement is the [MRTI](#)-based Arrhenius dose using Henriques and Moritz' parameters [135]. The selection of MRTI datasets is the same $N = 22$ cohort from Chapter 4.

2. **Model**

A model for the prediction of physical reality is the second component. In this Chapter, the model is expressed in Equations (5.4), (5.5), and (5.6) — which are derived from the Pennes bioheat transfer equation [160]. The model is discussed in Section 5.2.3.

3. Objective function

An objective function that can be minimized subsequently brings the model into agreement with physical reality. In this Chapter, the [Dice similarity coefficient \(DSC\)](#) is the primary objective function. Other objective functions are tracked and are discussed in [Section 5.2.4](#).

4. Optimization algorithm

An optimization algorithm that guides the selection of simulation parameters. In this Chapter, the optimization algorithm is a nested global search, as discussed in [Section 5.2.5](#).

5.2.2 Patient datasets

The description of the thermometry datasets is very accurately and concisely detailed in [Section 4.3.1](#). Again, this Chapter and [Chapter 4](#) use the same cohort of $N = 22$ thermometry datasets.

As this document is a dissertation, however, there is a greater availability of space to scrutinize the thermometry datasets — this is continued in [Appendix C](#).

5.2.3 Description of the steady state model

The [steady state model \(SSM\)](#) is the biothermal simulation kernel used within this entire chapter. The the analytic derivation and computational implementation are described here.

Analytic derivation

This subsection is a recapitulation of [Sections 4.3.2](#) and [4.3.3](#), with $u_{cooling}$ of [Section 4.3.2](#) being substituted with u_0 here. The governing equations for LITT are derived from Pennes

bioheat equation coupled with a source term provided by laser tissue interaction.

$$\begin{aligned}
\partial u_t - \nabla \cdot (\alpha \nabla u) + \frac{\omega c_{blood}}{\rho c_p} (u - u_a) &= \frac{1}{\rho c_p} q_{laser} \quad \text{in } U \setminus U_{tip} \\
q_{laser}(x, t) &= \int_{U_{tip}} \frac{p(t) \mu_{eff}^2}{\text{Vol}(U_{tip})} \frac{\exp(-\mu_{eff} \|x - \xi\|)}{4\pi \|x - \xi\|} d\xi \quad x \in U \setminus U_{tip} \\
\alpha &= \frac{k}{\rho c_p} \quad \mu_{eff} = \sqrt{3\mu_a \mu_{tr}} \quad \mu_{tr} = \mu_a + \mu_s(1 - g) \\
n \cdot (\alpha \nabla u) &= 0 \quad \text{on } \partial U \quad n \cdot (\alpha \nabla u) = h(u - u_0) \quad \text{on } \partial U_{tip}
\end{aligned} \tag{5.1}$$

Previous sensitivity analysis have indicated that uncertainty in the optical parameters, $\omega < k < \mu_{eff}$, provide the largest affect on the final temperature prediction outcomes [59].

A 1D spherically symmetric radial decomposition of the solution, $u(r) - u_a = \frac{\mathcal{R}(r)}{r}$, simplifies the analysis of the differential operator in spherical coordinates.

$$\frac{\omega c_{blood}}{\rho c_p} \frac{\mathcal{R}(r)}{r} - \frac{\alpha}{r} \frac{d^2 \mathcal{R}}{dr^2} = \frac{1}{\rho c_p} q_{laser} \quad q_{laser} = \frac{\mu_{eff}^2 \exp(-\mu_{eff} r)}{4 \pi r}$$

$$u(r_1) = u_0 \quad \left. \frac{du}{dr} \right|_{r_2} = 0 \quad r_1 < r_2$$

Constant coefficients are assumed. A 1D spherically symmetric radial decomposition of the solution simplifies the analysis of the differential operator in spherical coordinates. A particular solution, u_p , will be used to construct a solution.

$$-\nabla \frac{u_p(r)}{r} + \frac{\omega c_{blood}}{k} \frac{u_p(r)}{r} = \frac{1}{k} q_{laser} \quad \frac{u_p(r)}{r} = \frac{\mu_{eff}^2 P \exp(-\mu_{eff} r)}{4 \pi r (\omega c_{blood} - k \mu_{eff}^2)}$$

Notice that in spherical coordinates

$$\frac{d}{dr} \frac{u_p(r)}{r} = \frac{u_p'(r)}{r} - \frac{u_p(r)}{r^2} \quad \nabla \frac{u_p(r)}{r} = \frac{1}{r^2} \frac{d}{dr} \left(r^2 \frac{u_p(r)}{r} \right) = \frac{u_p''(r)}{r}$$

From classical theory [229], the general solution is the linear combination of the homogeneous solution, u_h , and a particular solution, $u_p = \frac{1}{r} (A \exp(-\mu_{eff} r) + B r \exp(-\mu_{eff} r))$. In this case, the particular solution was obtained from the method of undetermined coefficients for $A, B \in \mathbb{R}$.

$$u(r) = \underbrace{C_1 \frac{\exp\left(\sqrt{\frac{\omega c_{blood}}{k}} r\right)}{r} + C_2 \frac{\exp\left(-\sqrt{\frac{\omega c_{blood}}{k}} r\right)}{r}}_{u_h/r} + \underbrace{\frac{\mu_{eff}^2 P \exp(-\mu_{eff} r)}{4 \pi r (\omega c_{blood} - k \mu_{eff}^2)}}_{u_p/r} + u_a \quad (5.2)$$

The boundary conditions are used to determine the coefficients of the homogeneous solution. Applicator cooling is specified by the boundary condition at $r = r_1$. The domain is assumed large enough that no heat flux is observed at the far boundary $r = r_2$.

$$\begin{bmatrix} \frac{\exp\left(\sqrt{\frac{\omega c_{blood}}{k}} r_1\right)}{r_1} & \frac{\exp\left(-\sqrt{\frac{\omega c_{blood}}{k}} r_1\right)}{r_1} \\ \left. \frac{d}{dr} \frac{\exp\left(\sqrt{\frac{\omega c_{blood}}{k}} r\right)}{r} \right|_{r_2} & \left. \frac{d}{dr} \frac{\exp\left(-\sqrt{\frac{\omega c_{blood}}{k}} r\right)}{r} \right|_{r_2} \end{bmatrix} \begin{bmatrix} C_1 \\ C_2 \end{bmatrix} = \begin{bmatrix} u_0 - \frac{u_p(r_1)}{r_1} - u_a \\ - \left. \frac{du_p}{dr} \right|_{r_2} \end{bmatrix} \quad (5.3)$$

The 1D solution provides an estimate of the heating at a distance, r , from a single point source. The applicator boundary is at r_1 , and r_2 is a semi-infinite distance at which the temperature is body temperature, u_a .

Mathematica 7 (Wolfram, Champaign, IL) determined the coefficients of Equation (5.3), which makes an analytic/closed-form expression for temperature, $u(r)$, in Equation (5.4). Equation (5.4) is relatively long and it is conceivable that certain terms could be effectively approximated. The advantages of approximation include:

- 1.

Simpler implementation into MATLAB-based [central processing unit \(CPU\)](#) and/or CUDA-based [GPU](#) computation with reduced risk of introducing errors.

2.

Faster computation of the kernel, especially for CUDA-based GPU by reducing the magnitude of data transfer during memory calls.

3.

Greater numerical stability in the GPU environment, allowing for a greater range of parameter optimization space to be explored.

However, it was ultimately not necessary to find viable approximations.

$$\begin{aligned}
u(r) &= \frac{u_h(r)}{r} + \frac{u_p(r)}{r} + u_a = \\
&u_a + \left\{ \exp \left(-\mu_{eff}(r_1 + r_2 + r) - r\sqrt{\frac{c_{blood}\omega}{k}} \right) \times \right. \\
&\left[-\exp \left(\mu_{eff}(r_1 + r) + (2r_1 + r_2)\sqrt{\frac{c_{blood}\omega}{k}} \right) \mu_{eff}^2 P(1 + \mu_{eff}r_2) + \right. \\
&\quad \exp \left(\mu_{eff}(r_1 + r) + (r_2 + 2r)\sqrt{\frac{c_{blood}\omega}{k}} \right) \mu_{eff}^2 P(1 + \mu_{eff}r_2) - \\
&\quad \exp \left(\mu_{eff}(r_2 + r) + (r_1 + 2r_2)\sqrt{\frac{c_{blood}\omega}{k}} \right) \mu_{eff}^2 P \left(-1 + r_2\sqrt{\frac{c_{blood}\omega}{k}} \right) + \\
&\quad \exp \left(\mu_{eff}(r_1 + r_2) + (2r_2 + r)\sqrt{\frac{c_{blood}\omega}{k}} \right) \mu_{eff}^2 P \left(-1 + r_2\sqrt{\frac{c_{blood}\omega}{k}} \right) + \\
&\quad 4 \exp \left(\mu_{eff}(r_1 + r_2 + r) + (r_1 + 2r_2)\sqrt{\frac{c_{blood}\omega}{k}} \right) \times \\
&\quad \pi r (u_0 - u_a) (-k \mu_{eff}^2 + c_{blood}\omega) \left(-1 + r_2\sqrt{\frac{c_{blood}\omega}{k}} \right) + \\
&\quad 4 \exp \left(\mu_{eff}(r_1 + r_2 + r) + (2r_2 + r)\sqrt{\frac{c_{blood}\omega}{k}} \right) \times \\
&\quad \pi r u_a (-k \mu_{eff}^2 + c_{blood}\omega) \left(-1 + r_2\sqrt{\frac{c_{blood}\omega}{k}} \right) + \\
&\quad \exp \left(\mu_{eff}(r_1 + r_2) + (2r_1 + r)\sqrt{\frac{c_{blood}\omega}{k}} \right) \mu_{eff}^2 P \left(1 + r_2\sqrt{\frac{c_{blood}\omega}{k}} \right) - \\
&\quad \exp \left(\mu_{eff}(r_2 + r) + (r_1 + 2r)\sqrt{\frac{c_{blood}\omega}{k}} \right) \mu_{eff}^2 P \left(1 + r_2\sqrt{\frac{c_{blood}\omega}{k}} \right) + \\
&\quad 4 \exp \left(\mu_{eff}(r_1 + r_2 + r) + (r_1 + 2r)\sqrt{\frac{c_{blood}\omega}{k}} \right) \times \\
&\quad \pi r_1 (u_0 - u_a) (-k \mu_{eff}^2 + c_{blood}\omega) \left(1 + r_2\sqrt{\frac{c_{blood}\omega}{k}} \right) + \\
&\quad 4 \exp \left(\mu_{eff}(r_1 + r_2 + r) + (2r_1 + r)\sqrt{\frac{c_{blood}\omega}{k}} \right) \times \\
&\quad \left. \left. \pi r u_a (-k \mu_{eff}^2 + c_{blood}\omega) \left(1 + r_2\sqrt{\frac{c_{blood}\omega}{k}} \right) \right] \right\} / \\
&\quad \left\{ 4 \pi r (-k \mu_{eff}^2 + c_{blood}\omega) \times \right. \\
&\left[\exp \left(2r_2\sqrt{\frac{c_{blood}\omega}{k}} \right) \left(-1 + r_2\sqrt{\frac{c_{blood}\omega}{k}} \right) + \exp \left(2r_1\sqrt{\frac{c_{blood}\omega}{k}} \right) \left(1 + r_2\sqrt{\frac{c_{blood}\omega}{k}} \right) \right] \left. \right\}
\end{aligned} \tag{5.4}$$

Table 5.1: Constitutive data [183, 226, 227]

k [$\frac{\text{W}}{\text{mK}}$]	ρ [$\frac{\text{kg}}{\text{m}^3}$]	c_{blood} [$\frac{\text{J}}{\text{kgK}}$]	u_0 [$^{\circ}\text{C}$]	u_a [$^{\circ}\text{C}$]	r_1 [m^{-1}]	r_2 [m^{-1}]
0.527	1045	3840	21	37	7.5E-4	1

Discretization error of a point source array to approximate a line source

Here, a line source is approximated by an array of isotropic point sources evenly spaced along a 1.0 cm line segment. Increasing the number of isotropic point sources, M , provides a better approximation but increases the necessary computation time. One isotropic point source's temperature profile is generated by the SSM kernel, Equation (5.4). Superposition is used to sum the temperature profiles of the isotropic point sources. First, the nominal power of the modeled ablation is evenly split by the number of isotropic point sources, M . The power of a single point source is then $P_{\text{single}}(M) = P/M$. The temperature field, $u(r)$, is given by summing the individual isotropic point sources, $u_i(r)$, while recalling that the temperature begins at u_a :

$$u(r) = u_a + \sum_{i=1}^M u_i(r) , \quad u_i(r) = \frac{u_{h,i}(r)}{r} + \frac{u_{p,i}(r)}{r} . \quad (5.5)$$

In order to determine the number of isotropic point sources necessary to make an adequate approximation of a line source, an increasing number of isotropic point sources, $M = [1, 10, 15, 25, 50, 75, 100, 1\text{E}3, 1\text{E}4]$, was compared to a simulation assumed to be a perfect line source, $M = 1\text{E}5$. The simulation domain has two spatial dimensions and is further described in the [next subsection](#).

Spatial domain of steady state model kernel

Any point in three dimensional space can have a temperature calculated by the SSM kernel, Equation (5.4). For a given set of bioheat and optical parameters, an isotropic point source's temperature only depends on the Euclidean distance. Then, summing the M temperature fields is trivial, as described in Equation (5.5). In this Chapter, the temperature prediction

is a two-spatial dimensional plane, i.e., single slice, discretized by pixels. That 2D field is compared with patient MRTI data. The simulation’s in-plane spatial domain matches a [region of interest \(ROI\)](#) selected from MRTI. In the simulation, the in-plane sampling is five times as dense as the MRTI’s. However, the MRTI’s single slice measurement comes from a finite thickness. Here, the SSM kernel models that finite thickness by averaging five simulation slices together. The middle simulation slice, slice 3, is registered to the MRTI slice location. The edge simulation slices, slices 1 and 5, are placed at the edges of the MRTI’s nominal slice thickness. Simulation slice 2 is exactly halfway between simulation slices 1 and 3, while simulation slice 4 is exactly halfway between simulation slices 3 and 5. In summary, the simulation’s spatial domain is oversampled five-fold in all three spatial dimensions, compared to whatever MRTI dataset is considered.

Using the described geometry, the SSM kernel calculates the distance, r , between the M isotropic point sources and simulation’s sampled spatial points. That distance directly is substituted into Equation (5.4) and a temperature from each source point is known. Next, the simulation slices are averaged together. As part of the information recorded about the MRTI dataset’s ROI, the in-plane angle of rotation is available; the simulation’s in-plane ROI is rotated to match. The simulation ROI is designed to be large enough that after rotation, the simulation ROI can be cropped to match the MRTI’s ROI. Recall at this point, the simulation data is one slice, averaged together from five slices, and is oversampled by five-fold in both in-plane spatial dimensions, but the in-plane sampling points are rotated away from the MRTI’s pixel grid. The last geometric manipulation is to perform a two spatial dimensional interpolation — `interp2` in MATLAB — to re-grid the simulation ROI to match the MRTI’s pixel locations within the ROI. The ultimate result is the simulation’s spatial sampling points are in the exact spatial locations of the MRTI’s pixel centroids. The purpose of oversampling is to minimize spatial discretization error after rotation and re-gridding.

Temperature linearity with laser power

A convenient property of Equation (5.4) — and consequently Equation (5.5) — is that the temperature, u , is linear with the laser's power, P . Using a linear combination of simulations with zero power and a known power, a temperature field of arbitrary power can be generated: E.g., one 0 W temperature field and one 1 W temperature field can be linearly combined into a 15 W temperature field, or of any power desired. Ergo, the fact that patients receive different laser powers does not require the SSM to re-run with different powers, leading to tremendous speed advantages. Furthermore, the number of patients in the studied cohort does not change the number of SSM runs.

The equation to generate a temperature field of arbitrary laser power from 0 W and 1 W fields is

$$u_2(\vec{x}) = u_1(\vec{x}) \cdot (P_2 - P_0) - u_0(\vec{x}) \cdot (P_2 - P_1) \quad \vec{x} = (x_1, x_2) . \quad (5.6)$$

Here, $u_0(\vec{x})$, $u_1(\vec{x})$, and $u_2(\vec{x})$ are respectively the in-plane temperature fields when $P_0 = 0$ W, $P_1 = 1$ W, and P_2 from the patient-specific laser power are used. \vec{x} is the two-dimensional, in-plane spatial location. Equation (5.6) is valid for any number of spatial dimensions. Another convenient implication of the power linearity is that the $u_0(\vec{x})$ temperature field can be reused for different values of μ_{eff} as long as the bioheat parameters remain unchanged. Explicitly, if the bioheat parameters of Equation (5.1) — ω , ρ , k , c_{blood} , c_p , and u_a — remain the same, the same $P = 0$ W temperature field, $u_0(\vec{x})$, can be paired with any $u_1(\vec{x})$ in Equation (5.6) to produce $u_2(\vec{x})$. The reason this is possible is simple. μ_{eff} can only affect the power term of Equation (5.4); when $P = 0$ W, μ_{eff} does nothing.

5.2.4 Objective functions

The objective function is the [Dice similarity coefficient \(DSC\)](#) [9]. DSC is a metric that quantifies the overlap between two regions. In this application, the regions are thresholds of

damage. Damage can be indicated by Arrhenius damage, Section 2.3.1; cumulative equivalent minutes (CEM) damage, Section 2.3.3; or lethal threshold temperature damage model (LTTDM), Section 2.3.4. The LTTDM has relevance to this investigation and discussion can be found in Section 2.3.4; the chief reason is that the patient ablations are temporally short and reach high temperatures, i.e., $> 57^\circ\text{C}$. In this Chapter, however, Arrhenius dose with Henriques parameters is used in order to match Chapter 4. DSC is defined as

$$DSC = \frac{2|A \cap B|}{|A + B|}.$$

A is the region circumscribed by the Arrhenius dose of $\Omega = 1$ from patient MRTI data. B is the region enclosed by the 57°C isotherm contour for the SSM kernel.

Alternate objective functions are available for consideration — namely, the L_2 norm of the MRTI compared to the model prediction and the Hausdorf distance — and are explored in Appendix C.

5.2.5 Global parameter search in $\mu_{eff}-\omega$ space

The simplifying approximations of the SSM kernel allow its computation to be very fast. The result is the SSM kernel can be optimized using a global parameter search, as opposed to methods that utilize one or more objective functions. The parameter search domain is a two-dimensional $\mu_{eff}-\omega$ space; blood perfusion and effective optical coefficient values are searched. The global parameter search scheme is a regular grid search within a densely sampled $\mu_{eff}-\omega$ space.

In the regular grid search, the perfusion space is $\omega \in [3, 16.5] \text{ kg m}^{-3} \text{ s}^{-1}$ with 65 evenly spaced samples. The effective optical coefficient space is $\mu_{eff} \in [50, 400] \text{ m}^{-1}$ with 176 evenly spaced samples. The total number of $\mu_{eff}-\omega$ pairs is multiplicative; 65 ω samples \times 176 μ_{eff} samples is 11,440 total $\mu_{eff}-\omega$ pairs. For the regular grid search, there are 11,440 $P = 1 \text{ W}$ simulations but only 65 $P = 0 \text{ W}$ simulations since varying μ_{eff} does

not change a $P = 0$ W simulation, as [discussed beforehand](#).

5.2.6 Leave-one-out cross-validation and vector map manipulation

Similar to Chapter 4, leave-one-out cross-validation (LOOCV) is used here to simulate the $N + 1$ prediction case. However, the way that optimal $\mu_{eff}-\omega$ values are chosen during LOOCV is remarkably different. Described in Section 4.3.5, the previous method averages the parameter values that produced the optimal objective function performance in individual datasets; this creates a predictive parameter choice for the $N + 1$ dataset. Instead, access to the global behavior in $\mu_{eff}-\omega$ space provides far more powerful information.

Before LOOCV begins, the $\mu_{eff}-\omega$ global optimization using regular grid sampling is executed — described in Section 5.2.5. The result of optimization of a particular dataset is a 2D map in $\mu_{eff}-\omega$ space of the DSC performance. These maps of individual optimizations are superimposed to create a vector map of DSC performance among the datasets. It can also be conceived as a 3D dataset — one dimension of μ_{eff} , one dimension of ω , and one dimension of DSC performance among the datasets in cohort. The vector map is a mathematical entity critical to further analyses. Starting with the vector map, a variety of manipulations can be applied to interrogate the vector map. E.g., the mean, median, and standard deviation of the vector map respectively yield maps of the DSC’s mean, median, and standard deviation. A heuristic demonstration of the vector map’s construction is found in Figure 5.1. The vector map and its key position to understanding this Chapter can be explained as an analogy to the wave function in quantum mechanics. First of all, the wave function of quantum mechanics is the superposition of quantized, orthonormal states. Here, the vector map is the superposition of the DSC performance from the individual datasets. Second, once the wave function is known, an array of operators can be applied to find the expected values of a corresponding array of quantities of interest — e.g., position, momentum, and energy. Here, the vector map can be queried using descriptive statistics or DSC thresholds like the $DSC \geq 0.7$ limit demarking success/failure.

During one iteration of LOOCV of N number of patients, a vector map is constructed using the $N - 1$ individual optimization maps. Then, a mean operator is applied to the 3D vector map, resulting in a 2D mean map. In this $N - 1$ DSC mean map, the $\mu_{eff-\omega}$ pairing that produces the greatest DSC is subsequently used to predict the left-out patient dataset; the predictive DSC performance is recorded. This concludes one iteration of LOOCV. The remainder of the LOOCV algorithm is to permute the left-out dataset until all datasets have been left out once.

In addition to tracking DSC performance in a vector map, the L_2 norm and the Hausdorff distance performance data are logged in their respective vector maps. Like the DSC vector map, the L_2 and Hausdorff distance vector maps can be queried using descriptive statistics, thresholds, or any other interesting manipulation. The results of these alternate objective functions, i.e., L_2 and Hausdorff distance, can be found in [Appendix B](#).

Table 5.2: This table presents data regarding the convergence of the temperature field with increasing number of isotropic point sources, M . The same data is found in Figure B.3. The leftmost column displays the number of isotropic point sources, M . The remaining columns display the difference between a temperature field, u_{M_2} , and a temperature field generated with $M = 1\text{E}5$ sources, $u_{M=1\text{E}5}$. This difference is measured by the L_2 norm, and the maximum pixel-wise difference. The middle two columns are for temperature fields created using $\mu_{eff} = 200\text{ m}^{-1}$, while the right two columns use $\mu_{eff} = 2000\text{ m}^{-1}$. All simulations use $\omega = 6.0\text{ kg m}^{-3}\text{ s}^{-1}$ and parameter values from Table 5.1.

M	$\mu_{eff} = 200\text{ m}^{-1}$		$\mu_{eff} = 2000\text{ m}^{-1}$	
	L_2 norm	$\max\{u_{M=1\text{E}5} - u_{M_2}\} (\text{°C})$	L_2 norm	$\max\{u_{M=1\text{E}5} - u_{M_2}\} (\text{°C})$
1	8.6139E3	6.6128	6.2141E4	60.301
10	1.8825E2	-1.5909	1.2718E3	-6.3702
15	78.359	-1.026	5.3787E2	-4.1925
25	26.831	-0.60012	1.8704E2	-2.4865
50	6.4661	-0.29444	45.585	-1.2344
75	2.8394	-0.19505	20.073	-0.82105
100	1.5871	-0.14580	11.242	-0.61503
1E3	1.5343E-2	-1.4334E-2	0.10921	-6.0766E-2
1E4	1.2660E-4	-1.3015E-3	9.0191E-4	-5.5225E-3
1E5	0	0	0	0

Table 5.3: Here are the descriptive statistics for DSC performance during optimization — i.e., before cross-validation — for the $N = 22$ cohort. Steady state analysis using the 57 °C isotherm damage model is denoted SS. “opt.” refers to optimization during the regular grid search; “SS naïve choice” refers to the performance using literature values with the SSM kernel. “FEM” refers to the optimization results from gradient-based optimization; the FEM results are the same as Chapter 4. Note that all DSC, skewness, and kurtosis quantities are unitless. “%-ile” refers to percentiles. E.g., 25%-ile means the dataset’s DSC performance exceeds 25% of the population DSC values in ascending ranked order.

Descriptive Statistic	SS naïve choice	FEM DSC opt.	SS DSC opt.
Minimum	0.4986	0.4865	0.7224
25%-ile	0.6562	0.7394	0.8384
Median	0.7411	0.8142	0.8855
75%-ile	0.8183	0.8649	0.9156
Maximum	0.8799	0.8972	0.9386
DSC ≥ 0.7	15	19	22
Mean	0.7197	0.7824	0.8666
Standard Deviation	0.1275	0.1091	0.06498
Skewness	-1.020	-1.332	-1.014
Kurtosis	3.349	4.005	2.895

Table 5.4: Here are the descriptive statistics for DSC performance during LOOCV for the $N = 22$ cohort. Steady state analysis using the 57 °C isotherm damage model is denoted SS. “LOOCV” refers to the prediction results during the cross-validation of the trained SSM and FEM methods; “SS naïve choice” refers to the performance using literature values with the SS kernel. “FEM” refers to the LOOCV results after gradient-based optimization; the FEM results are the same as Chapter 4. This Table’s data is also presented in Figure 5.4. Note that all DSC, skewness, and kurtosis quantities are unitless. “%-ile” refers to percentiles. E.g., 25%-ile means the dataset’s DSC performance exceeds 25% of the population DSC values in ascending ranked order.

Descriptive Statistic	SS naïve choice	FEM DSC LOOCV	SS DSC LOOCV
Minimum	0.2988	0	0.4791
25%-ile	0.5965	0.6709	0.7143
Median	0.6564	0.8001	0.8297
75%-ile	0.7595	0.8429	0.8787
Maximum	0.8575	0.8859	0.9186
DSC ≥ 0.7	9	15	17
Mean	0.6513	0.7323	0.7771
Standard Deviation	0.1429	0.1930	0.1288
Skewness	-0.84288	-2.830	-0.9241
Kurtosis	3.241	9.919	2.961

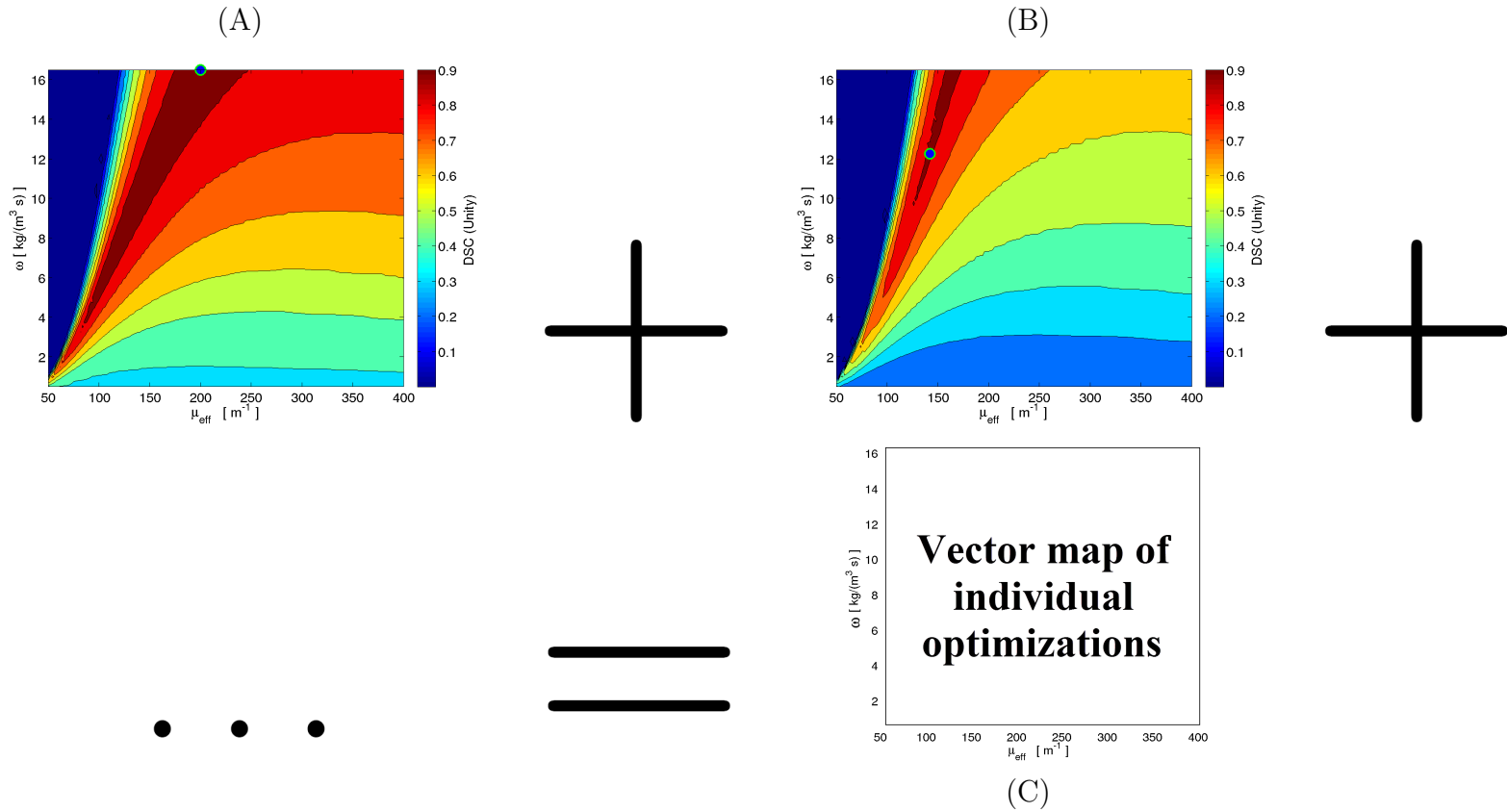


Figure 5.1: This is a cartoon demonstration of the superposition of individual datasets' global optimizations in $\mu_{\text{eff}}-\omega$ space. Each dataset's optimization performance, e.g. (A) and (B), can be superimposed pixel-wise in $\mu_{\text{eff}}-\omega$ space to create an optimization vector map (C). This optimization vector map has $N = 22$ individual optimization results for every point in $\mu_{\text{eff}}-\omega$ space. At every point in the optimization vector map, descriptive statistics can describe the distribution's behavior at that $\mu_{\text{eff}}-\omega$ point, see Figure 5.2. This is roughly analogous to the superposition of wave functions to describe the state of an atom using quantum mechanics and then using operators to find interesting quantities.

5.3 Results

5.3.1 Characterization of steady state model kernel

The temperature from a single isotropic point source is plotted in Figure B.1. There is a temperature buildup from the r_1 boundary up to the peak followed by a temperature decay out to the r_2 boundary. The behavior of the steady model while the number of source points, M , increases is shown in Figures B.2 and B.3 and Table 5.2. Table 5.2 demonstrates that maximum pixel-wise difference reduces linearly with increasing M . The $\mu_{eff} = 200 \text{ m}^{-1}$ portion of Table 5.2 is the more relevant data; however $\mu_{eff} = 2000 \text{ m}^{-1}$ provides a worst case scenario. $M = 50$ has an acceptable balance of simulation fidelity and computation time and is used in the subsequent simulations. The maximum pixel-wise difference between $M = 50$ and $M = 1\text{E}5$ is 0.29444°C . Figure B.4 is a demonstration of the SSM kernel’s linearity with power. A difference image between a 15 W image directly generated by the kernel and a 15 W image generated by 1 W and 0 W images shows that the methods are equivalent.

5.3.2 Optimization

The optimization performance is best summarized in the “SS DSC opt.” column of Table 5.3. The mean DSC performance was 0.8666 with all 22 patient datasets passing $\text{DSC} \geq 0.7$ during optimization. Individual optimization maps can be found throughout Appendix A. Optimization of the alternate objective functions, i.e., the L_2 and Hausdorff distance, are found in Figures B.5 and B.6 of Appendix B. The optimal mean Hausdorff distance is 4.732 mm. By comparing Figures 5.2A and B.6, the regions of superior performance in both Figures overlap in $\mu_{eff}-\omega$ space — i.e., the areas of smallest mean Hausdorff distance overlaps with the areas largest mean DSC. The L_2 map of Figure B.5 has a similar shape; however, the optimal L_2 region is shifted right (increasing μ_{eff}) relative the optimal regions of the optimal DSC and Hausdorff distance regions.

5.3.3 Leave-one-out cross-validation performance

Using the vector map method for parameter selection described in Section 5.2.6, the LOOCV performance is detailed in Table 5.4. The SSM kernel performs definitively better after training — DSC mean = 0.7771 and 17 of 22 pass $\text{DSC} \geq 0.7$ — as opposed to using naïve literature values — DSC mean = 0.6513 and 9 of 22 pass $\text{DSC} \geq 0.7$. Meanwhile, the trained FEM model of Chapter 4 has a mean DSC of 0.7323 and passes 15 of 22.

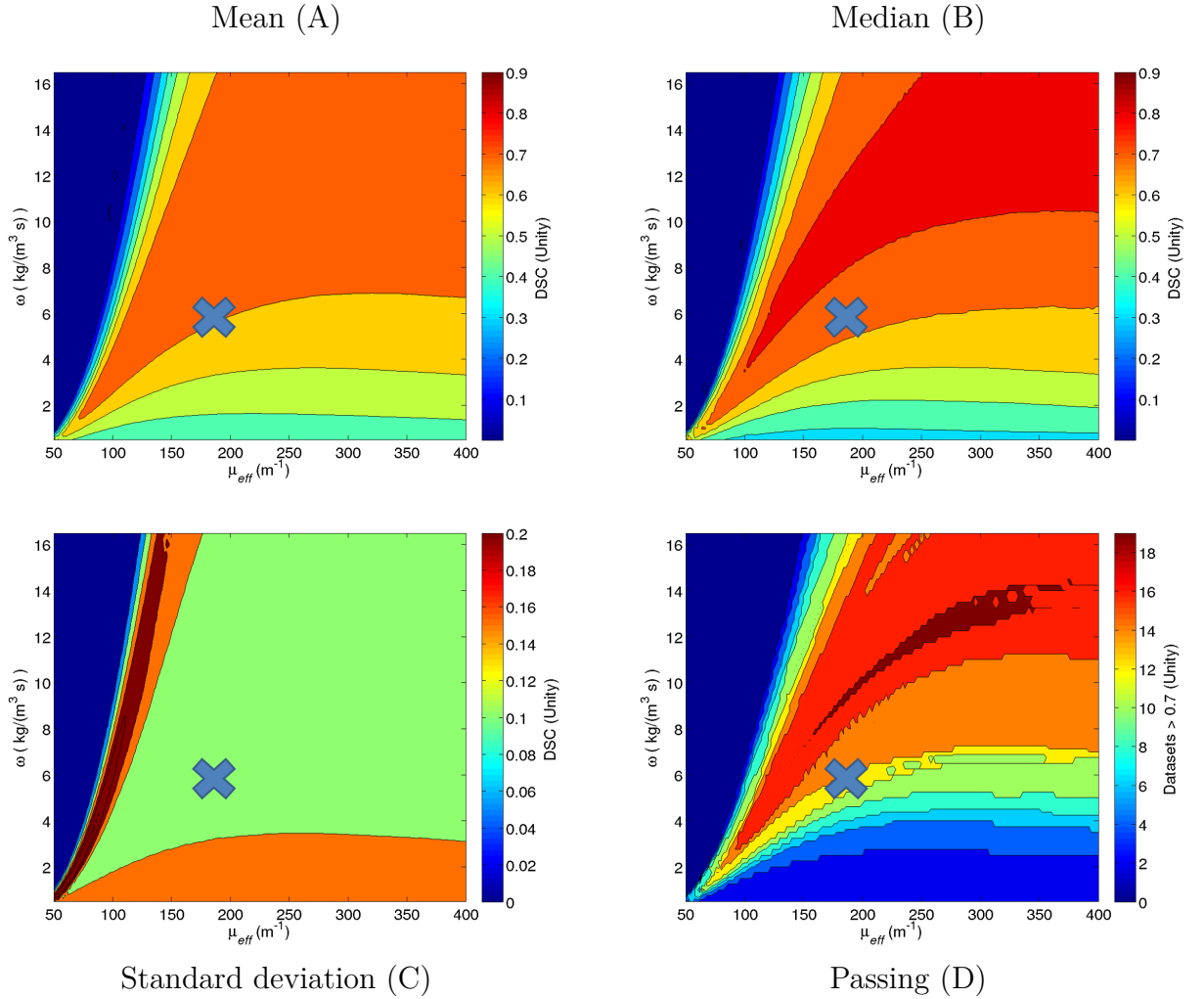


Figure 5.2: These are the descriptive statistic maps based on the vector map, described in Figure 5.1. The ‘x’ marks the naïve literature value choice, $\mu_{eff} = 180 \text{ m}^{-1}$ and $\omega = 6 \text{ kg m}^{-3} \text{ s}^{-1}$. (A) is the mean; (B) is the median; (C) is the standard deviation; (D) is the pass rate — i.e., $\text{DSC} \geq 0.7$.

5.4 Discussion

The accuracy achieved by the [steady state model \(SSM\)](#) is driven by two interrelated factors. First, the GPU-accelerated SSM kernel’s prodigious speed empowers a better approximation of the line source by using $M = 50$ point sources and the exhaustive, dense sampling of the $\mu_{eff}-\omega$ parameter space. Secondly, the 2D global optimization enables a far more effective LOOCV algorithm, i.e., the vector map optimization. The difference in Chapter 4’s LOOCV algorithm and this Chapter can be understood as the difference between optimizing the datasets individually versus optimizing all datasets mutually and simultaneously. The mutual optimization during LOOCV via the vector map results in $\mu_{eff}-\omega$ parameter choices that favor overall performance as opposed to expecting the average of individual optimizations to produce quality performance among all datasets. The most striking result of Chapter 5 is that more exhaustive training can empower a relatively simple model to perform similar to a more sophisticated model with less exhaustive training — i.e., Appendix C’s comparison of the SSM kernel with exhaustive sampling of $\mu_{eff}-\omega$ space versus the FEM kernel with gradient-based optimization of μ_{eff} space.

A remarkable advantage of the presented GPU-accelerated, vector map LOOCV method is that it heavily employs lookup tables and saved data. The 1 W and 0 W images are generated by the SSM kernel and saved; the kernel is then no longer used. By taking advantage of the model’s linearity with laser power, the 1 W and 0 W images can match an arbitrary single slice MRTI dataset by adjusting the power and in-plane laser fiber angle of orientation. The technique saves time by avoiding the need to run the kernel for each individual dataset; instead, it runs through every $\mu_{eff}-\omega$ pairing once for all datasets. The other time-saving feature is the LOOCV algorithm is provided by lookup tables. For every $\mu_{eff}-\omega$ pairing, the various objective functions are recorded. The data array represented by an exhaustive list of $\mu_{eff}-\omega$ pairings and the subsequent objective functions among the

N number of patient datasets is the vector map; the size of the vector map is

$$V_{size} = N_{\mu_{eff}} \times N_{\omega} \times N$$

where V_{size} the total number of elements in the vector map, $N_{\mu_{eff}}$ is the number of μ_{eff} samples, N_{ω} is the number of ω samples, and N is the number patients in the cohort. Executing the LOOCV algorithm is then trivial. For one LOOCV iteration, simply drop one patient dataset from the vector map, create a mean map by averaging, and find the maximum DSC value of the $N - 1$ mean map. The entire LOOCV algorithm is then only manipulations of a lookup table, i.e., the vector map.

Besides the use of the time-saving vector map LOOCV method, the train-and-predict algorithm's use is simplified by the order of computational tasks. The generation of 1 W and 0 W images for each $\mu_{eff}-\omega$ point by the SSM kernel is the longest single computation, taking 2.14E4 s and occurs first. The GPU is only used for the SSM kernel calculations. The subsequent operations to register the 1 W and 0 W images and record the objective functions is executed on CPU and takes 1.28E3 s per patient dataset — 3.85E4 s for the 30 datasets described in Appendix A. This means that adding more datasets to the cohort only takes about 1.28E3 s (~ 21 min) for new entries.

The advantage of global optimization of individual datasets superimposed into a vector map is exemplified by comparing to an alternative gradient-based optimization of the mean DSC among $N - 1$ datasets. In this alternative case, a $\mu_{eff}-\omega$ value is submitted to the kernel for $N - 1$ number of times; the mean DSC is recorded. The gradient-based optimization then requests more $\mu_{eff}-\omega$ values to run among the $N - 1$ individuals in an effort to maximize DSC. Once the gradient-based algorithm converges and reports a maximum DSC, the corresponding $\mu_{eff}-\omega$ value is used on the N^{th} dataset for the predictive case and the DSC is recorded. That procedure must be repeated N number of times. A back-of-the-envelope estimation of the number of realizations a gradient-based

algorithm must do to maximize DSC among all datasets is an inaccurate but illustrative exercise. If there are $N = 22$ datasets, then the gradient-based optimization must interrogate $N - 1 = 21$ datasets to execute a single iteration of the gradient-based optimization. Supposing the gradient-based optimization requires only 10 iterations (very favorable to the gradient-based optimization) to find the maximum DSC for the $N - 1$ datasets, then the total number of SSM kernel realizations is

$$N_{grad\ opt} = N \times (N - 1) \times M_{iter} = 22 \times 21 \times 10 = 4,620$$

where $N_{grad\ opt}$ is the total number of kernel realizations (4,620) necessary to execute LOOCV while optimizing the mean DSC among $N - 1$ datasets. N is the number of patient datasets (22) and M_{iter} is the assumed number of iterations for the gradient-based optimization to converge (10). While the gradient-based LOOCV requires about a third the quantity of realizations as the global optimization–vector map method, the gradient-based LOOCV algorithm is considerably less flexible than the vector map LOOCV. Consider the case where the patient cohort is modified. If patients are added or subtracted or swapped into the $N = 22$ cohort, the optimization space is modified and the gradient-based method must begin anew. In contrast, the vector map LOOCV algorithm just changes the vector map, which is a simple matrix manipulation. To be fair to the gradient-based method when faced with modified patient cohorts, there exist shortcuts to expedite the optimization, but the gestalt is that gradient-based optimization is an unwieldy method to maximize the mean DSC for LOOCV. Finally, the gradient-based method is discussed because it was used in Chapter 4’s FEM model implementation; however, other objective functions that minimize an objective function, such as a pattern search algorithm, face the same challenges.

Fundamentally, the success or failure of the trained SSM kernel is driven by the individual datasets’ DSC performance in response to different $\mu_{eff}-\omega$ values. Broadly speaking, a cohort which leads to successful prediction during LOOCV requires that the successful

parameter values are similar amongst the individual datasets in the cohort. Appendix A exhibits that quality as the lion’s share of datasets’ $DSC \geq 0.7$ regions have overlapping $\mu_{eff}-\omega$ values. Perhaps then, it may be argued that the failing datasets should be excluded. However, there is no *a priori* method available in this investigation of identifying that certain datasets does not belong with the others. In fact, all 22 datasets have optimal DSC values ≥ 0.7 .

Within this investigation, more metrics beyond DSC are available and the data is shown within Appendix B. The L_2 metric’s best region in $\mu_{eff}-\omega$ space does not overlap with the other metrics’ optimal regions. This is believed to occur because the L_2 metric is a spatially global measure — i.e., every pixel in the ROI is included — whereas the Hausdorff distance and DSC metrics are thresholded by the 57°C isotherm. Hence, it is possible for a superior DSC value to manifest while the L_2 metric performs relatively poorly because the region inside the 57°C isotherm is too hot and the region outside the 57°C isotherm be too cold. The chief interest here is matching the damaged regions, and consequently the L_2 norm is not found to have as much value. Nonetheless, the L_2 norm’s global optimization shape in $\mu_{eff}-\omega$ space is found to corroborate the shape of the global performance of the DSC and Hausdorff metrics via the comparison of Figures 5.2A, B.5, and B.6. Regarding the information yielded by the Hausdorff metric, the Hausdorff metric is the spatial distance-to-agreement between the 57°C isotherms from the model and patient MRTI data. By using a combination of DSC and Hausdorff distance, two commonsense questions about the goodness-of-fit between the model prediction and MRTI are addressed. The DSC indicates the fraction of overlap while the Hausdorff distance indicates the distance-to-agreement for the most distant discrepant pixel. By that standard, the mean LOOCV performance is > 0.75 DSC and < 5.0 mm Hausdorff distance. The median Hausdorff distance is considerably smaller at < 3.9 mm because the median is not sensitive to outliers, the most egregious being #0495.

The Hausdorff distance allows a comparison to a gold-standard intervention for brain

metastases: [stereotactic radiosurgery \(SRS\)](#). A common goodness-of-fit metric in radiation therapy is the gamma metric; it has two sub-metrics that compare a planned radiation dose field to a measured field. According to the gamma metric, SRS is considerably more precise as definitive treatment of brain metastases via Gamma Knife is characterized by a distance-to-agreement well under 1 mm [246]. However, the two interventions are not meant to be compared head-to-head for the same treatment task. SRS for brain metastases is the first-line treatment whereas MRgLITT is palliative. It is worth recalling, however, that patients treated with MRgLITT are unlikely to succumb due to brain metastases as long as they are able and willing to undergo more surgery.

Reaching a LOOCV prediction accuracy of 17 of 22 passing $DSC \geq 0.7$ through a computational technique that can be easily executed within two days represents progress in the effort to create clinically useful MRgLITT predictions. In order to improve further, there are a variety of deficiencies and corresponding investigations that can be done. First of all, the registration lacked out-of-plane spatial information. Naturally, MR images that provide 3D morphological data of the laser fiber and the target would be useful. Secondly, more patient datasets would provide more reliable results. Thirdly, it might be critical to know more about the disease state. As it stands, it was only known that patients were afflicted with brain metastases. Knowledge of the metastasis’ origin, e.g. lung vs. breast vs. melanoma, or its location, e.g., temporal cerebrum vs. midbrain, may allow the datasets to be grouped into subcohorts with superior predictive power. These three modifications are relatively straightforward to implement if the necessary data were available; i.e., there are no significant changes to the SSM kernel or the LOOCV execution.

While the previous three modifications are likely beneficial and manageable, more radical improvements are necessary to adequately predict dramatically heterogeneous/asymmetric ablations. Describing the SSM kernel disparagingly, the kernel is an ellipsoid with a size determined by laser power, effective optical coefficient, and microperfusion rate. A review of [Appendix A](#) shows that the simple kernel can succeed for a variety of situations,

ultimately the kernel simply cannot conform to ablation shapes that appreciably deviate from an ellipsoid; it simply cannot recapitulate the variety of observed clinical ablations in brain. To move laser ablation modeling forward to translation, a kernel must be able to recapitulate asymmetric shapes. One solution is to use kernels that are considerably more sophisticated than the SSM kernel. An excellent example would include finite element method models that use damage-dependent tissue parameters and convective boundary conditions like [62]. However, such complex models are profoundly more difficult to train which undermines the maximum achievable prediction accuracy. The SSM kernel may still be effective in the presence of convective boundaries if two primary challenges are met. First, the kernel must be able to modified to conform to convective boundaries; perhaps boundary conditions can be added to the GPU-accelerated kernel. Second, the training from prior datasets that have different boundary conditions must remain effective in kernel implementations of yet more novel differing boundary conditions.

5.5 Conclusion

It has been demonstrated that a relatively simple kernel can perform relatively well if it is given the opportunity for effective parameter training. The dramatic enhancement of accuracy motivates the implementation of model training as available in the future.

Declaration of interest

This research was supported in part through a grant from the National Center for Advancing Translational Sciences of the National Institutes of Health, TL1TR000369.

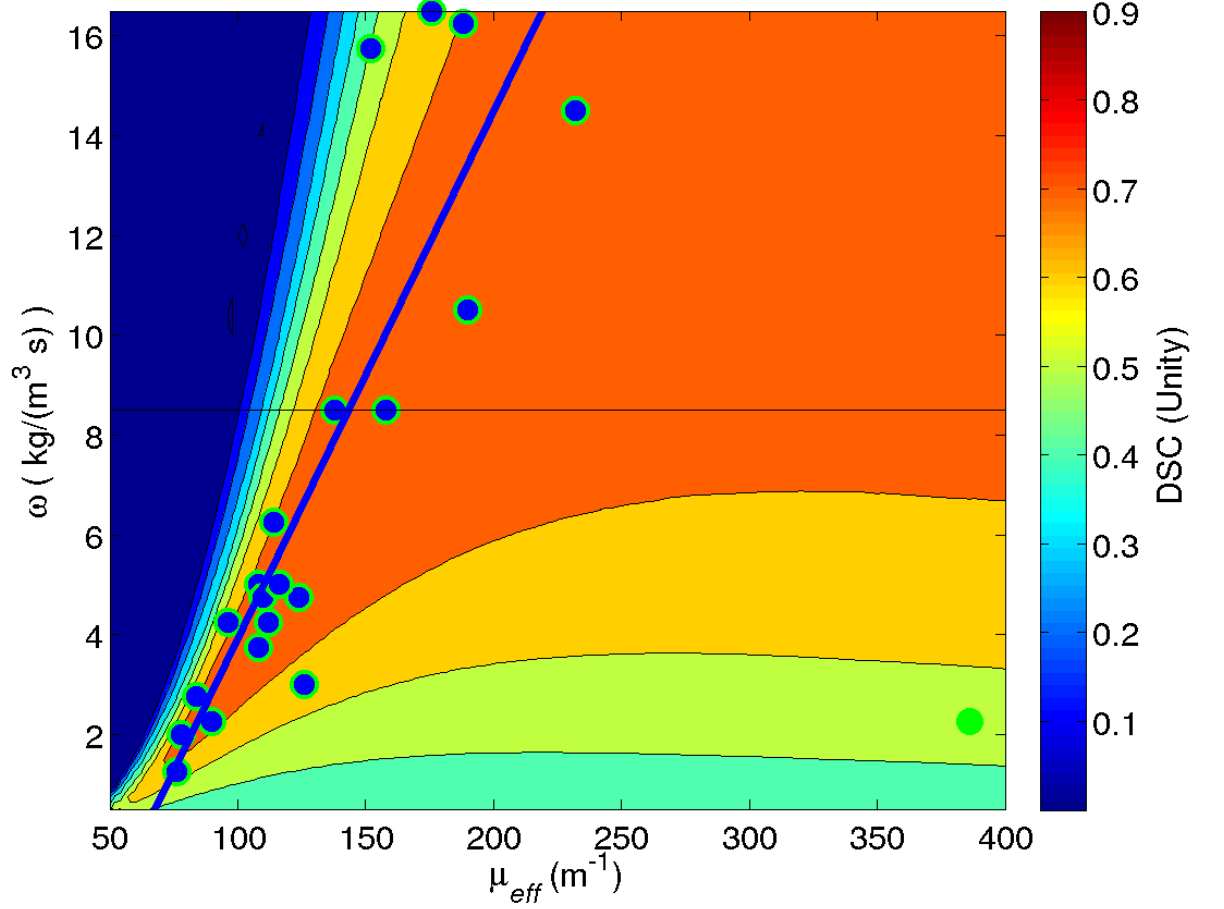


Figure 5.3: This is a scatter plot indicating the locations of the optimal $\mu_{eff}-\omega$ pair for each dataset among the $N = 22$ datasets. There is a least-squares line fit (in blue) of the 21 optimal points (markers are blue with green outlines) that define the line. There is one clearly outlying optimal point are marked in green exclusively. It is from 495 and can be viewed in Figure A.1. The scatter plot and fit line are superimposed over the mean of vector map, i.e., Figure 5.2(A).

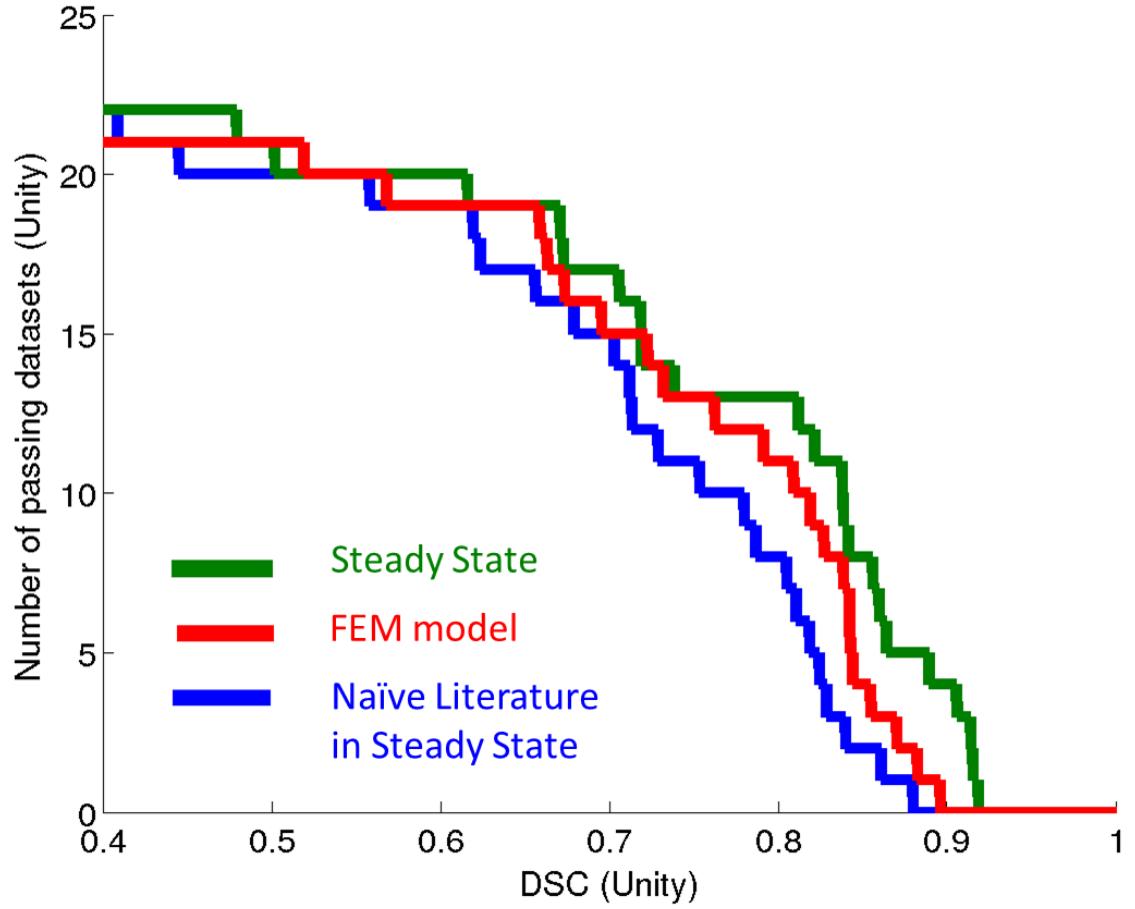


Figure 5.4: The predictive performance — as measured by DSC — is compared for the three models. In blue, is the [steady state model using naïve literature values](#). In red, is the [FEM model's](#) performance. Last and in green, is the globally optimized, trained [state state model](#).

Chapter 6

Conclusion

Magnetic resonance-guided laser induced thermal therapy (MRgLITT) is finding favor with neurosurgeons as a minimally invasive intervention in management of cancer and epilepsy. The surgical placement of the laser fiber stands to benefit from a computer modeling system that can indicate the largest probable laser ablation *a priori*. Chapter 2 described the history, significance, and key concepts of thermal therapy and laser-induced thermal therapy in particular. Chapters 3, 4, and 5 are steps in the process of creating a predictive model despite the dearth of available parameter data: identification of sensitive model parameters, model calibration, and model validation. Within the $N = 22$ cohort examined in Chapters 4 and 5, the calibrated SSM did not meet the Hypothesis' success criteria; however, the trained model was shown to effectively improve the predictive performance. Within the better-vetted $N = 20$ cohort examined in Appendix C, the trained [steady state model \(SSM\)](#) succeeds at the standard set by the Hypothesis. Critically, the $N = 20$ cohort aims to only include datasets that are steady state or nearly steady state, matching the assumptions of the SSM.

Nonetheless, at least two difficult tasks must be overcome before a model would be remotely considered as ready for *a priori* planning. First, the datasets within both cohorts had only one image plane available to analyze; a multi-slice dataset with three spatial dimensions would be preferred to ensure that the modeling is sufficiently accurate beyond

one image plane. Second, none of the datasets within either cohort exhibited convective heat loss associated with a relatively large blood vessel or brain ventricle, a major challenge in MRgLITT planning. A successful model should handle these convective boundaries, or at least the boundaries should be identified *a priori* with a high degree of confidence.

Chapter 3’s motivating concept is that quantifying the input parameter uncertainty and propagating that uncertainty to the temperature field would engender stochastic predictions that did not require perfect accuracy. Such a probabilistic prediction is useful if the accurate prediction occurs with reasonably high probability and a large majority confidence interval — e.g., 95% or 99% CI — remains within an acceptable tolerance. The results of Chapter 3 report probabilistic temperature fields with measures of central tendency, i.e., mean and median, that are near the desired marks based on MR temperature imaging in normal canine brain and canine prostate fixed in agar gel. The 95% CI of the probabilistic temperature predictions manifest variances that are too large to consider Chapter 3’s stochastic model as sufficiently precise for clinical predictions. The stochastic temperature predictions are essentially too imprecise given the available literature values. However, regarding the first Specific Aim, the results demonstrate that the most sensitive model parameters are within the three optical parameters. The variance of thermal conductivity and blood microperfusion are similar in magnitude, but microperfusion’s variance is greater beyond ~ 2 mm.

The lack of precision in Chapter 3’s results immediately motivate the train-and-predict paradigms in Chapters 4 and 5 and indicate what model parameters should be optimized. The purpose of calibration — i.e., parameter optimization or model training — is to provide parameter data to the model during subsequent prediction. Training circumnavigates the need to ascertain higher quality physical measurements of constitutive values, i.e., thermal conductivity, microperfusion rate, and optical coefficients. Furthermore, training somewhat avoids the task of defining what a quality measurement must be; e.g., “Does the measurement need to be *in vivo*, disease-specific, or even patient-specific?” Instead,

new questions emerge regarding the number of training datasets necessary for accurate prediction and defining subcohorts of parameters. Nonetheless, optimizing a model with MRTI data from a variety of patients seems a much more tractable challenge than acquiring physical measurements of constitutive values from a sufficiently large and diverse group of patients.

The other chief feature of Chapters 4 and 5 is the use of LOOCV to simulate the prediction of the $N + 1$ patient, which provides an avenue to compare the many conceivable models of varying complexity. Now then, there emerge two train-and-predict paradigms; each may be used with or without uncertainty quantification provided via gPC.

1. Optimize individual datasets; then use LOOCV

The gradient-based optimization method from Chapter 4 and discussed in Appendix C is an example of optimizing individual datasets, average the individual optimal parameter values, and then emulate prediction of the $N + 1$ dataset by using LOOCV. The advantage of this paradigm is that as the patient cohort changes, datasets that have already been optimized do not have to be reexamined. This paradigm is amenable to a gradient-based optimization. The disadvantage is this paradigm relies on the assumption that the average of the individual optimal model parameters is a surrogate for the optimization of the mean objective function among the cohort.

2. Mutually optimize cohort; then use LOOCV

This is the paradigm that motivates the vector map. The optimization is with respect to the mean of objective function among all datasets. Since mutual optimization of the cohort is a more complex task than optimizing individual datasets, this paradigm is better suited for relatively simple kernels. As discussed [previously](#), optimization schemes besides the vector map can be used. The vector map represents a very convenient method of execution.

If gPC is chosen to be integrated into these train-and-predict paradigms, the distri-

bution of trained parameters can be used to create an empirical probability distribution function (PDF) that in turn can be fitted to a PDF from the Wiener–Askey scheme via some means, e.g., moment matching. The treatment of stochastic predictions may require further consideration to understand the best use of such spatio-temporally plural information. A common-sense approach would be to look at the behavior of the measures of central tendency, with preference to the median — i.e., the most typical realization. Secondly, examining the worst case scenario or a surrogate of the worst case scenario that has an appreciable probability to realize — e.g., the 10%, 5%, or 1% worst case realizations. The application of stochastic predictions can empower predictions during cross validation or during a truly naïve $N + 1$ predictive scenario. If a hypothetical trained kernel were able to be successful in cross validation where success was defined by passing the 5% worst case realization, such a kernel could go into a clinical observational study or randomized controlled trial with a high confidence of success. Any optimistic speculation regarding the incorporation of gPC within the prediction hinges on how similar or different the empirical PDF conforms to a Wiener–Askey scheme distribution.

Another exciting future direction is the incorporation of more imaging data into the model training process. First of all, three dimensional spatial data can inform and improve the laser fiber registration, as discussed [earlier](#). A second opportunity for the use of MRI images is to non-invasively measure the magnitude of microperfusion. Either arterial spin labeling (ASL) or dynamic susceptibility imaging-MRI (DSC-MRI) can acquire such information, each MRI perfusion modality with its own challenges [247, 248]. A third, and arguably the most critical, addition of information from MRI is the inclusion of tissue labels into the model training procedure. Using either tissue segmentation from neuroradiologists or an algorithmic segmentation [245], the model training can expand from a homogeneous, one-label optimization to a heterogeneous, multi-label optimization.

If it is postulated that laser modeling is predictive within a clinically tolerable margin, a final mitigating consideration is the uncertainty that faces all proposed interventions.

Even if a hypothetical trained kernel is predictive in the clinic, what good does it do? Does accurate modeling/planning provide an effectual benefit to patients in randomized controlled trials? If the kernel is predictive, does it improve survival? Progression-free survival? Surgical complication rate? Time length of surgical intervention? Quality-of-life? Cost? An increase in stimulation of the neurosurgeon's zygomaticus major muscle? Careful prospective clinical trial design is necessary to isolate the effect of a predictive model applied to surgical planning in MRgLITT. Nevertheless, if progress is to be forged, research efforts must be made while the outcome is most uncertain.

Appendix A: 2D optimization of MRTI datasets

This Appendix shows four subfigures for each of the 30 MRTI datasets available. Further discussion can be found in Section 5.2.2 and Tables C.1 and C.2. Subfigure (A) is the model’s temperature prediction; Subfigure (B) is the MRTI at the hottest time point; Subfigure (C) is the damage indicated by the [lethal threshold temperature damage model \(LTTDM\)](#) using 57 °C as the threshold; Subfigure (D) is the result of the regular grid search described in Section 5.2.5. Subfigure (D) also includes a [blue dot](#) with a [green outline](#) that indicates the point in $\mu_{eff}-\omega$ space that has the optimal DSC value. The MRTI datasets are listed in the following order: [first](#), the most puzzling dataset, #0495; [second](#), the two datasets that are included in the $N = 22$ cohort but excluded in the $N = 20$ cohort; [third](#), the eight datasets that are excluded in both cohorts; [fourth](#), the twenty datasets that are included in both cohorts.

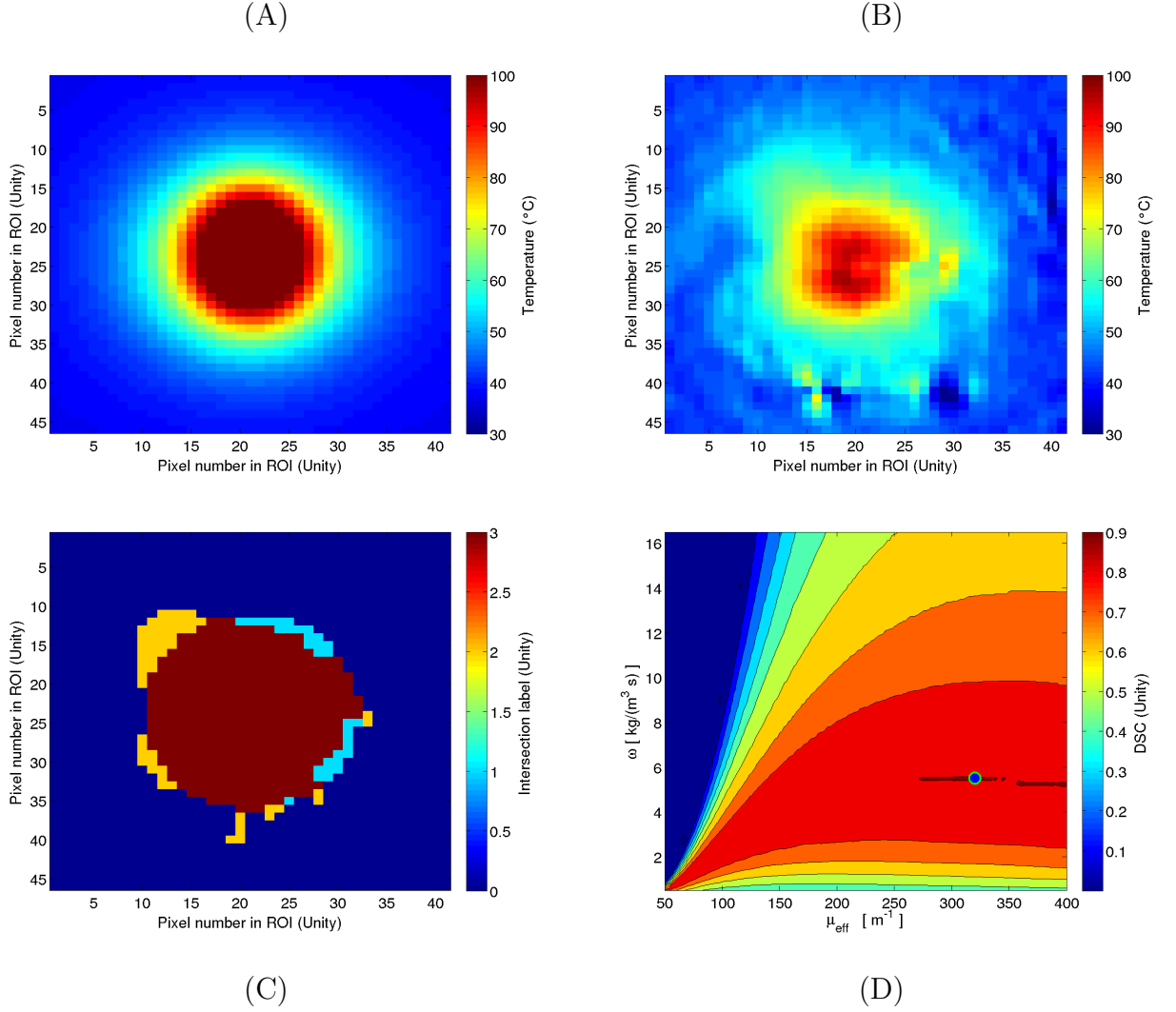


Figure A.1: MRTI #0495 FOV: 37.480 mm \times 42.165 mm. Maximum DSC in optimization: 0.90359. This MRTI dataset is the only one that was failed to be predicted with a DSC ≥ 0.7 . It is included in both 20 and 22 dataset lists. A failure prediction simply means that the average of μ_{eff} and ρ from the training was not similar to this dataset's optimal μ_{eff} and ρ . That result can be seen by reviewing subfigure (D); the passing regions are far from all the other datasets' passing regions. Why there is this separation of passing regions is puzzling. Dataset #0495 appears to be in-plane; the MRTI time series suggest that the ablation is near steady state. In short, #0495 appears to be the perfect ablation archetype.

APPENDIX A: DATASETS INCLUDED IN THE $N = 22$ COHORT BUT EXCLUDED FROM THE $N = 20$ COHORT

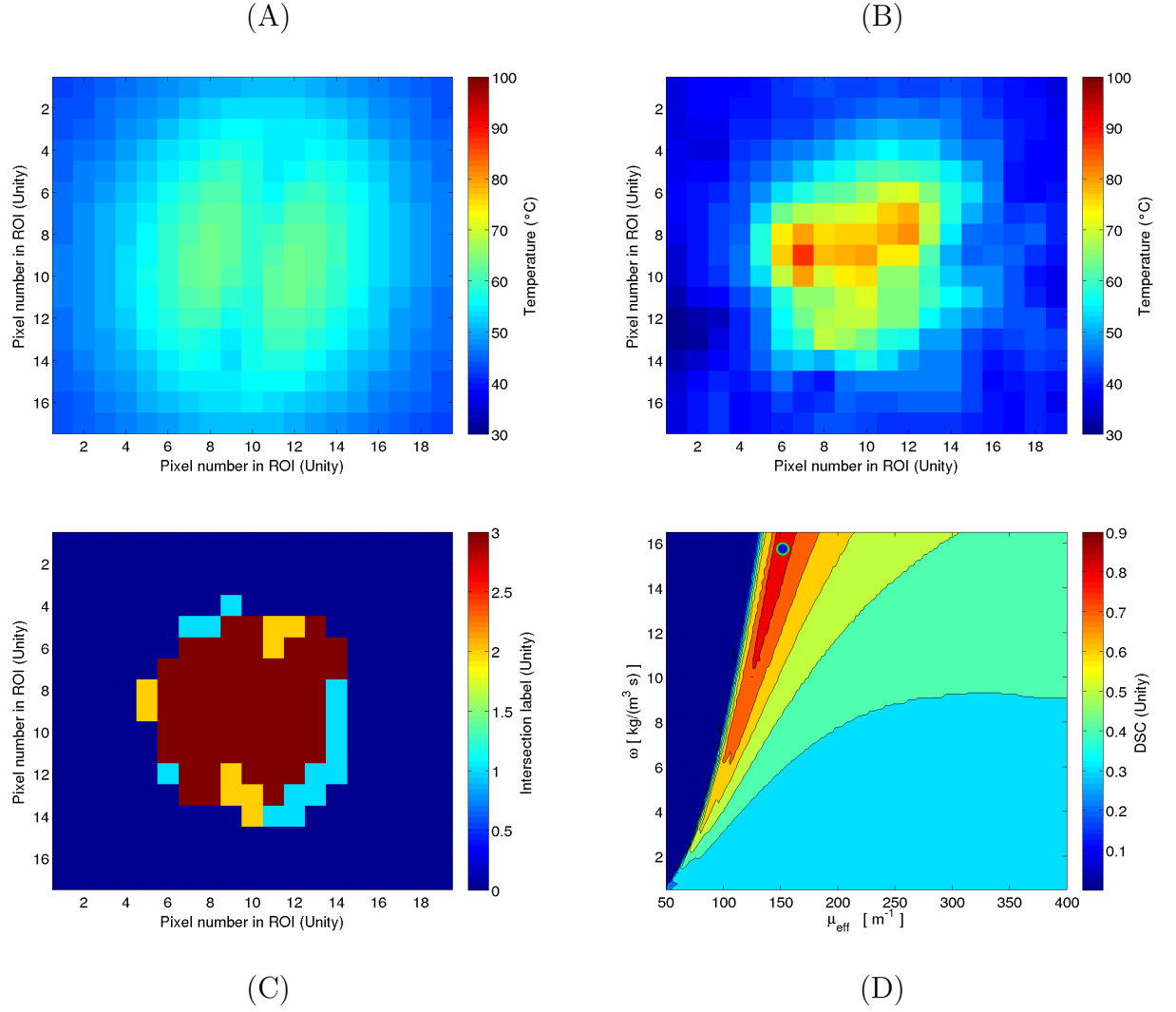


Figure A.2: MRTI #0415 FOV: 16.866 mm \times 14.992 mm. Maximum DSC in optimization: 0.86111.

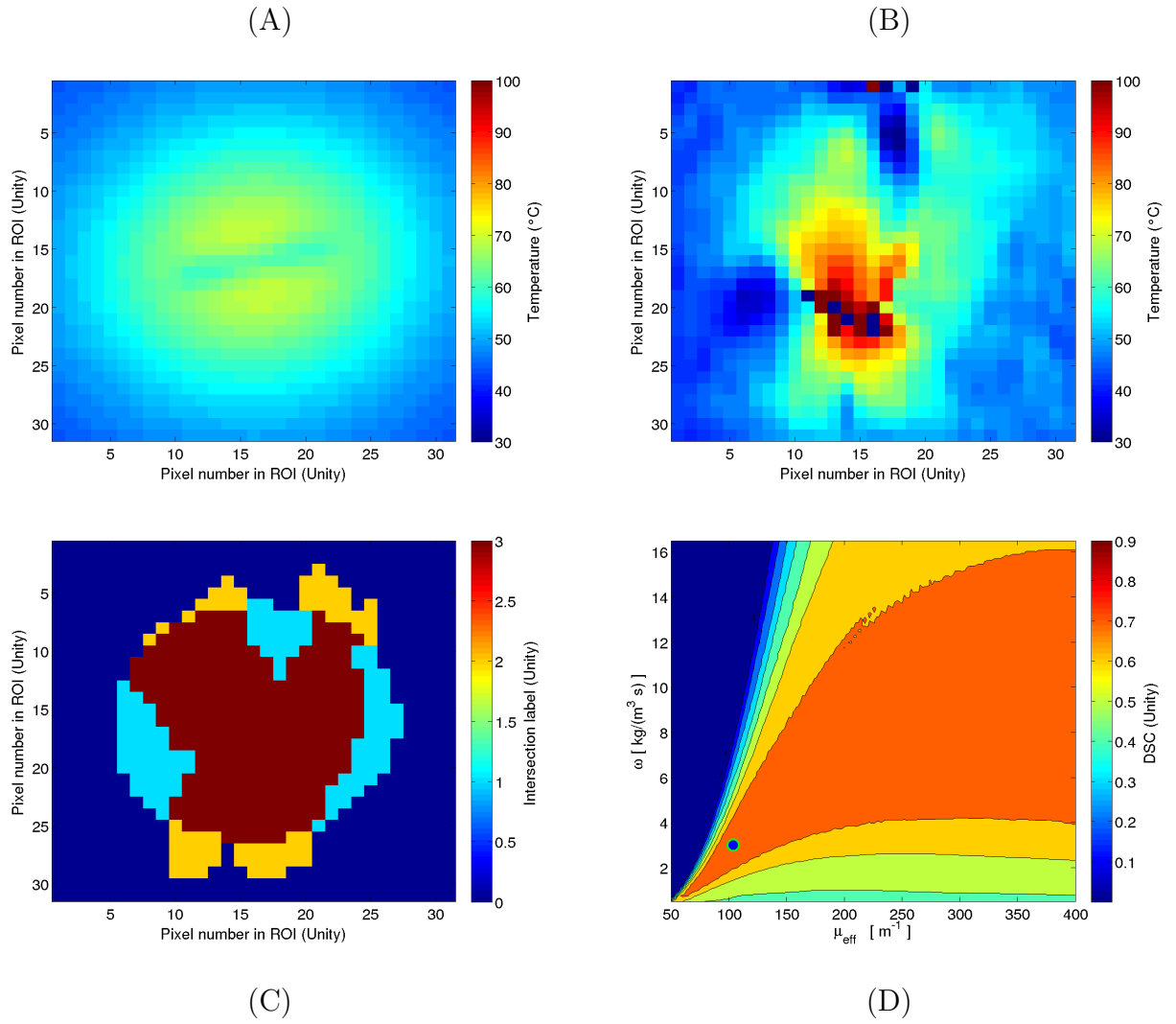


Figure A.3: MRTI #0435 FOV: 25.770 mm \times 25.770 mm. Maximum DSC in optimization: 0.76018.

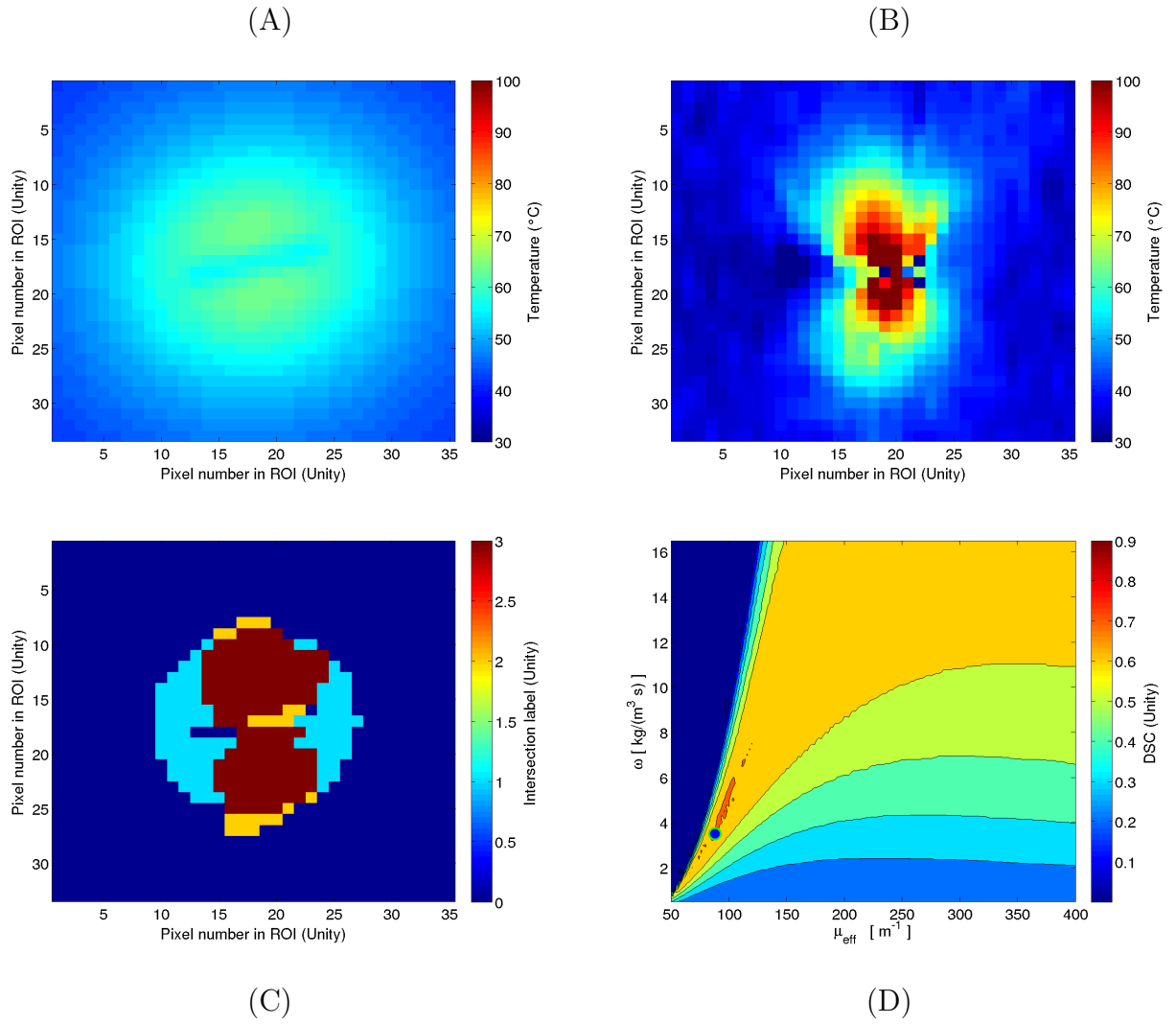


Figure A.4: MRTI #0440 FOV: 29.206 mm \times 27.488 mm. Maximum DSC in optimization: 0.71809.

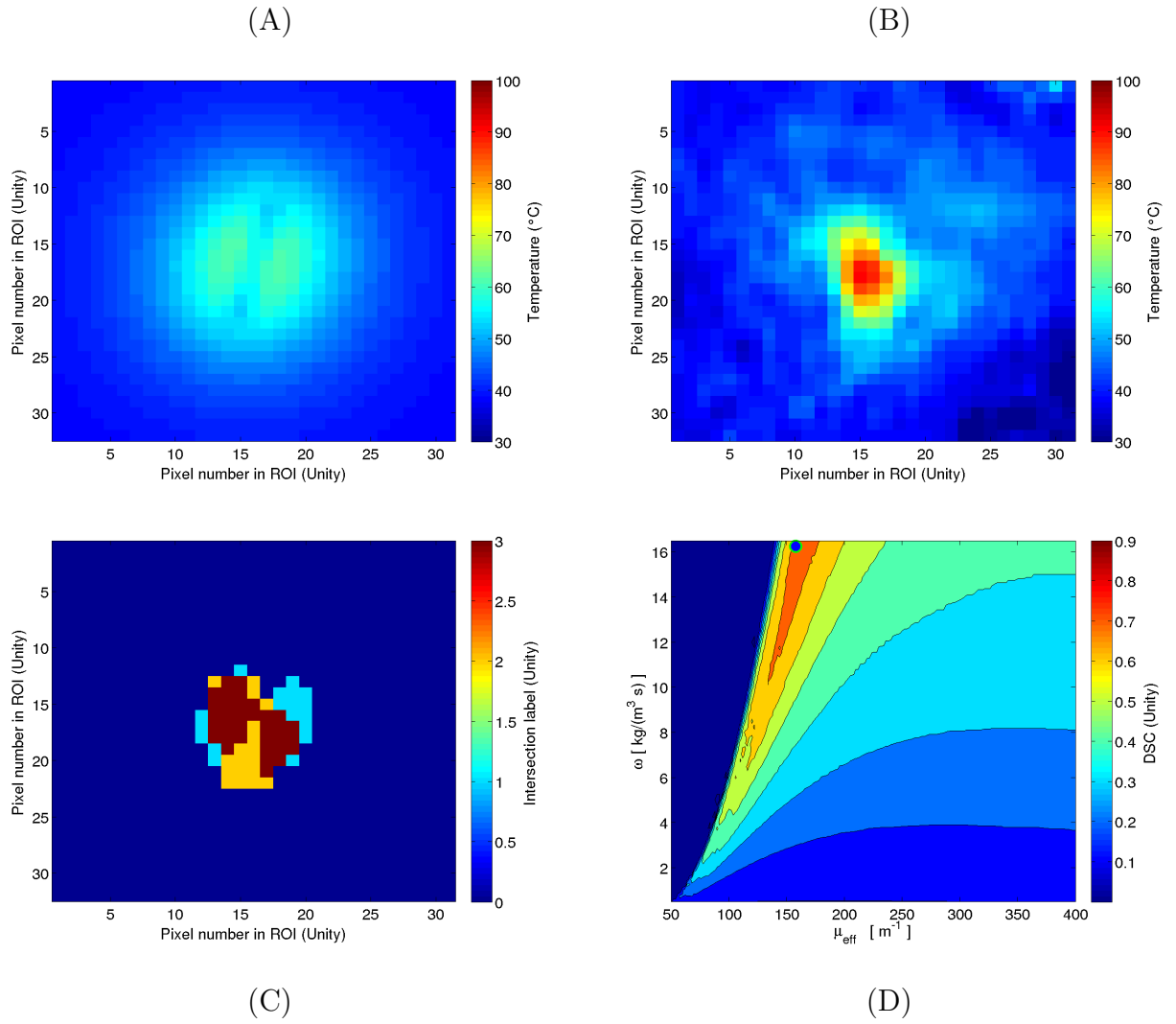


Figure A.5: MRTI #0447 FOV: 28.110 mm \times 29.047 mm. Maximum DSC in optimization: 0.76636.

APPENDIX A: DATASETS EXCLUDED FROM THE $N = 22$ COHORT BUT INCLUDED IN THE $N = 20$ COHORT

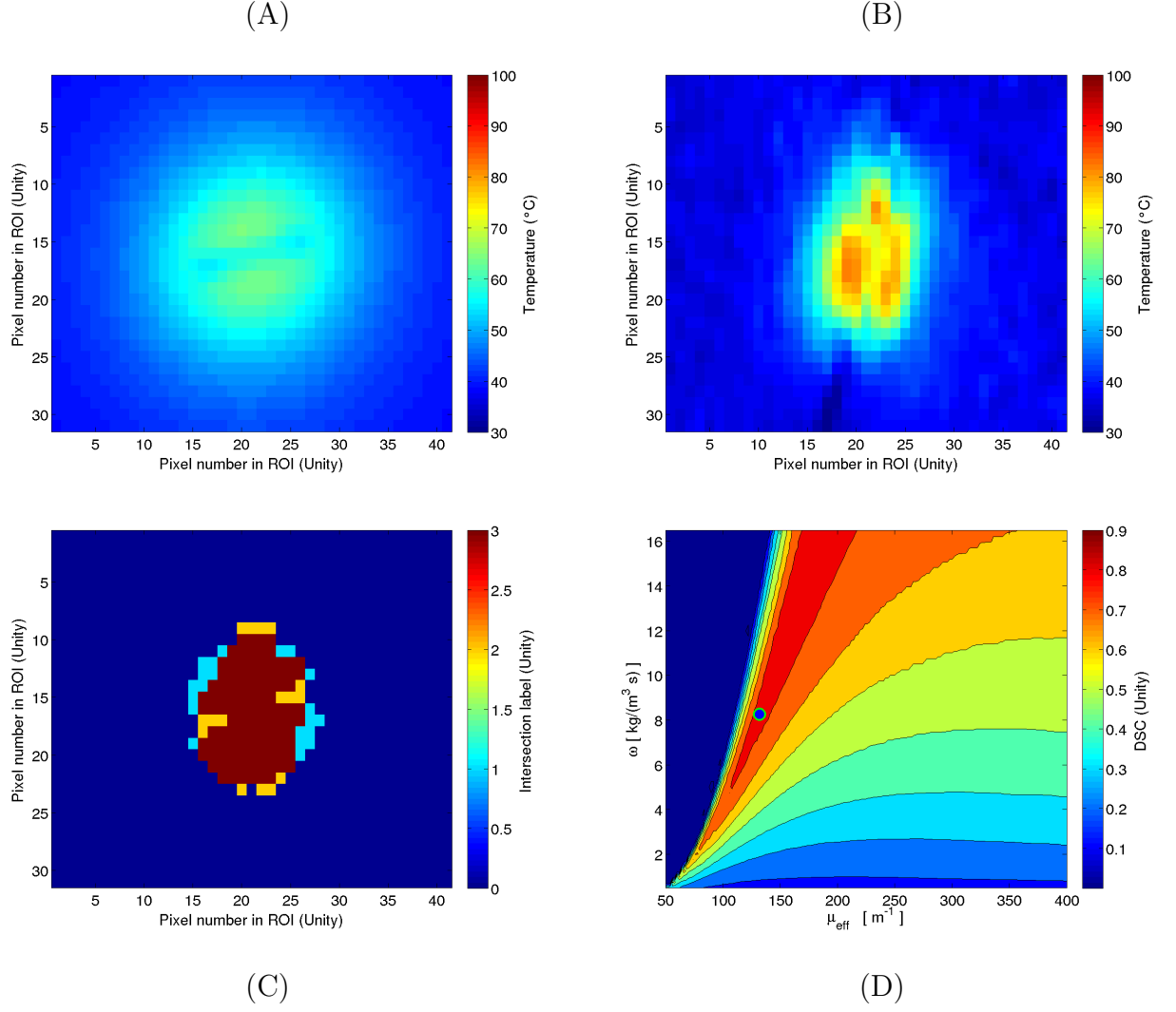


Figure A.6: MRTI #0436 FOV: 34.360 mm \times 25.770 mm. Maximum DSC in optimization: 0.85827.

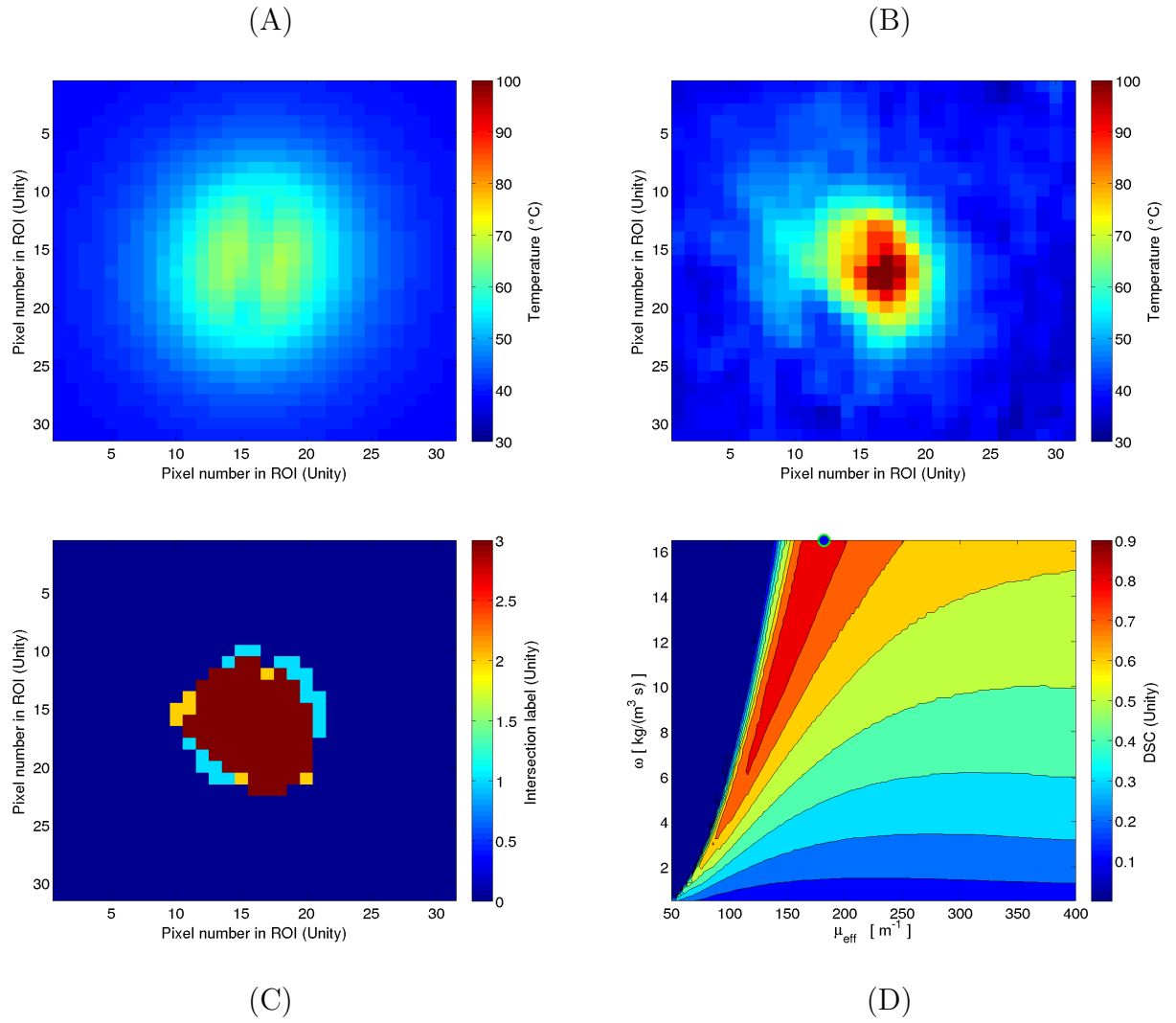


Figure A.7: MRTI #0457 FOV: 28.110 mm \times 28.110 mm. Maximum DSC in optimization: 0.87368.

APPENDIX A: DATASETS EXCLUDED FROM BOTH COHORTS

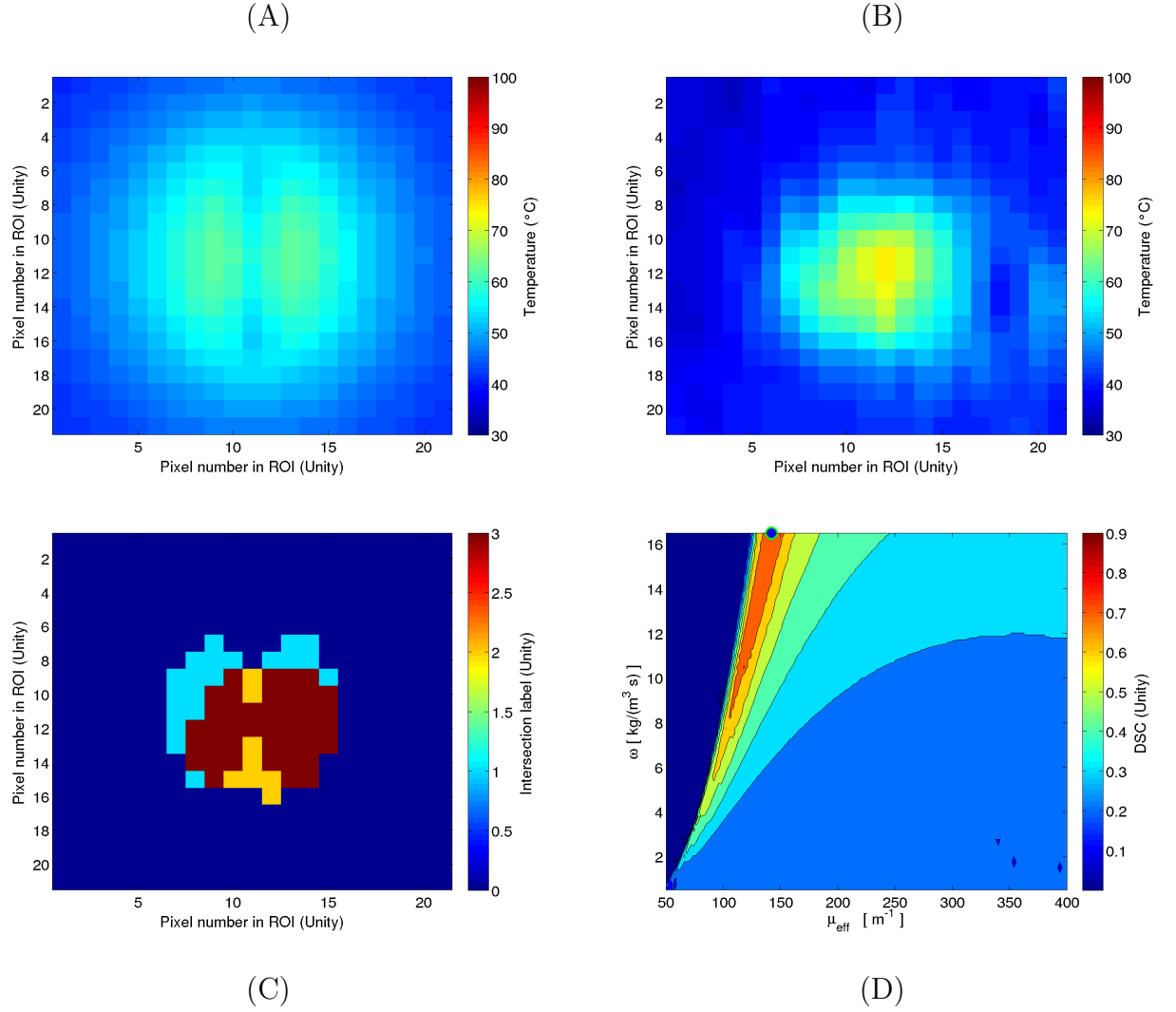


Figure A.8: MRTI #0497 FOV: 18.740 mm \times 18.740 mm. Maximum DSC in optimization: 0.80000. This ablation clearly did not reach steady state.

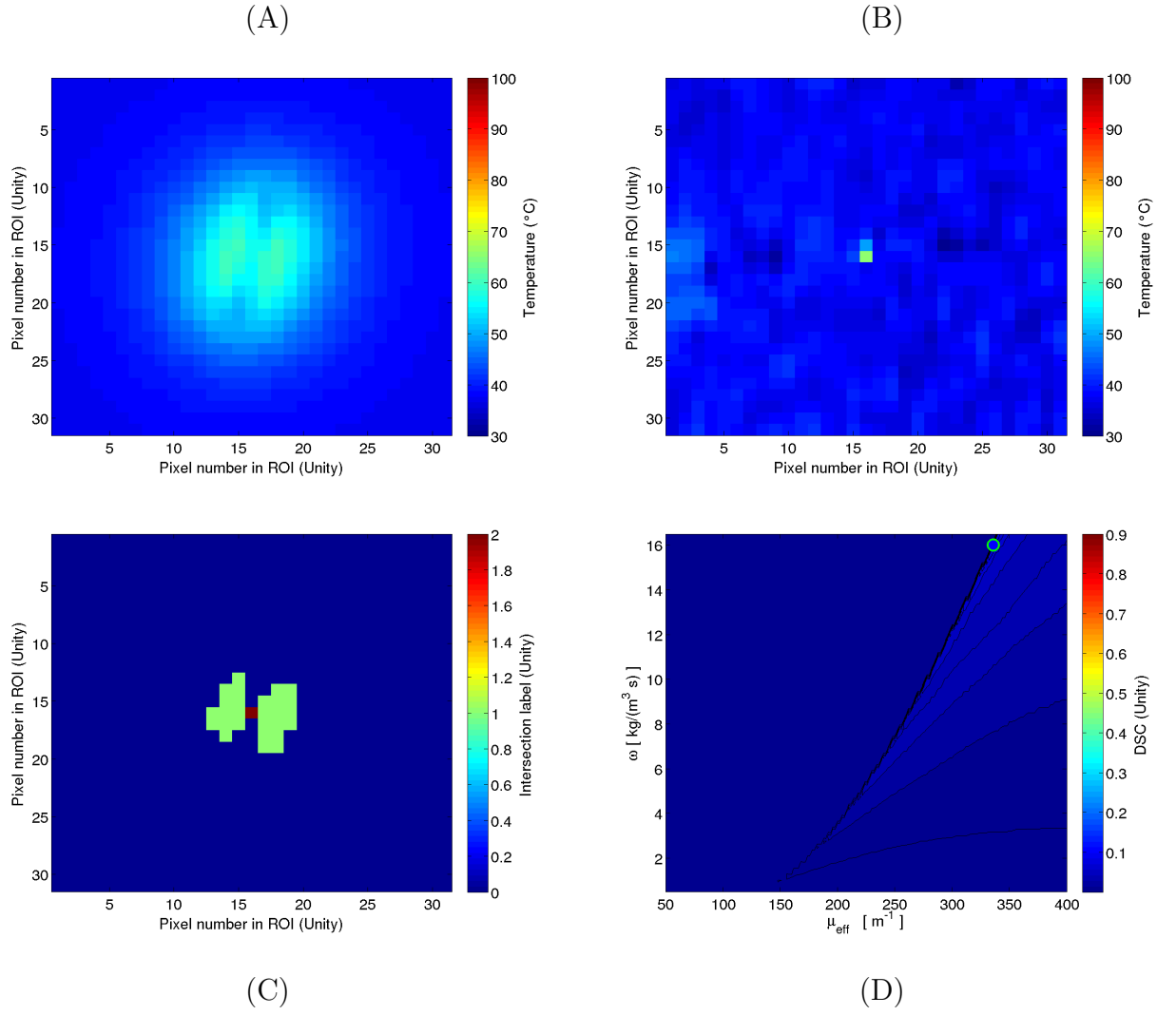


Figure A.9: MRTI #0409 FOV: 28.110 mm \times 28.110 mm. Maximum DSC in optimization: 0.080000. This ablation clearly was a test pulse.

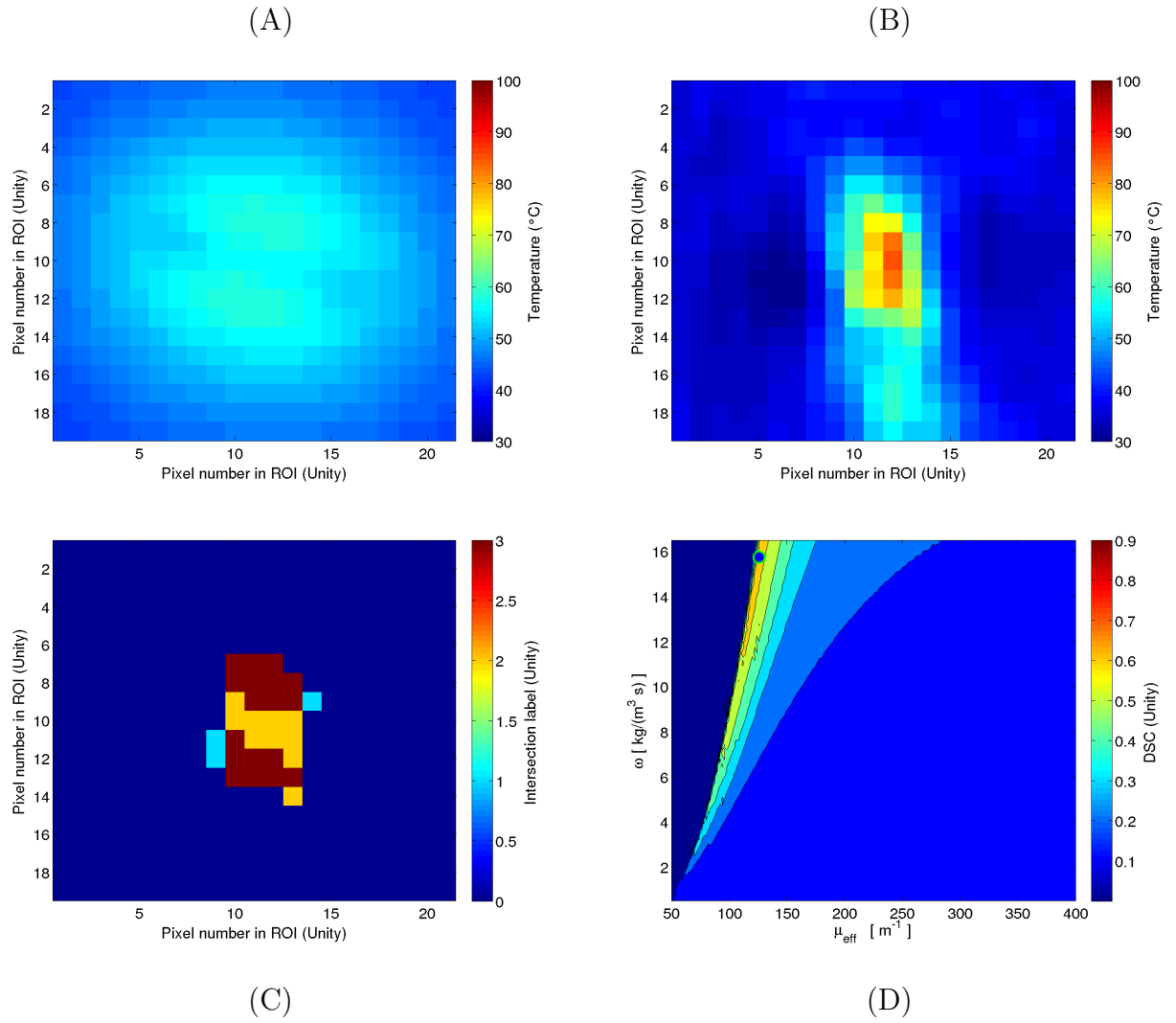


Figure A.10: MRTI #0466 FOV: 17.180 mm \times 15.462 mm. Maximum DSC in optimization: 0.70370.

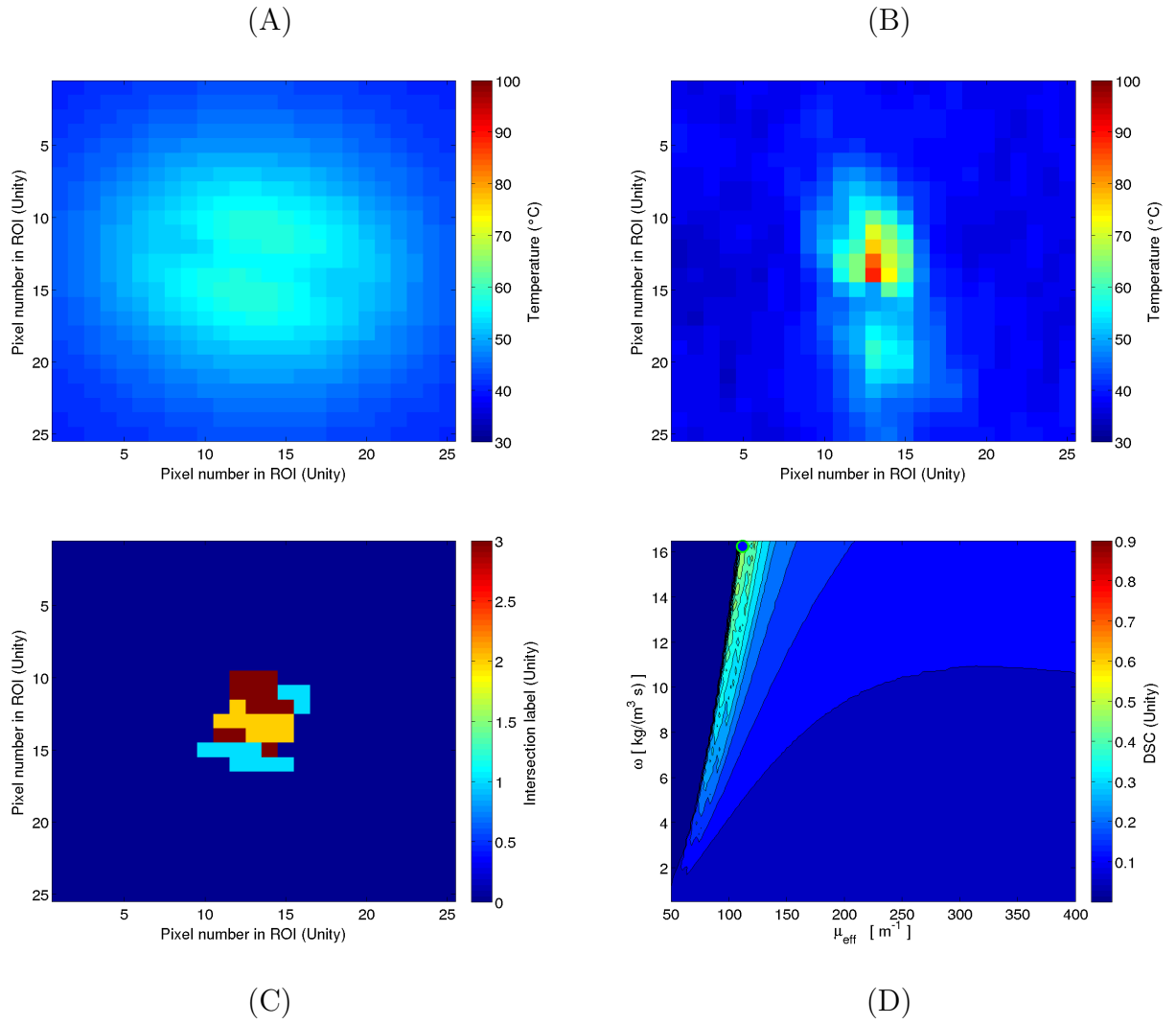


Figure A.11: MRTI #0468 FOV: 20.616 mm \times 20.616 mm. Maximum DSC in optimization: 0.50000.

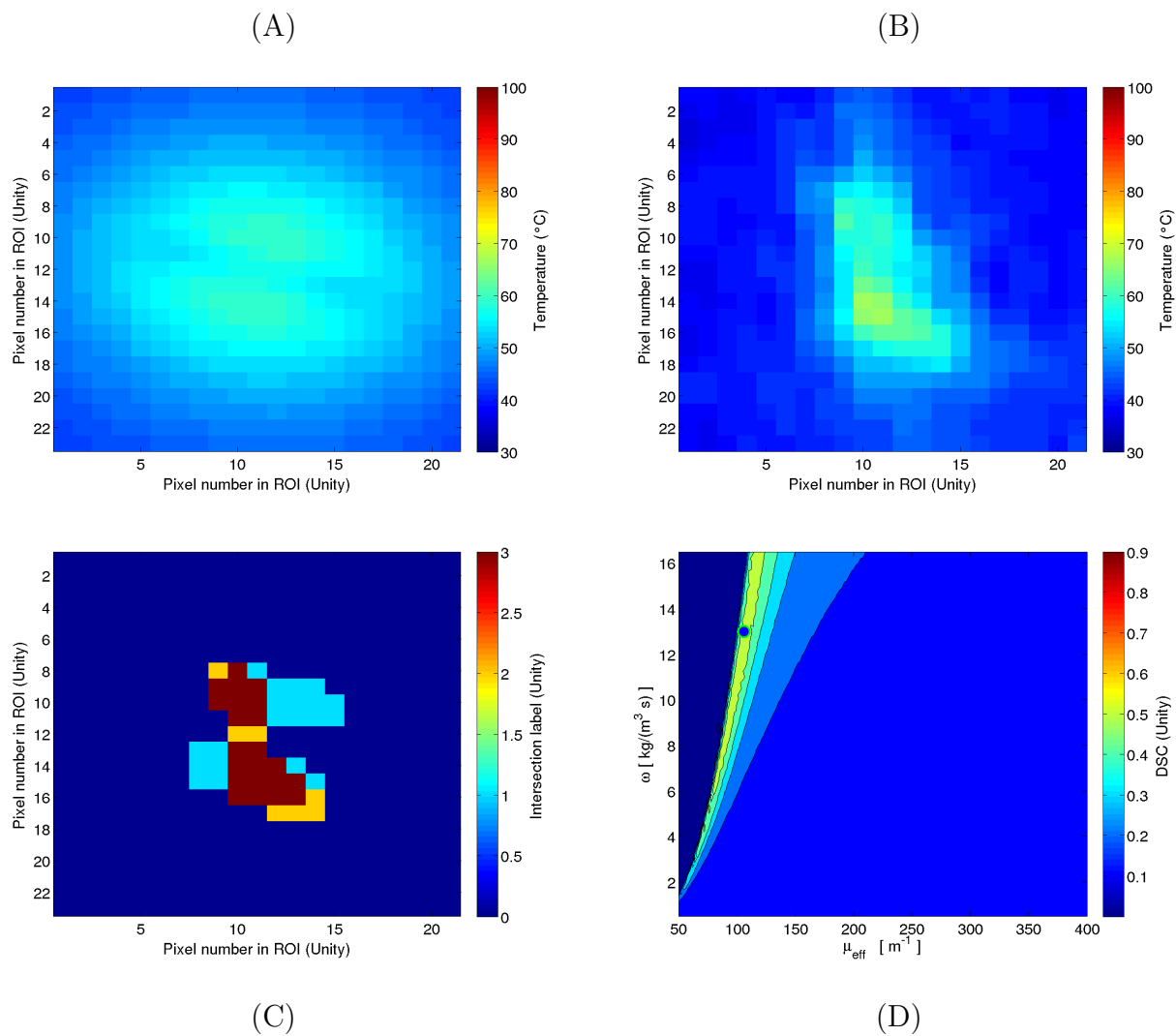


Figure A.12: MRTI #0471 FOV: 17.180 mm \times 18.898 mm. Maximum DSC in optimization: 0.60274.

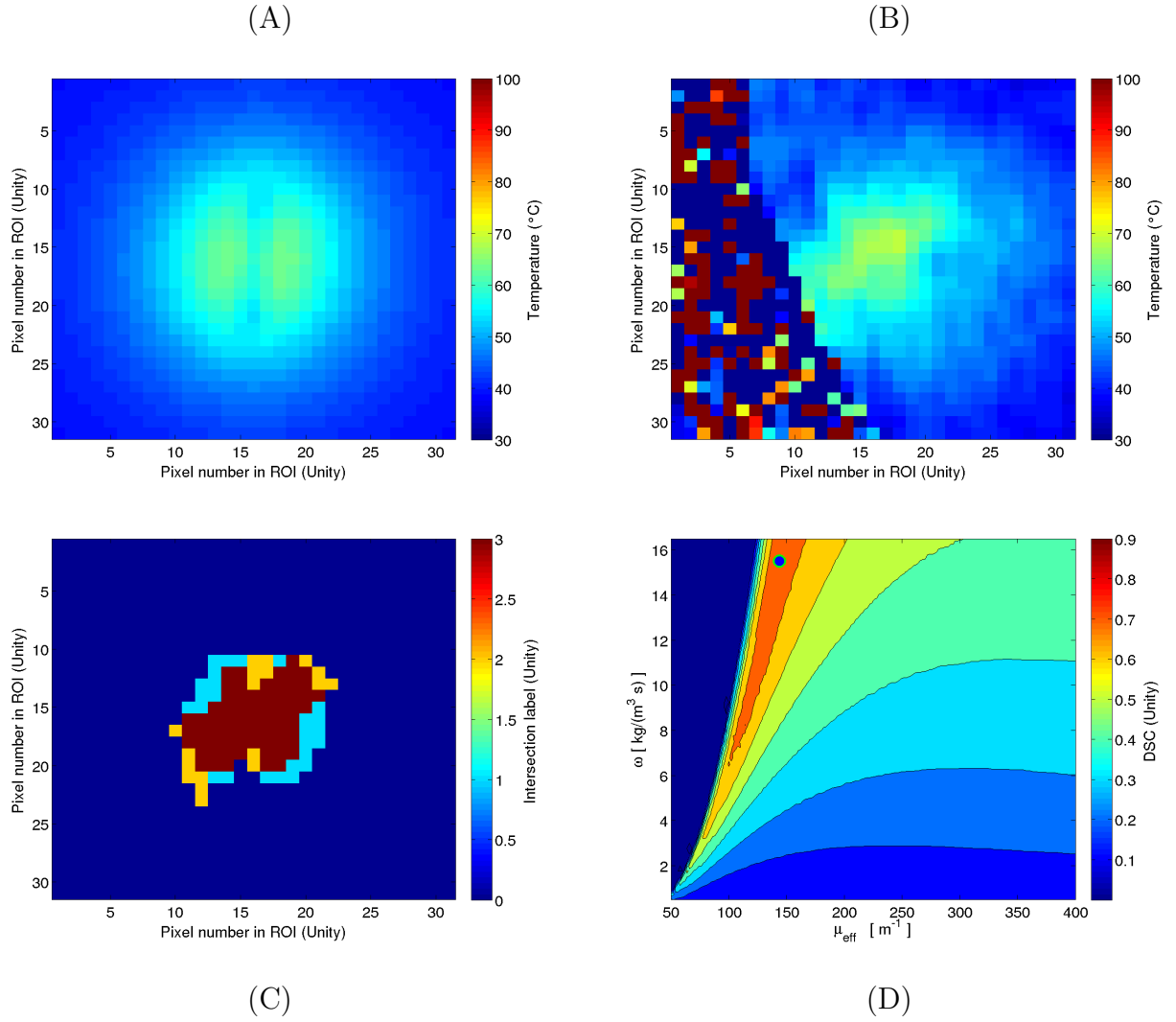


Figure A.13: MRTI #0476 FOV: 25.770 mm \times 25.770 mm. Maximum DSC in optimization: 0.77095.

APPENDIX A: INCLUDED DATASETS IN BOTH COHORTS

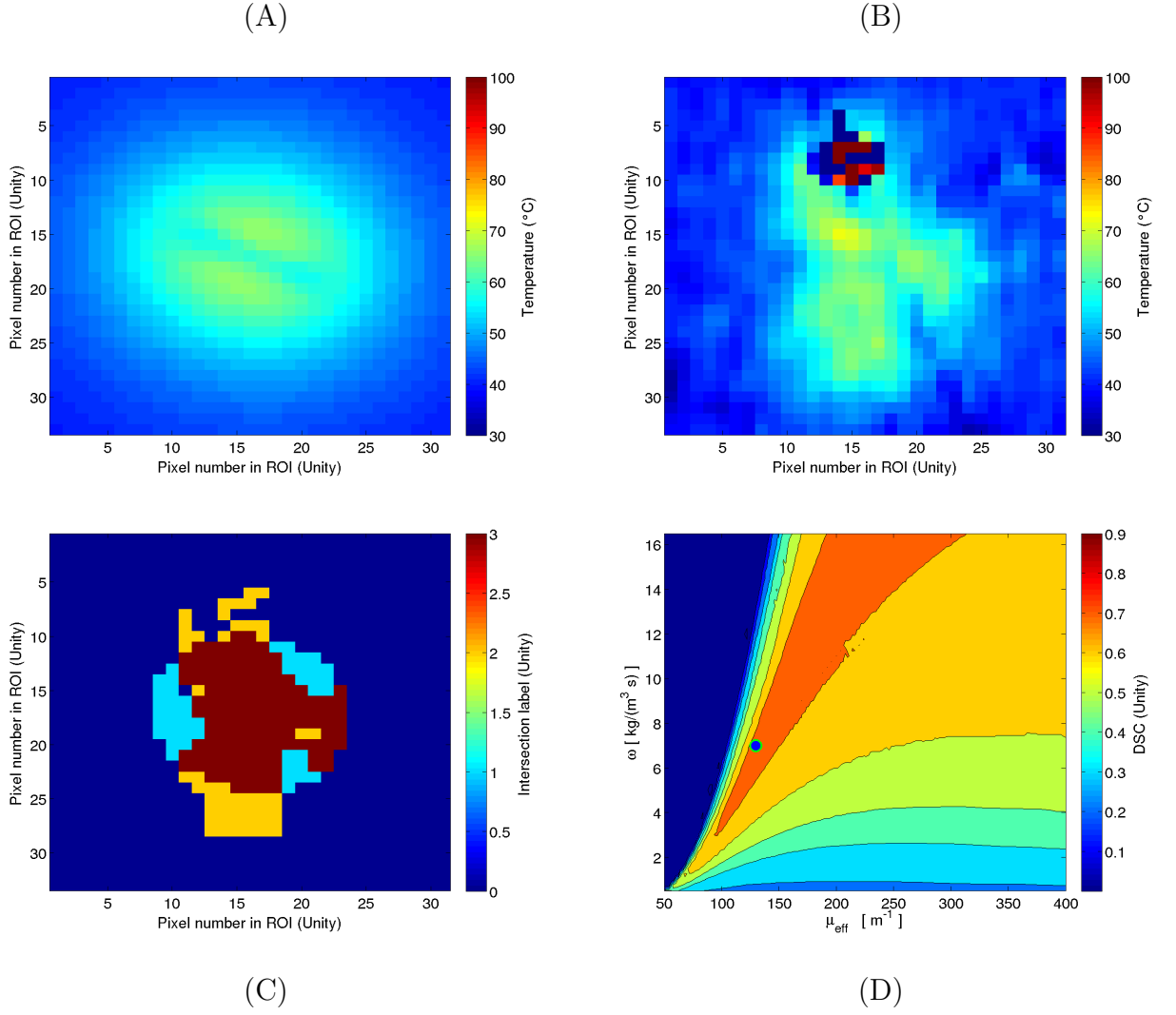


Figure A.14: MRTI #0417 FOV: 25.77 mm × 27.488 mm. Maximum optimal DSC: 0.74713.

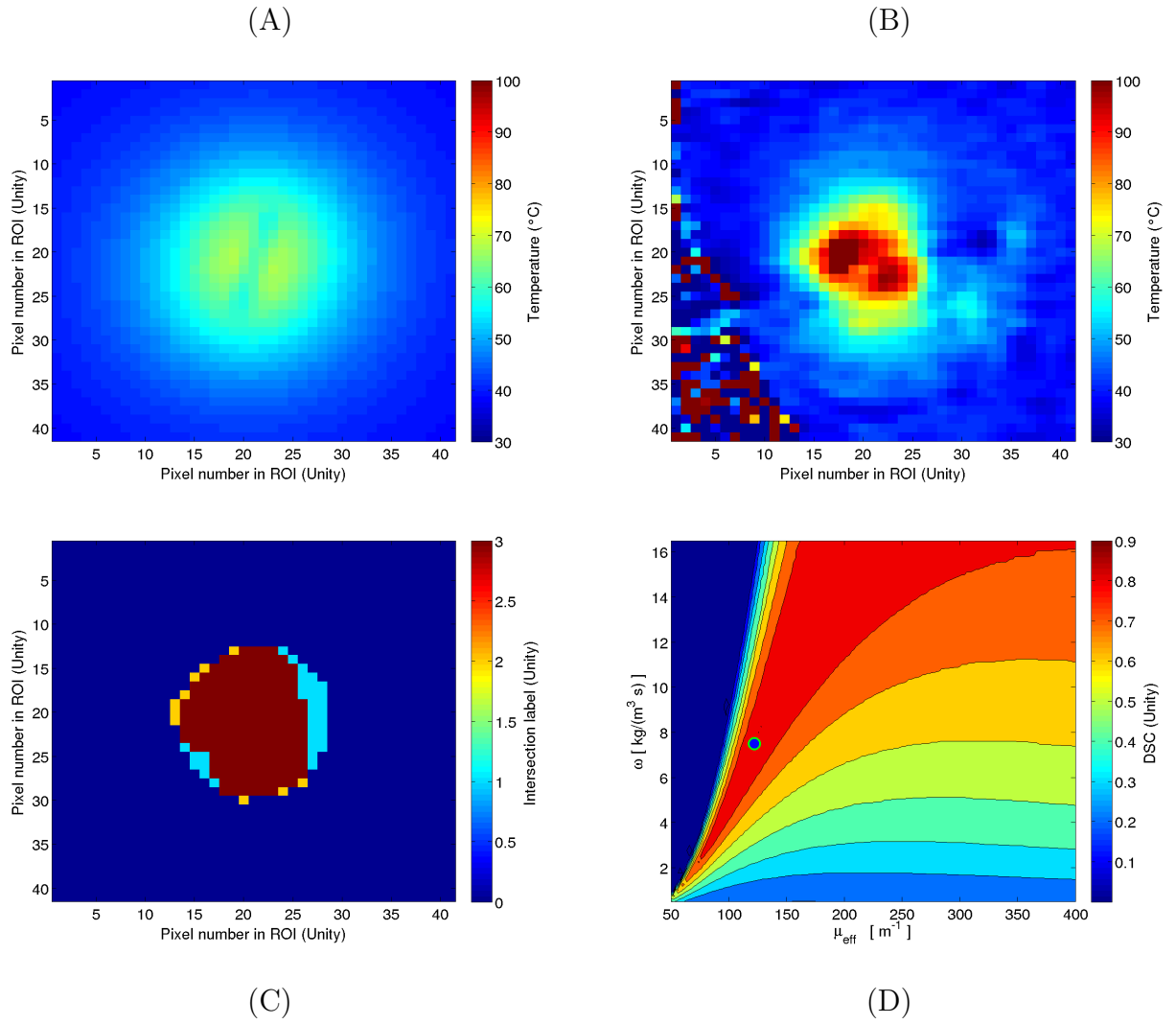


Figure A.15: MRTI #0477 FOV: 34.360 mm \times 34.360 mm. Maximum DSC in optimization: 0.90104.

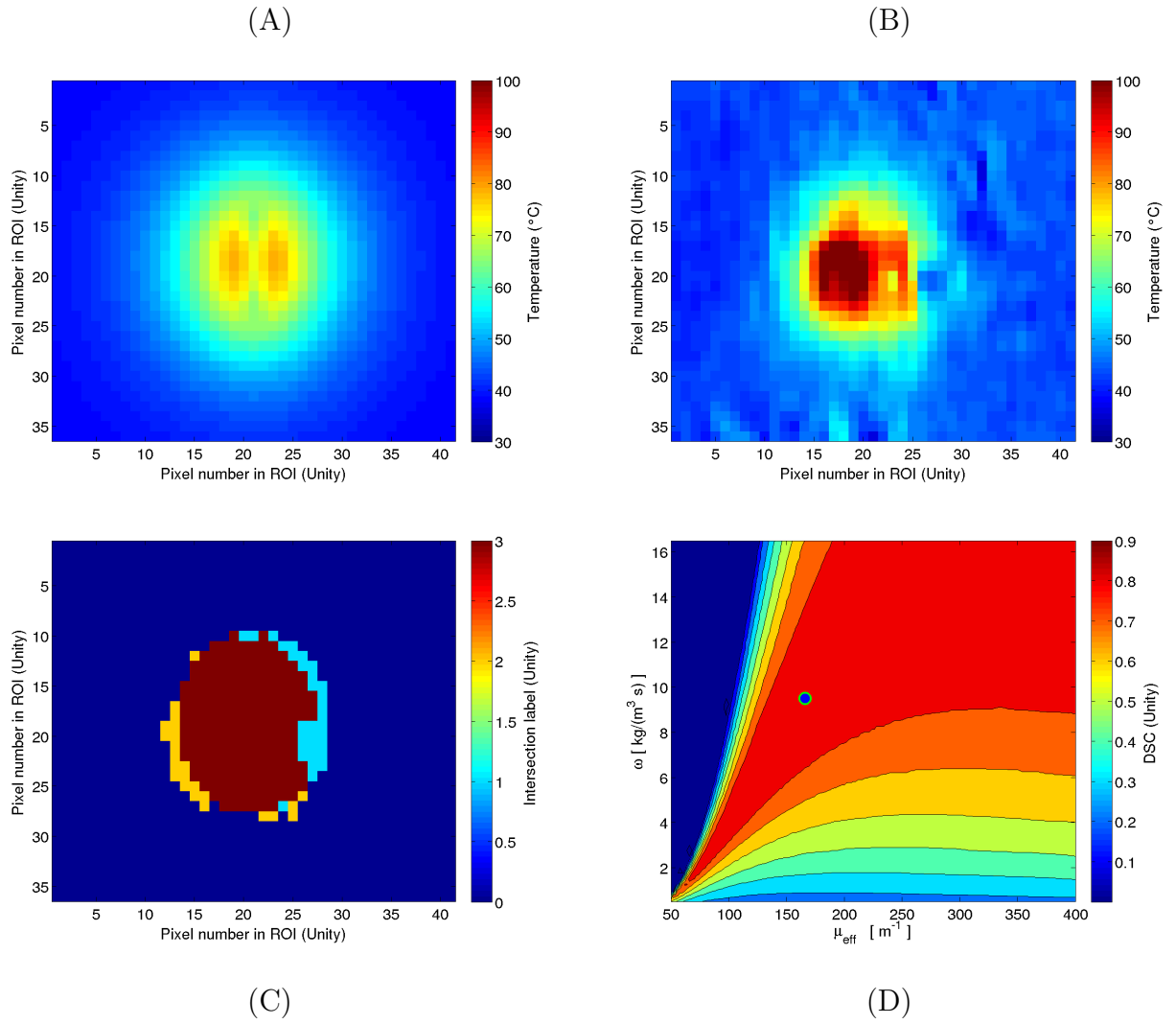


Figure A.16: MRTI #0488 FOV: 37.480 mm \times 32.795 mm. Maximum DSC in optimization: 0.87982.

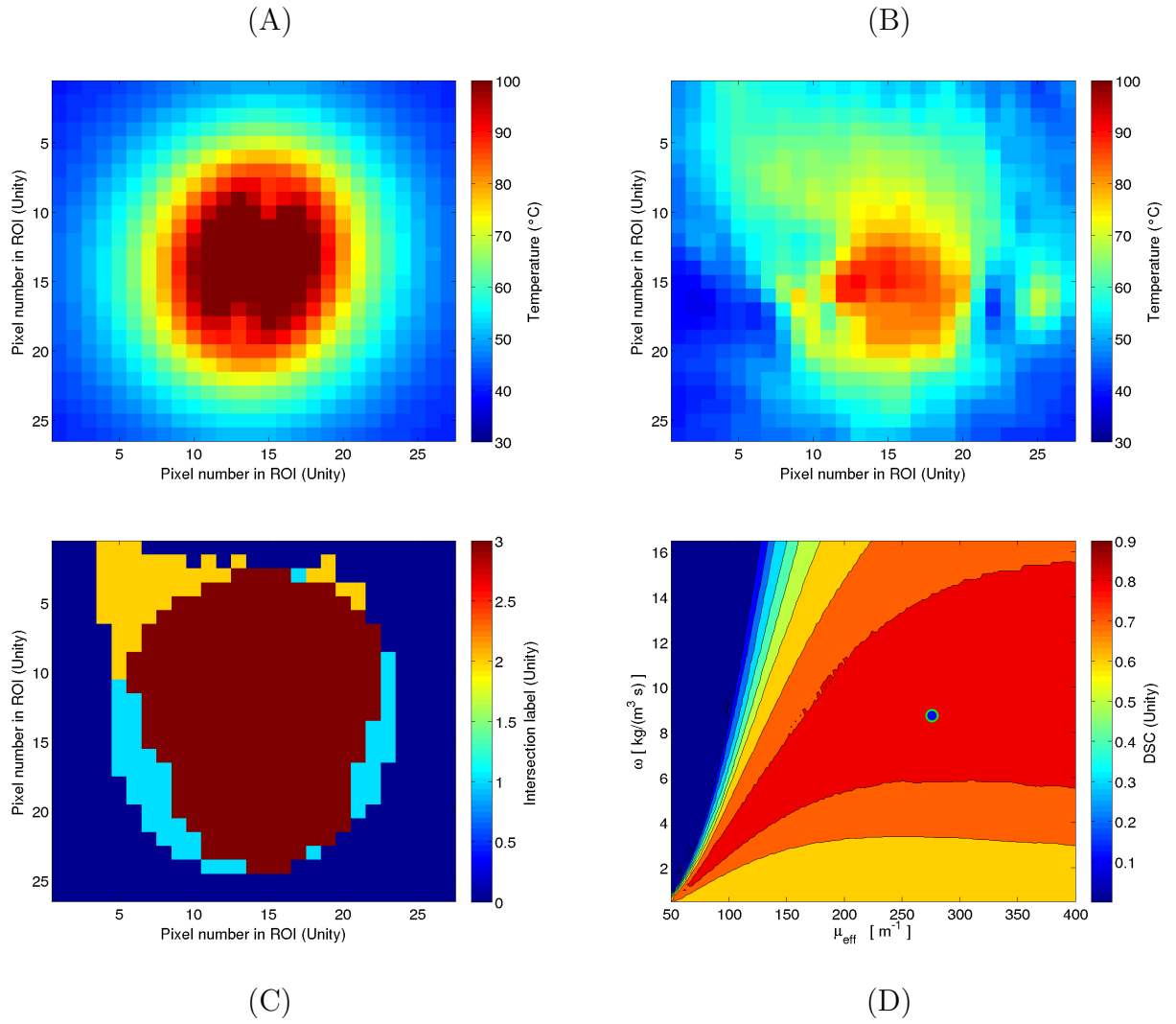


Figure A.17: MRTI #0491 FOV: 24.362 mm \times 23.425 mm. Maximum DSC in optimization: 0.84839.

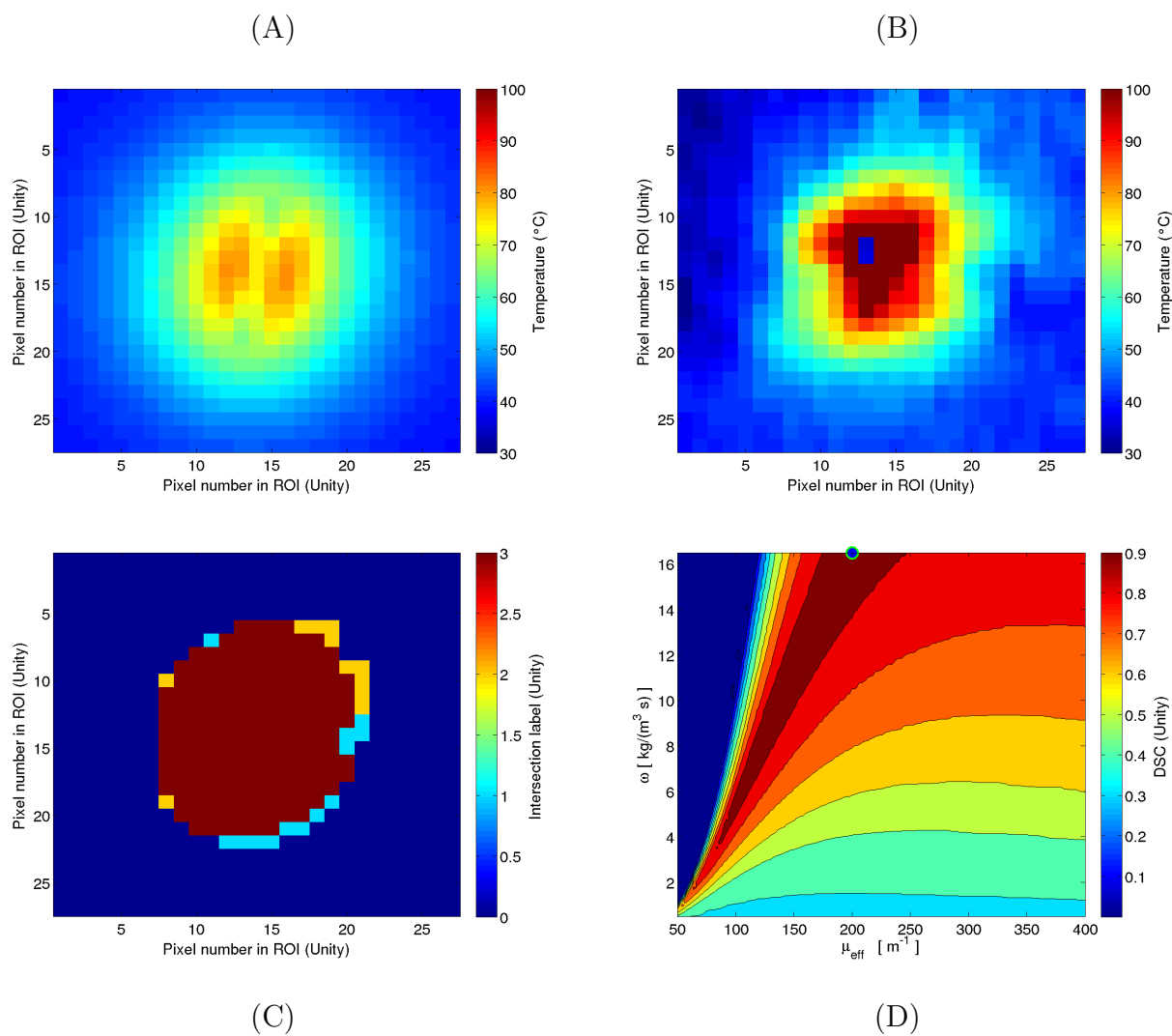


Figure A.18: MRTI #0496 FOV: 24.362 mm \times 24.362 mm. Maximum DSC in optimization: 0.93889.

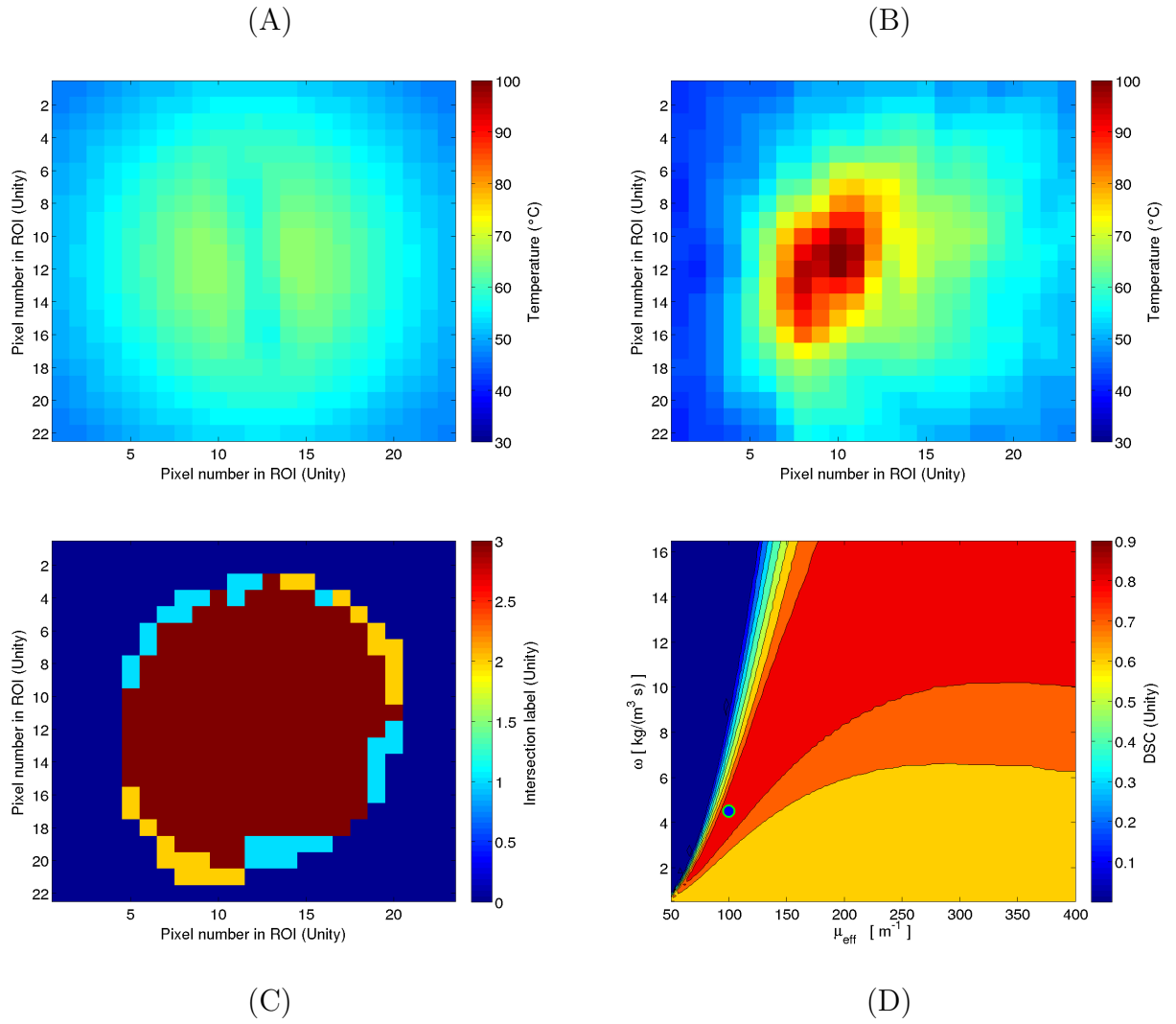


Figure A.19: MRTI #0490 FOV: 19.756 mm \times 18.858 mm. Maximum DSC in optimization: 0.89842.

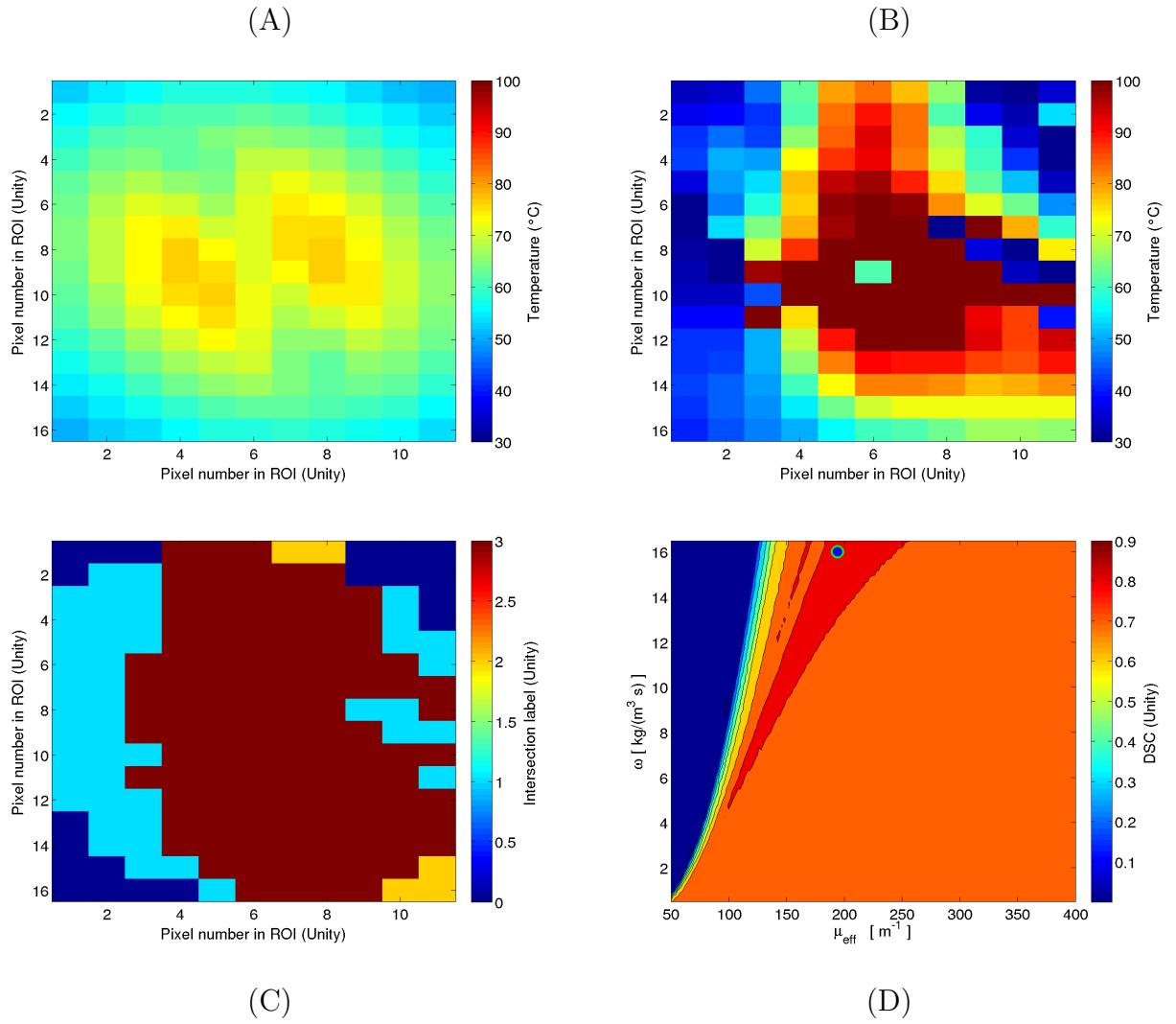


Figure A.20: MRTI #0378 FOV: 9.3700 mm \times 14.055 mm. Maximum DSC in optimization: 0.82443.

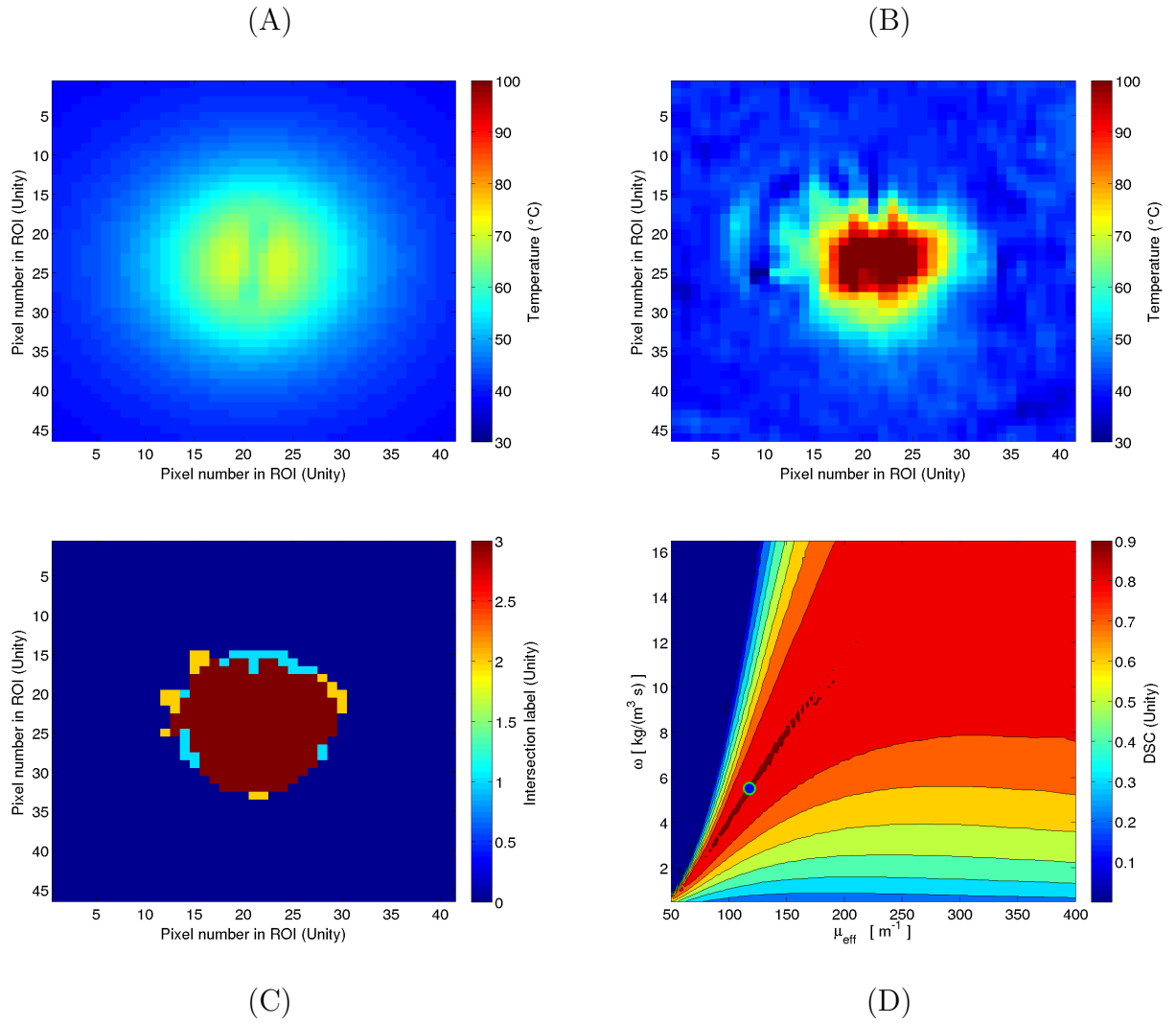


Figure A.21: MRTI #0402 FOV: 37.480 mm \times 42.165 mm. Maximum DSC in optimization: 0.91258.

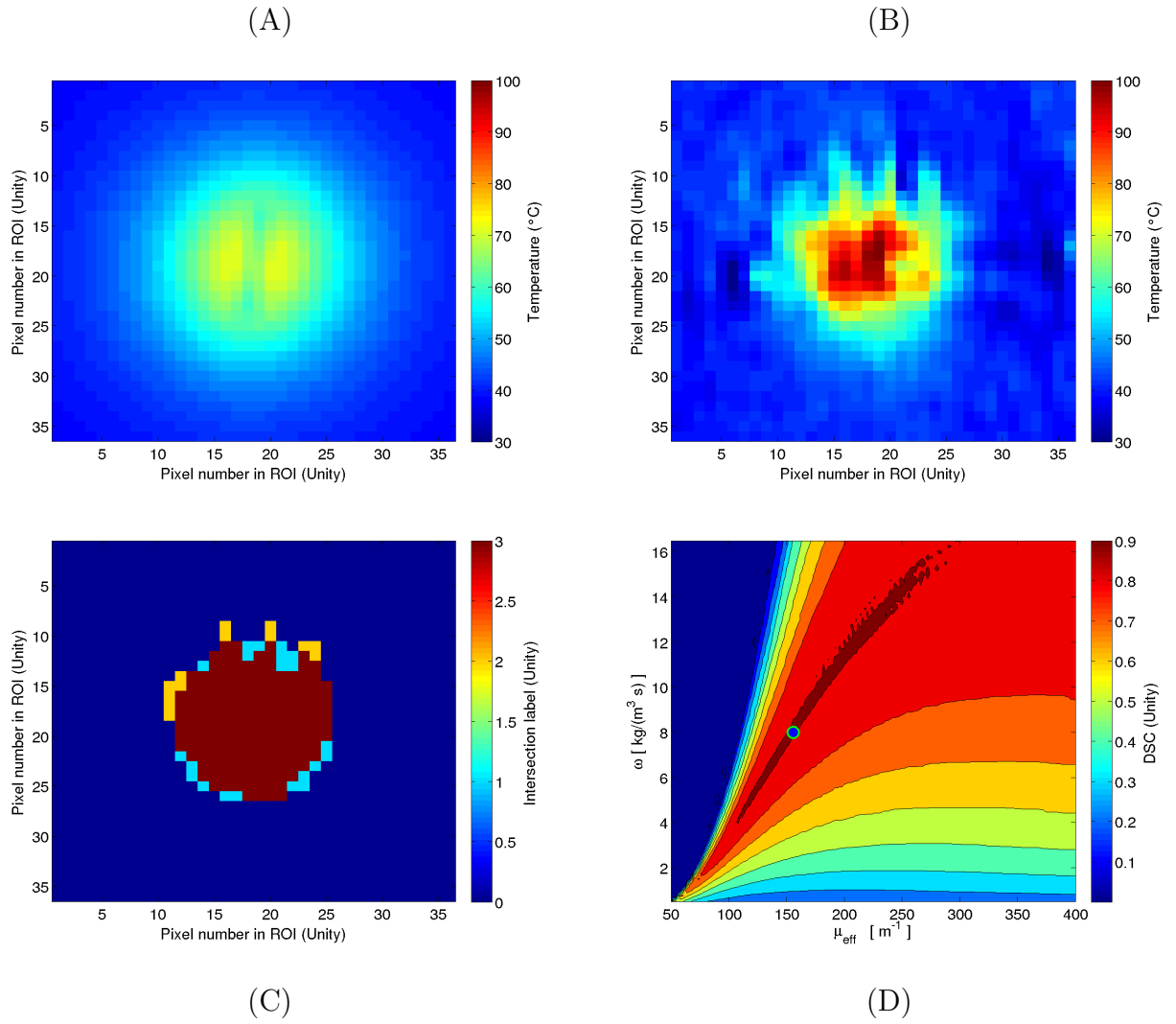


Figure A.22: MRTI #0389 FOV: 32.795 mm \times 32.795 mm. Maximum DSC in optimization: 0.91257.

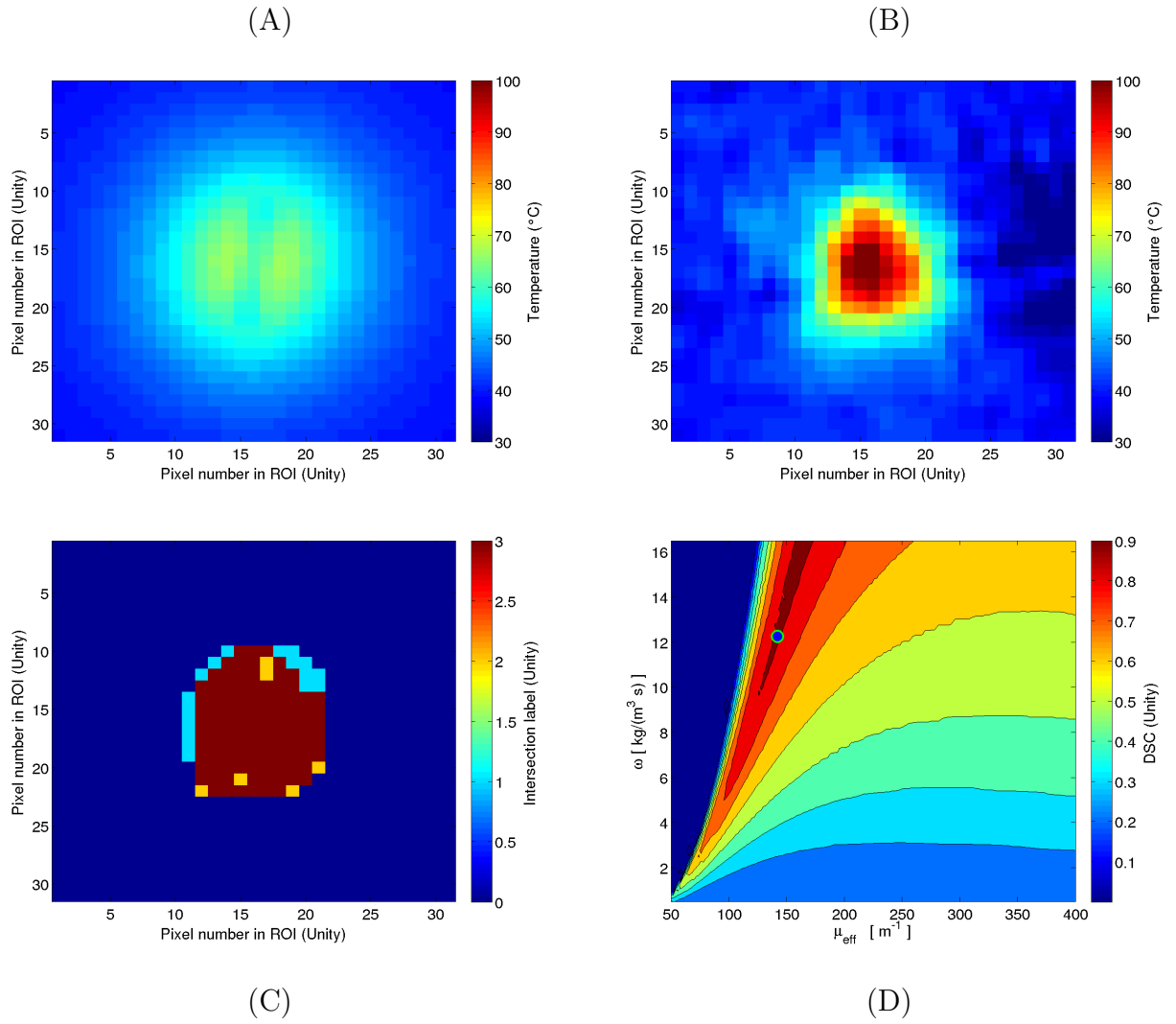


Figure A.23: MRTI #0385 FOV: 28.110 mm \times 28.110 mm. Maximum DSC in optimization: 0.92704.

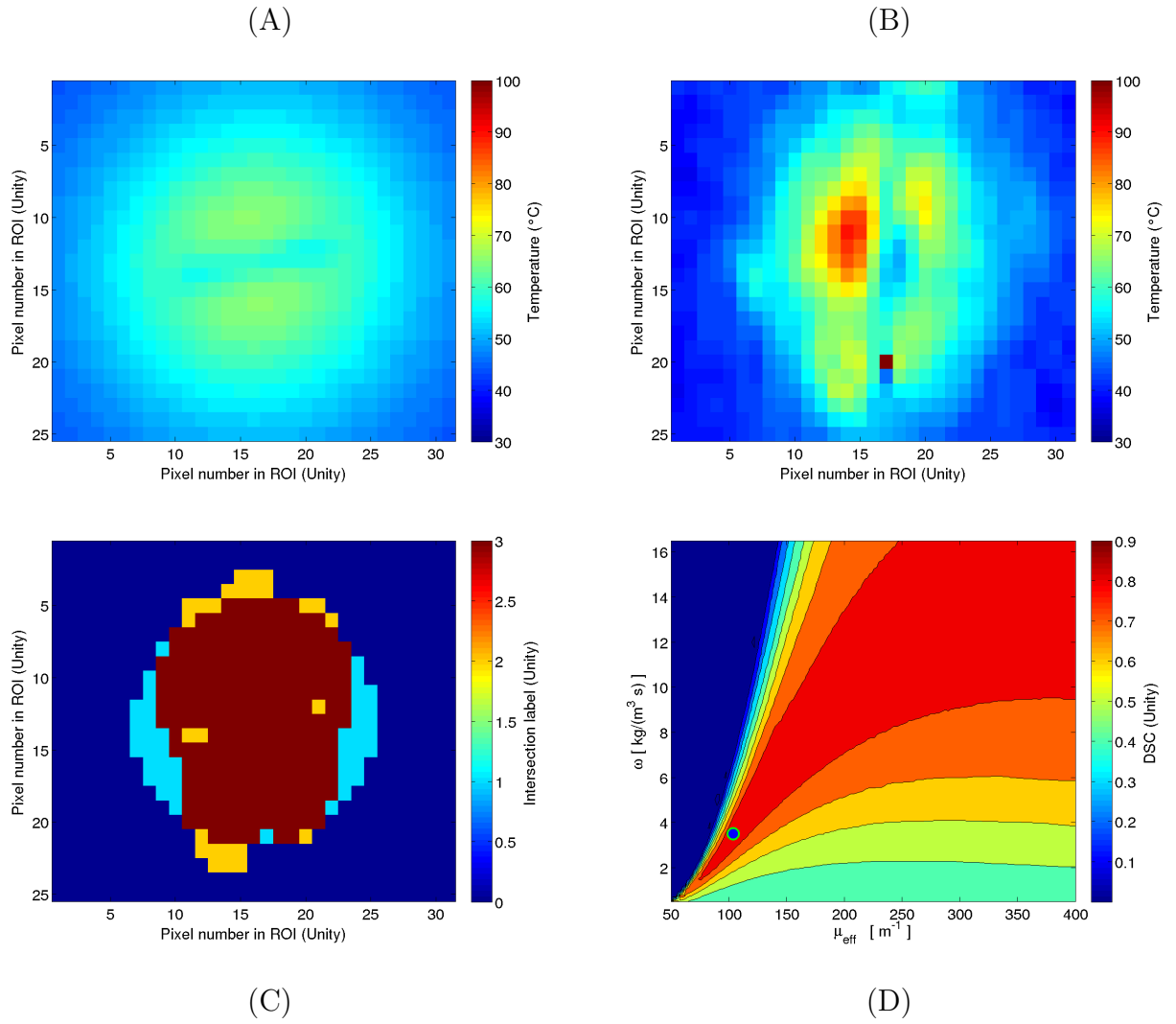


Figure A.24: MRTI #0438 FOV: 25.770 mm \times 20.616 mm. Maximum DSC in optimization: 0.86430.

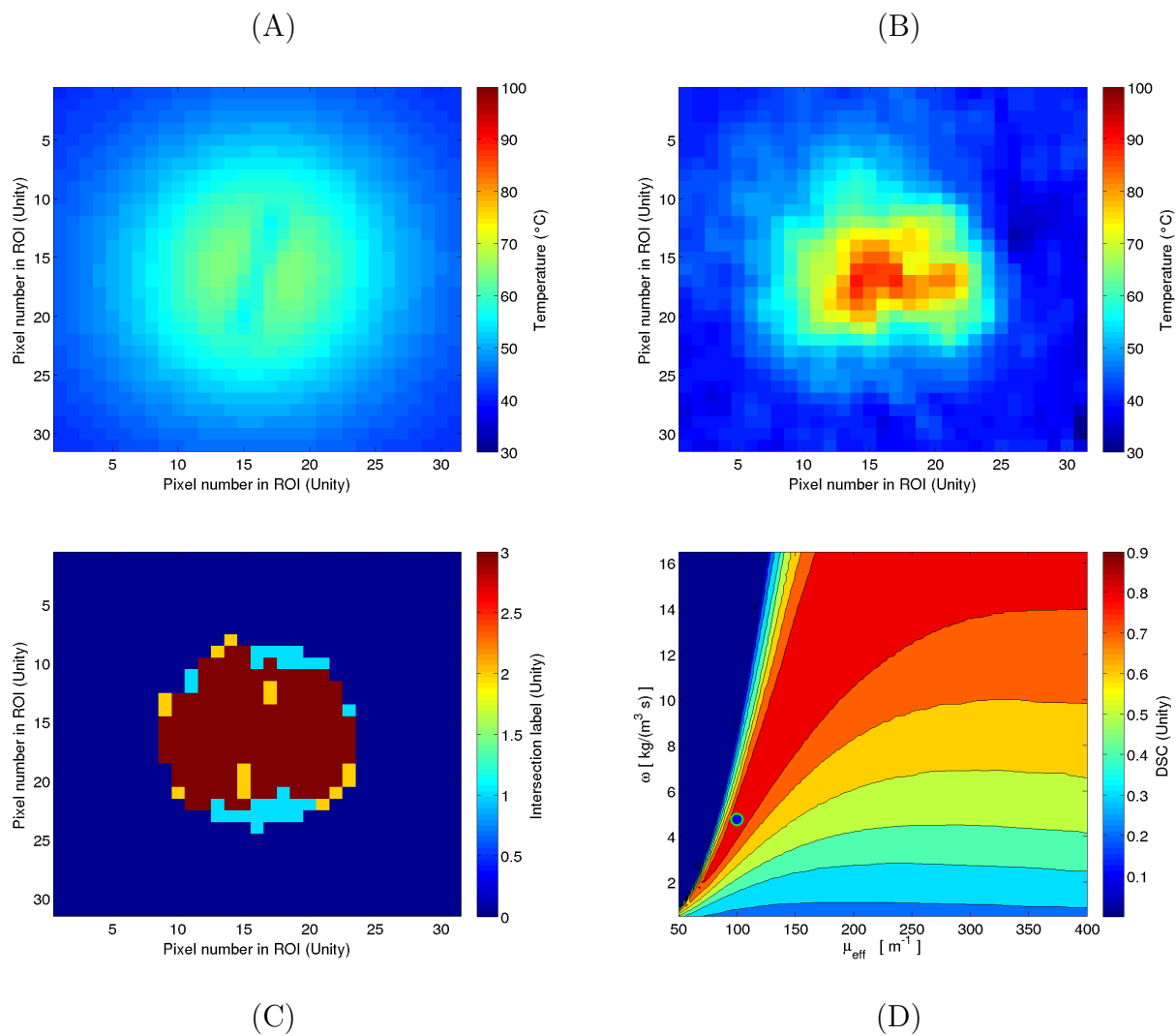


Figure A.25: MRTI #0455 FOV: 28.110 mm \times 28.110 mm. Maximum DSC in optimization: 0.89150.

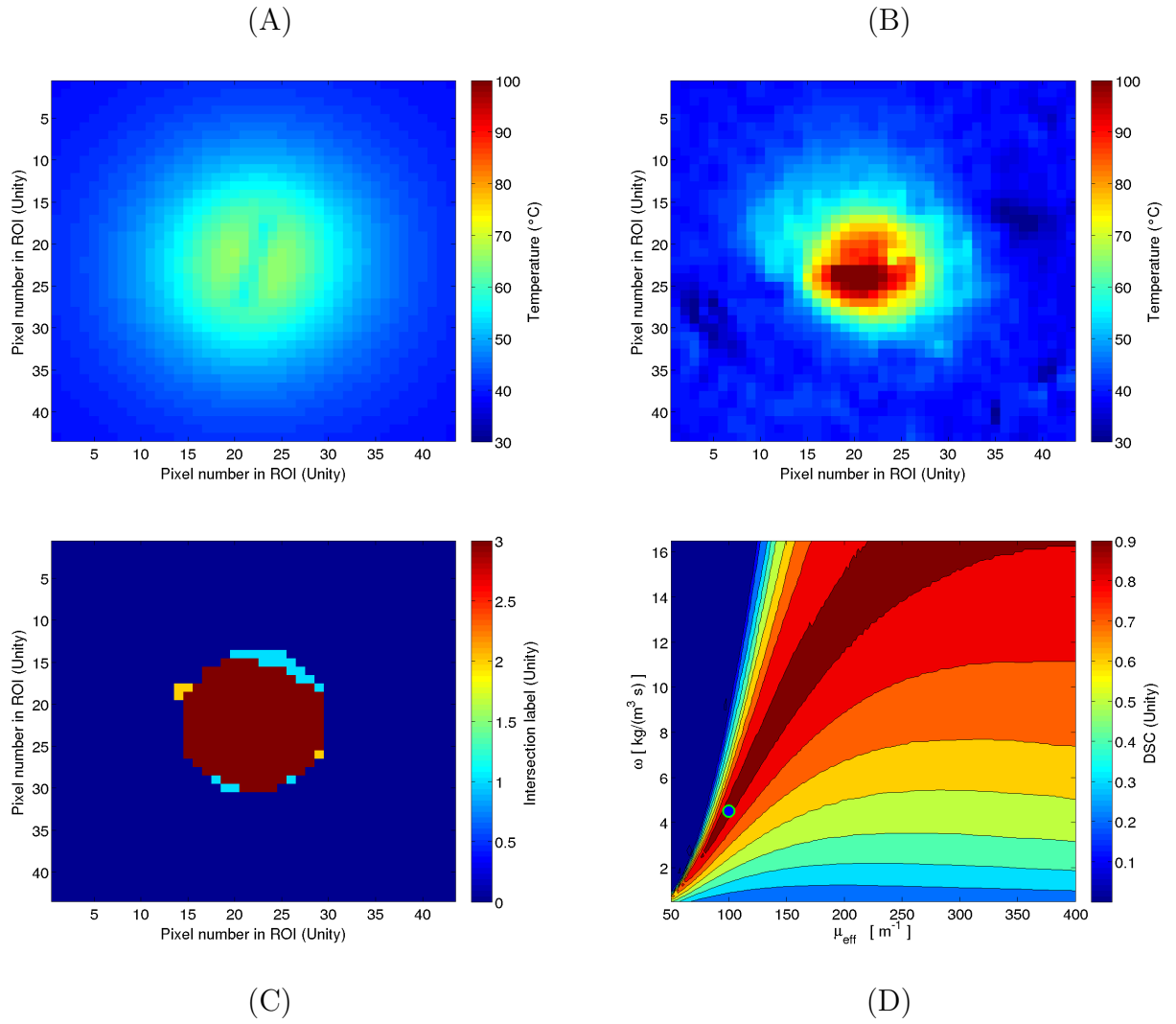


Figure A.26: MRTI #0453 FOV: 39.354 mm \times 39.354 mm. Maximum DSC in optimization: 0.94763.

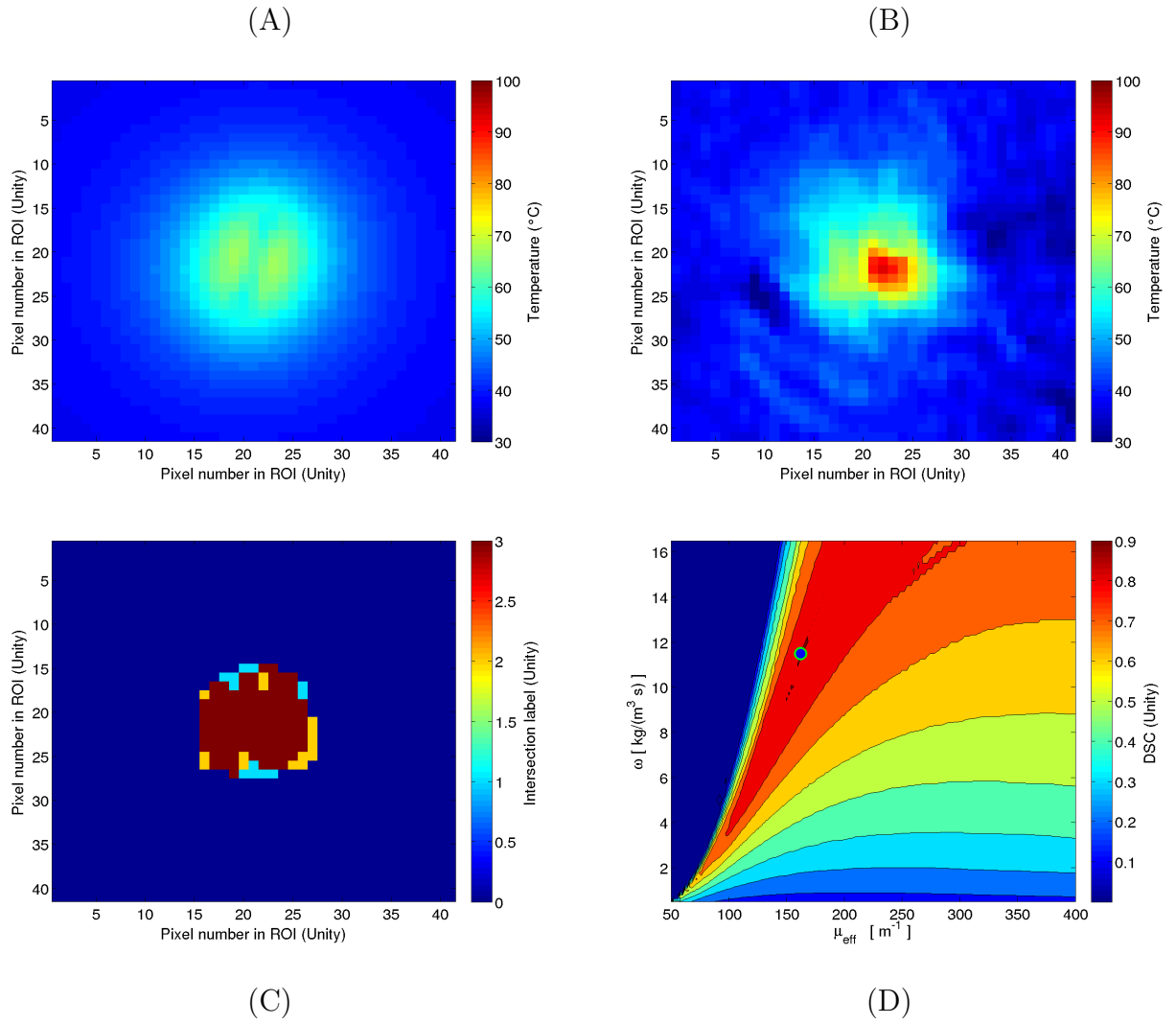


Figure A.27: MRTI #0450 FOV: 37.480 mm \times 37.480 mm. Maximum DSC in optimization: 0.90377.

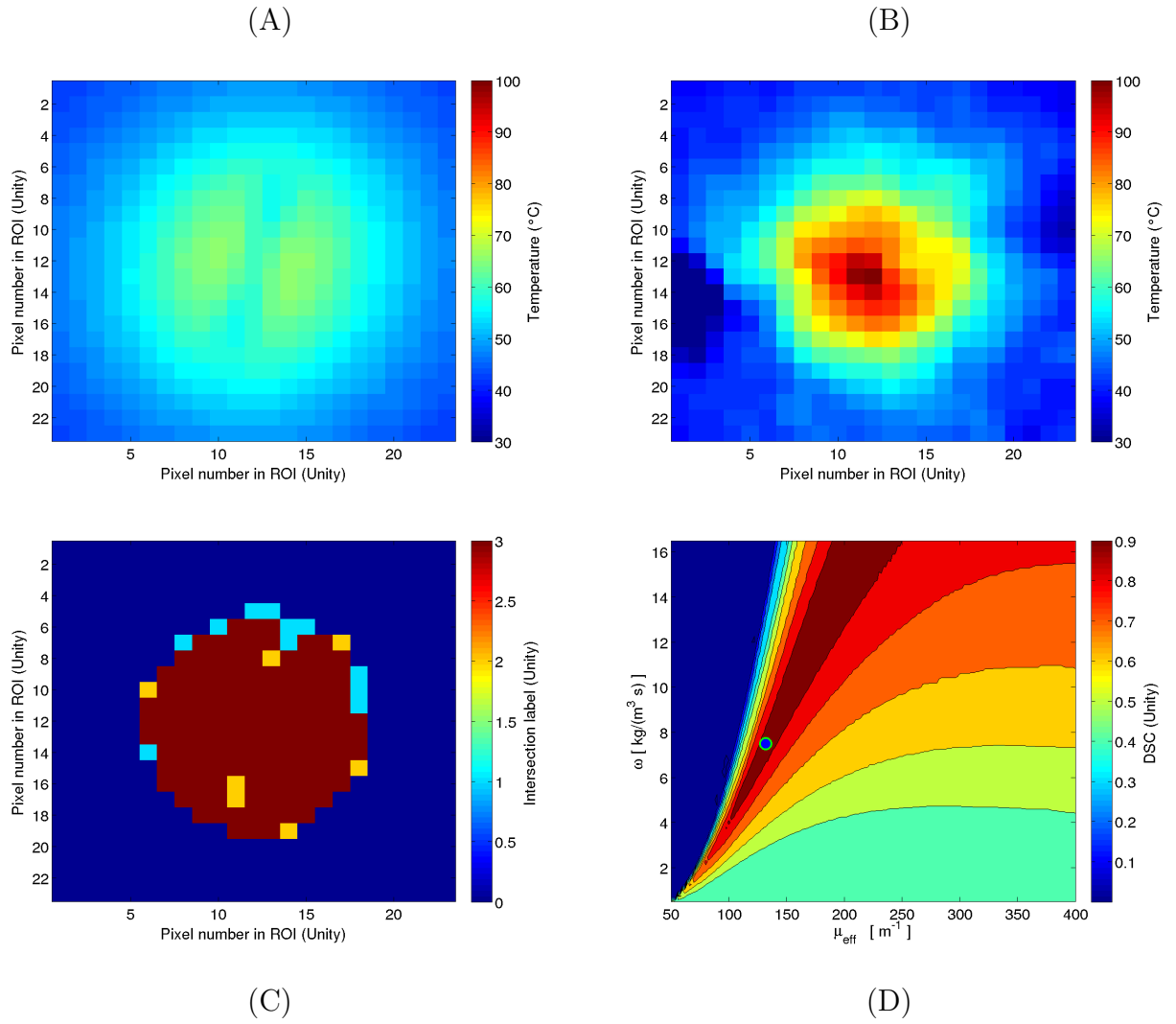


Figure A.28: MRTI #0451 FOV: 20.614 mm \times 20.614 mm. Maximum DSC in optimization: 0.95307.

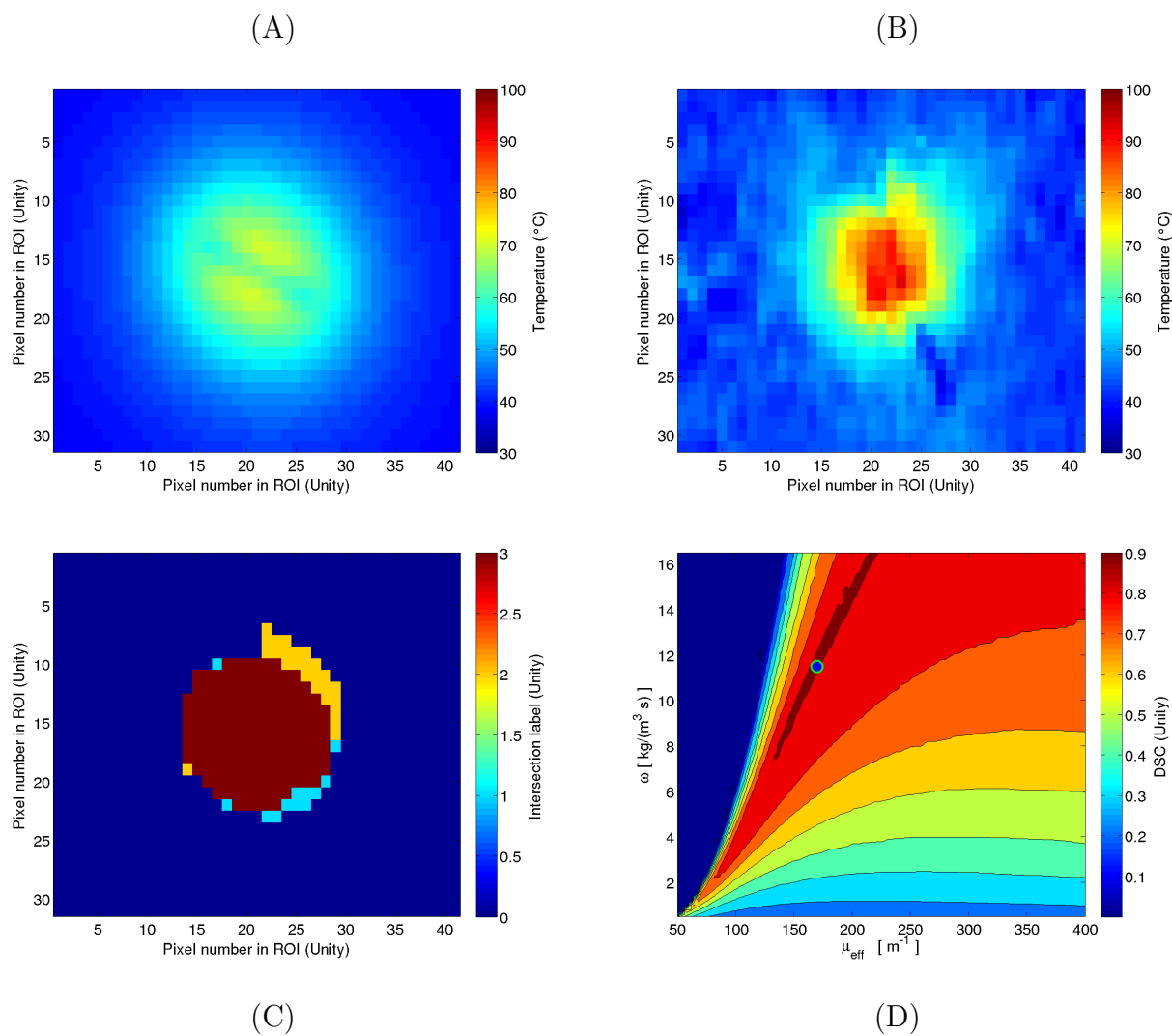


Figure A.29: MRTI #0418 FOV: 34.360 mm \times 25.770 mm. Maximum DSC in optimization: 0.91066.

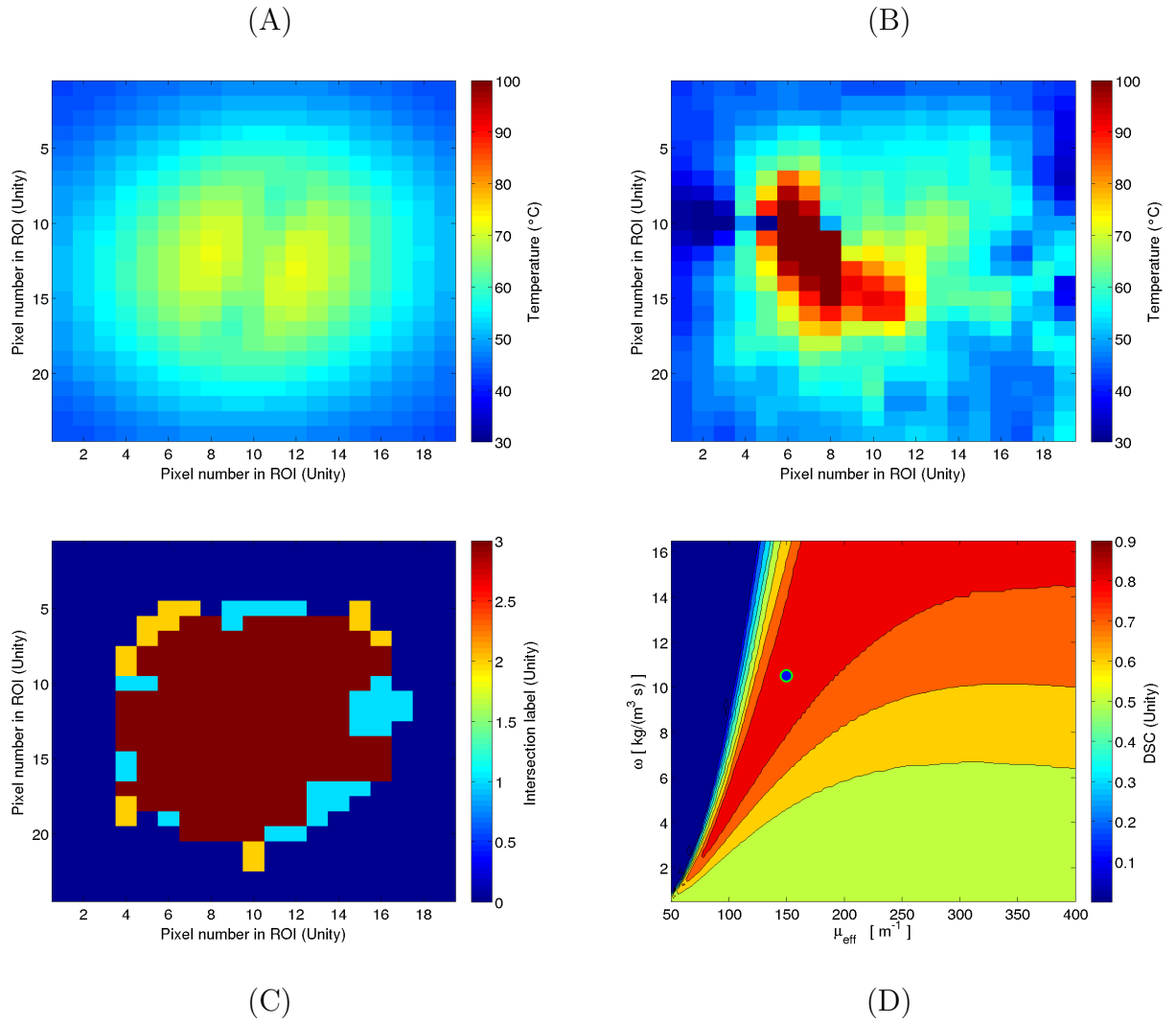


Figure A.30: MRTI #0414 FOV: 16.866 mm \times 21.551 mm. Maximum DSC in optimization: 0.88095.

Appendix B: Additional results for Chapter 5

This Appendix shows additional results from Chapter 5 regarding the convergence of the [steady state model \(SSM\)](#) kernel with increasing M source points, the power linearity of the SSM kernel, and the secondary objective functions (L_2 and Hausdorff distance).

The primary objective function for the SSM with global optimization is the DSC between the SSM’s predicted 57°C isotherm and the MRTI’s Arrhenius dose ≥ 1 using Henriques and Moritz’ dose model parameters. The secondary objective function is similar to the first: the DSC between the SSM’s predicted 57°C isotherm and the MRTI’s 57°C isotherm. The primary and secondary objective functions are shown in Appendix A on an individual optimization basis, as opposed to a global optimization.

Besides the two previous and highly related objective functions, there are two more objective functions available for consideration. The first is the L_2 norm between the two temperature fields — i.e., the MRTI compared to the SSM prediction. The second is the Hausdorff distance [249]:

$$d_H(A, B) = \max \left\{ \sup_{a \in A} \inf_{b \in B} d(a, b), \sup_{b \in B} \inf_{a \in A} d(a, b) \right\}.$$

$d_H(A, B)$ is the Hausdorff distance between regions A and B ; A and B have the same definitions as in the DSC definition. “inf” is the infimum and “sup” is the supremum of set theory. a is a pixel from the set A , and b is a pixel from the set B . $d(a, b)$ is then the Euclidean distance between a pixel from set A , and a pixel from set B .

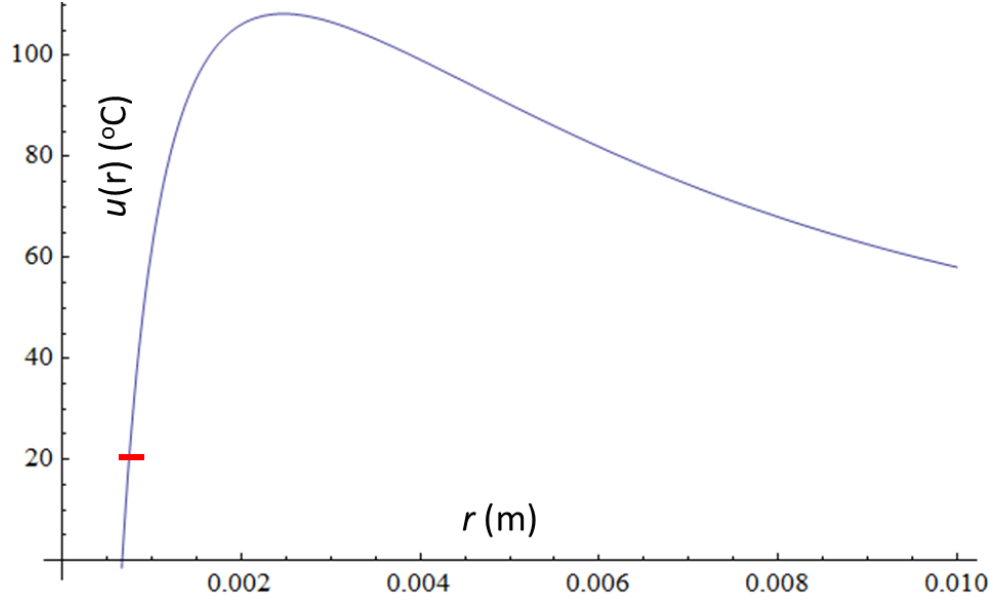


Figure B.1: This is a one-dimensional temperature field from a single isotropic point source, as calculated with Equation (5.4). The constitutive values are from Table 5.1 with $\mu_{eff} = 200 \text{ m}^{-1}$, $\omega = 6.0 \text{ kg m}^{-3} \text{ s}^{-1}$, and $P = 12 \text{ W}$. The red hash mark is the $r_1 = 0.00075 \text{ m}$ boundary for the cooling fiber where $u(r_1) = u_0 = 21^\circ\text{C}$. As r increases, the temperature, $u(r)$, builds up to the peak and falls back to $u(r_2) = u_a = 37^\circ\text{C}$. In the case of M number of isotropic point sources, the power is divided among the M points evenly as discussed earlier.

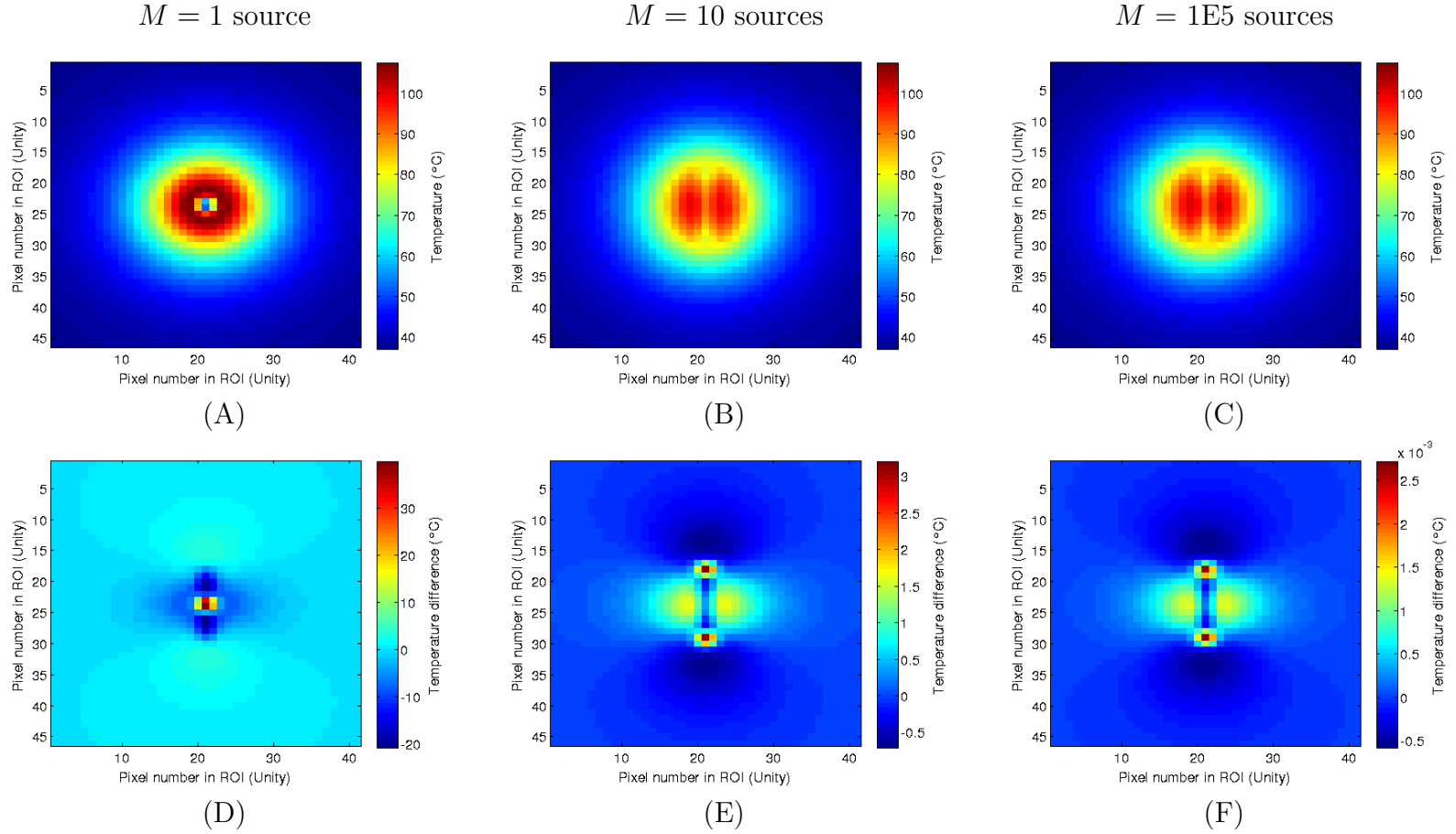


Figure B.2: These figures demonstrate of increasing M sources to approximate a line source. The top row are the temperature fields from simulations using $M = 1$, $M = 10$, and $M = 1E5$ sources; $M = 1E5$ sources is assumed to perfectly approximate a line source. The bottom row shows the difference in temperature fields generated by $M = 1E5$ and $M = 1$, $M = 10$, and $M = 1E4$ sources. Notice that with as little as $M = 10$ sources, the shape of the temperature maps appear to emulate the $M = 1E5$ temperature map. However, the second row shows pixel-wise differences varying from $\sim -0.5^\circ\text{C}$ to $\sim +3^\circ\text{C}$ for $M = 10$, whereas the $M = 1E4$ case variance is about 1/1000th versus $M = 10$.

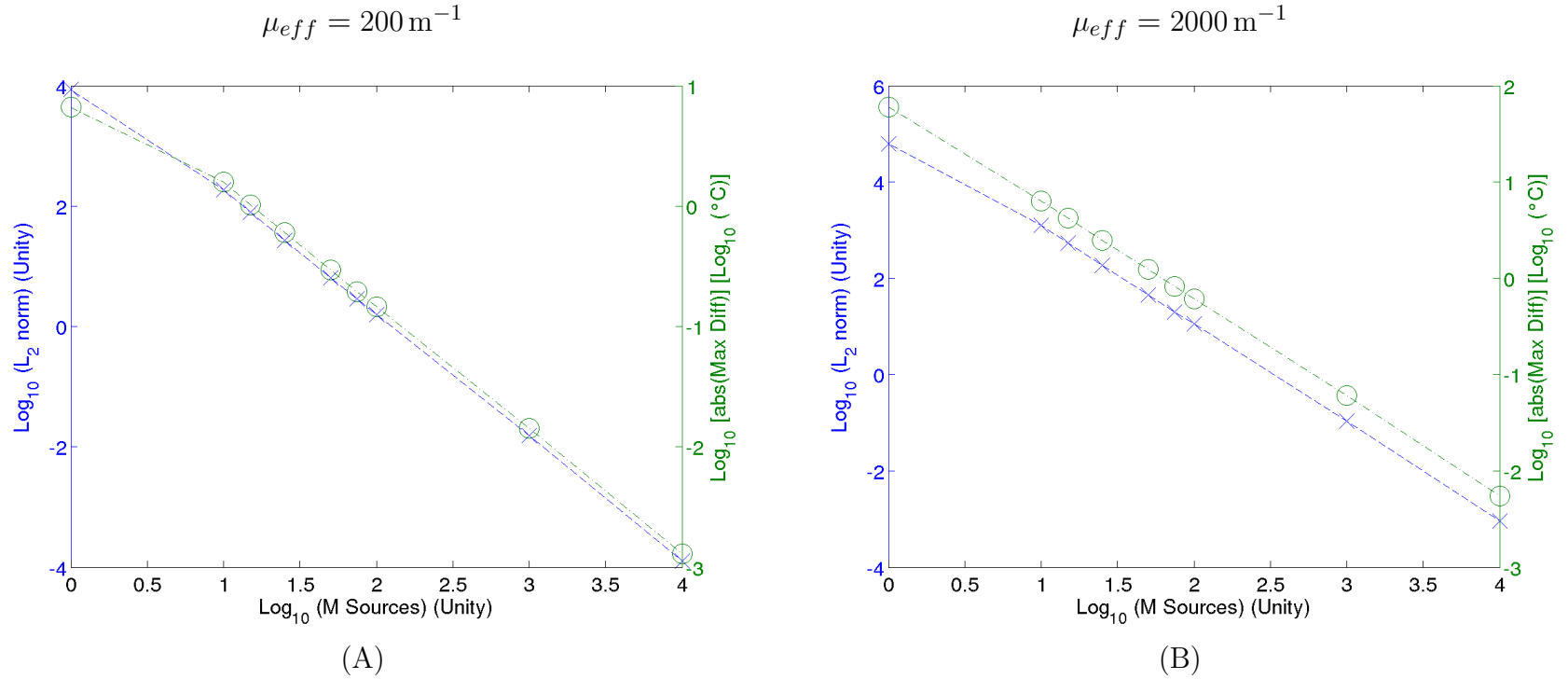


Figure B.3: The two plots demonstrate the convergence from increasing the number of isotropic source points by comparing $M = 1E5$ and $M = [1, 10, 15, 25, 50, 75, 100, 1E3, 1E4]$. All simulations use $\omega = 6.0 \text{ kg m}^{-3} \text{ s}^{-1}$ and Table 5.1 values. (A) uses $\mu_{eff} = 200 \text{ m}^{-1}$ while (B) uses $\mu_{eff} = 2000 \text{ m}^{-1}$. The horizontal axis is the number of source points, M . The left vertical axis is the $\text{log}_{10}(L_2)$, a metric sensitive to the entire temperature fields being compared. The right vertical axis is the $\max \{\text{log}_{10} (|u_{M=1E5} - u_{M_2}|)\}$, which is a surrogate of the maximum pixel-wise difference.

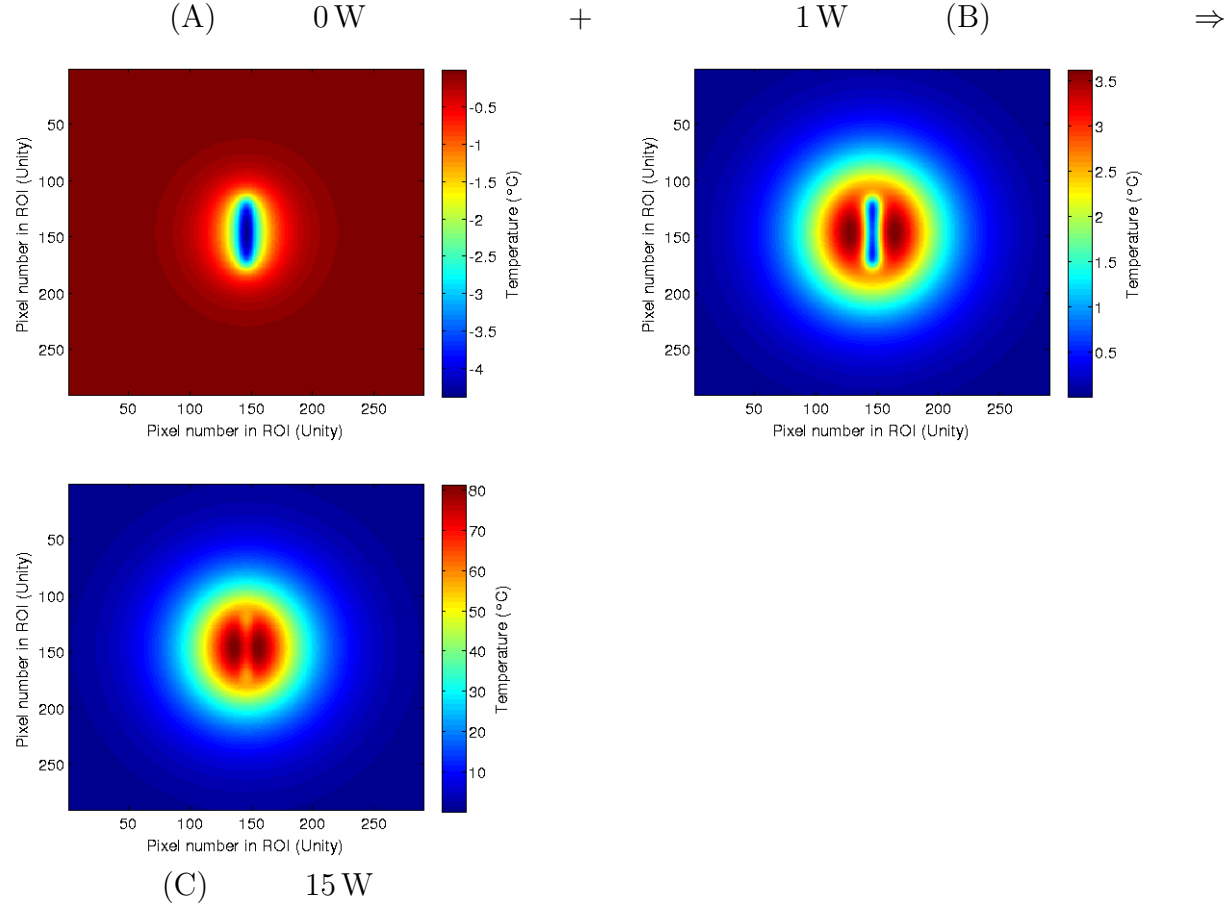


Figure B.4: The figures demonstrate the property of power linearity for the SSM kernel using Equation (5.6). The top row show 2D temperature fields from 0 W and 1 W power settings. The bottom figure is the linear combination of the top two figures to generate a 15 W temperature field. Compared to a temperature field generated by directly using $P = 15$ W, the L_2 norm is $1.2578\text{E-}3$ and the maximum pixel-wise difference is $1.8495\text{E-}5$ °C. For the temperature scale of all three subfigures, 0 °C on the scale is set to body temperature, or 37 °C.

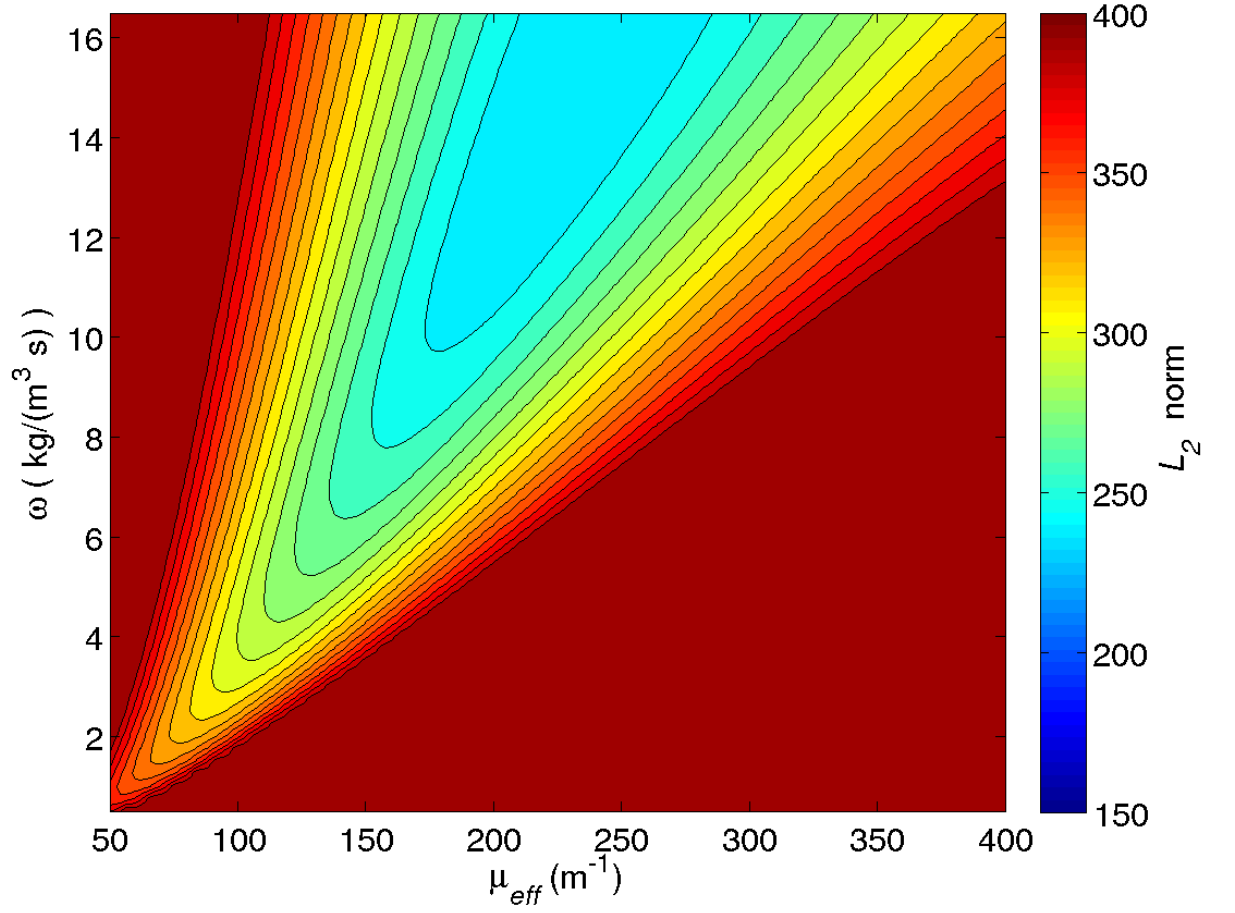


Figure B.5: For the $N = 22$ cohort, this Figure displays the mean map of the 2D regular grid optimization with respect to L_2 . The general shape of the optimal region — i.e., the minimal region of L_2 — is very similar to the DSC mean and median maps of Figures 5.2(A) and (B). However, the optimal regions of this L_2 is not coincident with the optimal DSC regions.

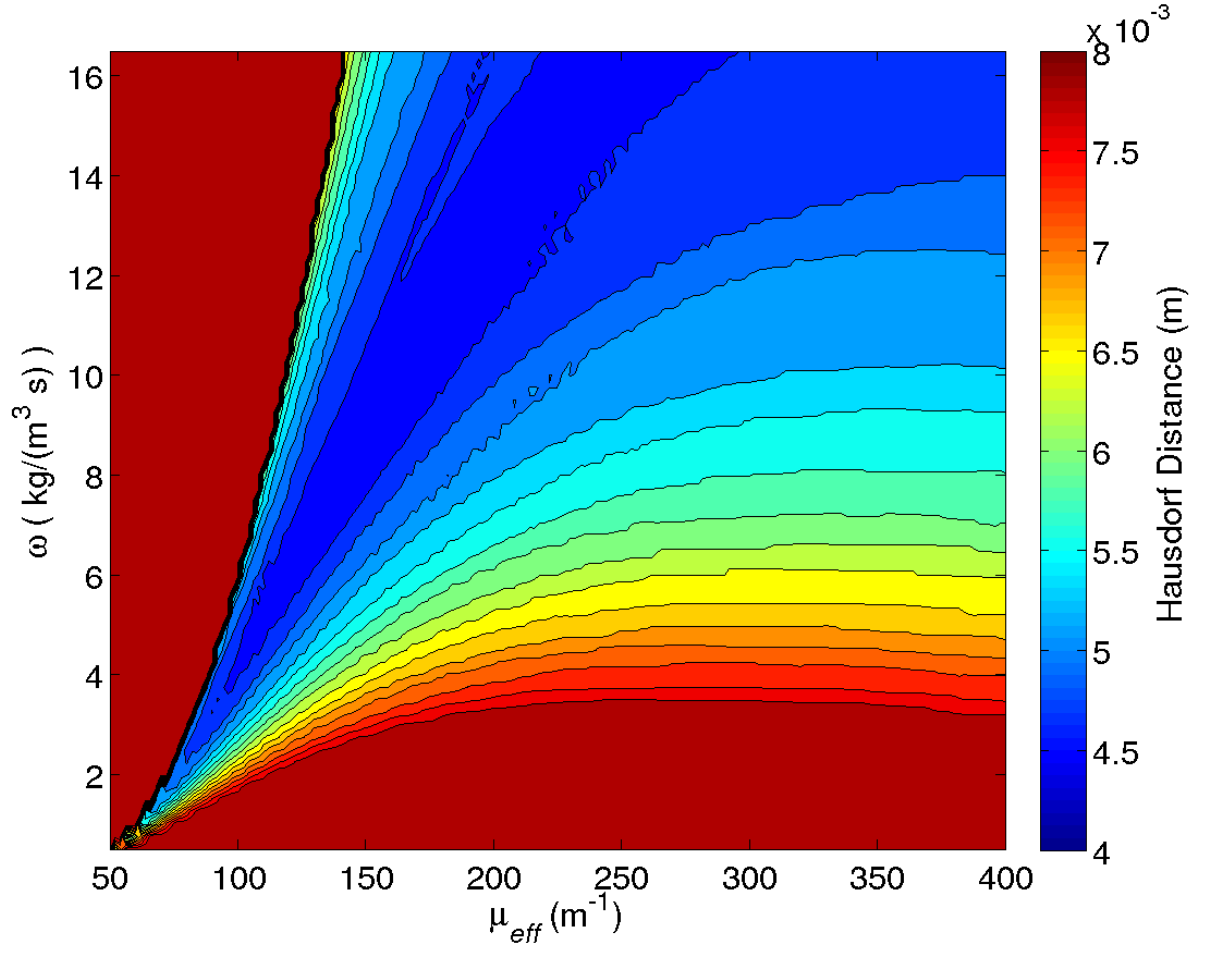


Figure B.6: For the $N = 22$ cohort, this Figure displays the mean map of the 2D regular grid optimization with respect to Hausdorff distance. The general shape of the optimal region — i.e., the minimal region of Hausdorff distance — is very similar to the DSC mean and median maps of Figures 5.2(A) and (B). Here, the optimal region of Hausdorff distance is coincident with the optimal DSC regions.

Appendix C: Alternate patient cohort and validation results

This Appendix is a method redux of Chapter 5’s [steady state model \(SSM\)](#). Namely, the unique contribution is to create a cohort that is best suited to the SSM. The primary distinction between this Appendix’s cohort and the $N = 22$ cohort used in Chapters 4 and 5 is that the included datasets reach, or very nearly reach, steady state.

Within the entire dissertation, there are two analyzed cohorts of patient datasets. Both groups are selected from an available list of 30 datasets. Of those 30, eight were excluded for the work in Chapters 4 and 5 [67]; a cohort of $N = 22$. Since Fahrenholtz et al. 2015 entered production, the exclusion criteria has become better defined. In this Appendix, a third cohort of $N = 20$ are modeled and analyzed using the [steady state model \(SSM\)](#) and global optimization method described Chapter 5. The criteria for dataset exclusion in the $N = 20$ are the following, with the first being the most important:

1. Does not reach steady state

The training of the steady state model kernel strongly depends on the MRTI datasets reaching steady state or at least being near steady state.

2. Out of plane

If the long axis of the laser fiber is not in the MRTI imaging plane, the modeling assumption that the fiber is in plane is violated. With the MR data available, it is not possible to discern the precise azimuthal angle relative the MRTI imaging plane.

3. The ablation is small

If the ablation is very small, i.e., ~ 0.5 cm, with a laser power that should ablate a

considerably larger area, the MRTI dataset is not useful. This may occur because of exclusion criteria **1.** and **2.**

4. MRTI dataset is a test pulse

Before commencing the ablation in earnest, neurosurgeons check the laser’s position with a short test pulse — e.g., 4 W for 30 s. If a MRTI dataset is only a test pulse, it should be excluded.

5. MR artifact

If the MRTI dataset is severely obfuscated by image artifacts, it is not a useful dataset.

Table C.1 lists MRTI datasets that are excluded. Appendix A is an exhaustive listing of the MRTI datasets.

Table C.1: These ten datasets are excluded from the original 30 for reasons enumerated [above](#) in order to create the $N = 20$ cohort.

Hash #	<i>Exclusion criterion</i>
0497	1. Does not reach steady state
0409	2. Test pulse
0415	
0466	
0468	3. Small ablation size
0471	4. Misses plane
0476	
0447	4. Misses plane
0435	5. MR artifact
0440	

Comparison of optimization algorithms within LOOCV

The primary purpose of this Appendix is to present the results of the SSM in optimization and leave-one-out cross-validation (LOOCV) within a cohort more appropriate to the

Table C.2: This table lists datasets in the $N = 22$ cohort that there are included in Chapters 4 and 5 but excluded in Appendix C’s $N = 20$ cohort, and vice versa.

Hash#	Cohort
0415	
0435	Included in $N = 22$ cohort
0440	Excluded in $N = 20$ cohort
0447	
0436	Excluded in $N = 22$ cohort
0457	Included in $N = 20$ cohort

SSM. However, a second opportunity for the Appendix is to juxtapose the subtly different LOOCV algorithms — the first from Section 4.3.5 and the second from Section 5.2.6. A key idea of LOOCV is that the parameter information that produces the best predictive results in training should be used to predict the ‘left out’ dataset within each iteration.

To the author’s interpretation, the gold standard LOOCV algorithm seeks to optimize the mutual performance among all training datasets. Emphatically, the optimization algorithm should seek to optimize the mean response function among all training datasets within a given LOOCV iteration. In Chapter 4’s methods, computational expenses render impractical the gold standard implementation of the LOOCV algorithm. Instead, Chapter 4’s method optimizes each dataset individually and averages the individually optimal parameters in order to predict the ‘left out’ case.

It is worth expounding upon the particulars of the computational costs associated with executing the gold standard LOOCV algorithm while using an optimization algorithm that minimizes a response/objective function. Firstly, the optimization algorithm’s objective function is an average of all training datasets. This requires the input parameter to be submitted to each training dataset to complete one iteration of the optimization. The optimization would then iterate and minimize the objective function. In Chapter 4’s case, the gradient-based optimization would submit a μ_{eff} value to 21 datasets and iterate to minimize the L_2 norm. Once minimization is complete, the optimal parameter value is tested on the ‘left out’ dataset, thus ending a single LOOCV iteration. The entire LOOCV

algorithm for Chapter 4 requires 22 LOOCV iterations with each iteration simultaneously optimizing 21 datasets. The second difficulty is that if ever the cohort is modified, the entire optimization must be repeated. In summary, in order to execute the gold standard LOOCV algorithm while using an optimization algorithm that minimizes an objective function, the resulting LOOCV algorithm is expensive in computational cost and inflexible regarding cohort modification. Chapter 4’s solution to this conundrum is to not execute the gold standard LOOCV and optimize individual datasets separately as a surrogate.

In Chapter 5, the result of global optimization is a vector map that represents an exhaustive list of every $\omega-\mu_{eff}$ pair and the resulting response function. Using the vector map, it is extremely simple to identify the input $\omega-\mu_{eff}$ that creates the optimal response function — see Section 5.2.6 for details. Chapter 5’s LOOCV method is able to relatively easily satisfy the ideal LOOCV algorithm. Furthermore, the vector map method can easily handle modifications to the cohort.

In order to investigate the difference between the gold standard LOOCV algorithm of Chapter 5 and the surrogate LOOCV algorithm of Chapter 4, this Appendix compares the two methods in Table C.5. The result is that the methods are very similar. It also suggests — but certainly does not guarantee — that using the surrogate LOOCV method with the FEM model is a close approximation of the gold standard LOOCV algorithm.

Table C.3: Here are the descriptive statistics for DSC performance during optimization and LOOCV for $N = 20$ datasets. Steady state analysis using the 57 °C isotherm damage model is denoted SS. “opt.” refers to optimization during the regular grid search; “Naïve” refers to the performance using literature values. Note that all DSC, skewness, and kurtosis quantities are unitless. “%-ile” refers to percentiles. E.g., 25%-ile means the dataset’s DSC performance exceeds 25% of the population DSC values in ascending ranked order.

Descriptive Statistic	SS DSC opt.	SS DSC LOOCV	Naïve choice
Minimum	0.74713	0.58552	0.45455
25%-ile	0.86899	0.77255	0.6068
Median	0.89973	0.85023	0.65639
75%-ile	0.91257	0.88146	0.76864
Maximum	0.95307	0.93007	0.85749
DSC ≥ 0.7	20	19	8
Mean	0.88889	0.82359	0.66848
Standard Deviation	0.04680	0.088955	0.11479
Skewness	-1.3368	-1.0174	-0.23154
Kurtosis	5.3510	3.634	2.2655

Table C.4: These percentiles correspond to several interesting DSC thresholds using the $N = 20$ cohort. The “opt.” and “LOOCV” and “Naïve” columns refer to the same datasets described in Table C.3. The smaller the percentile value, the better the model’s performance. ‘0’ indicates all values pass at the given threshold; ‘100’ indicates no values pass.

DSC threshold (Unity)	SS DSC opt. (%-ile)	SS DSC LOOCV (%-ile)	Naïve choice (%-ile)
0.5	0	0	10.794
0.6	0	3.0939	23.351
0.7	0	6.6574	59.445
0.8	5.9200	35.067	89.333
0.85	13.314	51.541	95.934
0.9	50.513	81.819	100
0.95	94.678	100	100
0.975	100	100	100

Table C.5: The table compares the two LOOCV algorithms in the $N = 20$ cohort, described [earlier](#). The “Parameter average” column refers to the LOOCV algorithm used with the FEM model; meanwhile, the “Vector map” column is the LOOCV algorithm outlined in Section 5.2.6. This Table’s “Vector map” column is also presented in Figure C.3 as the “SS DSC LOOCV”. Note that all DSC, skewness, and kurtosis quantities are unitless. “%-ile” refers to percentiles. E.g., 25%-ile means the dataset’s DSC performance exceeds 25% of the population DSC values in ascending ranked order.

Descriptive Statistic	Parameter average	Vector map
Minimum	0.6006	0.5855
25%-ile	0.7612	0.7726
Median	0.8230	0.8502
75%-ile	0.8787	0.8815
Maximum	0.9113	0.9395
DSC ≥ 0.7	17	19
Mean	0.8059	0.8236
Standard Deviation	0.0893	0.08896
Skewness	-0.9101	-1.017
Kurtosis	2.843	3.634

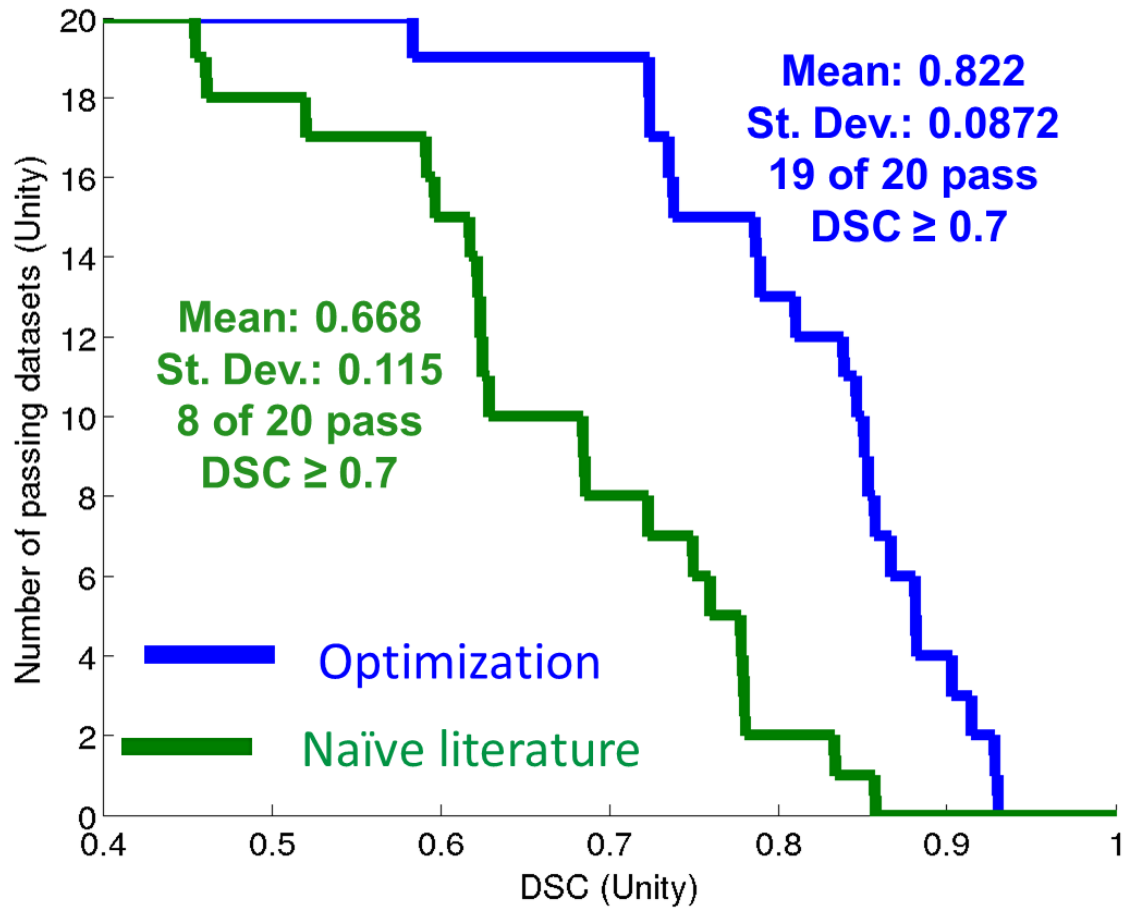


Figure C.1: For the $N = 20$ cohort, this Figure displays the simulated predictive performance of the regular grid optimization (in blue) versus a naïve literature value parameter choice (in green). A greater the area-under-the-curve (AUC), which is synonymous with the mean performance, indicates better performance.

Bibliography

- [1] Gellermann J, Hildebrandt B, Issels R, Ganter H, Wlodarczyk W, Budach V, Felix R, Tunn PU, Reichardt P, Wust P. Noninvasive magnetic resonance thermography of soft tissue sarcomas during regional hyperthermia. *Cancer*. 2006 Sep;107(6):1373–1382.
- [2] Gellermann J, Wlodarczyk W, Feussner A, Föhling H, Nadobny J, Hildebrandt B, Felix R, Wust P. Methods and potentials of magnetic resonance imaging for monitoring radiofrequency hyperthermia in a hybrid system. *International Journal of Hyperthermia*. 2005 Jan;21(6):497–513.
- [3] Al-Bataineh O, Jenne J, Huber P. Clinical and future applications of high intensity focused ultrasound in cancer. *Cancer Treatment Reviews*. 2012 Aug;38(5):346–353.
- [4] Prakash P, Diederich CJ. Considerations for theoretical modelling of thermal ablation with catheter-based ultrasonic sources: implications for treatment planning, monitoring and control. *International Journal of Hyperthermia*. 2012 Feb;28(1):69–86.
- [5] Salgaonkar VA, Diederich CJ. Catheter-based ultrasound technology for image-guided thermal therapy: current technology and applications. *International Journal of Hyperthermia*. 2015 Mar;31(2):203–215.
- [6] Ahmed M, Brace CL, Lee FT, Goldberg SN. Principles of and advances in percutaneous ablation. *Radiology*. 2011 Feb;258(2):351–369.
- [7] Lin SM, Lin CJ, Lin CC, Hsu CW, Chen YC. Radiofrequency ablation improves prognosis compared with ethanol injection for hepatocellular carcinoma 4 cm. *Gastroenterology*. 2004 Dec;127(6):1714–1723.

- [8] Habash RWY, Bansal R, Krewski D, Hafi T. Thermal therapy, part III: ablation. *Biomedical Engineering Online*. 2007;35:37–121.
- [9] Dice LR. Measures of the amount of ecologic association between species. *Ecological Society of America*. 1945;26(3):297–302.
- [10] Burns PB, Rohrich RJ, Chung KC. The levels of evidence and their role in evidence-based medicine. *Plastic and Reconstructive Surgery*. 2011 Jul;128(1):305–310.
- [11] Usman M, Moore W, Talati R, Watkins K, Bilfinger TV. Irreversible electroporation of lung neoplasm: a case series. *Medical Science Monitor*. 2012 Jun;18(6):CS43–CS47.
- [12] Deipolyi AR, Golberg A, Yarmush ML, Arellano RS, Oklu R. Irreversible electroporation: the evolution of a laboratory technique to be used in interventional oncology. *Diagnostic and Interventional Radiology*. 2014 Jan;20:147–154.
- [13] Sapareto SA, Hopwood LE, Dewey WC, Raju MR, Gray JW. Effects of hyperthermia on survival and progression of chinese hamster ovary cells. *Cancer Research*. 1978 Feb;38(2):393–400.
- [14] McDannold N. Quantitative MRI-based temperature mapping based on the proton resonant frequency shift: Review of validation studies. *International Journal of Hyperthermia*. 2005 Jan;21(6):533–546.
- [15] Rieke V, Butts Pauly K. MR thermometry. *Journal of Magnetic Resonance Imaging*. 2008 Feb;27(2):376–390.
- [16] McWilliams B, Schnell E, Curto S, Fahrbach T, Prakash P. A directional interstitial antenna for microwave tissue ablation: theoretical and experimental investigation. *IEEE Transactions on Biomedical Engineering*. 2015 Mar;.
- [17] Lauterbur PC. Image formation by induced local interactions: examples employing nuclear magnetic resonance. *Nature*. 1973 Mar;242(5394):190–191.

- [18] Mansfield P, Grannell PK. NMR ‘diffraction’ in solids? *Journal of Physics C: Solid State Physics*. 1973 Nov;6(22):L422.
- [19] Kumar A, Welte D, Ernst RR. NMR Fourier zeugmatography. *Journal of Magnetic Resonance*. 1975 Dec;18:69–83.
- [20] Hahn EL. Spin Echoes. *Physical Review*. 1950 Nov;80(4):580–594.
- [21] Hindman JC. Proton resonance shift of water in the gas and liquid states. *The Journal of Chemical Physics*. 1966 Jun;44(12):4582–4592.
- [22] Andrews DW, Scott CB, Sperduto PW, Flanders AE, Gaspar LE, Schell MC, Werner-Wasik M, Demas W, Ryu J, Bahary JP, Souhami L, Rotman M, Mehta MP, Curran WJ. Whole brain radiation therapy with or without stereotactic radiosurgery boost for patients with one to three brain metastases: phase III results of the RTOG 9508 randomised trial. *Lancet*. 2004 May;363(9422):1665–72.
- [23] Hart MG, Garside R, Rogers G, Stein K, Grant R. Temozolomide for high grade glioma. *Cochrane Database of Systematic Reviews*. 2015;(4).
- [24] Eichler AF, Chung E, Kodack DP, Loeffler JS, Fukumura D, Jain RK. The biology of brain metastases—translation to new therapies. *Nature Reviews: Clinical Oncology*. 2011 Jun;8(6):344–56.
- [25] Torchia MG, Tyc R, Pacak JS, McTaggart KJ. Hyperthermia treatment and probe therefor; 2008.
- [26] Cressman ENK, Geeslin MG, Shenoi MM, Hennings LJ, Zhang Y, Iaizzo PA, Bischof JC. Concentration and volume effects in thermochemical ablation in vivo: Results in a porcine model. *International Journal of Hyperthermia*. 2012 Feb;28(2):113–121.
- [27] Eichler AF, Loeffler JS. Multidisciplinary management of brain metastases. *The Oncologist*. 2007 Jul;12(7):884–98.

- [28] Nussbaum ES, Djalilian HR, Cho KH, Hall Wa. Brain metastases: histology, multiplicity, surgery, and survival. *Cancer*. 1996 Oct;78(8):1781–8.
- [29] Hall Wa, Djalilian HR, Nussbaum ES, Cho KH. Long-term survival with metastatic cancer to the brain. *Medical Oncology*. 2000 Nov;17(4):279–86.
- [30] Patchell RA. The management of brain metastases. *Cancer Treatment Reviews*. 2003 Dec;29(6):533–540.
- [31] Siegel RL, Miller KD, Jemal A. Cancer statistics, 2015. *CA: A Cancer Journal for Clinicians*. 2015 Jan;65(1):5–29.
- [32] Louis DN, Ohgaki H, Wiestler OD, Cavenee WK, Burger PC, Jouvet A, Scheithauer BW, Kleihues P. The 2007 WHO Classification of Tumours of the Central Nervous System. *Acta Neuropathologica*. 2007 Aug;114(2):97–109.
- [33] Sathornsumetee S, Rich JN, Reardon DA. Diagnosis and treatment of high-grade astrocytoma. *Neurologic Clinics*. 2007 Nov;25(4):1111–1139.
- [34] Wen PY, Kesari S. Malignant gliomas in adults. *New England Journal of Medicine*. 2008 Jul;359(5):492–507.
- [35] Owonikoko TK, Arbiser J, Zelnak A, Shu HKG, Shim H, Robin AM, Kalkanis SN, Whitsett TG, Salhia B, Tran NL, Ryken T, Moore MK, Egan KM, Olson JJ. Current approaches to the treatment of metastatic brain tumours. *Nature Reviews: Clinical Oncology*. 2014 Feb;11(4):203–222.
- [36] Patel TR, McHugh BJ, Bi WL, Minja FJ, Knisely JPS, Chiang VL. A comprehensive review of MR imaging changes following radiosurgery to 500 brain metastases. *American Journal of Neuroradiology*. 2011 Nov;32(10):1885–1892.

- [37] Curry DJ, Gowda A, McNichols RJ, Wilfong AA. MR-guided stereotactic laser ablation of epileptogenic foci in children. *Epilepsy & Behavior*. 2012 Aug;24(4):408–14.
- [38] Wilfong AA, Curry DJ. Hypothalamic hamartomas: Optimal approach to clinical evaluation and diagnosis. *Epilepsia*. 2013 Dec;54:109–114.
- [39] Tovar-Spinoza Z, Carter D, Ferrone D, Eksioglu Y, Huckins S. The use of MRI-guided laser-induced thermal ablation for epilepsy. *Child's Nervous System*. 2013 Jun;29(11):2089–2094.
- [40] Gonzalez-Martinez J, Vadera S, Mullin J, Enatsu R, Alexopoulos AV, Patwardhan R, Bingaman W, Najm I. Robot-assisted stereotactic laser ablation in medically intractable epilepsy: operative technique. *Neurosurgery*. 2014 Jun;10 Suppl 2(2):167–72; discussion 172–3.
- [41] Esquenazi Y, Kalamangalam GP, Slater JD, Knowlton RC, Friedman E, Morris SA, Shetty A, Gowda A, Tandon N. Stereotactic laser ablation of epileptogenic periventricular nodular heterotopia. *Epilepsy Research*. 2014 Mar;108(3):547–554.
- [42] Willie JT, Laxpati NG, Drane DL, Gowda A, Appin C, Hao C, Brat DJ, Helmers SL, Saindane A, Nour SG, Gross RE. Real-time magnetic resonance-guided stereotactic laser amygdalohippocampotomy for mesial temporal lobe epilepsy. *Neurosurgery*. 2014 Jun;74(6):569–585.
- [43] Nowell M, Miserocchi A, McEvoy AW, Duncan JS. Advances in epilepsy surgery. *Journal of Neurology, Neurosurgery, and Psychiatry*. 2014 Nov;85(11):1273–1279.
- [44] Attiah MA, Paulo DL, Danish SF, Stein SC, Mani R. Anterior temporal lobectomy compared with laser thermal hippocampectomy for mesial temporal epilepsy: a threshold analysis study. *Epilepsy Research*. 2015;.

- [45] Lewis EC, Weil AG, Duchowny M, Bhatia S, Ragheb J, Miller I. MR-guided laser interstitial thermal therapy for pediatric drug-resistant lesional epilepsy. *Epilepsia*. 2015 Aug;.
- [46] Ngugi AK, Kariuki SM, Bottomley C, Kleinschmidt I, Sander JW, Newton CR. Incidence of epilepsy. *Neurology*. 2011 Sep;77(10):1005–1012.
- [47] Brodie MJ, Shorvon SD, Canger R, Halász P, Johannessen S, Thompson P, Wieser HG, Wolf P. Commission on European Affairs: appropriate standards of epilepsy care across Europe. *Epilepsia*. 1997 Nov;38(11):1245–1250.
- [48] Kwan P, Brodie MJ. Early identification of refractory epilepsy. *The New England Journal of Medicine*. 2000 Feb;342(5):314–319.
- [49] Téllez-Zenteno JF, Dhar R, Wiebe S. Long-term seizure outcomes following epilepsy surgery: a systematic review and meta-analysis. *Brain*. 2005 May;128(5):1188–1198.
- [50] Widjaja E, Li B, Schinkel CD, Ritchie LP, Weaver J, Snead OC, Rutka JT, Coyte PC. Cost-effectiveness of pediatric epilepsy surgery compared to medical treatment in children with intractable epilepsy. *Epilepsy Research*. 2011 Mar;94(1-2):61–68.
- [51] Kerr MP, Mensah S, Besag F, de Toffol B, Ettinger A, Kanemoto K, Kanner A, Kemp S, Krishnamoorthy E, LaFrance Jr WC, Mula M, Schmitz B, van Elst LT, Trollor J, Wilson SJ. International consensus clinical practice statements for the treatment of neuropsychiatric conditions associated with epilepsy. *Epilepsia*. 2011 Nov;52(11):2133–2138.
- [52] Kirsch HE, Walker JA, Winstanley FS, Hendrickson R, Wong STC, Barbaro NM, Laxer KD, Garcia PA. Limitations of Wada memory asymmetry as a predictor of outcomes after temporal lobectomy. *Neurology*. 2005 Sep;65(5):676–680.

- [53] Webb H, Lubner MG, Hinshaw JL. Thermal ablation. *Seminars in Roentgenology*. 2011 Apr;46(2):133–141.
- [54] Sherman J, Hoes K, Marcus J, Komotar R, Brennan C, Gutin P. Neurosurgery for brain tumors: update on recent technical advances. *Current Neurology and Neuroscience Reports*. 2011 Jun;11(3):313–319.
- [55] Carpentier A, Chauvet D, Reina V, Beccaria K, Leclercq D, McNichols RJ, Gowda A, Cornu P, Delattre JY. MR-guided laser-induced thermal therapy (LITT) for recurrent glioblastomas. *Lasers in Surgery and Medicine*. 2012 Jul;44(5):361–368.
- [56] Roggan A, Ritz JP, Knappe V, Germer CT, Isbert C, Schädel D, Müller G. Radiation planning for thermal laser treatment. *Medical Laser Application*. 2001;16(2):65–72.
- [57] Feng Y, Fuentes D. Model-based planning and real-time predictive control for laser-induced thermal therapy. *International Journal of Hyperthermia*. 2011 Jan;27(8):751–61.
- [58] Jacques SL. Optical properties of biological tissues: a review. *Physics in Medicine and Biology*. 2013 Jun;58(11):R37.
- [59] Fahrenholtz SJ, Stafford RJ, Maier F, Hazle JD, Fuentes D. Generalised polynomial chaos-based uncertainty quantification for planning MRgLITT procedures. *International Journal of Hyperthermia*. 2013 Jun;29(4):324–35.
- [60] Kim BM, Jacques SL, Rastegar S, Thomsen S, Motamedi M. Nonlinear finite-element analysis of the role of dynamic changes in blood perfusion and optical properties in laser coagulation of tissue. *IEEE Journal of Selected Topics in Quantum Electronics*. 1996 Dec;2(4):922–933.
- [61] Schwarzmaier HJ, Yaroslavsky IV, Yaroslavsky AN, Fiedler V, Ulrich F, Kahn T. Treatment planning for MRI-guided laser-induced interstitial thermotherapy of brain

- tumors—the role of blood perfusion. *Journal of Magnetic Resonance Imaging*. 1998 Jan;8(1):121–127.
- [62] Mohammed Y, Verhey JF. A finite element method model to simulate laser interstitial thermo therapy in anatomical inhomogeneous regions. *Biomedical Engineering Online*. 2005 Jan;4(1):2.
- [63] Schutt DJ, Haemmerich D. Effects of variation in perfusion rates and of perfusion models in computational models of radio frequency tumor ablation. *Medical Physics*. 2008;35(8):3462–70.
- [64] Verhey JF, Mohammed Y, Ludwig A, Giese K. Implementation of a practical model for light and heat distribution using laser-induced thermotherapy near to a large vessel. *Physics in Medicine and Biology*. 2003 Nov;48(21):3595–610.
- [65] Fuentes D, Walker C, Elliott A, Shetty A, Hazle JD, Stafford RJ. Magnetic resonance temperature imaging validation of a bioheat transfer model for laser-induced thermal therapy. *International Journal of Hyperthermia*. 2011 Jan;27(5):453–64.
- [66] Oden T, Moser R, Ghattas O. Computer predictions with quantified uncertainty, part I. *SIAM News*. 2010;43(9):1–3.
- [67] Fahrenholtz SJ, Moon TY, Franco M, Medina D, Gowda A, Shetty A, Maier F, Hazle JD, Stafford RJ, Warburton T, Fuentes D. A model evaluation study for treatment planning of laser-induced thermal therapy thermal therapy. *International Journal of Hyperthermia*. 2015;31(7):705–14.
- [68] Horsman MR, Overgaard J. Hyperthermia: a potent enhancer of radiotherapy. *Clinical Oncology*. 2007 Aug;19(6):418–426.
- [69] Brested J. The Edwin Smith surgical papyrus. In: Licht S, editor. *Therapeutic Heat and Cold*. 2nd ed. Baltimore: Waverly Press; 1930. p. 196.

- [70] Overgaard J. History and heritage—an introduction. In: *Hyperthermic Oncology*. London: Taylor and Francis; 1985. p. 8–9.
- [71] Mattessich R. The oldest writings, and inventory tags of Egypt. *The Accounting Historians Journal*. 2002 Jun;29(1):195–208.
- [72] Storm F. Background, principles, and practice. In: Storm F, editor. *Hyperthermia in Cancer Therapy*. 1st ed. Boston: G.K. Hall; 1983. p. 8.
- [73] Nauts HC, Fowler GA, Bogatko FH. A review of the influence of bacterial infection and of bacterial products (Coley’s toxins) on malignant tumors in man; a critical analysis of 30 inoperable cases treated by Coley’s mixed toxins, in which diagnosis was confirmed by microscopic examination. *Acta Medica Scandinavica Supplementum*. 1953 Jan;276:1–103.
- [74] Thotathil Z, Jameson MB. Early experience with novel immunomodulators for cancer treatment. *Expert Opinion on Investigational Drugs*. 2007 Sep;16(9):1391–403.
- [75] Westermarck F. Über die behandlung des ulceration cervix-carcinoma. *Zentralbl Gynaekol*. 1898;22:1335.
- [76] Sapareto SA, Dewey WC. Thermal dose determination in cancer therapy. *International Journal of Radiation Oncology*Biology*Physics*. 1984 Apr;10(6):787–800.
- [77] Yarmolenko PS, Moon EJ, Landon C, Manzoor A, Hochman DW, Viglianti BL, Dewhirst MW. Thresholds for thermal damage to normal tissues: an update. *International Journal of Hyperthermia*. 2011 Jun;27(4):320–343.
- [78] Dewhirst MW, Viglianti BL, Lora-Michiels M, Hanson M, Hoopes PJ. Basic principles of thermal dosimetry and thermal thresholds for tissue damage from hyperthermia. *International Journal of Hyperthermia*. 2003;19(3):267–94.

- [79] Welch AJ, van Gemert MJC. *Optical-Thermal Response of Laser-Irradiated Tissue*. 2nd ed. New York, NY: Springer; 2010.
- [80] Diller KR, Valvano JW, Pearce JA. Bioheat transfer. In: Kreith F, editor. *The CRC Handbook of Thermal Engineering*. Boca Raton: CRC Press LLC; 2000. p. 4–114 to 4–215.
- [81] Pearce J. Mathematical models of laser-induced tissue thermal damage. *International Journal of Hyperthermia*. 2011 Dec;27(8):741–750.
- [82] Pearce JA. Comparative analysis of mathematical models of cell death and thermal damage processes. *International Journal of Hyperthermia*. 2013 Jun;29(4):262–280.
- [83] Dewey WC. Arrhenius relationships from the molecule and cell to the clinic. *International Journal of Hyperthermia*. 1994;10(4):457–483.
- [84] Lang J, Erdmann B, Seebass M. Impact of nonlinear heat transfer on temperature control in regional hyperthermia. *IEEE Transactions on Bio-Medical Engineering*. 1999 Sep;46(9):1129–38.
- [85] Cheng KS, Dewhirst MW, Stauffer PR, Das S. Effective learning strategies for real-time image-guided adaptive control of multiple-source hyperthermia applicators. *Medical Physics*. 2010;37(3):1285.
- [86] Westermann A, Mella O, Van Der Zee J, Jones EL, Van Der Steen-Banasik E, Koper P, Uitterhoeve ALJ, De Wit R, Van Der Velden J, Burger C, Schem BC, Van Der Wilt C, Dahl O, Prosnitz LR, Van Tinteren H. Long-term survival data of triple modality treatment of stage IIB/III/IVA cervical cancer with the combination of radiotherapy, chemotherapy and hyperthermia — an update. *International Journal of Hyperthermia*. 2012 Jul;28(6):549–553.

- [87] Rao W, Deng ZS, Liu J. A review of hyperthermia combined with radiotherapy/chemotherapy on malignant tumors. *Critical Reviews in Biomedical Engineering*. 2010;38(1):101–116.
- [88] Man J, Shoemake JD, Ma T, Rizzo AE, Godley AR, Wu Q, Mohammadi AM, Bao S, Rich JN, Yu JS. Hyperthermia sensitizes glioma stem-like cells to radiation by inhibiting AKT signaling. *Cancer Research*. 2015 Apr;75(8):1760–1769.
- [89] Atkinson RL, Zhang M, Diagaradjane P, Peddibhotla S, Contreras A, Hilsenbeck SG, Woodward WA, Krishnan S, Chang JC, Rosen JM. Thermal enhancement with optically activated gold nanoshells sensitizes breast cancer stem cells to radiation therapy. *Science Translational Medicine*. 2010 Oct;2(55):55ra79–55ra79.
- [90] Hainfeld JF, Lin L, Slatkin DN, Avraham Dilmanian F, Vadas TM, Smilowitz HM. Gold nanoparticle hyperthermia reduces radiotherapy dose. *Nanomedicine*. 2014 Nov;10(8):1609–1617.
- [91] Torigoe T, Tamura Y, Sato N. Heat shock proteins and immunity: application of hyperthermia for immunomodulation. *International Journal of Hyperthermia*. 2009 Jan;25(8):610–616.
- [92] Datta NR, Grobholz R, Puric E, Bode-Lesniewska B, Lomax N, Khan S, Gaip US, Fuchs B, Bodis S. Enhanced tumour regression in a patient of liposarcoma treated with radiotherapy and hyperthermia: hint for dynamic immunomodulation by hyperthermia. *International Journal of Hyperthermia*. 2015 Apr;0(0):1–4.
- [93] Kim Ys, Lee TH, O'Neill BE. Non-lethal heat treatment of cells results in reduction of tumor initiation and metastatic potential. *Biochemical and Biophysical Research Communications*. 2015;.

- [94] Refaat T, Sachdev S, Sathiaselvan V, Helenowski I, Abdelmoneim S, Pierce MC, Woloschak G, Small Jr W, Mittal B, Kiel KD. Hyperthermia and radiation therapy for locally advanced or recurrent breast cancer. *The Breast*. 2015;.
- [95] Shibata T, Iimuro Y, Yamamoto Y, Maetani Y, Ametani F, Itoh K, Konishi J. Small hepatocellular carcinoma: comparison of radio-frequency ablation and percutaneous microwave coagulation therapy. *Radiology*. 2002 May;223(2):331–337.
- [96] Lu MD, Xu HX, Xie XY, Yin XY, Chen JW, Kuang M, Xu ZF, Liu GJ, Zheng YL. Percutaneous microwave and radiofrequency ablation for hepatocellular carcinoma: a retrospective comparative study. *Journal of Gastroenterology*. 2005 Nov;40(11):1054–1060.
- [97] Ng KKC, Poon RTP, Chan SC, Chok KSH, Cheung TT, Tung H, Chu F, Tso WK, Yu WC, Lo CM, Fan ST. High-intensity focused ultrasound for hepatocellular carcinoma: a single-center experience. *Annals of Surgery*. 2011 May;253(5):981–987.
- [98] Shen HP, Gong JP, Zuo GQ. Role of high-intensity focused ultrasound in treatment of hepatocellular carcinoma. *The American Surgeon*. 2011 Nov;77(11):1496–1501.
- [99] Weis S, Franke A, Mössner J, Jakobsen JC, Schoppmeyer K. Radiofrequency (thermal) ablation versus no intervention or other interventions for hepatocellular carcinoma. *Cochrane Database of Systematic Reviews*. 2013;(12).
- [100] Crabtree T, Puri V, Timmerman R, Fernando H, Bradley J, Decker PA, Paulus R, Putnum Jr JB, Dupuy DE, Meyers B. Treatment of stage I lung cancer in high-risk and inoperable patients: comparison of prospective clinical trials using stereotactic body radiotherapy (RTOG 0236), sublobar resection (ACOSOG Z4032), and radiofrequency ablation (ACOSOG Z4033). *The Journal of Thoracic and Cardiovascular Surgery*. 2013 Mar;145(3):692–699.

- [101] Yang B, Zan Ry, Wang Sy, Li Xl, Wei Ml, Guo Wh, You X, Li J, Liao Zy. Radiofrequency ablation versus percutaneous ethanol injection for hepatocellular carcinoma: a meta-analysis of randomized controlled trials. *World Journal of Surgical Oncology*. 2015 Mar;13(1):96.
- [102] Stafford RJ, Fuentes D, Elliott AA, Weinberg JS, Ahrar K. Laser-induced thermal therapy for tumor ablation. *Critical Reviews in Biomedical Engineering*. 2010;38(1):79–100.
- [103] Wang Y, Jiang T. Understanding high grade glioma: molecular mechanism, therapy and comprehensive management. *Cancer Letters*. 2013 May;331(2):139–146.
- [104] Bogdahn U, Hau P, Stockhammer G, Venkataramana NK, Mahapatra AK, Suri A, Balasubramaniam A, Nair S, Oliushine V, Parfenov V, Poverennova I, Zaaroor M, Jachimczak P, Ludwig S, Schmaus S, Heinrichs H, Schlingensiepen KH. Targeted therapy for high-grade glioma with the TGF- β 2 inhibitor trabedersen: results of a randomized and controlled Phase IIb study. *Neuro-Oncology*. 2011 Jan;13(1):132–142.
- [105] Friedman HS, Prados MD, Wen PY, Mikkelsen T, Schiff D, Abrey LE, Yung WKA, Paleologos N, Nicholas MK, Jensen R, Vredenburgh J, Huang J, Zheng M, Cloughesy T. Bevacizumab alone and in combination with irinotecan in recurrent glioblastoma. *Journal of Clinical Oncology*. 2009 Oct;27(28):4733–4740.
- [106] Vogelbaum MA, Jost S, Aghi MK, Heimberger AB, Sampson JH, Wen PY, MacDonald DR, Van den Bent MJ, Chang SM. Application of novel response/progression measures for surgically delivered therapies for gliomas: Response Assessment in Neuro-Oncology (RANO) Working Group. *Neurosurgery*. 2012 Jan;70(1):234–244.
- [107] Johnson DR, Galanis E. Medical management of high-grade astrocytoma: current and emerging therapies. *Seminars in Oncology*. 2014 Aug;41(4):511–522.

- [108] Carpentier A, McNichols RJ, Stafford RJ, Guichard JP, Reizine D, Delaloge S, Vicaut E, Payen D, Gowda A, George B. Laser thermal therapy: Real-time MRI-guided and computer-controlled procedures for metastatic brain tumors. *Lasers in Surgery and Medicine*. 2011 Dec;43(10):943–950.
- [109] Torres-Reveron J, Tomaszewicz HC, Shetty A, Amankulor NM, Chiang VL. Stereotactic laser induced thermotherapy (LITT): a novel treatment for brain lesions regrowing after radiosurgery. *Journal of Neuro-Oncology*. 2013 Jul;113(3):495–503.
- [110] Hawasli AH, Bagade S, Shimony JS, Miller-Thomas M, Leuthardt EC. Magnetic resonance imaging-guided focused laser interstitial thermal therapy for intracranial lesions: single-institution series. *Neurosurgery*. 2013 Dec;73(6):1007–17.
- [111] Mohammadi AM, Hawasli AH, Rodriguez A, Schroeder JL, Laxton AW, Elson P, Tatter SB, Barnett GH, Leuthardt EC. The role of laser interstitial thermal therapy in enhancing progression-free survival of difficult-to-access high-grade gliomas: a multicenter study. *Cancer Medicine*. 2014 Aug;3(4):971–9.
- [112] Rao MS, Hargreaves EL, Khan AJ, Haffty BG, Danish SF. Magnetic resonance-guided laser ablation improves local control for postradiosurgery recurrence and/or radiation necrosis. *Neurosurgery*. 2014 Jun;74(6):658–67.
- [113] Rahmathulla G, Marko NF, Weil RJ. Cerebral radiation necrosis: A review of the pathobiology, diagnosis and management considerations. *Journal of Clinical Neuroscience*. 2013;20(4):485–502.
- [114] Blonigen BJ, Steinmetz RD, Levin L, Lamba Ma, Warnick RE, Breneman JC. Irradiated volume as a predictor of brain radionecrosis after linear accelerator stereotactic radiosurgery. *International Journal of Radiation Oncology Biology Physics*. 2010;77(4):996–1001.

- [115] Rahmathulla G, Recinos PF, Valerio JE, Chao S, Barnett GH. Laser interstitial thermal therapy for focal cerebral radiation necrosis: a case report and literature review. *Stereotactic and functional neurosurgery*. 2012 Jan;90(3):192–200.
- [116] Patel TR, Chiang VLS. Laser interstitial thermal therapy for treatment of post-radiosurgery tumor recurrence and radiation necrosis. *Photonics & Lasers in Medicine*. 2014 Apr;3(2):95–105.
- [117] Medvid R, Ruiz A, Komotar RJ, Jagid JR, Ivan ME, Quencer RM, Desai MB. Current applications of MRI-guided laser interstitial thermal therapy in the treatment of brain neoplasms and epilepsy: a radiologic and neurosurgical overview. *American Journal of Neuroradiology*. 2015 Jun;.
- [118] de Tisi J, Bell GS, Peacock JL, McEvoy AW, Harkness WF, Sander JW, Duncan JS. The long-term outcome of adult epilepsy surgery, patterns of seizure remission, and relapse: a cohort study. *The Lancet*. 2011 Oct;378(9800):1388–1395.
- [119] Hakimi AS, Spanaki MV, Schuh LA, Smith BJ, Schultz L. A survey of neurologists' views on epilepsy surgery and medically refractory epilepsy. *Epilepsy & Behavior*. 2008 Jul;13(1):96–101.
- [120] Englot DJ, Ouyang D, Garcia PA, Barbaro NM, Chang EF. Epilepsy surgery trends in the United States, 1990–2008. *Neurology*. 2012 Apr;78(16):1200–1206.
- [121] Anderson CT, Noble E, Mani R, Lawler K, Pollard JR. Epilepsy surgery: factors that affect patient decision-making in choosing or deferring a procedure. *Epilepsy Research and Treatment*. 2013 Sep;2013:e309284.
- [122] Hader WJ, Tellez-Zenteno J, Metcalfe A, Hernandez-Ronquillo L, Wiebe S, Kwon CS, Jette N. Complications of epilepsy surgery — a systematic review of focal surgical resections and invasive EEG monitoring. *Epilepsia*. 2013 May;54(5):840–847.

- [123] Hrazdil C, Roberts JI, Wiebe S, Sauro K, Vautour M, Hanson A, Murphy W, Pillay N, Federico P, Jetté N. Patient perceptions and barriers to epilepsy surgery: Evaluation in a large health region. *Epilepsy & Behavior*. 2013 Jul;28(1):52–65.
- [124] Kadipasaoglu CM, Baboyan VG, Conner CR, Chen G, Saad ZS, Tandon N. Surface-based mixed effects multilevel analysis of grouped human electrocorticography. *NeuroImage*. 2014 Nov;101:215–224.
- [125] Akiyama T, McCoy B, Go CY, Ochi A, Elliott IM, Akiyama M, Donner EJ, Weiss SK, Snead OC, Rutka JT, Drake JM, Otsubo H. Focal resection of fast ripples on extraoperative intracranial EEG improves seizure outcome in pediatric epilepsy. *Epilepsia*. 2011 Oct;52(10):1802–1811.
- [126] Ding YS, Chen BB, Glielmi C, Friedman K, Devinsky O. A pilot study in epilepsy patients using simultaneous PET/MR. *American Journal of Nuclear Medicine and Molecular Imaging*. 2014 Aug;4(5):459–470.
- [127] Kelly PJ, Alker GJ. A method for stereotactic laser microsurgery in the treatment of deep-seated CNS neoplasms. *Applied Neurophysiology*. 1980;43(3-5):210–215.
- [128] Jolesz FA, Bleier AR, Jakab P, Ruenzel PW, Huttli K, Jako GJ. MR imaging of laser-tissue interactions. *Radiology*. 1988 Jul;168(1):249–253.
- [129] Ishihara Y, Calderon A, Watanabe H, Okamoto K, Suzuki Y, Kuroda K, Suzuki Y. A precise and fast temperature mapping using water proton chemical shift. *Magnetic Resonance in Medicine*. 1995 Dec;34(6):814–823.
- [130] De Poorter J. Noninvasive MRI thermometry with the proton resonance frequency method: study of susceptibility effects. *Magnetic Resonance in Medicine*. 1995 Sep;34(3):359–367.

- [131] De Poorter J, De Wagter C, De Deene Y, Thomsen C, Ståhlberg F, Achten E. Noninvasive MRI thermometry with the proton resonance frequency (PRF) method: in vivo results in human muscle. *Magnetic Resonance in Medicine*. 1995 Jan;33(1):74–81.
- [132] Fuentes D, Yung J, Hazle JD, Weinberg JS, Stafford RJ. Kalman Filtered MR Temperature Imaging for Laser Induced Thermal Therapies. *IEEE Transactions on Medical Imaging*. 2012 Apr;31(4):984–994.
- [133] Roujol S, Moonen C, de Senneville B. Motion correction techniques for MR-guided HIFU ablation of abdominal organs. In: Chen C, editor. *Frontiers of Medical Imaging*. World Scientific; 2014. p. 355–376.
- [134] Pearce JA. Relationship between Arrhenius models of thermal damage and the CEM 43 thermal dose. *Proceedings of SPIE*. 2009 Feb;7181(1):718104–718104–15.
- [135] Henriques FC, Moritz AR. Studies of thermal injury: I. The conduction of heat to and through skin and the temperatures attained therein. A theoretical and an experimental investigation. *The American Journal of Pathology*. 1947 Jul;23(4):530–49.
- [136] Takegami K, Kaneko Y, Watanabe T, Maruyama T, Matsumoto Y, Nagawa H. Polyacrylamide gel containing egg white as new model for irradiation experiments using focused ultrasound. *Ultrasound in Medicine & Biology*. 2004 Oct;30(10):1419–1422.
- [137] Bjeldanes LF, Morris MM, Felton JS, Healy S, Stuermer D, Berry P, Timourian H, Hatch FT. Mutagens from the cooking of food. II. Survey by Ames/Salmonella test of mutagen formation in the major protein-rich foods of the American diet. *Food and Chemical Toxicology*. 1982;20(4):357–363.

- [138] Mañas P, Pagán R, Alvarez I, Condón Usón S. Survival of *Salmonella senftenberg* 775 W to current liquid whole egg pasteurization treatments. *Food Microbiology*. 2003 Oct;20(5):593–600.
- [139] Vega C, Mercadé-Prieto R. Culinary biophysics: on the nature of the 6X degree C egg. *Food Biophysics*. 2011 Jan;6(1):152–159.
- [140] Yung JP, Shetty A, Elliott A, Weinberg JS, McNichols RJ, Gowda A, Hazle JD, Stafford RJ. Quantitative comparison of thermal dose models in normal canine brain. *Medical Physics*. 2010;37(10):5313–5321.
- [141] Hazle JD, Stafford RJ, Price RE. Magnetic resonance imaging-guided focused ultrasound thermal therapy in experimental animal models: correlation of ablation volumes with pathology in rabbit muscle and VX2 tumors. *Journal of Magnetic Resonance Imaging*. 2002 Feb;15(2):185–194.
- [142] Carpentier A, Itzcovitz J, Payen D, George B, McNichols RJ, Gowda A, Stafford RJ, Guichard JP, Reizine D, Delaloge S, Vicaud E. Real-time magnetic resonance-guided laser thermal therapy for focal metastatic brain tumors. *Neurosurgery*. 2008 Jul;63(July):ONS21–ONS29.
- [143] Jethwa PR, Barrese JC, Gowda A, Shetty A, Danish SF. Magnetic resonance thermometry-guided laser-induced thermal therapy for intracranial neoplasms: initial experience. *Neurosurgery*. 2012;71:ons133—ons145.
- [144] Hawasli AH, Ray WZ, Murphy RK, Dacey Jr RG, Leuthardt EC. Magnetic resonance imaging-guided focused laser interstitial thermal therapy for subinsular metastatic adenocarcinoma: technical case report. *Neurosurgery*. 2012;70:332–7.
- [145] McNichols RJ, Gowda A, Kangasniemi M, Bankson Ja, Price RE, Hazle JD. MR thermometry-based feedback control of laser interstitial thermal therapy at 980 nm. *Lasers in surgery and medicine*. 2004 Jan;34(1):48–55.

- [146] Ulrich F. Interstitial laser irradiation of cerebral gliomas. *Medical Laser Application*. 2005 Jun;20(2):119–124.
- [147] Fuentes D, Feng Y, Elliott A, Shetty A, McNichols RJ, Oden JT, Stafford RJ. Adaptive real-time bioheat transfer models for computer-driven MR-guided laser induced thermal therapy. *IEEE transactions on bio-medical engineering*. 2010 May;57(5):1024–30.
- [148] Woodrum DA, Gorny KR, Mynderse LA, Amrami KK, Felmlee JP, Bjarnason H, Garcia-Medina OI, McNichols RJ, Atwell TD, Callstrom MR. Feasibility of 3.0 T magnetic resonance imaging-guided laser ablation of a cadaveric prostate. *Urology*. 2010;75(6):1514—e1.
- [149] Fuentes D, Yung J, Hazle J, Weinberg J, Stafford R. Kalman filtered MR temperature imaging for laser induced thermal therapies. *IEEE Transactions on Medical Imaging*. 2011 Jan;31:984–94.
- [150] Roujol S, Denis de Senneville B, Hey S, Moonen C, Ries M. Robust adaptive extended Kalman filtering for real time MR-thermometry guided HIFU interventions. *IEEE Transactions on Medical Imaging*. 2012 Mar;31(3):533–542.
- [151] Potocki JK, Tharp HS. Concurrent hyperthermia estimation schemes based on extended Kalman filtering and reduced-order modelling. *International Journal of Hyperthermia*. 1993;.
- [152] Todd N, Payne A, Parker DL. Model predictive filtering for improved temporal resolution in MRI temperature imaging. *Magnetic Resonance in Medicine*. 2010 May;63(5):1269–79.
- [153] Mougenot C, Quesson B, de Senneville BD, de Oliveira PL, Sprinkhuizen S, Palussière J, Grenier N, Moonen CTW. Three-dimensional spatial and temporal temperature

- control with MR thermometry-guided focused ultrasound (MRgHIFU). *Magnetic Resonance in Medicine*. 2009 Mar;61(3):603–14.
- [154] Fuentes D, Oden JT, Diller KR, Hazle JD, Elliott A, Shetty A, Stafford RJ. Computational modeling and real-time control of patient-specific laser treatment of cancer. *Annals of Biomedical Engineering*. 2009 Apr;37(4):763–82.
- [155] Minden V, Smith B, Knepley MG. Preliminary implementation of PETSc using GPUs. In: Yuen DA, Wang L, Chi X, Johnsson L, Ge W, Shi Y, editors. *GPU Solutions to Multi-Scale Problems in Science and Engineering*. springer ed. Berlin; 2013. p. 131–140.
- [156] Deisher M, Smelyanskiy M, Nickerson B, Lee VW, Chuvelev M, Dubey P. Designing and dynamically load balancing hybrid LU for multi/many-core. *Computer Science - Research and Development*. 2011 Apr;26(3-4):211–220.
- [157] Chen CCR, Miga MI, Galloway RL. Optimizing electrode placement using finite-element models in radiofrequency ablation treatment planning. *IEEE Transactions on Bio-Medical Engineering*. 2009;56(2):237–245.
- [158] de Greef M, Kok HP, Correia D, Bel A, Crezee J. Optimization in hyperthermia treatment planning: the impact of tissue perfusion uncertainty. *Medical Physics*. 2010;37(9):4540–1.
- [159] Fuentes D, Cardan R, Stafford RJ, Yung J, Dodd III GD, Feng Y. High-fidelity computer models for prospective treatment planning of radiofrequency ablation with in vitro experimental correlation. *Journal of Vascular and Interventional Radiology*. 2010 Nov;21(11):1725–1732.
- [160] Pennes HH. Analysis of tissue and arterial blood temperatures in the resting human forearm. *Journal of Applied Physiology*. 1948;1(2):1725–32.

- [161] Xiu D. *Numerical Methods for Stochastic Computations: A Spectral Method Approach*. Princeton, NJ, USA: Princeton University Press; 2010.
- [162] Dos Santos I, Haemmerich D, Schutt D, da Rocha AF, Menezes LR. Probabilistic finite element analysis of radiofrequency liver ablation using the unscented transform. *Physics in Medicine and Biology*. 2009 Feb;54(3):627–40.
- [163] Fahrenholtz S, Fuentes D, Stafford R, Hazle J. SU-F-BRCD-08: Uncertainty quantification by generalized polynomial chaos for MR-guided laser induced thermal therapy. In: *Proceeding at the 54th Annual Meeting for the American Association of Physicists*. vol. 39. Charlotte, NC: AAPM; 2012. p. 3857.
- [164] Niederreiter H. Quasi-Monte Carlo methods and pseudo-random numbers. *Bulletin of the American Mathematical Society*. 1978;84(6):957–1041.
- [165] McKay MD, Beckman RJ, Conover WJ. A comparison of three methods for selecting values of input variables in the analysis of output from a computer code. *Technometrics*. 1979 May;21(2):239–245.
- [166] Smith RL. Efficient Monte Carlo procedures for generating points uniformly distributed over bounded regions. *Operations Research*. 1984 Nov;32(6):1296–1308.
- [167] Prudencio E, Schulz K. The parallel C++ statistical library QUESO: Quantification of Uncertainty for Estimation, Simulation and Optimization. In: *In Euro-Par 2011: Parallel Processing Workshops*. Berlin: Springer; 2012. p. 398–407.
- [168] Prudencio E, Cheung SH. Parallel adaptive multilevel sampling algorithms for the Bayesian analysis of mathematical models. *International Journal for Uncertainty Quantification*. 2012;2(3):215–237.
- [169] Wiener N. The homogeneous chaos. *American Journal of Mathematics*. 1938 Oct;60(4):897–936.

- [170] Ghanem RG, Spanos PD. *Stochastic Finite Elements: A Spectral Approach*. New York, NY, USA: Springer-Verlag New York, Inc.; 1991.
- [171] Xiu D, Karniadakis GE. The Wiener-Askey polynomial chaos for stochastic differential equations. *SIAM Journal on Scientific Computing*. 2002;24(2):619–664.
- [172] Xiu D, Karniadakis GE. Modeling uncertainty in steady state diffusion problems via generalized polynomial chaos. *Computer Methods in Applied Mechanics and Engineering*. 2002;191:4927–4948.
- [173] Geneser SE, Hinkle JD, Kirby RM, Wang B, Salter B, Joshi S. Quantifying variability in radiation dose due to respiratory-induced tumor motion. *Medical Image Analysis*. 2011 Jul;15(4):640–649.
- [174] Reagan MT, Najm HN, Ghanem RG, Knio OM. Uncertainty quantification in reacting-flow simulations through non-intrusive spectral projection. *Combustion and Flame*. 2003 Feb;132(3):545–555.
- [175] Cassell JS, Williams MMR. An approximate method for solving radiation and neutron transport problems in spatially stochastic media. *Annals of Nuclear Energy*. 2008 May;35(5):790–803.
- [176] Kewlani G, Iagnemma K. A multi-element generalized polynomial chaos approach to analysis of mobile robot dynamics under uncertainty. In: *IEEE/RSJ International Conference on Intelligent Robots and Systems*. IEEE; 2009. p. 1177–1182.
- [177] Yaroslavsky AN, Schulze PC, Yaroslavsky IV, Schober R, Ulrich F, Schwarzmaier HJ. Optical properties of selected native and coagulated human brain tissues in vitro in the visible and near infrared spectral range. *Physics in medicine and biology*. 2002 Jun;47(12):2059–73.
- [178] Kreith F. *The CRC Handbook of Thermal Engineering*. Berlin: Springer; 2000.

- [179] Huttunen JMJ, Huttunen T, Malinen M, Kaipio JP. Determination of heterogeneous thermal parameters using ultrasound induced heating and MR thermal mapping. *Physics in Medicine and Biology*. 2006 Feb;51(4):1011–32.
- [180] Valvano JW. Tissue thermal properties and perfusion. In: Welch AJ, Gemert MJC, editors. *Optical-Thermal Response of Laser-Irradiated Tissue*. Springer Netherlands; 2011. p. 455–485.
- [181] Madsen SJ, Wilson BC. Optical properties of brain tissue. In: Madsen SJ, editor. *Optical Methods and Instrumentation in Brain Imaging and Therapy*. New York, NY: Springer New York; 2013. p. 1–22.
- [182] Beek JF, Blokland P, Posthumus P, Aalders M, Pickering JW, Sterenborg HJCM, van Gemert MJC. In vitro double-integrating-sphere optical properties of tissues between 630 and 1064 nm. *Physics in Medicine and Biology*. 1997 Nov;42(11):2255–2261.
- [183] Duck FA. *Physical Properties of Tissue: a Comprehensive Reference Book*. Academic Pr; 1990.
- [184] Cooper TE, Trezek GJ. Correlation of thermal properties of some human tissue with water content. *Aerospace Medicine*. 1971 Jan;42(1):24–27.
- [185] Kapin MA, Ferguson JL. Hemodynamic and regional circulatory alterations in dog during anaphylactic challenge. *American Journal of Physiology - Heart and Circulatory Physiology*. 1985 Aug;249(2):H430–H437.
- [186] Atzler E, Richter F. Über die Wärmekapazität des arteriellen und venösen Blutes. *Beiträge zur chemischen Physiologie und Pathologie*. 1920;112:310–312.
- [187] Valvano JW, Cochran JR, Diller KR. Thermal conductivity and diffusivity of bio-materials measured with self-heated thermistors. *International Journal of Thermophysics*. 1985 May;6(3):301–311.

- [188] Pickering JW, Prahl Sa, van Wieringen N, Beek JF, Sterenborg HJ, van Gemert MJ. Double-integrating-sphere system for measuring the optical properties of tissue. *Applied optics*. 1993 Feb;32(4):399–410.
- [189] Yaroslavsky I, Yaroslavsky A. Inverse hybrid technique for determining the optical properties of turbid media from integrating-sphere measurements. *Applied Optics*. 1996;35(34):6797–809.
- [190] Germer CT, Roggan A, Ritz JP, Isbert C, Albrecht D, Müller G, Buhr HJ. Optical properties of native and coagulated human liver tissue and liver metastases in the near infrared range. *Lasers in Surgery and Medicine*. 1998 Jan;23(4):194–203.
- [191] Schwarzmaier Hj, Yaroslavsky A, Yaroslavsky I, Goldbacha T, Kahn T, Ulrichc F, Schulze PC, Schober R. Optical properties of native and coagulated human brain structures. In: *Proceedings of SPIE, Lasers in Surgery: Advanced Characterization, Therapeutics, and Systems VII*. vol. 2970; 1997. p. 492–499.
- [192] Ritz JP, Roggan A, Germer CT, Isbert C, Müller G, Buhr HJ. Continuous changes in the optical properties of liver tissue during laser-induced interstitial thermotherapy. *Lasers in Surgery and Medicine*. 2001 Jan;28(4):307–12.
- [193] Friebel M, Do K, Hahn A, Mu G, Berlin D, Medizin L, Universita F. Optical properties of circulating human blood in the wavelength range 400-2500 nm. *Journal of Biomedical Optics*. 1999;4(1):36–46.
- [194] Bankson JA, Stafford RJ, Hazle JD. Partially parallel imaging with phase-sensitive data: Increased temporal resolution for magnetic resonance temperature imaging. *Magnetic Resonance in Medicine*. 2005;53(3):658–665.
- [195] Dickey DJ, Partridge K, Moore RB, Tulip J. Light dosimetry for multiple cylindrical diffusing sources for use in photodynamic therapy. *Physics in Medicine and Biology*. 2004 Jul;49(14):3197–3208.

- [196] Blacker TD, Bohnhoff W, Edwards T. *CUBIT Mesh Generation Environment. Volume 1: Users Manual*. Albuquerque, NM, USA: Sandia National Laboratories; 2004.
- [197] Eldred MS, Giunta AA, van Bloemen Waanders BG, Wojtkiewicz SF, Hart WE, All-eva MP. *DAKOTA, a Multilevel Parallel Object-Oriented Framework for Design Optimization, Parameter Estimation, Uncertainty Quantification, and Sensitivity Analysis: Version 4.1 Reference Manual*. Albuquerque, NM, USA: Sandia National Laboratories; 2007.
- [198] Butler T, Dawson C, Wildey T. A posteriori error analysis of stochastic differential equations using polynomial chaos expansions. *SIAM Journal on Scientific Computing*. 2011;33(3):1267–1291.
- [199] Babuška I, Nobile F, Tempone R. Worst case scenario analysis for elliptic problems with uncertainty. *Numerische Mathematik*. 2005 Jun;101(2):185–219.
- [200] MacLellan CJ, Fuentes D, Elliott AM, Schwartz J, Hazle JD, Stafford RJ. Estimating nanoparticle optical absorption with magnetic resonance temperature imaging and bioheat transfer simulation. *International Journal of Hyperthermia*. 2014 Dec;30(1):47–55.
- [201] Fasano A, Hömberg D, Naumov D. On a mathematical model for laser-induced thermotherapy. *Applied Mathematical Modelling*. 2010 Dec;34(12):3831–3840.
- [202] Ibanez L, Schroeder W, Ng L, Cates J. *The ITK Software Guide*. Clifton Park, NY: Kitware; 2005.
- [203] Henderson A, Ahrens J. *The ParaView Guide: a Parallel Visualization Application*. Clifton Park, NY: Kitware; 2004.
- [204] Kirk BS, Peterson JW. *libMesh-a C++ Finite Element Library*; 2003.

- [205] Siegel R, Naishadham D, Jemal A. Cancer statistics. *CA: A Cancer Journal for Clinicians*. 2013;63(1):11–30.
- [206] Kalkanis SN, Linskey ME. Evidence-based clinical practice parameter guidelines for the treatment of patients with metastatic brain tumors: introduction. *Journal of Neuro-Oncology*. 2010 Jan;96(1):7–10.
- [207] Gavrilovic IT, Posner JB. Brain metastases: epidemiology and pathophysiology. *Journal of Neuro-Oncology*. 2005 Oct;75(1):5–14.
- [208] Bafaloukos D, Gogas H. The treatment of brain metastases in melanoma patients. *Cancer Treatment Reviews*. 2004 Oct;30(6):515–520.
- [209] Alexander E, Moriarty TM, Davis RB, Wen PY, Fine HA, Black PM, Kooy HM, Loeffler JS. Stereotactic radiosurgery for the definitive, noninvasive treatment of brain metastases. *Journal of the National Cancer Institute*. 1995 Jan;87(1):34–40.
- [210] Schwarzmaier HJ, Eickmeyer F, Fiedler VU, Ulrich F. Basic principles of laser induced interstitial thermotherapy in brain tumors. *Medical Laser Application*. 2002;17(2):147–158.
- [211] Schulze PC, Vitzthum HE, Goldammer A, Schneider JP, Schober R. Laser-induced thermotherapy of neoplastic lesions in the brain—underlying tissue alterations, MRI-monitoring and clinical applicability. *Acta Neurochirurgica*. 2004 Aug;146(8):803–12.
- [212] de Senneville BD, Quesson B, Moonen CTW. Magnetic resonance temperature imaging. *International Journal of Hyperthermia*. 2005 Jan;21:515–531.
- [213] Stafford RJ, Shetty A, Elliott AM, Klumpp SA, McNichols RJ, Gowda A, Hazle JD, Ward JF. Magnetic resonance guided, focal laser induced interstitial thermal therapy in a canine prostate model. *The Journal of Urology*. 2010 Oct;184(4):1514–20.

- [214] McDannold N, Tempany CM, Fennessy FM, So MJ, Rybicki FJ, Stewart EA, Jolesz FA, Hynynen K. Uterine leiomyomas: MR imaging-based thermometry and thermal dosimetry during focused ultrasound thermal ablation. *Radiology*. 2006 Jul;240(1):263–272.
- [215] McNichols RJ, Kangasniemi M, Gowda A, Bankson JA, Price RE, Hazle JD. Technical developments for cerebral thermal treatment: water-cooled diffusing laser fibre tips and temperature-sensitive MRI using intersecting image planes. *International Journal of Hyperthermia*. 2004 Feb;20(1):45–56.
- [216] Breiman L. Statistical modeling: the two cultures (with comments and a rejoinder by the author). *Statistical Science*. 2001 Aug;16(3):199–231.
- [217] Hastie T, Tibshirani R, Friedman J. The elements of statistical learning: data mining, inference and prediction. *The Mathematical Intelligencer*. 2005 Nov;27(2):83–85.
- [218] Stone M. Cross-validatory choice and assessment of statistical predictions. *Journal of the Royal Statistical Society Series B (Methodological)*. 1974 Jan;36(2):111–147.
- [219] Geisser S. The predictive sample reuse method with applications. *Journal of the American Statistical Association*. 1975 Jun;70(350):320–328.
- [220] Kohavi R. A study of cross-validation and bootstrap for accuracy estimation and model selection. In: *Proceedings of the Fourteenth International Joint Conference on Artificial Intelligence*. San Francisco, CA; 1995. p. 1137–1143.
- [221] Browne M. Cross-validation methods. *Journal of Mathematical Psychology*. 2000 Mar;44(1):108–132.
- [222] Arlot S, Celisse A. A survey of cross-validation procedures for model selection. *Statistics Surveys*. 2010;4:40–79.

- [223] Stafford RJ, Price RE, Diederich CJ, Kangasniemi M, Olsson LE, Hazle JD. Interleaved echo-planar imaging for fast multiplanar magnetic resonance temperature imaging of ultrasound thermal ablation therapy. *Journal of Magnetic Resonance Imaging*. 2004 Oct;20(4):706–714.
- [224] Pearce J, Thomsen S. Rate process analysis of thermal damage. In: Welch AJ, Gemert MJC, editors. *Optical-Thermal Response of Laser-Irradiated Tissue*. Lasers, Photonics, and Electro-Optics. Springer US; 1995. p. 561–606.
- [225] Yeniaras E, Fuentes DT, Fahrenholtz SJ, Weinberg JS, Maier F, Hazle JD, Stafford RJ. Design and initial evaluation of a treatment planning software system for MRI-guided laser ablation in the brain. *International Journal of Computer Assisted Radiology and Surgery*. 2013 Oct;9(4):659–667.
- [226] Diller KR, Valvano JW, Pearce JA. Bioheat transfer. In: Kreith F, Goswami Y, editors. *The CRC Handbook of Mechanical Engineering*. 2nd ed. Boca Raton: CRC Press; 2005. p. 4–278.
- [227] Welch AJ, Gemert. *Optical-Thermal Response of Laser-Irradiated Tissue*. 1st ed. Welch AJ, Gemert MJC, editors. Springer; 1995.
- [228] Medina DS, St-cyr A, Warburton T. OCCA : A unified approach to multi-threading languages. *arXiv*. 2014 Mar;p. 1–25.
- [229] Boyce WE, DiPrima RC, Haines CW. *Elementary Differential Equations and Boundary Value Problems*. 7th ed. New York, NY, USA: Wiley; 2001.
- [230] Giordano MA, Gutierrez G, Rinaldi C. Fundamental solutions to the bioheat equation and their application to magnetic fluid hyperthermia. *International Journal of Hyperthermia*. 2010 Jan;26(5):475–84.

- [231] Vyas R. Green's function solution to the tissue bioheat equation. *Medical Physics*. 1992;19(5):1319.
- [232] Deng ZS, Liu J. Analytical study on bioheat transfer problems with spatial or transient heating on skin surface or inside biological bodies. *Journal of Biomechanical Engineering*. 2002 Dec;124(6):638–649.
- [233] Zou KH, Wells WM, Kikinis R, Warfield SK. Three validation metrics for automated probabilistic image segmentation of brain tumours. *Statistics in Medicine*. 2004 Apr;23(8):1259–82.
- [234] Mueller E, Guo X, Scheichl R, Shi S. Matrix-free GPU implementation of a preconditioned conjugate gradient solver for anisotropic elliptic PDEs. *Computing and Visualization in Science*. 2013 Sep;16(2):18.
- [235] Knepley MG, Terrel AR. Finite element integration on GPUs. *ACM Transactions on Mathematical Software*. 2013 Feb;39(2):1–13.
- [236] Jaynes ET, Bretthorst GL. *Probability Theory: The Logic of Science*. Cambridge University Press; 2003.
- [237] Knepley MG, Brown J, Rupp K, Smith BF. Achieving high performance with unified residual evaluation. *arXiv*. 2013 Sep;p. 4.
- [238] Knepley MG, Kupp K, Terrel AR. Finite element integration with quadrature on accelerators. *ACM Transactions on Mathematical Software*. 2015;0(0).
- [239] Carp SA, Prahl SA, Venugopalan V. Radiative transport in the delta-P1 approximation: accuracy of fluence rate and optical penetration depth predictions in turbid semi-infinite media. *Journal of Biomedical Optics*. 2004;9(3):632–647.
- [240] Fuentes D, Elliott A, Weinberg JS, Shetty A, Hazle JD, Stafford RJ. An inverse problem approach to recovery of in vivo nanoparticle concentrations from thermal

image monitoring of MR-guided laser induced thermal therapy. *Annals of Biomedical Engineering*. 2012 Aug;41(1):100–111.

- [241] Diller KR, Oden JT, Bajaj C, Browne JC, Hazle JD, Babuška I, Bass J, Biduat L, Demkowicz L, Elliott A, Feng Y, Fuentes D, Goswami S, Hawkins A, Khoshnevis B, Kwon S, Prudhomme S, Stafford RJ. Computational infrastructure for the real-time patient-specific treatment of cancer. In: *Numerical Implementation of Bioheat Models and Equations*. New York, NY: CRC Press; 2009. .
- [242] Feng Y, Fuentes D, Hawkins A, Bass JM, Rylander MN. Optimization and real-time control for laser treatment of heterogeneous soft tissues. *Computer Methods in Applied Mechanics and Engineering*. 2009;198(21):1742–1750.
- [243] Rasmussen CE, Williams CKI. *Gaussian Processes for Machine Learning*. MIT Press; 2006.
- [244] Constantinescu EM, Anitescu M. Physics-based covariance models for Gaussian processes with multiple outputs. *International Journal for Uncertainty Quantification*. 2013;3(1):47–71.
- [245] Menze B, Jakab A, Bauer S, Kalpathy-Cramer J, Farahani K, Kirby J, Burren Y, Porz N, Slotboom J, Wiest R, Lanczi L, Gerstner E. The Multimodal Brain Tumor Image Segmentation Benchmark (BRATS). *IEEE Transactions on Medical Imaging*. 2014;PP(99):1–32.
- [246] Li H, Dong L, Zhang L, Yang JN, Gillin MT, Zhu XR. Toward a better understanding of the gamma index: investigation of parameters with a surface-based distance methoda). *Medical Physics*. 2011 Dec;38(12):6730–6741.
- [247] Nael K, Meshksar A, Liebeskind DS, Wang DJJ, Ellingson BM, Salamon N, Villablanca JP. Periprocedural arterial spin labeling and dynamic susceptibility contrast

perfusion in detection of cerebral blood flow in patients with acute ischemic syndrome. *Stroke*. 2013 Mar;44(3):664–670.

- [248] Johnston ME, Lu K, Maldjian JA, Jung Y. Multi-TI arterial spin labeling MRI with variable TR and bolus duration for cerebral blood flow and arterial transit time mapping. *IEEE Transactions on Medical Imaging*. 2015 Jun;34(6):1392–1402.
- [249] Henrikson J. Completeness and total boundedness of the Hausdorff metric. *MIT Undergraduate Journal of Mathematics*. 1999;.

Vita

Samuel John Fahrenholtz was born on May Day 1987 to Randall Kevin Fahrenholtz, M.D., and Janice Faye Fahrenholtz in Kingman, Kansas. His two older sisters are Ashley Jo Angell and Cameron Beth Jeter, Ph.D. His entire primary and secondary education was in the Goddard Unified School District in Kansas. After graduating as the sole valedictorian of Goddard H.S. in 2005, Samuel matriculated in Kansas State University and sought a Bachelor of Science degree. He finished his physics B.Sc. in 2009 and began a doctor of philosophy degree in medical physics at The University of Texas M.D. Anderson Cancer Center in Houston, Texas. In 2010, Samuel married Monica Marie Frey, *née*.

Permanent address as of December 18, 2015:

2425 Underwood Street

Unit 156

Houston, Texas 77030